

Feasibility Investigation of General Time-Domain Unsteady Aerodynamics of Rotors

Wayne Johnson

Johnson Aeronautics
Palo Alto, California

Prepared for
Ames Research Center
CONTRACT NUMBER NAS2-13125
October 1990



National Aeronautics and
Space Administration

Ames Research Center
Moffett Field, California 94035-1000



TABLE OF CONTENTS

	Page
SYMBOLS AND ABBREVIATIONS.....	v
SUMMARY.....	1
1. INTRODUCTION.....	3
1.1 Background.....	3
1.2 Research Requirements.....	4
1.3 Objectives of the Feasibility Investigation.....	5
2. THEORY.....	7
2.1 General Theory.....	7
2.2 Rotor Aeroelastic Problems.....	11
2.2.1 Flap Equation.....	11
2.2.2 Flap-Pitch Equations.....	14
2.3 Rotor Wake Equations.....	16
2.3.1 Integral Equation.....	16
2.3.2 Differential Equations.....	20
2.4 Wake Aerodynamic Models.....	24
2.4.1 Undistorted Wake.....	24
2.4.2 Rolled Up Wake.....	25
2.4.3 Wake Geometry Perturbations.....	27
2.4.4 Rotor Velocity Perturbations.....	29
3. RESULTS.....	32
3.1 Previous Results.....	32
3.2 Undistorted Wake.....	33
3.2.1 Impulse Response.....	33
3.2.2 System Function.....	34
3.2.3 Identification.....	37
3.2.4 Model Order Reduction.....	40
3.3 Rolled Up Wake.....	42
3.4 Wake Geometry Perturbations.....	43
4. CONCLUSIONS AND RECOMMENDATIONS.....	45
4.1 Conclusions.....	45
4.1.1 Identification.....	45
4.1.2 Model Order Reduction.....	45
4.1.3 Wake Geometry Perturbations.....	45
4.2 Recommendations.....	46
REFERENCES.....	47

SYMBOLS AND ABBREVIATIONS

a	two-dimensional lift-curve-slope
c	blade chord
C_T	rotor thrust coefficient, $T/\rho(\Omega R)^2\pi R^2$
g	generalized coordinate vector for circulation
h	impulse response
H	system function
I_b	blade flap moment of inertia
l	generalized coordinate vector for inflow
M_f	blade pitch aerodynamic moment
M_F	blade flap aerodynamic moment
N	number of blades
p	inflow radial mode shapes
P	matrix of inflow radial mode shapes
q	circulation radial mode shapes
Q	matrix of circulation radial mode shapes
r	blade radial station
R	blade radius
s	Laplace variable; wake distance
t	time
T	rotor thrust; multiblade coordinate transform
W	weighting matrix
z	hub vertical motion; wake vertical distance
β	blade flap degree of freedom
γ	blade Lock number, $\rho acR^4/I_b$
$\Delta\psi$	azimuth distance between blades, $2\pi/N$
Γ	blade bound circulation
θ	blade pitch control input or degree of freedom
λ	inflow velocity
μ	rotor velocity perturbation
ν	blade flap natural frequency
ρ	air density; blade radial coordinate
σ	rotor solidity (ratio of blade area to disk area)
τ	time
ϕ	wake age
ψ	blade azimuth angle
ω	frequency
Ω	rotor rotational speed

subscripts

non	nonrotating
rot	rotating
s	shed wake
t	trailed wake
V	rotor velocity perturbation
$0,nc,ns,N/2$	multiblade coordinates
0	collective mode
1c,1s	cyclic modes
nc,ns	reactionless modes
N/2	differential collective mode

FEASIBILITY INVESTIGATION OF GENERAL TIME-DOMAIN UNSTEADY AERODYNAMICS OF ROTORS

SUMMARY

The feasibility of a general theory for the time-domain unsteady aerodynamics of helicopter rotors is investigated. The wake theory gives a linearized relation between the downwash and the wing bound circulation, in terms of the impulse response obtained directly in the time domain. This approach makes it possible to treat general wake configurations, including discrete wake vorticity with rolled-up and distorted geometry. The investigation establishes the approach for model order reduction; determines when a constrained identification method is needed; verifies the formulation of the theory for rolled-up, distorted trim wake geometry; and verifies the formulation of the theory for wake geometry perturbations. The basic soundness of the approach is demonstrated by the results presented. A research program to complete the development of the method is outlined. The result of this activity will be an approach for analyzing the aeroelastic stability and response of helicopter rotors, while retaining the important influence of the complicated rotor wake configuration.



1. INTRODUCTION

1.1 Background

With current computational techniques, there is increased interest in the aeroelastic behavior of general rotary-wing configurations undergoing arbitrary motion. For such problems, a time-domain model of the aerodynamics is required, preferably in the form of ordinary differential equations, from which the rotor stability and response can be calculated. To be consistent with the sophistication of these problems and computational methods, an aerodynamic theory is needed that does not require significant approximations for the wake configuration.

The unsteady aerodynamic loading of wings has traditionally been analyzed in the frequency domain, usually with the objective of relating the wing loading to the wing motion. That approach is found in both traditional work, such as Theodorsen's and Wagner's functions (Bisplinghoff, Ashley, and Halfman, 1955), and in recent work. Moreover, much of the recent work is still focused on the frequency domain (Laplace form in general), notably analytic continuation of solutions from harmonic to arbitrary motion (Vepa, 1977; Edwards, 1977; Edwards, Ashley, and Breakwell, 1979; Venkatesan and Friedmann, 1986; Brase and Eversman, 1987), although there are time domain aerodynamic analyses as well (Stark, 1984; Miyazawa and Washizu, 1983). To obtain the loading response to motion, it is necessary to completely solve for the influence of the wake. With this approach it is possible to make much progress analytically, particularly in the frequency domain, but the derivation and results are complicated and it is usually necessary to make significant approximations regarding the wake configuration. Rotary wing aerodynamics has a long history of dealing with wake-induced velocities directly (Johnson, 1980), yet unsteady aerodynamic analyses for rotors have still required simplified models, such as an actuator disk (Miller, 1964; Pitt and Peters, 1981) or use of the acceleration potential (Peters and He, 1987).

The present work takes a different approach. The unsteady aerodynamic problem is split into separate wing and wake analyses. The wing theory must be formulated in terms of the wake-induced velocity (and include the non-circulatory loads). The wake analysis must obtain the induced downwash at the wing, from the wing circulatory loading. A linear relation between the downwash and the bound circulation will be obtained directly in the time domain, in terms of an impulse response. With this approach it is possible to treat general wake configurations, for example: (a) not just planar wake sheets, but also distorted wake geometry, rolled-up tip vortices, and multiple wings (such as wing-tail-canard, or multi-blade rotors); (b) not just time-invariant wake geometry (straight flight of fixed wings, or hovering rotors), but also arbitrary motion (including the periodic geometry of rotors in forward flight); (c) not just prescribed wake geometry, but also perturbations to the wake geometry produced by the unsteady loading (important for multiple wings, and for rotors at hover and low speed). Moreover, with this approach it is possible

to make direct use of wake models developed for the trim loading problem. Such models are generally much more sophisticated than those used for aeroelasticity analyses. By making use of existing trim wake models, both the development effort and the computation time can be significantly reduced.

The principal assumption of the work so far is that an incompressible wake of concentrated vorticity is being dealt with. The objective is to derive a linearized relation between the downwash and circulation, that can be used in aeroelastic analyses of the perturbed wing motion. The restriction to an incompressible wake does not preclude incorporating compressible effects in the wing model in some fashion; a compressible version of the theory is one of the areas requiring research. After obtaining a linear model in terms of the impulse response, there remains the task of identifying an approximate differential equation representation, probably with model order reduction.

1.2 Research Requirements

This section outlines the research required to complete the development of the analysis, including research to extend the theory, establish methods for implementing the theory, and develop unsteady aerodynamic models for particular rotorcraft problems.

a) Wake theory

The manner in which rolled-up and distorted trim wake geometry can be treated must be established, in particular the relation of the strength of the rolled-up wake to the wing bound circulation. Wake geometry perturbations are produced by both loading and flight speed changes. The formulation of the theory to account for wake geometry perturbations must be completed. The theory can also be extended to a compressible wake (consistent with a compressible wing model), and to a lifting-surface or panel model for the wing

b) Model order reduction

The functional form of the downwash series must be established (the answer may be problem dependent). The downwash series must be consistent with the aerodynamics of the wake model. The objective is to find a series that produces accurate results with a small number of modes.

c) Identification

The identification method must be developed. Entirely new techniques are probably not needed for this theory, but it must be determined how existing techniques can be applied. Identification in the frequency domain is probably best.

The proper use of the parameters must be established: order of the differential equations, maximum time, time step, and identification frequency range.

Least-squared-error identification is simplest, if the occurrence of positive (unstable) roots can be avoided. If the occurrence of positive roots can not be avoided by proper selection of parameters (including frequency weighting in the identification), a constrained identification method will be required.

The identification methods must be developed for time-varying systems. Specifically, for helicopter rotors the periodic case must be considered, including a constant coefficient approximation.

d) Applications

Rotary wing problems where the wake configuration is important in determining aeroelastic behavior must be identified. The stability and response results must be compared with experiment, with the objectives of verifying the theory; establishing how to perform the model order reduction and identification tasks; and determining when such features as wake geometry perturbations and rolled-up wakes are required.

Differential equation models for standard problems may be developed. Such models could be used directly, without repeating the calculation of the impulse response and the identification for each new application. The method must be implemented in computer programs for calculation of aeroelastic stability and response. In particular, use should be made of existing complicated models for the trim wake.

1.3 Objectives of the Feasibility Investigation

The purpose of the present investigation was to establish the feasibility and soundness of the approach. Specific objectives included the following: (a) establish the approach for model order reduction; (b) determine whether a constrained identification method is needed; (c) verify the formulation of the theory for rolled-up, distorted trim wake geometry; (d) verify the formulation of the theory for wake geometry perturbations.

The report first outlines the theory, and then presents results. The theory section reviews the general development; presents the equations for the flap and pitch-flap dynamics problems to be investigated; and discusses the wake equations, including model order reduction, multiblade coordinates, and the identification of a differential equation model. Finally the theory section presents the equations for various wake models, including undistorted and rolled-up wake geometry, and wake geometry perturbations produced by loading and flight speed changes. The results section presents the calculated impulse response, system function,

eigenvalues, and response for various flap and pitch-flap rotor problems. These applications are specifically directed at the objectives described in the preceding paragraph.

2. THEORY

2.1 General Theory

The initial development of the theoretical basis for a time-domain analysis of the unsteady aerodynamics of general rotary-wing configurations undergoing arbitrary motion has been documented by Johnson (1987, 1988). The downwash induced by a wake can be evaluated by integrating over the wake vorticity at time t :

$$\mathbf{v}(\mathbf{x}, t) = -\frac{1}{4\pi} \int_{wake} \frac{\mathbf{s} \times \boldsymbol{\omega}}{s^3} dA(\mathbf{y}) \quad (1)$$

where \mathbf{v} is the velocity at point \mathbf{x} on a wing; $\boldsymbol{\omega} dA$ is the vortex sheet strength at point \mathbf{y} on the wake surface; and $\mathbf{s} = \mathbf{x} - \mathbf{y}$. In general, the wake can consist of line, sheet, and volume distributions of vorticity. Equation 1 relates the downwash at time t to the wake position and strength at the same time. For unsteady aerodynamics, the relation required is between the downwash at the current time, and the loading at all earlier times (which created the current wake). For simple configurations, this relation can be obtained from equation 1 by a coordinate transform from streamwise distance in the wake to the time at which the wake elements were created. For complicated configurations, the relation can be obtained from the trim downwash influence coefficients.

Define the wake surface and vorticity at t in terms of two variables: past time τ , and some wing spanwise coordinate η . An element in the wake is identified by $(t - \tau)$, the time it was created. A wake element has shed circulation strength proportional to the time derivative of the bound circulation, $\dot{\Gamma}$; and trailed circulation strength proportional to the spanwise derivative Γ' . Hence equation 1 gives the downwash λ as follows:

$$\lambda(\mathbf{x}, t) = \int_0^\infty \int [\dot{\Gamma}(t-\tau) h_s(\tau, t-\tau) + \Gamma'(t-\tau) h_t(\tau, t-\tau)] d\eta d\tau \quad (2)$$

The first term (subscript s) is the shed wake, and the second term (subscript t) is the trailed wake. Discretizing the bound circulation over the wing span gives:

$$\lambda(\mathbf{x}, t) = \sum_l \int_0^\infty [\dot{\Gamma}_l(t-\tau) h_{ls}(\tau, t-\tau) + \Gamma'_l(t-\tau) h_{lt}(\tau, t-\tau)] d\tau \quad (3)$$

Hence the integral over the wake surface becomes a convolution integral relating λ to Γ . From linear system theory, h is recognized as the impulse response, which completely describes this relation, directly in the time domain. The objective of the wake theory is to obtain h for specific cases, which is a relatively simple task, even for complicated wake configurations. For time-invariant configurations (fixed wings and hovering rotors), $h = h(\tau)$.

Consider the case where the wake model, theory, and software have been developed to calculate the wake-induced downwash for trim flight conditions. The discretization of equation 1, both spanwise and streamwise, gives an influence coefficient formulation:

$$\lambda(x,t) = \sum_{l,k} \Gamma(y_l, \tau_k) C_{lk}(x,t) \quad (4)$$

The trim wake model can include tip vortex rollup, and self-induced distortion of the geometry. Both the impulse response and the influence coefficients are the downwash produced by unit circulation in the wake, but the trim wake has been discretized streamwise. A piecewise-constant bound circulation distribution means a vortex-lattice wake model. The trim wake shed lines are integrated spanwise and impulsive streamwise, hence $h_s = C_s$. The trim wake trailed lines are impulsive spanwise and integrated streamwise, hence $C_t = \text{average of } h_t \text{ over the time step}$. The correct h_t is obtained from the integrand of the line vortex element.

The wake geometry will vary during the unsteady motion of the wing, because of the self-induced velocities at the wake surface produced by the perturbation loading. An additional contribution to the impulse response can be found, in terms of the downwash at the wake surface and the effect of the geometry perturbations on the downwash at the wing. Velocity perturbations of the wing will also produce perturbations of the wake geometry. An analysis of this effects leads to an impulse response relating the downwash to the velocity perturbations.

The convolution integral relates the downwash and circulation of all points on all the wings (a vector equation), with the wake coupling the wings. It is frequently useful to transform to global downwash and circulation variables. An example is the use of multiblade coordinates for rotors. With the downwash evaluated at many points on the wing, there may be too many degrees of freedom for an efficient differential equation model. To minimize the number of states, the downwash and circulation can be expanded as series in a small number of generalized coordinates. The downwash coordinates may be interpreted as weighted averages over the wing, and the circulation coordinates as integrated loads or perhaps generalized forces.

This wake theory is to be used in the calculation of time-domain stability and response. Although it is possible to make use of the impulse response directly, using equivalent differential equations is probably of most general interest. Hence

the next step is to use the information contained in h_s and h_t to define approximate differential equations relating the downwash variables to the circulation variables. The wing theory is formulated in terms of the downwash, so the aeroelastic equations of the aircraft are coupled with these wake equations. The wing theory also gives the circulation, for the wake equations, in terms of the downwash and the wing motion.

Calculating the impulse response may conclude the wake analysis, but there remains the task of identifying a model for use in time-domain aeroelastic stability and response calculations. The preferred model is a set of ordinary differential equations relating the downwash and circulation (or the appropriate reduced order variables). There are other possibilities: Laplace transform (Edwards, 1977); time-domain approximation using functions other than exponentials (Stark, 1984); direct application of the convolution integral; or transformation of the impulse response to a discrete-time equation. A differential equation representation probably offers the most flexibility for incorporating unsteady aerodynamics in aeroelasticity calculations.

Calculation of the wake aerodynamics, in terms of the impulse response, is performed in the time domain. The identification task however can be performed in the frequency domain (although not necessarily on the imaginary axis). Thus h can be numerically transformed (by FFT) to obtain the system function H :

$$H(\omega) = \int_0^{\infty} h(\tau) e^{-i\omega\tau} d\tau \quad (5)$$

(for a time-invariant system; a generalization is required for time-varying systems). At this point the shed and trailed wake response can be combined. Representing the wake aerodynamics by a differential equation implies approximating H by a ratio of polynomials in $i\omega$ (i.e. a rational function, or Pade approximant). Before proceeding with the identification task, it is necessary to consider whether a ratio of polynomials is the appropriate functional form, either in terms of the actual behavior of the aerodynamic solutions (Vepa, 1977; Edwards, Ashley, and Breakwell, 1979), or in terms of the accuracy of the resulting approximate aeroelastic behavior (Edwards, Ashley, and Breakwell, 1979). For three-dimensional problems, a rational function should be a good approximation, with the numerator and denominator polynomials having the same order. Note that the shed wake alone would have the constant term of the numerator equal to zero; while the trailed wake alone would have the numerator order one less than the denominator order.

Assuming that a rational function is the appropriate form for an approximation, it is necessary to identify the coefficients of the numerator and denominator polynomials. This identification problem has received considerable attention in recent work on unsteady aerodynamics. Substituting the actual linear relation into the assumed differential equation $D(s)\lambda = N(s)\Gamma$ (where D and N are

polynomials in the Laplace variable s), produces $D(i\omega)H(\omega) = N(i\omega)$. This is a linear equation for the polynomial coefficients at a given set of frequencies, which can be solved by the method of weighted least-squared-error (Vepa, 1977). Several other identification methods have been developed (Dunn, 1980; Dowell, 1980; Roger, 1978; Karpel, 1982; Miyazawa and Washizu, 1983), including application of nonlinear programming techniques (Tiffany and Adams, 1987). Important considerations are identifying a common set of poles using matrix representations (Vepa, 1979); ensuring that all the poles are stable (Dunn, 1980); and obtaining a minimum order approximation, i.e. minimum number of augmented states (Tiffany and Adams, 1987). For the general case considered here, the aerodynamic model may not be time-invariant, hence the differential equation representation will have time-varying coefficients. For the case of periodic coefficients, methods similar to those for the constant coefficient case are applicable.

In summary, a general theory for the time-domain unsteady aerodynamics of rotors has been described. The wing theory must be formulated in terms of the wake-induced downwash. Then the wake theory gives a linear relation between the downwash and the wing bound circulation, in terms of the impulse response. This is in contrast to the traditional approach, which relates the wing loading directly to the wing motion. The present approach permits calculation of aeroelastic behavior of wings without requiring simplifications of the wake configuration. It is possible to include distorted wake geometry (trim and perturbations), tip vortex rollup, multiple wings, and time varying wake geometry. Moreover, if a wake model is available for the trim loading problem, it can be used as a basis for calculating the perturbation impulse response with little more development effort or computation time. Consider the assumptions and approximations involved in this approach.

- a) Incompressible wake of concentrated vorticity. Concentrated vorticity implies wings rather than general bodies, but there is no restriction on the wake configuration. The wing theory can include compressible effects in some fashion. This time-domain approach should still be possible with a compressible wake.
- b) The examples investigated so far have used lifting line theory. However, the wake theory is not restricted to lifting line wing models (although these are important cases for rotors).
- c) Wake discretization. Spanwise discretization of the wing bound circulation (typically piecewise constant, implying a vortex-lattice wake model) is required for many applications, particularly with arbitrary wing and wake geometry. The effect of such discretization is the subject of numerous investigations. Note that while the impulse response is evaluated at a set of discrete times, that does not imply here a timewise discretization of the wing bound circulation.
- d) Model order reduction. Many practical applications of the theory will require expansion of the downwash as series, which will be truncated at a small number of generalized coordinates. Significant approximations can be introduced by both the

functional form of the series, and by the truncation. It will be important to establish minimum model requirements (probably problem and configuration dependent) so that efficiency does not compromise accuracy.

e) Representation by differential equations. This identification task assumes that the response can be correctly represented by a sum of exponentials (time-domain) or ratio of polynomials (frequency-domain). The degree of approximation can be controlled by the resolution and extent of the wake (frequency range and resolution) and the order of the polynomials. Again it will be important to establish minimum model requirements. Also, there are alternatives to the differential equation representation.

The model order reduction and identification are major aspects of the development of a practical unsteady aerodynamics representation. It is expected that the level of approximation will be controllable, so it should be possible to achieve good accuracy, only perhaps at the cost of increased number of states. Most importantly, the aerodynamic theory is not constrained to simplified wake configurations in order to obtain a practical model.

2.2 Rotor Aeroelastic Problems

The feasibility of the rotor wake analysis will be assessed in the context of two rotor aeroelastic problems: flap motion and pitch-flap motion. The eigenvalues and the response to control and hub motion for these two problems will be examined. The flap motion is considered since it is fundamental to the behavior of helicopter rotors. Moreover, the flap motion produces a direct lift change, and hence will be strongly coupled with the wake. The flap-pitch problem is considered in order to examine higher frequency dynamic behavior. These problems are both involve primarily linear aerodynamic and dynamic forces, so developing the perturbation equations of motion is trivial. Only hovering flight conditions are considered.

The equations of motion are derived by Johnson (1980; pages 381, 390, 429, 435, 556, 564, 579, 583 for the flap equation; pages 403, 598, 638 for the flap-pitch motion). The principal extension required here is a rotor induced velocity that varies with both radial station and time.

2.2.1 Flap Equation

Consider a rotor with N blades, at azimuth station $\psi_m = \psi + m\Delta\psi$, where $\psi = \Omega t$, $m = 1$ to N , and $\Delta\psi = 2\pi/N$. Rigid flap motion β is assumed (positive flap up). For simplicity, hinge offset and tip loss factor are ignored in the aerodynamics, but an arbitrary flap natural frequency ν is allowed (containing the effects of hinge offset

and spring, as well as centrifugal stiffening). The equation of motion for the m th blade is:

$$\ddot{\beta}^m + v^2 \beta^m = \gamma M_F^m - S_b \ddot{z} \quad (6)$$

where γ is the blade Lock number; M_F is the aerodynamic flap moment; S_b ($= 1.5$ for a uniform blade) is the ratio of the first moment and second moments of inertia about the flap hinge; and z is the hub vertical motion (positive up). This equation is dimensionless, based on the rotor rotational speed Ω , rotor radius R , and air density ρ . Assuming constant chord and small angles, and ignoring stall, the aerodynamic flap moment is:

$$M_F^m = \int r \frac{L}{ac} dr = M_\theta \theta^m + M_\beta \dot{\beta}^m + M_z \dot{z} + M_\lambda \lambda^m \quad (7)$$

where θ is the blade pitch control (positive nose up), and λ is a vector of the inflow ratio $\lambda(r_k)$ at the aerodynamic radial stations r_k along the length of the blade. The blade span is divided into M aerodynamic panels ($k = 1$ to M , from the root to the tip), with panel widths Δr_k , and r_k at the midpoints of the panels. Aerodynamic quantities, including the induced velocity and the bound circulation, are assumed to have constant value over the length of each panel. Under the present assumptions, the aerodynamic coefficients are:

$$M_\theta = \frac{1}{8} \quad (8)$$

$$M_\beta = -\frac{1}{8} \quad (9)$$

$$M_z = -\frac{1}{6} \quad (10)$$

$$M_\lambda = \left[\dots - \int \frac{1}{2} r^2 dr \dots \right] \quad (11)$$

Model order reduction will normally be used, in which the inflow is expanded as a series with radial mode shapes p_i and generalized coordinates l_i :

$$\lambda(r_k, t) = \sum_i p_i(r_k) l_i(t) \quad (12)$$

or $\lambda = Pl$, where l is a vector of the generalize coordinates l_i . The same modes shapes p_i are used for each blade, so P is the same for each blade. Hence

$$\ddot{\beta}^m + \frac{\gamma}{8}\dot{\beta}^m + v^2\beta^m - \gamma M_\lambda P l^m = \frac{\gamma}{8}\theta^m - S_b \ddot{z} - \frac{\gamma}{6}\dot{z} \quad (13)$$

is the rotating frame equation for the flap motion of the mth blade.

Next, multiblade coordinates will be introduced. It is assumed that the rotor has 3 or more blades (most of the results will be for $N = 3$). Without the wake model, equation 13 for the mth blade is independent of the other blades. With the wake model, the equations and response of the N blades are coupled to each other. As usual, multiblade coordinates are the natural representation of the coupled motion of rotor blades. In hover, introducing multiblade coordinates decouples the N equations into independent sets, consisting of the collective motions (β_0 and l_0), cyclic motions ($\beta_{1c}, \beta_{1s}, l_{1c}, l_{1s}$), reactionless motions ($\beta_{nc}, \beta_{ns}, l_{nc}, l_{ns}$), and differential collective motions ($\beta_{N/2}$ and $l_{N/2}$). Additionally, multiblade coordinates offer the usual benefits in representing the coupled motion of the rotor with shaft motion or gusts. Hence

$$\left(s^2 + \frac{\gamma}{8}s + v^2\right)\beta_0 - \gamma M_\lambda P l_0 = \frac{\gamma}{8}\theta_0 + \left(-S_b s - \frac{\gamma}{6}\right)\dot{z} \quad (14)$$

$$\begin{bmatrix} s^2 + \frac{\gamma}{8}s + v^2 - 1 & 2s + \frac{\gamma}{8} \\ -\left(2s + \frac{\gamma}{8}\right) & s^2 + \frac{\gamma}{8}s + v^2 - 1 \end{bmatrix} \begin{pmatrix} \beta_{1c} \\ \beta_{1s} \end{pmatrix} + \begin{bmatrix} -\gamma M_\lambda P & 0 \\ 0 & -\gamma M_\lambda P \end{bmatrix} \begin{pmatrix} l_{1c} \\ l_{1s} \end{pmatrix} = \frac{\gamma}{8} \begin{pmatrix} \theta_{1c} \\ \theta_{1s} \end{pmatrix} \quad (15)$$

are the nonrotating frame equations for the collective and cyclic flap and inflow modes (in Laplace form). As required, expressions for the hub reactions can also be derived. For example,

$$\gamma \frac{C_T}{\sigma a} = \left(-S_b s^2 - \frac{\gamma}{6}s\right)\beta_0 + \gamma T_\lambda P l_0 + \frac{\gamma}{6}\theta_0 + \left(-M_b s - \frac{\gamma}{4}\right)\dot{z} \quad (16)$$

is the rotor thrust reaction on the hub. For the aerodynamic thrust force, only the terms containing the Lock number γ are retained in equation 16.

The wake equations give the inflow at the blade in terms of the blade bound circulation $\Gamma(r)$. Hence to complete the equations it is necessary to obtain an expression for $\Gamma(r)$ in terms of the blade motion. For the motion and aerodynamic model considered here, the bound circulation is:

$$\Gamma(r) = \frac{ac}{2} \left(r\theta - \lambda - r\dot{\beta} + \dot{z}\right) \quad (17)$$

(This expression will be different for each rotor aeroelastic problem considered.) Let Γ be the vector of the bound circulation $\Gamma(r_k)$ at the aerodynamic radial stations r_k . Then

$$\Gamma^m = G_{\dot{\beta}} \dot{\beta}^m + G_{\lambda} Pl^m + G_{\theta} \theta^m + G_z \dot{z}^m \quad (18)$$

where the coefficient matrices are

$$G_{\theta} = \begin{bmatrix} \vdots \\ acr/2 \\ \vdots \end{bmatrix} \quad (19)$$

$$G_{\dot{\beta}} = \begin{bmatrix} \vdots \\ -acr/2 \\ \vdots \end{bmatrix} \quad (20)$$

$$G_z = \begin{bmatrix} \vdots \\ -ac/2 \\ \vdots \end{bmatrix} \quad (21)$$

$$G_{\lambda} = \begin{bmatrix} \ddots & & 0 \\ 0 & -ac/2 & \ddots \end{bmatrix} \quad (22)$$

Model order reduction can be applied to the circulation as well, although it will not normally be used here. The circulation can be expanded as a series with radial mode shapes q_i and generalized coordinates or forces g_i :

$$\Gamma(r_k, t) = \sum_i q_i(r_k) g_i(t) \quad (23)$$

or $\Gamma = Qg$, where g is the vector of the generalize coordinates g_i . Model order reduction is not required for the circulation in order to reduce the system states. Also, finding the inverse $g = Q_{inv}\Gamma$, which is needed to express g in terms of the motion (replacing equation 18), presents some difficulties (for example, Q_{inv} is not unique). For these reasons, model order reduction is generally not used here for the bound circulation ($Q = I$). The multiblade coordinate transformation of equation 18 is easily obtained, since the coefficient matrices are constants.

2.2.2 Flap-Pitch Equations

Consider a rotor with rigid flap motion β and rigid pitch motion θ (positive nose up). The pitch motion has nonrotating natural frequency ω , representing the

flexibility of the control system. The input pitch control is θ_{con} . The equations of motion for the m th blade are:

$$\ddot{\beta}^m + v^2\beta^m - I_x(\ddot{\theta}^m + \theta^m) = \gamma M_F^m \quad (24)$$

$$I_f(\ddot{\theta}^m + (\omega^2+1)\theta^m) - I_x(\ddot{\beta}^m + \beta^m) = \gamma M_f^m + I_f \omega^2 \theta_{con}^m \quad (25)$$

where M_f is the aerodynamic pitch moment; I_f is the blade pitch moment of inertia; and I_x ($= 1.5 x_l/R$ for a uniform blade, where x_l is the chordwise offset of the blade center-of-gravity, aft of the pitch axis) is the inertial coupling between the flap and pitch motion. Unsteady aerodynamic theory must be used when the blade pitch degree of freedom is included. Assuming that the blade pitch axis is at the aerodynamic center (quarter-chord), the aerodynamic flap and pitch moments are:

$$M_F^m = M_\theta \theta^m + M_{\dot{\beta}} \dot{\beta}^m + M_\lambda \lambda^m + M_{\dot{\theta}} \dot{\theta}^m + M_\beta \beta^m \quad (26)$$

$$M_f^m = m_\theta \dot{\theta}^m + m_\beta \beta^m \quad (27)$$

Under the present assumptions, the new aerodynamic coefficients (obtained from unsteady aerodynamic theory) are:

$$M_\theta = \frac{c}{8} \quad (28)$$

$$M_\beta = \frac{c}{12} \quad (29)$$

$$m_\theta = -\frac{c^2}{32} \quad (30)$$

$$m_\beta = -\frac{c^2}{64} \quad (31)$$

Since here there is no chordwise offset of the pitch axis from the quarter-chord, there is no direct effect of the wake (inflow l) on the aerodynamic pitch moment. However, the pitch motion is strongly coupled with flap motion, so even these equations will exhibit a strong wake influence on the behavior. In Laplace form, the rotating frame flap-pitch equations for the m th blade are:

$$\begin{aligned}
& \begin{bmatrix} s^2 + \frac{\gamma}{8}s + v^2 - \frac{\gamma c}{12} & -I_x s^2 - \frac{\gamma c}{8}s - \frac{\gamma}{8} - I_x \\ -I_x s^2 + \frac{\gamma c^2}{64} - I_x & I_f s^2 + \frac{\gamma c^2}{32}s + I_f(\omega^2 + 1) \end{bmatrix} \begin{pmatrix} \beta^m \\ \theta^m \end{pmatrix} + \begin{bmatrix} -\gamma M_{\lambda^1 P} \\ 0 \end{bmatrix} l^m \\
& = \begin{bmatrix} 0 \\ I_f \omega^2 \end{bmatrix} \theta_{con}^m
\end{aligned} \tag{32}$$

Application of the multiblade coordinate transform to these equations is straightforward, since the coefficients are constant.

2.3 Rotor Wake Equations

This section presents the general wake equations, applicable to all the aerodynamic wake models considered in the investigation. The trim operating condition is assumed to be hover.

2.3.1 Integral Equation

Consider a rotor with N blades, at azimuth stations $\psi_m = \psi + m\Delta\psi$, where $\psi = \Omega t$, $m = 1$ to N , and $\Delta\psi = 2\pi/N$. The wake model provides a relation between the inflow ratio $\lambda(t)$ at r_k on the n th blade and the bound circulation $\Gamma(t-\tau)$ at ρ_l on the m th blade. The blade aerodynamic parameters are discretized radially, assuming that the inflow and bound circulation are piecewise constant. Then the wake theory (see section 2.1) provides the impulse response h_s (shed) and h_t (trailed) relating the inflow and circulation:

$$\lambda_k^n = \sum_m \sum_l \int_0^\infty \left[h_s(\tau) \dot{\Gamma}_l^m(t-\tau) + h_t(\tau) \Gamma_l^m(t-\tau) \right] d\tau \tag{33}$$

In hover the relation between inflow and circulation is time invariant and the trim wake geometry is axisymmetric. It follows that h is a function of τ , $j = m-n$, r_k , and ρ_l . The impulse response h depends on the particular wake model used. The form of the integral equation remains the same however, and the transformations and identification required are the same.

Equation 33 implies that the inflow ratio at each of the M aerodynamic radial stations on each of the N blades is a degree of freedom. The order of the differential equation equivalent to equation 33 must be large for accuracy. Hence in general the wake model requires a very large number of states. Model order reduction is therefore desirable for the inflow variables, to limit the number of states in a

particular problem. Let λ^n and Γ^m be vectors of the inflow and circulation at all radial stations on the n th and m th blades, respectively. The inflow is expanded as a series with radial mode shapes $p_i(r_k)$ and generalized coordinates $l_i(t)$: $\lambda^n = Pl^n$. If the order is indeed being reduced, there are more equations than variables after substituting this relation into equation 33. Hence it is necessary to transform the equations as well, which will be accomplished by multiplying by P^TW , where W is a suitable weighting matrix. To interpret this transformation, assume that equation 33 is solved for λ , and then the task is to find l such that Pl is a best estimate of λ . If "best" means a weighted least-squared-error estimate, then $l = (P^TW P)^{-1} P^TW \lambda$, which can also be obtained by transforming the equations and solving for l . The transformation P^TW can also be interpreted as a weighted integral of the inflow $\lambda(r)$ over the blade span:

$$P^TW \lambda = \begin{bmatrix} \vdots \\ \sum_k p_i(r_k) w_k \lambda(r_k) \\ \vdots \end{bmatrix} \equiv \begin{bmatrix} \vdots \\ \int p_i(r) \tilde{w}(r) \lambda(r) dr \\ \vdots \end{bmatrix} \quad (34)$$

Letting p_i be a polynomial of order i gives a general representation of the spanwise distribution of the inflow, and $p = 1$ (uniform) or $p = r$ (linear) are commonly used in dynamic inflow theories. Orthogonal polynomials (i.e. shifted Legendre polynomials, with an appropriate weight W) offer some advantages, but are not essential to the theory.

A similar variable transformation can be applied to the circulation as well, although it will not normally be used here. The circulation can be expanded as a series with radial mode shapes $q_i(\rho_l)$ and generalized forces $g_i(t)$: $\Gamma = Qg$. While such a transformation is commonly used for dynamic inflow theories, with the generalized force being either the rotor thrust or moment, it is not suitable for a general theory. The circulation variables (at M radial stations on each of N blades) are not degrees of freedom, but rather are the interface between the wake model and the rotor dynamics. So reducing the number of circulation variables means that information is lost at that interface, but has no effect on the size of the coupled wake and blade equations. This loss of information is reflected in the task of finding the (nonunique) inverse $g = Q_{inv} \Gamma$, which is needed to express g in terms of the motion. The wake differential equation is identified in terms of the circulation variables, so the identification task is smaller and perhaps easier with model order reduction applied to the circulation. In the absence of problems with the identification, that consideration does not outweigh the loss of information. Additionally, care would be required to keep the radial mode shape q_i consistent with the wake structure. For

example, $q = r$ gives a nonzero circulation at the tip of the blade, which requires a fully rolled-up, line tip vortex in the wake directly behind the blade.

Introducing transformations of both the inflow and circulation variables (though usually $Q = I$ here) gives the integral equation relating l on the n th blade to g on the m th blade:

$$l^n(t) = \sum_m \int_0^\infty [h_s^j(\tau) \dot{g}^m(t-\tau) + h_t^j(\tau) g^m(t-\tau)] d\tau \quad (35)$$

where $j = m-n$. The transformation of the (matrix) impulse response is

$$h = D^{-1}P^TWhQ \quad (36)$$

where $D = P^TWP$ (diagonal for an orthogonal inflow transformation).

That in hover h only depends on τ means that the system is time invariant, and a constant coefficient differential-equation form of equation 33 can be considered. (In forward flight, h is a periodic function of $t-\tau$ as well, implying a periodic coefficient differential-equation.) Even though the equations have constant coefficients, they couple all the blades. Hence it is best to introduce the multiblade coordinate transform, which is the natural representation of the coupled motion of rotor blades. Reorder the variables in equation 35, to obtain the inflow for all blades at radial station r_k , in terms of the circulation for all blades at radial station r_l :

$$l_k(t) = \sum_l \int_0^\infty [h_{kls}(\tau) \dot{g}_l(t-\tau) + h_{klt}(\tau) g_l(t-\tau)] d\tau \quad (37)$$

where for hover

$$h_{kl}(\tau) = [h^{nm}(\tau)]_{kl} = [h^{j=m-n}(\tau)]_{kl} \quad (38)$$

($n = 1$ to N , $m = 1$ to N). Multiblade coordinates are obtained by a time-varying transformation of the inflow and circulation variable at each radial station, from the rotating to nonrotating frame: $(l_k)_{rot} = T(l_k)_{non}$ and $(g_l)_{rot} = T(g_l)_{non}$. The equations are transformed by multiplying by DT^T , where $DT^TT = I$. Hence the (matrix) impulse response (for each k, l) transforms as follows:

$$h_{s_{non}}(\tau) = D T^T(t) h_{s_{rot}}(\tau) T(t-\tau) \quad (39)$$

$$h_{t_{non}}(\tau) = D T^T(t) h_{t_{rot}}(\tau) T(t-\tau) + D T^T(t) h_{s_{rot}}(\tau) \dot{T}(t-\tau) \quad (40)$$

Note that the static response is given by the integral of the trailed wake impulse response over $\tau = 0$ to ∞ ; the shed wake gives a response to the rate of change of circulation, hence does not contribute to the static response. Equation 40 shows however that the rotating frame shed impulse response contributes to the nonrotating frame trailed impulse response, and hence to the nonrotating frame static response.

The multiblade coordinates are $l_{non} = (l_0 \ l_{kc} \ l_{ks} \ l_{N/2})^T$ and $g_{non} = (g_0 \ g_{kc} \ g_{ks} \ g_{N/2})^T$ ($k = 1$ to K , with K such that the total number of coordinates is N), and the transformation is

$$T = \begin{bmatrix} & & \vdots & & \\ & 1 & \cos k\psi_m & \sin k\psi_m & (-1)^m \\ & & \vdots & & \end{bmatrix} \quad (41)$$

where $\psi = \Omega t + m\Delta\psi$, $m = 1$ to N , and $DT^T\dot{T} = E$. Since in hover the rotating frame impulse response has the form shown in equation 38, it follows that the nonrotating frame impulse response is:

$$h_{s_{non}}(\tau) = \sum_{j=0}^{N-1} h_s^j(\tau) C^T(\psi_j) \quad (42)$$

$$h_{t_{non}}(\tau) = \sum_{j=0}^{N-1} h_t^j(\tau) C^T(\psi_j) + h_s^j(\tau) C^T(\psi_j) E \quad (43)$$

where $\psi_j = \Omega\tau - j\Delta\psi$, and

$$C^T = \begin{bmatrix} 1 & & & & \\ & \cos k\psi_j & -\sin k\psi_j & & \\ & \sin k\psi_j & \cos k\psi_j & & \\ & & & & \\ & & & & (-1)^j \end{bmatrix} \quad (44)$$

$$C^T E = \begin{bmatrix} 0 & & & \\ & k\Omega \sin k\psi_j & k\Omega \cos k\psi_j & \\ & -k\Omega \cos k\psi_j & k\Omega \sin k\psi_j & \\ & & & 0 \end{bmatrix} \quad (45)$$

(see Johnson, 1988). For each radial station (k,l) , the N values of the rotating frame impulse response give the $N \times N$ nonrotating frame matrix impulse response. The form of C^T (equation 44) shows that as usual in hover the 0, kc/ks , and $N/2$ multiblade coordinates are decoupled from each other.

The final form of the integral equation describing the aerodynamics of the wake is:

$$l(t) = \int_0^\infty [h_s(\tau) \dot{g}(t-\tau) + h_l(\tau) g(t-\tau)] d\tau \quad (46)$$

where l and g are the generalized coordinates for the inflow and circulation (all modes, or all radial stations if model order reduction is not used). In hover, decoupled equations of this form are obtained for the collective (0), cyclic (1c/1s), reactionless (nc/ns), and differential collective ($N/2$) multiblade coordinates.

2.3.2 Differential Equations

The wake analysis produces a convolution integral equation relating the induced velocity to the bound circulation, in terms of an impulse response calculated in the time domain. For use with rotor stability and response calculations, a differential equation is preferable to an integral equation. Hence the next task is to identify a differential equation that is a good approximation to the integral equation. The integral equation implies a linear, time-invariant model of the wake response. A differential equation implies additionally that the impulse response can be represented by a sum of exponentials with real or complex conjugate eigenvalues. In the frequency domain, a differential equation implies that the system function can be represented by a ratio of polynomials. In fact however, the impulse response or system function given by the wake analysis has different behavior. For example, the impulse response always decays with $1/\tau$ to some integer power (see Johnson, 1987, 1988). Hence a finite-order differential equation must always be an approximation to the integral equation, and obtaining a good approximation (for a particular problem) is a key objective of the identification task.

The impulse response is calculated directly in the time domain, but the identification task can be performed in the frequency domain. Thus h can be transformed to the system function H :

$$H(\omega) = \int_0^{\infty} h(\tau) e^{-i\omega\tau} d\tau \quad (47)$$

The shed and trailed impulse response are transformed to H_s and H_t , respectively, and combined in the frequency domain to give a total system function $H = l(\omega)/g(\omega) = i\omega H_s + H_t$. Identification of the differential equation in the frequency domain is chosen because (a) it leads to a linear parameter identification problem; (b) it allows the shed and trailed wake effects to be combined; and (c) it allows the identification to focus on the frequency range of interest.

Transformation of the impulse response $h(\tau)$ to the system function $H(\omega)$ is performed numerically using the FFT. The impulse response is evaluated at a specified sample rate (per rev) for a specified length of time (revs). The result is a system function with a bandwidth (per rev, equal to one-half the sample rate) and resolution (per rev, equal to the inverse of the length in revs). The sample rate and length must be large enough so that the resolution is adequate in the time and frequency domains, so the bandwidth covers the range of interest, and most especially so aliasing is minimized over the frequency range of interest. However, computation efficiency requires that the sample rate and length be no larger than necessary for accuracy.

Assuming that the integral equation is equivalent to a differential equation means that the system function H can be approximated by a rational function. The differential equation, of order N , is:

$$\sum_{n=0}^N A_n l^{(n)} = \sum_{n=0}^N B_n g^{(n)} \quad (48)$$

The equation is linear, so $A_0 = I$ is assumed, without loss of generality. The presence of three-dimensional trailed wake means that H approaches a nonzero constant at low frequency, i.e. $B_0 \neq 0$. The low frequency (3D trailed wake) response will here be matched exactly by always setting $B_0 = H(0)$. The static response is affected by the accuracy of the FFT, but the identification then introduces no further approximation. The presence of the shed wake means that H approaches a constant value at high frequency, i.e. the order (highest derivative) is the same (N) for both l and g (the number of zeros equals the number of poles). The system function at $\omega = \infty$ could be obtained from h_s at $\tau = 0$, but the identification will usually be restricted to a finite frequency range. The frequency domain version of equation 48 is

$$D(i\omega)l = N(i\omega)g \quad (49)$$

where D and N are the denominator and numerator matrix polynomials in $i\omega$. Substituting $l = Hg$, where H is the calculated system function, gives (for arbitrary g)

$$D(i\omega) H(\omega) - N(i\omega) = 0 \quad (50)$$

The task is to identify the coefficient matrices A_n and B_n in the polynomials D and N , so that equation 50 is best satisfied over the required frequency range. This equation is linear in A_n and B_n , so least-squared-error methods can be applied, which gives a direct and efficient calculation of the parameters.

There are additional assumptions implied by the form of equation 48. Let N_k and N_l be the number of inflow and circulation variables, respectively. The system response H is an $N_k \times N_l$ matrix, the H_{kl} element giving the response of l_k to g_l . It would be possible to separately identify a differential equation for each H_{kl} , but the resulting equations would not be convenient. The form of equation 48 means that a common set of poles is being used to describe all elements of H . Equation 48 has $N_l N$ poles, and if the A_n matrices are full it means that each H_{kl} is being described these poles and its own $N_l N$ zeros. Alternatively, if the A_n matrices are diagonal, it means that each l_k equation is being identified separately -- there are N poles for each equation, and H_{kl} is being described by these poles and its own N zeros. It might seem that full A_n matrices, with more poles and zeros for each H_{kl} , would produce a better identification. However, there are not enough free parameters in the off-diagonal elements of A_n to provide the extra zeros, so it is required that the A_n matrices be diagonal. Hence the identification is performed separately for each l_k (scalar D and row-matrix N in equation 50).

A least-squared-error identification of equation 50 proceeds as follows (since an objective of this investigation is to determine whether least-squared-error identification is sufficient, more sophisticated techniques are not considered). Considering separately the response of l_k to g (i.e. diagonal A_n), equation 48 becomes

$$\sum_{n=1}^N a_n l_k^{(n)} + l_k = \sum_{n=1}^N b_n g^{(n)} + b_0 g \quad (51)$$

where a_n are scalars, b_n are row matrices, and $b_0 = H_k(0)$. With H_k the k th row of H , equation 50 becomes, for one frequency ω

$$[a_N \cdots a_1 \ b_N \cdots b_1] \begin{pmatrix} (i\omega)^N H_k \\ \vdots \\ (i\omega) H_k \\ -(i\omega)^N I \\ \vdots \\ -(i\omega) I \end{pmatrix} = [H_k(0) \ - \ H_k] \quad (52)$$

or $\Theta X_\omega = Y_\omega$. Concatonating all frequencies in the desired range for identification gives $\Theta X = Y$, which has the weighted least-squared-error solution

$$\Theta = (\text{Re } Y W \bar{X}^T) (\text{Re } X W \bar{X}^T)^{-1} \quad (53)$$

Note that X and Y are complex (the overbar denotes complex conjugate); but only positive frequencies need be included. W is a diagonal weighting matrix, so

$$X W \bar{X}^T = \sum_{\omega} w(\omega) X_{\omega} \bar{X}_{\omega}^T \quad (54)$$

$$X W \bar{X}^T = \sum_{\omega} w(\omega) X_{\omega} \bar{X}_{\omega}^T \quad (55)$$

The weight over frequency, $w(\omega)$, is used to control the identification results.

The differential equations are developed in terms of the generalized coordinates l . For a arbitrary transformation P in the model order reduction, different results will be obtained if the modal truncation is performed before or after the identification. However, if the transformation is orthogonal (i.e. $P^T W P$ diagonal), the identification and modal truncation are independent. Hence it is possible to investigate the effects of modal truncation by first obtaining a single set of equations for the maximum number of modes, and then deleting modes from the differential equations.

It is preferable to find solutions to the equations in standard form, hence equation 48 for the wake response is transformed to first order form:

$$\dot{L} + AL = Bg \quad (56)$$

$$l = CL + Dg \quad (57)$$

where the state vector L contains $N_k N$ variables. A static wake model can be obtained by neglecting the time derivatives in equation 48 or 56, or more simply by introducing a factor of about 0.001 on the time derivative in equation 56. Coupling equations 56 and 57 with the equations of the rotor motion (equations 14, 15, or 32) and circulation (equation 18) produces the differential equations for the complete aeroelastic and wake system.

2.4 Wake Aerodynamic Models

A wake aerodynamic model is required to derive the impulse response h that characterizes the behavior. Various levels of sophistication are possible in the wake model. Here an N -bladed rotor is considered, but only hovering operating conditions. To investigate the identification and model-order-reduction tasks, the simplest possible wake model is used: helical sheets of vorticity, with no distortion or rollup, and no wake geometry perturbation because of the loading changes.

Next a rolled-up, distorted trim wake is considered. In this wake model, the rolled-up tip vortex contains all the trailed vorticity outboard of the peak bound circulation; and for hover the trim distortion consists of radial contraction and vertical convection. The objective is to establish the proper formulation of the theory, and examine the influence of the rolled-up wake on the identification and model-order-reduction.

Finally, wake geometry perturbations produced by loading and velocity changes are considered. Again the objective is to verify the formulation of the theory. Hence only perturbations from the undistorted trim wake geometry are considered.

2.4.1 Undistorted Wake

Consider an N -bladed hovering rotor, with the wake modeled by undistorted helical sheets behind each blade (Johnson, 1988). The Biot-Savart law (equation 1) gives the downwash at radial station r on the n th blade, as the sum of contributions from the wakes of the m th blades:

$$\lambda^n(r,t) = \sum_{m=1}^N \frac{1}{4\pi} \iint \frac{r \sin\theta \gamma_s^m + (r \cos\theta - \rho) \delta_t^m}{s^3} \rho d\phi d\rho \quad (58)$$

$$s^2 = (r \sin\theta)^2 + (\rho - r \cos\theta)^2 + z^2 \quad (59)$$

where ϕ and ρ are the helical and radial coordinates in the wake; the shed and trailed vorticity strength is $\rho\gamma_s = -d\Gamma/dt$ and $\delta_t = d\Gamma/d\rho$, evaluated at the time the wake

element was created; $\theta = \psi_m - \psi_n - \phi = (m-n)\Delta\psi - \phi$; and $\phi = \tau + c/4\rho$ (shed) or $\phi = \tau$ (trailed). The vertical wake position z equals $v_0\phi$ for uniform convection by the mean induced velocity v_0 (no distortion of the helix). For an undistorted wake, the radial integration can be performed analytically.

The inflow is required at discrete radial stations r_k , from piecewise constant bound circulation evaluated at ρ_l (extending from ρ_L to ρ_R). The impulse response, required for equation 33, is:

$$h_s(\tau) = \frac{1}{4\pi} \frac{-r \sin\theta (\rho - r \cos\theta)}{\left((r \sin\theta)^2 + z^2 \right) s} \Bigg|_{\rho_L}^{\rho_R} \quad (60)$$

$$h_t(\tau) = \frac{1}{4\pi} \frac{\rho (\rho - r \cos\theta)}{s^3} \Bigg|_{\rho_L}^{\rho_R} \quad (61)$$

Note that for hover, h is a function of τ , $j = m-n$, r_k , and ρ_l .

2.4.2 Rolled Up Wake

For this model, the trim wake of the rotor has rolled-up tip vortices and distorted geometry (prescribed convection and contraction for hover). Perturbations of the wake geometry produced by the loading changes are not yet considered. As in developing wake models for trim (Johnson, 1990), it is here necessary to assume the structure of the wake rollup process. The trim circulation distribution has a peak at r_p . It is assumed that the trim wake rolls up into a tip vortex with strength equal to the bound circulation at r_p (errors in this assumption must be compensated for in the choice of the vortex core size). The inboard wake sheet is stretched and distorted by the rollup process, but the exact distribution of vorticity along the sheet is not calculated. Hence in the modeled wake structure, the strength of the inboard sheet also depends only on $\Gamma(r_p)$. This same model is used for the unsteady aerodynamic model, which calculates the perturbation inflow produced by changes in the bound circulation. Furthermore, it is assumed that the change of the radial location of the peak bound circulation during the unsteady motion is a higher order effect. Then the perturbed strength of the rolled-up tip vortex can be obtained from the perturbed bound circulation at r_p . For hover at normal loading, the core size and other factors that are important for close blade-vortex interactions can be ignored.

Divide the wake into two parts, with a boundary at a wake age of $\phi_{\text{bound}} = \pi/N$ (half-way between the blades). For the wake directly behind the blade, it is the detailed distribution of the trailed and shed vorticity that is important. Hence for $\phi < \phi_{\text{bound}}$, the result for the undistorted wake is used (equations 60 and 61).

When the wake encounters the following blades ($\phi > \phi_{\text{bound}}$), the rollup and distorted geometry are important. The impulse response required is the inflow at r_k

from the circulation at ρ_l . In the rolled-up wake the strength depends only on the bound circulation at r_p , so $h_{kl} = 0$ except for l corresponding to r_p . The rolled-up tip vortex is modeled as a line, so the Biot-Savart law for a line rather than a sheet must be used. Let $z_T(\phi)$ and $\rho_T(\phi)$ define the vertical and radial position of the tip vortex, as function of the wake age ϕ (helix angle, measured aft from the present blade position; with no distortion, $z_T = -v_0\phi$ and $\rho_T = 1$). The contribution of the tip vortex to the trailed impulse response is then:

$$\Delta h_t(\tau) = \frac{1}{4\pi} \frac{\rho_T (\rho_T - r \cos\theta) + \rho_T' r \sin\theta}{s^3} \quad (62)$$

where s is given by equation 59; $\theta = \psi_m - \psi_n - \phi = (m-n)\Delta\psi - \phi$; and $\phi = \tau$. This is similar to the undistorted wake result for ρ_R , with additionally the $\rho_T' = d\rho_T/d\phi$ term, produced by contraction of the wake. Since the distortion and rollup eliminates detailed information about the trailed and shed vorticity strength in the inboard sheet, a modeling assumption is required. As for the trim wake, it is assumed that the strength of the inboard trailed vorticity is constant over the span of the sheet. This is the strength that would be produced if the bound circulation varied linearly from zero at the root ($r = r_{root}$) to $\Gamma(r_p)$ at the tip ($r = 1$). The wake geometry is defined by $z(\phi)$ and $\rho(\phi)$ at the inside and outside edges of the sheet, with linear interpolation between. The Biot-Savart result for this sheet is not used here, since the tip vortex dominates the downwash. Instead, the impulse response from the undistorted wake model (equations 60 and 61) is used, with $z(\phi)$ and $\rho(\phi)$ of the rolled-up geometry (it is necessary to use $z = (z_L + z_R)/2$, since the radial tilt of the inboard sheet is not being properly accounted for). The wake from all radial stations ρ_l contribute to Δh from the bound circulation at r_p . Hence the contribution of the inboard wake to the shed and trailed impulse response is:

$$\Delta h(\tau) = \sum_l h_l \left(\frac{\rho_l - r_{root}}{1 - r_{root}} \right) \quad (63)$$

where h_l is from equation 60 or 61, excluding the h_t term from ρ_R at the tip segment (which is already accounted for by equation 62).

Hover loading calculations show that the trim bound circulation has a peak at typically 90 to 95% radius (with a rolled-up, contracted wake). For the calculations presented here, $r_p = .93$ is used. The standard prescribed wake model for hover is used, consisting of exponential radial contraction and two-stage vertical convection. The parameters for this prescribed geometry depend on the rotor thrust coefficient, twist, and number of blades; and are obtained from Kocurek and Tangler (1977).

2.4.3 Wake Geometry Perturbations

The wake has a geometry and strength in trim, and the unsteady aerodynamic theory considers the inflow change produced by circulation changes, because of perturbations to this trim wake. A loading change produces an inflow change (described by equation 33) through two mechanisms:

- 1) The loading change produces a perturbation of the wake strength (for fixed geometry), which induces a velocity change at the rotor blade. This is the effect considered so far, e.g. equations 60 and 61 for an undistorted trim wake.
- 2) The loading change produces a perturbation of the wake geometry (for fixed strength), which changes the velocity induced by the trim strength at the rotor blades. This is the effect considered in the present section, contributing an increment in the impulse response, Δh , to equation 33.

The second contribution can be substantial; for example, for the low frequency response to thrust changes in hover, it reduces the inflow by a factor of 2. The objective is to verify the formulation of the theory, so assumptions are made: the operating condition is hover; only the vertical perturbation of the geometry is used; the trim geometry is undistorted (a constant-pitch helix, hence the geometry is time-invariant).

The mechanisms involved in the wake geometry perturbations are as follows. The loading change produces a change in the strength of the wake. This strength change induces a perturbation velocity on the wake itself (as well as on the wing). The wake convects with the local velocity, so the perturbation velocity is integrated in time to get the perturbation geometry. A perturbation of the geometry of the wake with trim strength produces a change in the velocity induced at the wing. The result for this velocity at the wing is reordered as required to get the convolution form (equation 33), and the incremental impulse response identified.

Consider the wake at time t . To evaluate the wake geometry perturbation, the velocity is required at a wake element with age τ_w , produced by the vorticity of a wake element with age τ . Note that $\delta = t - \tau_w$ and $t - \tau$ are the times that these two wake elements were created; and $\tau - \tau_w = \tau + \delta - t$ is the time (or helix angle) between the two points. Analogous to equation 33, the induced velocity at r_i on the p th wake, from a bound circulation changes at r_l on the m th blade, is:

$$\lambda_{wi}^p(t, \delta) = \sum_m \sum_l \int_0^\infty \left[h_s(\tau - \tau_w) \Gamma_l^m(t - \tau) + h_t(\tau - \tau_w) \Gamma_l^m(t - \tau) \right] d\tau \quad (64)$$

The h for this velocity depends on r_i , r_l , $j = m - p$, and $\tau - \tau_w$. In general, h would depend on $\tau - \tau_w$, $t - \tau$, and t . Since the trim geometry of the wake is here time-invariant (hover, with no distortion; so the vertical separation between the two

wake points depends only on $\tau - \tau_w$, h depends only on $\tau - \tau_w$. This impulse response can be calculated as for the velocities on the wing surface. If the distorted wake geometry is calculated for the trim problem, then the impulse response will be available with little more computation. As usual with wake geometry calculations, evaluating the velocity at a wake point that is produced by the vorticity at that same point requires special attention.

The geometry perturbation of the wake element at δ is given by the time integral of the velocity. The vertical position change (positive down) at r_i on the p th wake is:

$$\Delta z_{wi}^p(t, \delta) = \int_{\delta}^t \lambda_{wi}^p(\sigma, \delta) d\sigma \quad (65)$$

The integration is over the velocity on a specific wake element, which is identified by a value of δ (that is why equation 64 is written in terms of t and δ), and has existed from time $t - \tau_w (= \delta)$ to t . If the geometry perturbations are significant in all three directions, the equations 64 and 65 are for vector velocity and displacement.

The velocity change at the wing produced by a geometry perturbation at a single point is D , and the total velocity change is given by the integral of D over the entire wake. The inflow increment at r_k on the n th blade is:

$$\Delta \lambda_{Gk}^n(t) = \sum_p \sum_i \int_{-\infty}^t D(\tau_w) \Delta z_{wi}^p(t, \delta) d\delta \quad (66)$$

where D is a function of $r_k, r_i, j = p - n$, and $\tau_w = t - \delta$. D is the influence of the geometry on the trim downwash, which can be obtained from numerical or analytical perturbation of the trim influence coefficients.

Substituting equations 64 and 65 into equation 66, and reordering the integrations, produces the required convolution form, and the increment to the impulse response for equation 33 can be identified. Here the wake geometry is time-invariant, so the integral over σ produces a factor $\min(\tau_w, \tau)$, which is the time that the velocity (constant for time-invariant geometry) from the wake at τ has been acting on the wake at τ_w . The result is

$$\Delta h_{kl}^j(\tau) = \sum_i \sum_{p=0}^{N-1} \int_0^{\infty} [\min(\tau_w, \tau) D_{ki}^p(\tau_w) h_i^{j-p}(\tau - \tau_w)] d\tau_w \quad (67)$$

for the shed and trailed wake. The integration over τ_w must be discretized, e.g. using trapezoidal integration. Evaluating Δh using equation 67 is very expensive

compared to the direct contribution (equations 60 and 61). Both D and h in equation 67 have wide variations in magnitude (they are large only when s is small), so it should be possible to develop an efficient computation procedure (perhaps in parallel with the calculation of the trim free wake geometry).

As a specific example, consider the case of undistorted trim wake geometry. The contributions of the wake strength perturbations to the impulse response are given by equations 60 and 61. The same wake model is used to derive the impulse response required by equation 64, which is the velocity on the wake surface rather than on the wing. The result is

$$h_s(\tau) = \frac{1}{4\pi} \frac{-r \sin\theta (\rho - r \cos\theta)}{\left((r \sin\theta)^2 + z^2 \right) s} \left| \begin{array}{l} \rho_R \\ \rho_L \end{array} \right. \quad (68)$$

$$h_i(\tau) = \frac{1}{4\pi} \frac{\rho (\rho - r \cos\theta)}{s^3} \left| \begin{array}{l} \rho_R \\ \rho_L \end{array} \right. \quad (69)$$

where s is given by equation 59; $\theta = \psi_m - \psi_p - \phi + \phi_w = (m-p)\Delta\psi - (\tau - \tau_w)$; and $z = v_0(\tau - \tau_w)$. Care is required to evaluate the velocity induced by a vortex sheet or line on itself. Here the cutoff method is used: the velocity contribution (hence h) is zero from vortex elements within a small distance ϵ from the point where the velocity is calculated. The other quantity required by equation 66 is the function D . Integrating over the trailed wake produced by the trim loading gives the trim induced velocity at the n th blade:

$$\lambda_{trim}^n = \sum_p \sum_i \int_0^\infty \Gamma_{i_{trim}} \left[\frac{1}{4\pi} \frac{\rho (\rho - r \cos\theta)}{s^3} \left| \begin{array}{l} \rho_R \\ \rho_L \end{array} \right. \right] d\tau_w \quad (70)$$

where s is given by equation 59; $\theta = \psi_p - \psi_n - \phi_w = (p-n)\Delta\psi - \tau_w$; and $z_{trim} = v_0\phi_w$. Perturbing z in equation 70 gives the function D of equation 66:

$$D = \Gamma_{i_{trim}} \left(-\frac{3z}{s^2} \right) \frac{1}{4\pi} \frac{\rho (\rho - r \cos\theta)}{s^3} \left| \begin{array}{l} \rho_R \\ \rho_L \end{array} \right. \quad (71)$$

This expression requires the trim bound circulation. For the present purposes, $\Gamma(\rho_i)$ is assumed to vary linearly from zero at the root, to a maximum at r_p , to zero at the tip; and the maximum trim bound circulation is estimated from the rotor thrust using $\Gamma_{max} = 9.8 C_T/N$ (for $r_p = .93$).

2.4.4 Rotor Velocity Perturbations

A perturbation of the velocity of the rotor relative to the air, from either rotor hub motion or gusts, with change the loading on the rotor and therefore change the induced velocity, as described by equation 33 (including wake geometry perturbation produced by the loading change). In addition, such rotor velocity perturbations will directly change the wake geometry, and thereby produce further inflow changes. Thus a new term must be added to equation 33:

$$\Delta\lambda_{V_k}^n(t) = \int_0^{\infty} h_V(\tau) \mu(t-\tau) d\tau \quad (72)$$

where μ is a vector of variables describing the rotor velocity perturbations; and h_V is a function of r_k , n , and τ . This effect can be substantial; for example, for the low frequency response to vertical hub motion in hover, it reduces the inflow by a factor of 2. The formulation of the theory for equation 72 parallels what has been derived so far.

Consider hover, and the vertical geometry perturbations produced by vertical velocity perturbations on the wake. The vertical velocity (of the air relative to the rotor, positive downward) at r_i on the p th wake can be written:

$$\mu_{zi}^p(t, \delta) = M_i^p(\delta) \mu(t) \quad (73)$$

For example, vertical velocity, pitch rate, and roll rate of the hub give

$$\mu_{zi}^p(t, \delta) = \begin{bmatrix} 1 & -r_i \cos \psi & r_i \sin \psi \end{bmatrix} \begin{pmatrix} \dot{z} \\ \dot{\alpha}_y \\ \dot{\alpha}_x \end{pmatrix} \quad (74)$$

where $\psi = \psi_p - \phi_w = t - \tau_w + p\Delta\psi = \delta + p\Delta\psi$ (actually this is the velocity at the rotor disk, which will be close for the near wake). Then the vertical position change produced by this velocity is given by equation 65 (with μ_z used in place of λ_w), and the inflow increment produced by the geometry perturbation is given by equation 66 (giving $\Delta\lambda_V$ here instead of $\Delta\lambda_G$).

Substituting equations 74 and 65 into equation 66, and reordering the integrations, produces the required convolution form, and the impulse response for equation 72 can be identified. The result is

$$h_{V_k}^n(\tau) = \sum_p \sum_i \int_{\tau}^{\infty} D_{ki}^{p-n}(\tau_w) M_i^p(\tau-\tau_w) d\tau_w \quad (75)$$

Evaluation of equation 75 will follow the methods for equation 67.

After equation 72 is introduced as a new term on the right-hand side of equation 33, it is necessary to follow the steps discussed in section 3. Model order reduction for the inflow variables will transform the impulse response as follows:

$$h_V^n = D^{-1}P^TW h_V^n \quad (76)$$

The multiblade coordinates are introduced, transforming the impulse response as follows:

$$h_{V_{non}}(\tau) = DT^T(t) h_{V_{rot}}(\tau) \quad (77)$$

It can be shown that the form of $h_{V_{rot}}$ is such that (for hover) $h_{V_{non}}$ is only a function of τ ; and that the equations are decoupled as usual by the multiblade coordinates (e.g. vertical velocity only affects the collective modes, and hub pitch rate and roll rate only affect the cyclic modes).

Including now the rotor velocity effects, equation 46 is replaced by:

$$l(t) = \int_0^{\infty} [h_s(\tau) \dot{g}(t-\tau) + h_l(\tau) g(t-\tau) + h_v(\tau) \mu(t-\tau)] d\tau \quad (78)$$

or in terms of the system function, $l = Hg + H_V\mu$. The equivalent differential equation is obtained by approximating the system functions as ratios of polynomials, hence equation 49 becomes

$$D(i\omega)l = N(i\omega)g + N_V(i\omega)\mu \quad (79)$$

Then the identification task must simply consider more input variables, i.e. μ as well as g for each inflow equation. Since there will normally be many more variables in g than in μ , the identification accuracy should not be degraded too much. Finally, the differential equations describing the wake become

$$\dot{L} + AL = Bg + B_V\mu \quad (80)$$

$$l = CL + Dg + D_V\mu \quad (81)$$

3. RESULTS

This section presents results directed at establishing the feasibility of the theory developed above. Key aspects to be investigated are the model order reduction, identification, wake rollup model, and wake geometry perturbations.

Most of the results are calculated for a hovering rotor with three blades, solidity ratio $\sigma = 0.075$, and blade loading $C_T/\sigma = 0.08$. The blade is divided into 19 aerodynamic panels, from $r/R = .14$ to 1.00, with the panel width ranging from 0.02R at the tip to 0.08R at the root.

3.1 Previous Results

Several examples of the impulse response are presented by Johnson (1987, 1988). The wing model used for these examples was lifting line theory, which allows direct interpretation of the downwash without chordwise integration. The impulse response was examined for the following cases.

- a) Two-dimensional airfoils. Two-dimensional problems have the advantage of analytical solutions, but the behavior is very different from that of three-dimensional wings. Theodorsen's problem provided a way to examine the manner in which the shed wake was treated in the unsteady lifting-line theory used. More complicated cases were an airfoil in a time-varying (periodic) free stream, and with the returning shed wake (wake sheets below the airfoil, similar to Loewy's model). These results were quite simple: the impulse response is just the downwash produced by an element of wake vorticity. In contrast, the lift deficiency functions for these two problems are complicated in derivation and form.
- b) Three-dimensional wings. These problems showed the influence of three dimensions on the impulse response; and showed the functional form in the time domain and frequency domain, as a guide to the identification task. The wake for these cases was undistorted sheets. The bound circulation was piecewise constant spanwise. Then it is possible to integrate the shed vorticity spanwise, and thus obtain analytical expressions for the impulse response of the shed and trailed wake. A fixed wing at constant flight speed is such a case. Another case is a helicopter rotor in hover, or even in forward flight. In contrast with other methods, the helical geometry of the rotor caused no additional problems with this approach.
- c) Hovering rotor. These problems showed the method in use for multiple wings (an N-bladed rotor, using multiblade coordinates), with prescribed wake geometry (contraction and two-stage vertical convection), and with model order reduction. The wake consisted of undistorted helical sheets (no rollup). The generalized coordinates used were uniform downwash response to blade thrust, and linearly-varying downwash response to blade flap moment. These are the conventional variables of simple rotor wake models, but are not truly proper for the aerodynamics

of the problem. These examples showed the mathematics of the model order reduction were correctly formulated, but did not establish the correct generalized coordinates to use.

d) Rotor in forward flight. This problem has time-varying wake geometry, so the impulse response depends on the blade azimuth when the wake element was created, as well as on the time since it was created.

e) Computational example. This case illustrated a complicated configuration, and the calculation of the impulse response in parallel with computation of the trim wake influence coefficients. The case was a three-bladed single main-rotor helicopter in forward flight. The wake model had rolled-up tip vortices, and self-induced distortion of the trim wake geometry. The calculation of the impulse response was added to an existing computer program for the trim wake model. The computation time was increased by only 5%.

3.2 Undistorted Wake

3.2.1 Impulse Response

The identification and model order reduction will be investigated using the undistorted wake model (section 2.4.1). Figures 1-3 show the impulse response as a function of time (wake age in revs). Figure 1 shows the effect of the wake directly behind the blade. The inflow at $0.77R$ from the trailed and shed wake produced by bound circulation at 0.77 , 0.81 , and $0.845R$ is shown. The near wake effect is comparable to that on fixed wings (Johnson, 1988), and exists only for about 0.01 revs. Figure 2 shows the impulse response from the far wake as well. The trailed wake generates pulses and the shed wake generates doublets at intervals of $1/\text{rev}$ as the blade rotates over it. The magnitude of h at the peaks (including $\tau = 0$) depends strongly on the width of the aerodynamic panels. Figures 1 and 2 show the effect of the wake of blade 1 on blade 1. Figure 3 shows the impulse response from the wake of all three blades (at $0.77R$), acting on blade 1 (at $0.77R$). The impulse response appears as a succession of pulses, because of the returning wake of a hovering rotor.

Figures 4 and 5 show the impulse response with the transformations of model order reduction applied to both inflow and circulation. A single inflow and a single circulation mode are used, uniform for figure 4 and linear (proportional to r) for figure 5. Model order reduction has the effect of broadening the peaks in the impulse response, implying less high frequency content in the system function. (Model order reduction is only used for the inflow, not the circulation, for the remainder of the investigation.)

Figures 6 and 7 show the impulse response with the multiblade coordinate transformation applied (but not model order reduction). The inflow at $0.77R$ from the circulation at $0.77R$ is shown for the various multiblade coordinates. Note that

for a hovering rotor, the axisymmetry implies $l_{nc}/g_{nc} = l_{ns}/g_{ns}$ and $l_{nc}/g_{ns} = -l_{ns}/g_{nc}$. Figure 7 is for a four-bladed rotor, to show the differential collective mode. Comparing figures 3 and 6, it is evident that the multiblade coordinate transformation primarily just adds the responses from all the blades (with some sign changes at longer times). Specifically, the transformation multiplies the rotating frame h_j by one of the factors $(1, \cos k\psi_j, \sin k\psi_j, (-1)^j)$, where $\psi_j = \tau - j\Delta\psi$. Hence the collective mode (l_0/g_0) indeed just sums the rotating frame impulse responses, and the differential collective mode $(l_{N/2}/g_{N/2})$ sums them with alternating signs (figure 7). For the hovering rotor, the rotating frame impulse response h_j is large only near the peaks at $\tau = j\Delta\psi + n\pi$ ($n = 0$ to ∞). So where h_j is large, $\cos k\psi_j \cong \pm 1$ and $\sin k\psi_j \cong 0$. Hence the direct cyclic and reactionless modes $(l_{nc}/g_{nc}, l_{ns}/g_{ns})$ also primarily sum h_j (with sign changes at larger time than shown in figure 6), and the off-diagonal cyclic and reactionless modes $(l_{nc}/g_{ns}, l_{ns}/g_{nc})$ are small.

Figure 8 shows the impulse response with model order reduction (for the inflow modes only) and multiblade coordinates. The response of a single, uniform inflow mode to the circulation at $0.77R$ is shown. The model order reduction broadens the peaks, but still the collective and direct cyclic modes $(l_0/g_0, l_{1c}/g_{1c}, l_{1s}/g_{1s})$ are similar, and the off-diagonal cyclic modes $(l_{1c}/g_{1s}, l_{1s}/g_{1c})$ are small. It follows that for the present feasibility investigation, focusing on the identification and model order reduction, it will be sufficient to consider just the collective modes. Of course, for the aerodynamic and dynamic behavior of rotors, the cyclic modes are important as well.

3.2.2 System Function

The behavior of the system function will be examined for the collective, uniform inflow mode from circulation at $0.77R$. The FFT applied to the impulse response produces the system function. It is necessary to establish the sample rate r (per rev) and length T_{max} (rev) in the time domain that will give an accurate system function. The time step is $\Delta t = 360/r$ degrees of azimuth. The system function will have a bandwidth of $\omega_{max} = r/2$ (per rev) and a resolution of $\Delta\omega = 1/T_{max}$ (per rev). Small r and T_{max} are desired, to minimize the computation time. Note that calculations of the trim wake-induced velocity typically use an azimuthal step of 10-15 deg ($r = 36-24/\text{rev}$), and 2-4 revs of wake (with an inexpensive far wake model in hover, to extend the wake to 20 revs or so). If T_{max} is too small, the resolution in the frequency domain will be too large. If the sample rate is too small, the peaks of the impulse response will not be resolved well, and the bandwidth of the system function will not be large enough. The rotor dynamics suggest that the required bandwidth is perhaps 3/rev for problems involving the flap motion, and at most about 10/rev in general. The identification of the wake differential equations will consider such a frequency range. It is found that the primary factor determining the sample rate is the need to avoid significant aliasing in the system function over the frequency range of the rotor dynamics.

Figure 9 shows the impulse response of the trailed and shed wake, for sample rates from 256/rev to 32/rev. Even 32/rev gives a reasonable resolution of the peaks in the time domain, losing little information compared to 256/rev.

Consider the behavior of the system function implied by the form of the impulse response in figure 9. Since $h(0)$ is finite and nonzero, it follows that H behaves like $h(0)/s$ at large s (Laplace form), for both the shed and trailed h . Since $H(0)$ (equal to the integral of $h(\tau)$ from 0 to ∞) is finite, it follows that H approaches a constant at small s , for both the shed and trailed h . The total system function is $H = H_t + i\omega H_s$. The shed wake contribution to H ($i\omega H_s$) is proportional to s at small s and approaches a constant at large s . So the total system function H has a constant, nonzero value at low frequency, from the static trailed wake influence (three-dimensional wing); and a constant, nonzero value at high frequency, from the unsteady shed wake influence (lift deficiency function). Such behavior can be approximated by a polynomial system function, with equal number of poles and zeros.

Figure 10 shows the system function: H_t and H_s , obtained by FFT of the impulse response; $i\omega H_s$; and the total $H = H_t + i\omega H_s$. With a sample rate of 256/rev, $\omega_{\max} = 128/\text{rev}$, but the results in figure 10 are significantly affected by aliasing above about 40/rev (figure 9 gives $h_s(0) = 0.374$, hence $H(\infty)$ should be 0.374). Figure 11 shows the system function for only the near wake part of the impulse response ($\tau < 1/6$ rev in figure 9). The high frequency behavior comes from near shed wake, while the oscillations in H are the effect of the far wake. The near wake part of the impulse response is a pulse at $\tau = 0$. This pulse has a width of about 0.006 rev, which implies a break frequency in the system function of around 25/rev. This is a typical frequency range for two-dimensional shed wake effects (25/rev corresponds to a reduced frequency k of around 0.8). Note that H is the induced velocity produced by the circulation change, so a positive phase for H gives a phase lag in the lift-deficiency function. A two-dimensional wing would have no static effect of the wake ($H(0) = 0$). The nonzero value of $H(0)$ here is the static induced velocity of a three-dimensional wing. It is necessary to consider the bound circulation over the entire span (not just $0.77R$ as in figures 9-11) to determine the relative effects of the trailed and shed wake.

The far wake contribution to the trailed impulse response h_t is roughly a train of pulses, occurring at N/rev :

$$\Delta h_t = \sum_{n=1} h_n(\tau - n\Delta\psi) \quad (82)$$

where h_n is a single pulse at $\tau = 0$. The system function for equation 82 is

$$\Delta H_t = \sum_{n=1} H_n e^{-i\omega n\Delta\psi} \quad (83)$$

H_n is the system function of h_n , so it has a slow variation over a wide frequency range (like the near wake term). The exponential factor in equation 83 has unit magnitude and a phase that increases linearly with frequency. The exponential factor has the effect of rotating the complex vector H_n with a period (in frequency) of (N/n) per-rev. If the near wake pulse is dominant, then the effect of the first far wake pulse in h_t (at $\tau = 1/N$ rev) is to produce an oscillation in the magnitude and phase of the total system function, with a period in ω of N/rev . This case is illustrated in figure 10 ($N = 3$ here). The oscillation decays in amplitude as frequency increases because of the reduction in amplitude of H_1 ; this decay has a bandwidth roughly the same as the near wake term. If instead the first far wake pulse is dominant, the system function will have a magnitude varying slowly with frequency, while the phase varies linearly with frequency, changing by 2π when ω increases by N/rev . The far wake contribution to the shed impulse response h_s has a similar behavior, except that it is roughly a train of doublets instead of pulses.

Figure 12 shows the system function over the range 0 to 10/rev, for $T_{\max} = 4$ rev and sample rates from 256/rev to 32/rev. The corresponding time step, frequency resolution, and bandwidth are shown in the following table.

r	T_{\max}	Δt	$\Delta\omega$	ω_{\max}
256/rev	4 rev	1.4 deg	0.250/rev	128/rev
128	4	2.8	0.250	64
64	4	5.6	0.250	32
32	4	11.2	0.250	16
128	8	2.8	0.125	64

Aliasing demands a higher sample rate than indicated by the time domain resolution of the peaks. Up to 10/rev a sample rate of 128/rev is good, while 64/rev gives a noticeable effect of aliasing, and 32/rev may not be acceptable. Figure 13 shows the effect of increasing the sample length to 8 rev. The smaller frequency resolution has a minor effect. While reducing $\Delta\omega$ produces a smoother looking system function, it does not introduce more information, and so can not help the identification process.

For the remainder of this investigation, $T_{\max} = 4$ rev and $r = 128/\text{rev}$ are used, to avoid any possibility that errors caused by aliasing would produce misleading results in the identification task. A wake azimuthal increment of 2.8 deg is much smaller than desired for computational efficiency however. When the development of this method is completed, one objective must be to establish practical minimums for the sample rate and length (e.g. 2 rev of wake, padded with 2 rev of zeros, and $r = 32/\text{rev}$), in the context of specific rotor problems.

For a quantitative assessment of the system function, consider the response of the inflow to rotor thrust changes. A single inflow mode is used (uniform over the blade span), but model order reduction is not used to replace the circulation as a function of radius by a generalized force equivalent to the thrust. Instead, the rotor frequency response during collective pitch input is calculated. Omitting the flap and hub velocity terms, equations 16 and 18 give the rotor thrust C_T and bound circulation in terms of collective pitch and the inflow mode l_{u0} (uniform, collective). The calculated system function relates l_{u0} to the bound circulation (at all radial locations). Eliminating the bound circulation from these equations gives $\partial l / \partial \theta$ and $\partial C_T / \partial \theta$, and their ratio gives the inflow response to thrust $\partial l / \partial C_T$ (during collective pitch input). Figure 14 shows these three quantities for a three-bladed rotor. Vortex theory (i.e. with fixed wake geometry) gives a static response of $\partial l / \partial C_T = 9.1$, while figure 14 shows a value of 7.1, confirming the magnitude of the calculated system function. The difference is likely caused by the assumption of uniform inflow for collective pitch changes with a discrete wake model. (Note that momentum theory, which includes the static effects of wake geometry changes, gives $\partial l / \partial C_T = 4.6$.) In form figure 14 is similar to figure 12, so the inflow response to the bound circulation at $0.77R$ does reflect the global behavior of the rotor.

Figure 15 shows the inflow response to thrust as the number of blades varies from 3 to 8. Increasing the number of blades moves the peaks of the system function to higher frequency (multiples of N/rev), resulting in a simpler variation of H over the frequency range of interest (but more multiblade coordinates). The identification task will be examined only for the worst case, of a three-bladed rotor.

3.2.3 Identification

The identification task approximates the calculated system function by a ratio of polynomials, thereby defining a differential equation that approximates the integral equation. Figure 16 shows the calculated system function for uniform inflow from the bound circulation at several radial stations along the blade. There are some interesting differences between radial stations, also reflected in the radial variation of the impulse response (as in figure 17; the oscillation is a result of integrating along the span for the inflow model order reduction), but generally the system function behaves in a similar fashion along the blade. This is the case that will be used to investigate the identification and model order reduction tasks. Least-squared-error identification is used (as described in section 2.3.2), with weighting as a function of frequency. The basic frequency range of the identification means a weight of 1 within that range and a weight of 0 outside it. The frequency range of interest for rotor dynamics extends from zero (static) to some maximum that depends on the problem, but is usually less than $10/\text{rev}$. Selection of this basic frequency range serves to focus the identified wake model for a specific problem. A further use of the weighting over frequency will be to control the placement of the poles produced by the least-squared-error solution.

It is important to remember that a rational function representation of the system function, i.e. a discrete set of poles and zeros, must always be an approximation. A pole-zero representation implies that the impulse response decays exponentially with τ , but in fact the wake model will always produce a decay with $1/\tau$ to some power. In addition, a common problem of finite-state aerodynamic theories with unconstrained identification is the appearance of positive (unstable) roots in the wake model. When they occur here, these roots are very large (outside the frequency range of the identification). Such large roots (positive or negative) imply that the functional form of the approximation has a limited ability to match the correct response. For stability and frequency response calculations the positive roots could be ignored, but for most purposes they are not acceptable, and a key question is the ability of the least-squared-error method to avoid this problem.

The form of the system function (figure 16) suggests what pole-zero representation will be required. The drop in magnitude and the phase shift at low frequency, produced primarily by the trailed wake (see figure 12), imply at least one small pole (on the order of $.1/\text{rev}$). The near shed wake effect (see figure 11) will require at least one large pole (on the order of $20/\text{rev}$, probably outside the identification frequency range). The combination of these two effects requires a minimum of two poles and two zeros. The magnitude change and phase shift occurring near N/rev , $2N/\text{rev}$, etc (see figure 12) will require at least two complex poles and two complex zeros for each peak, with a frequency around N/rev , etc. Hence the basic character of the system function determines the minimum order, which is twice the number of peaks (including the static peak) within the identification frequency range. Additional poles and zeros should improve the identification. However, as the order is increased the least-squared-error method tends to place the new poles and zeros well outside the identification frequency range, in order to produce just a slight improvement within the range. The sign of these large roots is not constrained by the response within the identification range, hence the method allows unstable roots to occur.

Consider first the identification of the system function for uniform inflow response to the bound circulation at a single radial station, $r = 0.77R$ (figure 12, with 4 revs of wake and 128/rev sample rate). Figure 18 shows the influence of the assumed frequency range and order on the identification. The results show that the minimum order is indeed twice the number of peaks with the identification frequency range. That minimum order provides a fair fit, and one more pole-zero pair gives a good fit. Two more pole-zero pairs beyond the minimum order (i.e. the maximum order shown in figure 18 for each frequency range) give a good fit, but with a large positive (unstable) pole. The identified poles and zeros are listed in table 1. At frequencies beyond the specified range of identification, the identified system function has very different behavior than the calculated H . It is assumed that the content of the rotor dynamics will make this behavior unimportant.

The complete identification considers the inflow modes separately (see section 2.3.2), but the bound circulation at all radial stations simultaneously. Hence

the system functions are identified with separate zeros for each bound circulation variable, but a common set of poles. Requiring the same set of poles to provide a fit for several system functions (here 19 radial stations are used) degrades the identification. Figure 19 shows the calculated and identified system function for uniform inflow from circulation at 0.77R, when the identification covers all radial stations. Comparing figures 18 and 19, it is observed that for a fixed order the fit is indeed worse in figure 19. The identified poles, and the zeros for 0.77R, are listed in table 2. A problem introduced by considering all radial stations is the erratic appearance of positive roots. It is not practical to plot the system function for all modes and all radial stations. Instead, the accuracy of the identification will be assessed in terms of the rms system function error ϵ for each l_k and g_l combination, defined as:

$$\epsilon^2 = \frac{1}{K} \sum_{\omega} |H - H_{id}|^2 \quad (84)$$

where the sum is over the K frequency points within the identification frequency range. Note that the least-squared-error method minimizes a different quantity, namely

$$\sum_{\omega} |\Theta X - Y|^2 = \sum_{\omega} |DH - N|^2 = \sum_{\omega} |D_{id}|^2 |H - H_{id}|^2 \quad (85)$$

(see equation 52). The error ϵ is not normalized, so its magnitude is not directly meaningful. Hence a value of ϵ is given for the plotted system function, to provide a reference for judging the values at other radial stations. Table 2 presents the rms error for 0.77R, and the minimum and maximum values among the other radial stations. Generally, the fit at 0.77R is characteristic of the entire span, and the fit steadily decreases as the order is increased. Note however that the appearance of unstable poles at low order is also accompanied by increased identification error.

With the objective of eliminating the positive poles, several schemes for choosing the frequency weighting in the identification were tried. Introducing a small weight for frequencies above the basic identification range helped control the appearance of positive poles for one radial station (figure 18), but did not improve the fit much (the additional poles tend to be wasted on a poor fit at high frequency) and did not help control the positive poles for all radial stations (figure 19). Observing that the fit in figure 19 is particularly worse at low frequency, compared to figure 18, an increased weight was tried for the low frequencies within the basic identification range. Figure 20 and table 3 show the results for an identification range of 0 to 4.5/rev (basic weight = 1), with the weight increased to 4 and to 16 over the range 0 to 1.5/rev. The fit is improved with this scheme, and the appearance of positive roots is more consistent and is delayed to higher order.

The next step is to perform the identification for more than one inflow mode. For the model order reduction, the inflow is represented by a series of polynomials.

The series begins with uniform inflow, and is orthogonal when integrated with unit weight from the root to the tip (i.e. shifted Legendre polynomials). By using orthogonal functions, the first (uniform) mode has the same system function regardless of the total number of modes retained. Figure 21 shows the system function of the first three inflow modes, from the circulation at $0.77R$. The three modes exhibit similar behavior, so similar results of the identification process are expected. The identification is accomplished separately for each inflow mode. So each inflow mode has its own poles, which are common to the system functions for the circulation at all radial stations. Figure 22 and table 4 show the influence of the order and frequency weighting on the identified system function, poles, and rms error for three inflow modes. The fit is somewhat worse for the higher modes, but the weighting that improved the identification for the first mode works for the higher modes as well.

For investigation of the effects of model order reduction, the wake equations were constructed for the following case: collective modes of a three-bladed rotor; identification frequency range of 0 to 4.5/rev (with weight = 16 for 0 to 1.5/rev) and order = 6; six inflow modes; and $C_T/\sigma = 0.08$ and 0.02. Figures 23 and 24 show the system function, and table 5 lists the poles and rms error. The other multiblade coordinates are important for rotor aerodynamic and dynamic behavior, but not this feasibility investigation, since the form of the system function is similar for all degrees of freedom. This frequency range includes the first peak of the system function, and is enough to examine rotor flap and pitch-flap dynamics. The order provides good identification (although how good a fit is required is not established yet). Six inflow modes will be enough to investigate convergence of the model order reduction. With six inflow modes and sixth order equations, the wake model has a total of 36 states. A relatively low value of thrust, $C_T/\sigma = 0.02$, is examined in order to check for different behavior associated with increased magnitude of the induced velocity (as shown in figure 24).

3.2.4 Model Order Reduction

A model order reduction transformation is applied to the inflow variables in order to minimize the number of states introduced by the time-domain model of the wake. It is necessary to establish how few modes can be used, while retaining an accurate representation of the unsteady aerodynamics. This issue is examined by varying the number of inflow modes and looking at (a) the convergence of the rotor eigenvalues and response; and (b) the radial variation of the inflow during the rotor motion.

Two aeroelastic problems are considered: flap and flap-pitch motion of a rotor blade. The eigenvalues of the coupled blade-wake system are examined, as well as the response of the rotor motion to collective pitch input (and the response to vertical hub motion for the flap problem). Only collective motions are analyzed. The blade parameters required are flap frequency $\nu = 1.05/\text{rev}$; Lock number $\gamma = 8$;

pitch frequency $\omega_\theta = 3.0/\text{rev}$ (resonant with the wake effect for a three-bladed rotor); pitch inertia $I_f/I_b = 0.1(c/R)^2$ (dimensionless, with c the rotor chord); and the center-of-gravity 3% chord aft of the pitch axis (stable, but near enough to flutter and divergence to provide significant coupling of flap and pitch).

Figure 25 and table 6 show the roots of the coupled flap motion and wake model. The static wake model neglects all the time derivatives of the inflow states. The uncoupled flap root has a magnitude (natural frequency) equal to the flap frequency ν , and a real part of $-\gamma/16$. With a static wake model, the only change is to replace the Lock number by an effective values, $\gamma^* = C\gamma$, where C is a lift deficiency function, and a static value of $\partial\lambda/\partial C_T$ (dl/dT in table 6) can be calculated from C . The momentum theory result $\lambda = \kappa\sqrt{C_T/2}$ gives $\partial\lambda/\partial C_T = f/\lambda_0$, $f = \kappa^2/2$ (where λ_0 is the mean induced velocity). It is more appropriate to compare the present results with vortex theory, which by assuming fixed wake geometry gives twice the induced velocity perturbation as momentum theory: $f = \kappa^2/4$. The factor f is given in table 6. Table 6 shows that two inflow modes are sufficient to define the static root. Moreover, the values of C and f deduced from the wake model results are close to the vortex theory values, confirming the magnitude of the calculated wake effect (the differences may be caused by the assumption of uniform inflow in the vortex theory result). Table 6 shows that three to four inflow modes are needed for convergence of the flap roots when the dynamics of the wake are retained.

Figure 26 shows the frequency response of the flap motion to collective pitch and vertical hub motion input, for $C_T/\sigma = 0.08$ and 0.02 . Two to three inflow modes are needed for convergence of the response. It must be remembered that the static response (at least) in these figures is affected too much by the wake, because wake geometry perturbations have not been accounted for. Regarding the wake aerodynamics illustrated by figure 26, it is clear that the static wake model is not appropriate. The phase shows more of an influence of the returning wake (near $3/\text{rev}$) because with a flap frequency near $1/\text{rev}$ the magnitude of the response is small at the high frequencies. The wake effect near $3/\text{rev}$ is increased for the lower thrust value.

For the flap-pitch motion, the pitch frequency is set to $3/\text{rev}$ and the center-of-gravity moved aft of the pitch axis, in order to produce a significant amount of motion at high frequency. Table 7 lists the flap and pitch roots (for the blade center-of-gravity 0% as well as 3% chord aft of the pitch axis). Figure 27 shows the frequency response of the flap and the pitch motion to collective pitch input. Two to four inflow modes are needed for convergence. The influence of the wake roots near $3/\text{rev}$ is evident in the response, especially for low thrust.

While the blade motion is being excited in these models, the wake model produces an induced velocity along the span of the blade. Figures 28 and 29 show the radial variation of the inflow response at frequencies of 0, 0.40, and 2.25/rev; for the rotor with flap motion at $C_T/\sigma = 0.08$. Similar results are obtained for the inflow response at $C_T/\sigma = 0.02$, and for the rotor with flap-pitch motion. Plotted is the

cumulative effect of the modes, using the wake model with six inflow modes. Two modes give the magnitude well out to about 85% radius, but three or four modes are needed for the magnitude at the tip. Note that this variation at the tip is obtained without rollup or contraction in the wake. The static response however might be well represented by a single, simple mode; but the mode shape required is different for collective and vertical hub motion input (linear and constant inflow respectively). Two or three modes are needed to define the phase variation over the span of the blade. Note that one mode can never give a phase shift that varies with radius. So the significant phase shift over the span (90 to 180 deg) shown in figures 28 and 29 means that one mode (even with the correct magnitude variation) is not sufficient.

3.3 Rolled Up Wake

A model for the impulse response of a hovering rotor wake, including the effects of the wake distortion and the tip vortex rollup, was developed in section 2.4.2. A principal objective is to verify the formulation of that model, in particular the relationship between the wake strength and the peak bound circulation. Thus the calculations for the undistorted wake model are repeated with the rolled-up wake model. It must be established whether this change in wake model modifies the conclusions regarding identification and model order reduction. A secondary objective is to examine the effects of the wake distortion and rollup on the results. Note that calculating the impulse response (in the rotating frame, before model order reduction) is at the lowest level in the analysis, so replacing the undistorted wake model with the rolled-up wake model is straightforward, and all other operations (model order reduction, multiblade coordinates, identification, coupling with the blade equations, etc.) remain unchanged.

Figure 30 shows the shed and trailed wake impulse response obtained using the rolled-up wake model (compare with figure 9 for the undistorted wake). The peak bound circulation of the trim loading is assumed to occur at 93% radius. That circulation value determines the strength of the far wake, hence figure 30 shows the uniform inflow response to the perturbation bound circulation at $0.93R$. Figure 31 shows the corresponding system function (compare with figure 12). Since this system function contains the effect of all the far wake, there is more influence of the trailed wake than in figure 12. Also, the phase shows a linear increase with frequency, which is a consequence of the dominance of the first peak from the returning wake compared to the near wake (figure 30). Figure 32 shows the system function at other radial stations, which now contain only a near wake effect (compare with figure 16).

Figure 33 and table 8 show the identified system function with the rolled-up wake model (compare with figure 23 and table 5). Generally, the behavior observed in the identification task for the undistorted wake model was found here as well. The fit of the identification for the second and sixth modes could be improved.

Also, with the weight = 16 for frequencies from 0 to 1.5/rev and 1 from 1.5 to 4.5/rev, the fourth inflow mode has a positive pole. For just the fourth mode, an additional weight of 10^{-9} from 4.5 to 9/rev was used, which eliminated the positive root (using a lower order model for this mode might also have been sufficient). So the wake model change did influence the identification, but minor modifications of the techniques established using the undistorted wake model were satisfactory.

Table 9 shows the flap roots, and figure 34 shows the flap response to collective pitch (compare with table 6 and figure 26). As for the undistorted wake, two to three modes are needed for convergence of the response. Figure 35 compares the response calculated using the undistorted and rolled-up wake models. The response behavior near 0.5/rev with the rolled-up wake might be associated with the identification error in the second inflow mode.

Figures 36 and 37 show the inflow response along the span of the blade, during collective and vertical hub motion input respectively (compare with figures 28 and 29). The number of modes required is generally the same as with the undistorted wake. Figure 38 compares the inflow response obtained using the undistorted and rolled-up wake models. At low frequency, the rolled-up wake model produces much more variation of the inflow near the tip. It is possible that even more inflow modes are needed to fully define this behavior. At high frequency there is much less effect of the rollup.

3.4 Wake Geometry Perturbations

A theory that includes the effects of wake geometry perturbations on the impulse response was developed in section 2.4.3. An objective of this investigation is to verify the formulation of this theory. Thus the calculations of the impulse response for the undistorted wake model are repeated, including the wake geometry perturbations. Since wake geometry is involved, efficiency is also an issue. Including the wake geometry perturbations in the analysis again only affects the impulse response calculation, at the lowest level in the analysis.

Figure 39 compares the shed and trailed wake impulse response obtained with and without the wake geometry perturbations. The near wake effect, at small τ , is not changed by the geometry perturbations. The returning wake effects, especially from the trailed wake, are reduced by the geometry perturbations. That is the expected result for a collective, uniform inflow mode, since vortex theory shows that wake geometry changes reduce the steady induced velocity by a factor of two. Note that for the first two interactions between the blade and the wake, the strength perturbations dominate and the trailed pulses are positive; while for subsequent interactions the geometry perturbations dominate, and the pulse are negative.

Regarding efficiency, including the wake geometry perturbations increases the time required to compute the impulse response by 2 or 3 orders of magnitude. That

is a typical result for free wake geometry analyses where no effort has been made to develop efficient methods.

4. CONCLUSIONS AND RECOMMENDATIONS

4.1 Conclusions

4.1.1 Identification

The least-squared-error method gave satisfactory results for the cases considered. It was not difficult to find a weighting over frequency that controlled the occurrence of positive roots. The behavior of the method was similar for different inflow modes and different thrusts, and with an undistorted or rolled-up wake model. However, there was a limit to how accurate an identification could be achieved. This limit might reflect the fact that a ratio of polynomials is not in fact the proper form for the system function.

Further work is needed to establish how accurate the identification needs to be. This can only be done in the context of specific applications, for a wide range of parameters and operating conditions. It appears that the least-squared-error method will be satisfactory, but a target is needed against which to judge it. The next stage of the investigation should apply a constrained identification method, at least to provide that target.

4.1.2 Model Order Reduction

For the cases considered, with either undistorted or rolled-up wake models, two to four inflow modes were needed for convergence. A single mode (linear or constant) does not in general give good results. In fact, the phase shift of the inflow response over the span of the blade precludes the use of a single (real) mode, regardless of its shape. The rolled-up wake model influenced the inflow distribution near the tip for low frequencies.

Further work is needed to establish how accurate the radial distribution of the inflow needs to be. The accuracy must be assessed in terms of specific measures, such as damping levels, stability boundaries, or static derivatives.

4.1.3 Wake Geometry Perturbations

Application of the theory for the wake geometry perturbations confirmed its development for a hovering rotor. Efficiency is the key issue. As for a trim free wake analysis, a direct method is not practical because of excessive computation time. It is anticipated, based on experience with the trim problem, that a 2 or 3 order-of-magnitude reduction in computation time is achievable, using the appropriate numerical methods. Future work should focus on a discretized, distorted wake model however.

4.2 Recommendations

The following research is required to produce a general time-domain unsteady aerodynamic model for rotors.

- a) The work should focus on a discretized wake model, with rolled-up and distorted geometry, since the advantage of the approach is its ability to handle such wake configurations. Forward flight must be considered, not just hover.
- b) The development of the identification and model order reduction techniques must be completed. It is necessary to establish an approach that consistently gives good accuracy and no problems with the differential equation form. For forward flight, it is necessary to develop the identification techniques to handle periodic coefficient equations (as a constant coefficient approximation).
- c) The development of the theory for wake geometry perturbations must be completed. For accuracy it is essential that the effects of wake geometry perturbations, from both loading and velocity changes, be included in the induced velocity. It is necessary to develop an efficient method (perhaps efficient when implemented in parallel with a trim wake geometry calculation).
- d) The theory must be applied to rotor problems. It is necessary to establish what aspects of the theory are important for what problems. The analysis should be used to investigate the unsteady aerodynamics of helicopter rotors. It is necessary to compare the stability and response calculations with experiment.
- e) Standard differential-equation models should be developed, probably low order differential equations with precalculated coefficients. Such models can be easily incorporated in simple analyses of rotor dynamics.
- f) The theory should be implemented for routine use in rotorcraft aeroelastic calculations. For this purpose, a general form suitable for a comprehensive analysis is required.
- g) The theoretical basis can be extended, for example to include a compressible wing and wake; or a lifting surface or panel model of the wing.

REFERENCES

- Bisplinghoff, R.L., Ashley, H., and Halfman, R.J. Aeroelasticity, Addison-Wesley, Reading, MA, 1955.
- Brase, L.O., and Eversman, W. "The Application of Transient Aerodynamics to the Structural Nonlinear Flutter Problem." AIAA Paper No. 87-0908, April 1987.
- Dowell, E.H. "A Simple Method for Converting Frequency-Domain Aerodynamics to the Time Domain." NASA TM 81844, October 1980.
- Dunn, H.J. "An Analytical Technique for Approximating Unsteady Aerodynamics in the Time Domain." NASA TP 1738, November 1980.
- Edwards, J.W. "Unsteady Aerodynamic Modeling for Arbitrary Motions." AIAA Journal, Vol 15, No 4, April 1977.
- Edwards, J.W., Ashley, H., and Breakwell, J.V. "Unsteady Aerodynamic Modeling for Arbitrary Motions." AIAA Journal, Vol 17, No 4, April 1979.
- Johnson, W. Helicopter Theory, Princeton University Press, Princeton, NJ, 1980.
- Johnson, W. "General Time-Domain Unsteady Aerodynamics of Wings." 25th Aircraft Symposium of Japan Society for Aeronautical and Space Sciences, Tokyo, December 1987.
- Johnson, W. "Time-Domain Unsteady Aerodynamics of Rotors with Complex Wake Configuration." Vertica, Vol 12, No 1/2, 1988.
- Johnson, W. "Airloads, Wakes, and Aeroelasticity." NASA CR 177551, April 1990.
- Karpel, M. "Design for Active Flutter Suppression and Gust Alleviation Using State-Space Aeroelastic Modeling." Journal of Aircraft, Vol 19, No 3, March 1982.
- Kocurek, J.D., and Tangler, J.L. "A Prescribed Wake Lifting Surface Hover Performance Analysis." Journal of the American Helicopter Society, Vol 17, No 4, October 1977.
- Miller, R.H. "Rotor Blade Harmonic Air Loading." AIAA Journal, Vol 2, No 7, July 1964.
- Miyazawa, Y., and Washizu, K. "A Finite State Aerodynamic Model for a Lifting Surface in Incompressible Flow." AIAA Journal, Vol 21, No 2, February 1983.

Peters, D.A., and He, C.J. "A Closed-Form Unsteady Aerodynamic Theory for Lifting Rotors in Hover and Forward Flight." Annual National Forum of the American Helicopter Society, May 1987.

Pitt, D.M., and Peters, D.A. "Theoretical Prediction of Dynamic-Inflow Derivatives." Vertica, Vol 5, No 1, 1981.

Roger, K.L. "Airplane Math Modeling Methods for Active Control Design." Structural Aspects of Active Controls, AGARD CP 228, 1978.

Stark, V.J.E. "General Equations of Motion for an Elastic Wing and Method of Solution." AIAA Journal, Vol 22, No 8, August 1984.

Tiffany, S.H., and Adams, W.M., Jr. "Nonlinear Programming Extensions to Rational Function Approximations of Unsteady Aerodynamics." AIAA Paper No. 87-0854, April 1987.

Venkatesan, C., and Friedmann, P.P. "New Approach to Finite-State Modeling of Unsteady Aerodynamics." AIAA Journal, Vol 24, No 12, December 1986.

Vepa, R. "Finite State Modeling of Aeroelastic Systems." NASA CR 2779, February 1977.

Table 1a. Influence of frequency range and order on identification

hovering rotor, undistorted wake
 nonrotating frame, 3 blades; uniform inflow, circulation at 0.77R
 identified equation

ks = static response (zero frequency)
 k1 = high frequency response
 order = equation order
 wmax = identification frequency range
 (weight = 1 for 0 to wmax)

wmax	order	zeros		poles		k1	ks
		real	imag	real	imag		
2.	2	-0.0184	0.7531	-20.3248	0.0000	0.8259	0.1519
		-0.0184	-0.7531	-0.1519	0.0000		
2.	3	-0.0386	0.6869	-0.0905	0.0000	0.0783	0.1519
		-0.0386	-0.6869	-1.0758	3.4397		
		-4.8135	0.0000	-1.0758	-3.4397		
2.	4	-0.0384	0.6850	3.1006	0.0000	0.0227	0.1519
		-0.0384	-0.6850	-0.6450	3.3719		
		-12.2160	0.0000	-0.6450	-3.3719		
		3.9379	0.0000	-0.0926	0.0000		

Table 1b. Continued

hovering rotor, undistorted wake
 nonrotating frame, 3 blades; uniform inflow, circulation at 0.77R
 identified equation

ks = static response (zero frequency)
 k1 = high frequency response
 order = equation order
 wmax = identification frequency range
 (weight = 1 for 0 to wmax)

wmax	order	zeros		poles		k1	ks
		real	imag	real	imag		
4.5	2	0.0209	3.8888	0.5887	3.5463	0.1298	0.1519
		0.0209	-3.8888	0.5887	-3.5463		
4.5	3	-0.1459	3.1713	1.9942	0.0000	-0.0308	0.1519
		-0.1459	-3.1713	0.0216	3.0990		
		-9.3606	0.0000	0.0216	-3.0990		
4.5	4	0.0028	0.9419	-0.2961	3.0517	0.8187	0.1519
		0.0028	-0.9419	-0.2961	-3.0517		
		-0.1861	3.6733	-0.2464	0.0000		
		-0.1861	-3.6733	-27.9306	0.0000		
4.5	5	-0.2121	3.7057	-0.0929	0.0000	0.1477	0.1519
		-0.2121	-3.7057	-0.2883	2.9973		
		-0.0247	0.6852	-0.2883	-2.9973		
		-0.0247	-0.6852	-2.6069	6.8144		
		-7.1159	0.0000	-2.6069	-6.8144		
4.5	6	-0.0250	0.6883	-1.9727	6.6735	0.0538	0.1519
		-0.0250	-0.6883	-1.9727	-6.6735		
		-0.2158	3.7046	-0.2874	2.9961		
		-0.2158	-3.7046	-0.2874	-2.9961		
		-10.7162	0.0000	-0.0951	0.0000		
		25.1753	0.0000	14.9668	0.0000		

Table 1c. Concluded

hovering rotor, undistorted wake
 nonrotating frame, 3 blades; uniform inflow, circulation at 0.77R
 identified equation

ks = static response (zero frequency)
 k1 = high frequency response
 order = equation order
 wmax = identification frequency range
 (weight = 1 for 0 to wmax)

wmax	order	zeros		poles		k1	ks
		real	imag	real	imag		
7.5	6	0.0289	1.5199	-0.5276	6.0970	0.5632	0.1519
		0.0289	-1.5199	-0.5276	-6.0970		
		-0.1758	3.8756	-0.4958	2.9540		
		-0.1758	-3.8756	-0.4958	-2.9540		
		-0.3692	6.7727	-0.9990	0.0000		
		-0.3692	-6.7727	-17.7890	0.0000		
7.5	7	-10.8510	0.0000	-0.1173	0.0000	0.1610	0.1519
		-0.4096	6.8035	-0.2863	2.9864		
		-0.4096	-6.8035	-0.2863	-2.9864		
		-0.2187	3.7145	-0.5141	6.0120		
		-0.2187	-3.7145	-0.5141	-6.0120		
		0.0090	0.7648	-3.1939	10.1199		
0.0090	-0.7648	-3.1939	-10.1199				
7.5	8	-0.0133	0.7288	-1.3992	9.3850	-0.2803	0.1519
		-0.0133	-0.7288	-1.3992	-9.3850		
		-0.2216	3.7011	-0.5027	5.9940		
		-0.2216	-3.7011	-0.5027	-5.9940		
		-0.4158	6.8114	-0.2800	3.0003		
		-0.4158	-6.8114	-0.2800	-3.0003		
		-3.5510	14.3415	-0.1120	0.0000		
-3.5510	-14.3415	41.3862	0.0000				

Table 2a. Influence of frequency range and order on identification

hovering rotor, undistorted wake
 nonrotating frame, 3 blades; uniform inflow
 identification for all radial stations
 zeros for circulation at 0.77R
 identified equation

ks = static response (zero frequency)
 k1 = high frequency response
 order = equation order
 wmax = identification frequency range
 (weight = 1 for 0 to wmax)

wmax	order	zeros		poles		k1	ks
		real	imag	real	imag		
2.	2	0.0095	0.8613	-10.1646	0.0000	0.4572	0.1519
		0.0095	-0.8613	-0.2197	0.0000		
2.	3	-0.0212	0.8215	-0.1527	0.0000	0.0778	0.1519
		-0.0212	-0.8215	-1.1977	3.7510		
		-6.8447	0.0000	-1.1977	-3.7510		
2.	4	-0.0180	0.6961	-0.7805	0.0000	0.1284	0.1519
		-0.0180	-0.6961	-0.1208	0.0000		
		-1.5031	0.4830	-1.4664	2.9472		
		-1.5031	-0.4830	-1.4664	-2.9472		
2.	5	-0.0168	0.7025	-0.9007	2.7650	0.1435	0.1519
		-0.0168	-0.7025	-0.9007	-2.7650		
		-0.9509	0.0000	-0.8760	0.0000		
		-1.6420	2.1971	-0.1094	0.0000		
		-1.6420	-2.1971	-4.1204	0.0000		
2.	6	-0.0281	0.6935	-0.8007	2.6209	0.1517	0.1519
		-0.0281	-0.6935	-0.8007	-2.6209		
		-1.1083	0.0000	-0.5034	0.0000		
		-0.6314	0.0000	-0.1052	0.0000		
		-1.1344	2.2670	-2.5165	0.0000		
		-1.1344	-2.2670	-2.1631	0.0000		
2.	7	-0.4393	2.2831	0.8538	0.0000	0.1379	0.1519
		-0.4393	-2.2831	-0.7487	0.0000		
		-1.8572	0.0000	-0.1132	0.0000		
		0.9160	0.0000	-0.3724	2.3230		
		-0.0326	0.6974	-0.3724	-2.3230		
		-0.0326	-0.6974	-2.0777	2.3942		
		-0.9895	0.0000	-2.0777	-2.3942		

Table 2b. Continued

hovering rotor, undistorted wake
 nonrotating frame, 3 blades; uniform inflow
 identification for all radial stations
 zeros for circulation at 0.77R
 identified equation

ks = static response (zero frequency)
 k1 = high frequency response
 order = equation order
 wmax = identification frequency range
 (weight = 1 for 0 to wmax)

wmax	order	zeros		poles		k1	ks
		real	imag	real	imag		
4.5	4	0.0676	1.0747	-0.4748	3.0829	0.4906	0.1519
		0.0676	-1.0747	-0.4748	-3.0829		
		-0.1959	3.7613	-0.3952	0.0000		
		-0.1959	-3.7313	-13.8179	0.0000		
4.5	5	-0.1818	3.7508	-0.4497	0.0000	0.0347	0.1519
		-0.1818	-3.7508	-0.4735	3.1055		
		0.0759	1.0992	-0.4735	-3.1055		
		0.0759	-1.0992	-7.4407	0.0000		
		188.6838	0.0000	22.3287	0.0000		
4.5	6	0.0462	0.8584	-0.5560	3.3421	0.4374	0.1519
		0.0462	-0.8584	-0.5560	-3.3421		
		-0.3488	3.0977	-0.1930	2.9946		
		-0.3488	-3.0977	-0.1930	-2.9946		
		-0.1730	3.7528	-0.2047	0.0000		
		-0.1730	-3.7528	-13.7957	0.0000		
4.5	7	-0.2154	3.7184	-0.1451	0.0000	0.1469	0.1519
		-0.2154	-3.7184	-0.2521	2.9846		
		-0.4881	3.0353	-0.2521	-2.9846		
		-0.4881	-3.0353	-0.5870	3.0609		
		-0.0035	0.8091	-0.5870	-3.0609		
		-0.0035	-0.8091	-2.8005	7.1782		
		-9.0448	0.0000	-2.8005	-7.1782		

Table 2c. Continued

hovering rotor, undistorted wake
 nonrotating frame, 3 blades; uniform inflow
 identification for all radial stations
 zeros for circulation at 0.77R
 identified equation

ks = static response (zero frequency)
 k1 = high frequency response
 order = equation order
 wmax = identification frequency range
 (weight = 1 for 0 to wmax)

wmax	order	zeros		poles		k1	ks
		real	imag	real	imag		
4.5	8	-0.0248	0.7944	10.7621	0.0000	-0.1871	0.1519
		-0.0248	-0.7944	-0.1499	6.6247		
		-0.5202	2.8659	-0.1499	-6.6247		
		-0.5202	-2.8659	-0.1489	0.0000		
		-0.2148	3.7417	-0.5095	2.9198		
		-0.2148	-3.7417	-0.5095	-2.9198		
		2.1618	7.5408	-0.3379	3.0192		
		2.1618	-7.5408	-0.3379	-3.0192		
4.5	9	-0.4050	4.2727	-0.1412	0.0000	0.1122	0.1519
		-0.4050	-4.2727	-0.5401	2.6735		
		-0.1880	3.7237	-0.5401	-2.6735		
		-0.1880	-3.7237	-0.3933	2.9484		
		0.0056	0.7733	-0.3933	-2.9484		
		0.0056	-0.7733	-0.4094	4.3332		
		-0.5324	2.4999	-0.4094	-4.3332		
		-0.5324	-2.4999	-3.4847	8.5369		
		-20.2454	0.0000	-3.4847	-8.5369		

Table 2d. Continued

hovering rotor, undistorted wake
 nonrotating frame, 3 blades; uniform inflow
 identification for all radial stations
 zeros for circulation at 0.77R
 identified equation

ks = static response (zero frequency)
 k1 = high frequency response
 order = equation order
 wmax = identification frequency range
 (weight = 1 for 0 to wmax)

wmax	order	zeros		poles		k1	ks
		real	imag	real	imag		
7.5	6	0.0974	1.5985	-0.7381	6.1393	0.4287	0.1519
		0.0974	-1.5985	-0.7381	-6.1393		
		-0.1589	3.9407	-0.7801	2.8148		
		-0.1589	-3.9407	-0.7801	-2.8148		
		-0.3729	6.8656	-9.3213	0.0000		
		-0.3729	-6.8656	-1.7509	0.0000		
7.5	7	-0.3216	6.8330	16.6242	0.0000	0.0456	0.1519
		-0.3216	-6.8330	-0.7046	6.2742		
		-0.1336	4.0259	-0.7046	-6.2742		
		-0.1336	-4.0259	-1.8312	3.4735		
		0.0772	1.7010	-1.8312	-3.4735		
		0.0772	-1.7010	-1.0186	2.2094		
		91.5750	0.0000	-1.0186	-2.2094		
7.5	8	0.1201	0.9874	-11.9025	0.0000	0.3702	0.1519
		0.1201	-0.9874	-0.3088	0.0000		
		-0.1637	3.7809	-0.4643	3.1307		
		-0.1637	-3.7809	-0.4643	-3.1307		
		-0.9126	5.7860	-1.0223	6.6067		
		-0.9126	-5.7860	-1.0223	-6.6067		
		-0.3543	6.8840	-0.4641	5.8325		
		-0.3543	-6.8840	-0.4641	-5.8325		
7.5	9	9.1896	0.0000	-10.5339	0.0000	0.3114	0.1519
		0.0775	1.0818	7.9732	0.0000		
		0.0775	-1.0818	-0.9418	6.6749		
		-0.1727	3.8034	-0.9418	-6.6749		
		-0.1727	-3.8034	-0.3941	5.9035		
		-0.7732	6.0050	-0.3941	-5.9035		
		-0.7732	-6.0050	-0.4150	0.0000		
		-0.3687	6.8818	-0.5081	3.1359		
		-0.3687	-6.8818	-0.5081	-3.1359		

Table 2e. Concluded

hovering rotor, undistorted wake
 nonrotating frame, 3 blades; uniform inflow
 identification for all radial stations
 zeros for circulation at 0.77R
 identified equation

order = equation order
 wmax = identification frequency range
 (weight = 1 for 0 to wmax)
 ** = unstable identified pole

wmax	order	for 0.77R	rms system function error	
			minimum	maximum
2.	2	0.0198	0.0081	0.0335
2.	3	0.0115	0.0052	0.0198
2.	4	0.0048	0.0018	0.0056
2.	5	0.0037	0.0012	0.0048
2.	6	0.0029	0.0011	0.0078
2.	7 **	0.0037	0.0014	0.0053

4.5	4	0.0307	0.0108	0.0497
4.5	5 **	0.0330	0.0113	0.0548
4.5	6	0.0139	0.0063	0.0250
4.5	7	0.0077	0.0037	0.0157
4.5	8 **	0.0104	0.0052	0.0228
4.5	9	0.0091	0.0063	0.0263

7.5	6	0.0502	0.0142	0.1006
7.5	7 **	0.0583	0.0157	0.1111
7.5	8	0.0212	0.0081	0.0312
7.5	9 **	0.0257	0.0093	0.0439

Table 3a. Influence of order and weight on identification

hovering rotor, undistorted wake
 nonrotating frame, 3 blades; uniform inflow
 identification for all radial stations
 zeros for circulation at 0.77R
 identified equation

ks = static response (zero frequency)
 k1 = high frequency response
 order = equation order
 wmax = identification frequency range
 weight = 4 for 0 to 1.5/rev,
 weight = 1 for 1.5 to wmax

wmax	order	zeros		poles		k1	ks
		real	imag	real	imag		
4.5	4	0.0507	0.8964	-0.4492	3.0975	0.5140	0.1519
		0.0507	-0.8964	-0.4492	-3.0975		
		-0.1933	3.7399	-0.2492	0.0000		
		-0.1933	-3.7399	-15.6761	0.0000		
4.5	5	-0.2024	3.74618	-0.2344	0.0000	0.1904	0.1519
		-0.2024	-3.74618	-0.4473	3.0879		
		0.0406	0.88574	-0.4473	-3.0879		
		0.0406	-0.88574	-10.9747	13.6101		
		-50.2905	0.00000	-10.9747	-13.6101		
4.5	6	0.0165	0.80809	-0.4575	3.3206	0.4892	0.1519
		0.0165	-0.80809	-0.4575	-3.3206		
		-0.2837	3.08339	-0.1757	2.9962		
		-0.2837	-3.08339	-0.1757	-2.9962		
		-0.1561	3.74532	-0.1741	0.0000		
		-0.1561	-3.74532	-16.0896	0.0000		
4.5	7	-0.2175	3.72655	-0.1404	0.0000	0.1454	0.1519
		-0.2175	-3.72655	-0.1977	2.9484		
		-0.3555	2.94083	-0.1977	-2.9484		
		-0.3555	-2.94083	-0.5413	3.0021		
		-0.0078	0.78710	-0.5413	-3.0021		
		-0.0078	-0.78710	-2.9457	7.0526		
		-8.6772	0.00000	-2.9457	-7.0526		

Table 3b. Continued

hovering rotor, undistorted wake
 nonrotating frame, 3 blades; uniform inflow
 identification for all radial stations
 zeros for circulation at 0.77R
 identified equation

ks = static response (zero frequency)
 k1 = high frequency response
 order = equation order
 wmax = identification frequency range
 weight = 4 for 0 to 1.5/rev,
 weight = 1 for 1.5 to wmax

wmax	order	zeros		poles		k1	ks
		real	imag	real	imag		
4.5	8	-0.0093	0.75958	-1.1355	5.2527	0.4452	0.1519
		-0.0093	-0.75958	-1.1355	-5.2527		
		-0.6014	2.53204	-0.1375	0.0000		
		-0.6014	-2.53204	-0.3514	2.9632		
		-0.1871	3.71765	-0.3514	-2.9632		
		-0.1871	-3.71765	-0.6043	2.6978		
		-1.5008	5.20242	-0.6043	-2.6978		
		-1.5008	-5.20242	-17.2290	0.0000		
4.5	9	0.1095	0.00000	-6.8112	0.0000	0.2652	0.1519
		-0.0220	0.73300	-0.2094	0.0000		
		-0.0220	-0.73300	0.0670	0.0000		
		-0.6645	2.48809	-1.3080	4.4653		
		-0.6645	-2.48809	-1.3080	-4.4653		
		-0.1628	3.80579	-0.3027	2.8015		
		-0.1628	-3.80579	-0.3027	-2.8015		
		-1.0988	3.82174	-0.6286	3.0217		
-1.0988	-3.82174	-0.6286	-3.0217				

Table 3c. Continued

hovering rotor, undistorted wake
 nonrotating frame, 3 blades; uniform inflow
 identification for all radial stations
 zeros for circulation at 0.77R
 identified equation

ks = static response (zero frequency)
 k1 = high frequency response
 order = equation order
 wmax = identification frequency range
 weight = 16 for 0 to 1.5/rev,
 weight = 1 for 1.5 to wmax

wmax	order	zeros		poles		k1	ks
		real	imag	real	imag		
4.5	4	0.0259	0.8210	-0.4247	3.0989	0.5294	0.1519
		0.0259	-0.8210	-0.4247	-3.0989		
		-0.1947	3.7138	-0.1928	0.0000		
		-0.1947	-3.7138	-17.2476	0.0000		
4.5	5	-0.2217	3.7446	-0.1712	0.0000	0.1583	0.1519
		-0.2217	-3.7446	-0.4379	3.0699		
		0.0120	0.8044	-0.4379	-3.0699		
		0.0120	-0.8044	-4.4775	9.9312		
		-20.5786	0.0000	-4.4775	-9.9312		
4.5	6	0.0004	0.7807	-0.3745	3.2909	0.5629	0.1519
		0.0004	-0.7807	-0.3745	-3.2909		
		-0.2477	3.0273	-0.1665	2.9657		
		-0.2477	-3.0273	-0.1665	-2.9657		
		-0.1428	3.7325	-0.1555	0.0000		
		-0.1428	-3.7325	-19.3137	0.0000		
4.5	7	-6.1274	0.0000	-0.1338	0.0000	0.1808	0.1519
		-0.2178	3.7401	-0.2302	2.8494		
		-0.2178	-3.7401	-0.2302	-2.8494		
		-0.0112	0.7699	-0.5299	2.8924		
		-0.0112	-0.7699	-0.5299	-2.8924		
		-0.3289	2.7508	-3.2364	6.2302		
		-0.3289	-2.7508	-3.2364	-6.2302		

Table 3d. Continued

hovering rotor, undistorted wake
 nonrotating frame, 3 blades; uniform inflow
 identification for all radial stations
 zeros for circulation at 0.77R
 identified equation

ks = static response (zero frequency)
 k1 = high frequency response
 order = equation order
 wmax = identification frequency range
 weight = 16 for 0 to 1.5/rev,
 weight = 1 for 1.5 to wmax

wmax	order	zeros		poles		k1	ks
		real	imag	real	imag		
4.5	8	-3.1015	0.0000	-0.6303	0.0000	0.1852	0.1519
		-0.0080	0.6732	-0.1145	0.0000		
		-0.0080	-0.6732	-0.3152	3.0076		
		-1.0272	0.0000	-0.3152	-3.0076		
		-0.2202	3.7076	-0.8337	2.9787		
		-0.2202	-3.7076	-0.8337	-2.9787		
		-0.9055	3.1451	-2.7370	5.8083		
		-0.9055	-3.1451	-2.7370	-5.8083		
4.5	9	3.7402	0.0000	3.5865	0.0000	0.1745	0.1519
		-0.0006	0.6960	-1.0253	0.0000		
		-0.0006	-0.6960	-0.1258	0.0000		
		-1.8140	1.0875	-0.3327	3.0230		
		-1.8140	-1.0875	-0.3327	-3.0230		
		-0.2110	3.6974	-0.8969	2.9315		
		-0.2110	-3.6974	-0.8969	-2.9315		
		-1.1050	3.2525	-2.4151	5.6271		
-1.1050	-3.2525	-2.4151	-5.6271				

Table 3e. Concluded

hovering rotor, undistorted wake
 nonrotating frame, 3 blades; uniform inflow
 identification for all radial stations
 zeros for circulation at 0.77R
 identified equation

order = equation order
 wmax = identification frequency range
 ** = unstable identified pole

wmax	order	for 0.77R	rms system function error minimum	maximum

weight = 1 for 0-4.5/rev				
4.5	4	0.0307	0.0108	0.0497
4.5	5 **	0.0330	0.0113	0.0548
4.5	6	0.0139	0.0063	0.0250
4.5	7	0.0077	0.0037	0.0157
4.5	8 **	0.0104	0.0052	0.0228
4.5	9	0.0091	0.0063	0.0263

weight = 4 for 0-1.5/rev, 1 for 1.5-4.5/rev				
4.5	4	0.0228	0.0089	0.0314
4.5	5	0.0217	0.0085	0.0297
4.5	6	0.0121	0.0060	0.0320
4.5	7	0.0091	0.0045	0.0195
4.5	8	0.0072	0.0043	0.0132
4.5	9 **	0.0196	0.0098	0.1120

weight = 16 for 0-1.5/rev, 1 for 1.5-4.5/rev				
4.5	4	0.0199	0.0082	0.0342
4.5	5	0.0184	0.0076	0.0303
4.5	6	0.0126	0.0063	0.0435
4.5	7	0.0099	0.0061	0.0235
4.5	8	0.0037	0.0024	0.0070
4.5	9 **	0.0048	0.0037	0.0053

Table 4a. Influence of order and weight on identification

hovering rotor, undistorted wake
 nonrotating frame, 3 blades
 identification for all radial stations; three inflow modes
 identified equation

order = equation order
 wmax = identification frequency range
 weight = 1 for 0 to wmax

wmax	order	poles, mode 1		poles, mode 2		poles, mode 3	
		real	imag	real	imag	real	imag
4.5	4	-0.4757	3.0829	-0.6361	3.1211	-0.6573	3.1161
		-0.4757	-3.0829	-0.6361	-3.1211	-0.6573	-3.1161
		-0.3966	0.0000	-0.4849	0.0000	-8.1862	0.0000
		-13.7688	0.0000	-9.1806	0.0000	-0.6535	0.0000
4.5	5	-0.4533	0.0000	-0.4936	0.0000	-0.6120	0.0000
		-0.4742	3.1065	-0.6412	3.1239	-0.6572	3.0886
		-0.4742	-3.1065	-0.6412	-3.1239	-0.6572	-3.0886
		-7.3186	0.0000	-8.2513	0.0000	-12.1863	8.5857
		21.9282	0.0000	40.4850	0.0000	-12.1863	-8.5857
4.5	6	-0.5546	3.3379	-0.7012	3.3832	-0.8288	3.4841
		-0.5546	-3.3379	-0.7012	-3.3832	-0.8288	-3.4841
		-0.1919	2.9922	-0.2539	2.9932	-0.3427	2.9834
		-0.1919	-2.9922	-0.2539	-2.9932	-0.3427	-2.9834
		-0.2033	0.0000	-0.3595	0.0000	-7.5157	0.0000
		-13.8507	0.0000	-9.0959	0.0000	-0.5267	0.0000
4.5	7	-0.1445	0.0000	-0.3109	0.0000	-0.3614	2.9884
		-0.2501	2.9843	-0.3060	2.9626	-0.3614	-2.9884
		-0.2501	-2.9843	-0.3060	-2.9626	-1.1114	3.4564
		-0.5756	3.0466	-0.7881	3.0892	-1.1114	-3.4564
		-0.5756	-3.0466	-0.7881	-3.0892	-0.2563	0.0000
		-2.6440	7.3696	-3.5849	6.3927	-4.6433	0.0000
		-2.6440	-7.3696	-3.5849	-6.3927	-1.3210	0.0000

Table 4b. Continued

hovering rotor, undistorted wake
 nonrotating frame, 3 blades
 identification for all radial stations; three inflow modes
 identified equation

order = equation order
 wmax = identification frequency range
 weight = 1 for 0 to wmax

wmax	order	poles, mode 1		poles, mode 2		poles, mode 3	
		real	imag	real	imag	real	imag
4.5	8	12.9421	0.0000	-0.3115	0.0000	-0.4400	0.0000
		-0.3404	6.4782	4.6435	0.0000	3.6680	0.0000
		-0.3404	-6.4782	-0.3374	2.9877	-0.3505	2.9902
		-0.1447	0.0000	-0.3374	-2.9877	-0.3505	-2.9902
		-0.5610	2.9437	-0.7751	3.0449	-0.9683	2.8490
		-0.5610	-2.9437	-0.7751	-3.0449	-0.9683	-2.8490
		-0.2878	2.9504	-1.8848	7.2257	-2.7294	5.0006
		-0.2878	-2.9504	-1.8848	-7.2257	-2.7294	-5.0006
4.5	9	-0.1346	0.0000	-1.4991	6.9447	4.6150	0.0000
		-0.3577	2.3488	-1.4991	-6.9447	-2.3294	0.0000
		-0.3577	-2.3488	3.4262	0.0000	-0.4761	0.0000
		-0.3197	3.0331	-0.3343	2.9458	-0.4515	3.0488
		-0.3197	-3.0331	-0.3343	-2.9458	-0.4515	-3.0488
		-0.4644	3.6799	-0.7754	3.0407	-1.0101	2.6041
		-0.4644	-3.6799	-0.7754	-3.0407	-1.0101	-2.6041
		-0.4660	11.4747	-0.3082	0.0000	-1.8731	4.6561
-0.4660	-11.4747	-13.5740	0.0000	-1.8731	-4.6561		

Table 4c. Continued

hovering rotor, undistorted wake
 nonrotating frame, 3 blades
 identification for all radial stations; three inflow modes
 identified equation

order = equation order
 wmax = identification frequency range
 weight = 16 for 0 to 1.5/rev,
 weight = 1 for 1.5 to wmax

wmax	order	poles, mode 1		poles, mode 2		poles, mode 3	
		real	imag	real	imag	real	imag
4.5	4	-0.4258	3.0989	-0.5903	3.1426	-0.6109	3.1472
		-0.4258	-3.0989	-0.5903	-3.1426	-0.6109	-3.1472
		-0.1934	0.0000	-0.3535	0.0000	-0.5169	0.0000
		-17.1864	0.0000	-10.2615	0.0000	-9.0196	0.0000
4.5	5	-0.1721	0.0000	-0.3413	0.0000	-0.4805	0.0000
		-0.4385	3.0707	-0.6007	3.1222	-0.6272	3.0883
		-0.4385	-3.0707	-0.6007	-3.1222	-0.6272	-3.0883
		-4.5720	10.0105	-8.2291	6.8358	-5.2461	4.9872
		-4.5720	-10.0105	-8.2291	-6.8358	-5.2461	-4.9872
4.5	6	-0.3796	3.2827	-0.6118	3.3818	-0.6971	3.5096
		-0.3796	-3.2827	-0.6118	-3.3818	-0.6971	-3.5096
		-0.1594	2.9603	-0.3030	2.9004	-0.3839	2.9225
		-0.1594	-2.9603	-0.3030	-2.9004	-0.3839	-2.9225
		-0.1560	0.0000	-0.3169	0.0000	-0.4756	0.0000
		-19.2778	0.0000	-10.8879	0.0000	-9.1029	0.0000
4.5	7	-0.1332	0.0000	-0.2803	0.0000	-0.3580	2.9307
		-0.2416	2.8479	-0.3063	2.9553	-0.3580	-2.9307
		-0.2416	-2.8479	-0.3063	-2.9553	-1.2077	3.4471
		-0.5434	2.8700	-1.0411	3.2690	-1.2077	-3.4471
		-0.5434	-2.8700	-1.0411	-3.2690	-0.3537	0.0000
		-3.2938	6.0200	-3.6821	1.8219	-4.4951	0.0000
		-3.2938	-6.0200	-3.6821	-1.8219	-1.4726	0.0000

Table 4d. Continued

hovering rotor, undistorted wake
 nonrotating frame, 3 blades
 identification for all radial stations; three inflow modes
 identified equation

order = equation order
 wmax = identification frequency range
 weight = 16 for 0 to 1.5/rev,
 weight = 1 for 1.5 to wmax

wmax	order	poles, mode 1		poles, mode 2		poles, mode 3	
		real	imag	real	imag	real	imag
4.5	8	-0.2135	0.0000	-0.3413	2.9479	6.7132	0.0000
		-0.0059	0.0000	-0.3413	-2.9479	-1.1935	3.1095
		-0.2910	3.0179	-0.9523	3.1868	-1.1935	-3.1095
		-0.2910	-3.0179	-0.9523	-3.1868	-0.3708	2.9299
		-0.8064	2.9763	-0.2789	0.0000	-0.3708	-2.9299
		-0.8064	-2.9763	-3.1056	0.0000	-3.0536	0.0000
		-2.8333	5.7149	-9.7224	0.0000	-4.7642	0.0000
		-2.8333	-5.7149	41.3149	0.0000	-0.4071	0.0000
4.5	9	3.6995	0.0000	2.6983	0.0000	4.8936	0.0000
		-1.5203	0.0000	-0.8423	0.0000	-0.4345	0.0000
		-0.1270	0.0000	-0.2888	0.0000	0.0666	0.0000
		-0.3348	3.0218	-0.3732	3.0149	-0.3557	3.0423
		-0.3348	-3.0218	-0.3732	-3.0149	-0.3557	-3.0423
		-1.0326	2.9118	-0.8139	2.9452	-1.1436	3.1491
		-1.0326	-2.9118	-0.8139	-2.9452	-1.1436	-3.1491
		-2.5323	5.1575	-2.2090	5.9900	-3.5028	2.5622
-2.5323	-5.1575	-2.2090	-5.9900	-3.5028	-2.5622		

Table 4e. Continued

hovering rotor, undistorted wake
 nonrotating frame, 3 blades
 identification for all radial stations; three inflow modes
 identified equation

order = equation order
 wmax = identification frequency range
 ** = unstable identified pole

wmax	order	for 0.77R	rms system function error minimum	maximum
inflow mode 1				
weight = 1 for 0-4.5/rev				
4.5	4		0.0308	0.0499
4.5	5	**	0.0331	0.0551
4.5	6		0.0138	0.0249
4.5	7		0.0076	0.0145
4.5	8	**	0.0072	0.0135
4.5	9		0.0081	0.0226
inflow mode 1				
weight = 16 for 0-1.5/rev, 1 for 1.5-4.5/rev				
4.5	4		0.0199	0.0342
4.5	5		0.0184	0.0304
4.5	6		0.0125	0.0437
4.5	7		0.0099	0.0225
4.5	8		0.0043	0.0113
4.5	9	**	0.0050	0.0061
inflow mode 2				
weight = 1 for 0-4.5/rev				
4.5	4		0.0281	0.0679
4.5	5	**	0.0287	0.0691
4.5	6		0.0082	0.0465
4.5	7		0.0046	0.0363
4.5	8	**	0.0045	0.0352
4.5	9	**	0.0088	0.0584
inflow mode 2				
weight = 16 for 0-1.5/rev, 1 for 1.5-4.5/rev				
4.5	4		0.0288	0.0449
4.5	5		0.0281	0.0433
4.5	6		0.0118	0.0478
4.5	7		0.0079	0.0336
4.5	8	**	0.0086	0.0304
4.5	9	**	0.0069	0.0208

Table 4f. Concluded

hovering rotor, undistorted wake
 nonrotating frame, 3 blades
 identification for all radial stations; three inflow modes
 identified equation

order = equation order
 wmax = identification frequency range
 ** = unstable identified pole

wmax	order	for 0.77R	rms system function error minimum	error maximum

inflow mode 3				
weight = 1 for 0-4.5/rev				
4.5	4	0.0219	0.0061	0.0706
4.5	5	0.0209	0.0056	0.0713
4.5	6	0.0158	0.0074	0.0356
4.5	7	0.0093	0.0072	0.0281
4.5	8 **	0.0129	0.0083	0.0832
4.5	9 **	0.0115	0.0059	0.0696

inflow mode 3				
weight = 16 for 0-1.5/rev, 1 for 1.5-4.5/rev				
4.5	4	0.0178	0.0116	0.0655
4.5	5	0.0169	0.0099	0.0607
4.5	6	0.0186	0.0110	0.0432
4.5	7	0.0098	0.0051	0.0278
4.5	8 **	0.0101	0.0069	0.0137
4.5	9 **	0.0114	0.0083	0.0208

Table 5a. Identification for hovering rotor with undistorted wake

hovering rotor, undistorted wake
 nonrotating frame, 3 blades
 identification for all radial stations; six inflow modes
 identified equation

order = equation order
 wmax = identification frequency range
 weight = 16 for 0 to 1.5/rev,
 weight = 1 for 1.5 to wmax

wmax	order	inflow mode	poles, CT/s = 0.08		poles, CT/s = 0.02		
			real	imag	real	imag	
4.5	6	1	-0.3897	3.3050	-0.1056	3.3703	
			-0.3897	-3.3050	-0.1056	-3.3703	
			-0.1761	2.9543	-0.1747	3.0824	
			-0.1761	-2.9543	-0.1747	-3.0824	
			-0.1530	0.0000	-0.1615	0.0000	
			-18.9011	0.0000	-89.3653	0.0000	
			2	-0.6440	3.3661	-0.1669	3.6042
				-0.6440	-3.3661	-0.1669	-3.6042
				-0.2974	2.8729	-0.2750	3.0296
				-0.2974	-2.8729	-0.2750	-3.0296
				-0.3138	0.0000	-0.2277	0.0000
				-10.5975	0.0000	-30.5039	0.0000
			3	-0.7390	3.5250	-0.2052	3.6435
			-0.7390	-3.5250	-0.2052	-3.6435	
			-0.3826	2.9284	-0.3078	3.0257	
			-0.3826	-2.9284	-0.3078	-3.0257	
			-0.4833	0.0000	-0.3286	0.0000	
			-8.5163	0.0000	-16.3804	0.0000	

Table 5b. Continued

hovering rotor, undistorted wake
 nonrotating frame, 3 blades
 identification for all radial stations; six inflow modes
 identified equation

order = equation order
 wmax = identification frequency range
 weight = 16 for 0 to 1.5/rev,
 weight = 1 for 1.5 to wmax

wmax	order	inflow mode	poles, CT/s = 0.08		poles, CT/s = 0.02	
			real	imag	real	imag
4.5	6	4	-0.5780	3.6495	-0.1858	3.7066
			-0.5780	-3.6495	-0.1858	-3.7066
			-0.4805	3.0053	-0.3660	3.0367
			-0.4805	-3.0053	-0.3660	-3.0367
			-0.6310	0.0000	-0.4233	0.0000
			-7.7913	0.0000	-12.0282	0.0000
	5	5	-0.4297	3.8271	-0.1773	3.7959
			-0.4297	-3.8271	-0.1773	-3.7959
			-0.6268	3.0669	-0.4134	3.0343
			-0.6268	-3.0669	-0.4134	-3.0343
			-0.7794	0.0000	-0.4835	0.0000
			-6.7275	0.0000	-10.4208	0.0000
	6	6	-0.1305	4.1607	-0.1831	3.9066
			-0.1305	-4.1607	-0.1831	-3.9066
			-0.7974	3.0865	-0.4650	3.0292
			-0.7974	-3.0865	-0.4650	-3.0292
			-0.9144	0.0000	-0.5431	0.0000
			-6.4736	0.0000	-9.2193	0.0000

Table 5c. Concluded

hovering rotor, undistorted wake
 nonrotating frame, 3 blades
 identification for all radial stations; six inflow modes
 identified equation

order = equation order
 wmax = identification frequency range
 weight = 16 for 0 to 1.5/rev,
 weight = 1 for 1.5 to wmax

wmax	order	CT/s	inflow mode	rms system function error		
				for 0.77R	minimum	maximum
4.5	6	0.08	1	0.0113	0.0062	0.0415
			2	0.0134	0.0078	0.0450
			3	0.0153	0.0107	0.0451
			4	0.0149	0.0053	0.0546
			5	0.0146	0.0053	0.0486
			6	0.0177	0.0102	0.1744
4.5	6	0.02	1	0.0401	0.0153	0.1265
			2	0.0517	0.0181	0.2003
			3	0.0382	0.0128	0.2534
			4	0.1144	0.0098	0.2917
			5	0.0391	0.0140	0.3219
			6	0.0605	0.0126	0.2677

Table 6a. Flap motion of hovering rotor with undistorted wake

hovering rotor, undistorted wake
 nonrotating frame, 3 blades
 roots of coning mode

equivalent values, derived from
 real part of flap root:
 C = lift deficiency function
 dl/dT = derivative inflow with thrust
 = f / (mean inflow)

wake model	CT/s	inflow modes	flap root real	flap root imag	natural freq	C	dl/dT	f
uncoupled	0.08		-0.500	0.923	1.050			
dynamic	0.08	1	-0.484	0.973	1.087			
		2	-0.410	0.992	1.074			
		3	-0.451	0.974	1.073			
		4	-0.477	0.947	1.060			
		5	-0.485	0.943	1.061			
		6	-0.487	0.943	1.062			
static	0.08	1	-0.312	1.002	1.049	0.624	6.86	0.406
		2	-0.239	1.022	1.050	0.478	13.31	0.787
		3	-0.242	1.021	1.049	0.484	12.95	0.766
		4	-0.248	1.020	1.049	0.496	12.25	0.725
		5	-0.251	1.019	1.049	0.502	11.92	0.705
		6	-0.253	1.018	1.049	0.506	11.71	0.792
vortex theory (no wake geometry distortion)						0.544	9.86	0.583
momentum theory						0.693	4.93	0.292

Table 6b. Concluded

hovering rotor, undistorted wake
 nonrotating frame, 3 blades
 roots of coning mode

equivalent values, derived from
 real part of flap root:
 C = lift deficiency function
 dl/dT = derivative inflow with thrust
 = f / (mean inflow)

wake model	CT/s	inflow modes	flap root		natural freq	C	dl/dT	f
			real	imag				
uncoupled	0.02		-0.500	0.923	1.050			
dynamic	0.02	1	-0.521	0.942	1.076			
		2	-0.448	0.959	1.056			
		3	-0.496	0.904	1.031			
		4	-0.501	0.841	0.979			
		5	-0.512	0.828	0.974			
		6	-0.519	0.827	0.977			
static	0.02	1	-0.284	1.010	1.050	0.528	10.59	0.313
		2	-0.194	1.031	1.049	0.388	20.68	0.612
		3	-0.194	1.031	1.050	0.388	20.68	0.612
		4	-0.197	1.031	1.049	0.394	20.04	0.593
		5	-0.199	1.030	1.049	0.398	19.63	0.581
		6	-0.200	1.030	1.049	0.400	19.43	0.575
vortex theory (no wake geometry distortion)						0.397	19.72	0.583
momentum theory						0.544	9.86	0.292

Table 7. Flap-pitch motion of hovering rotor with undistorted wake

hovering rotor, undistorted wake
 nonrotating frame, 3 blades
 roots of flap/pitch, collective modes
 no wake model

center of gravity location (% chord)	flap roots		pitch roots	
	real	imag	real	imag
25	-0.492	0.973	-1.258	2.881
	-0.492	-0.973	-1.258	-2.881
28	-1.554	0.000	-0.378	2.185
	-0.802	0.000	-0.378	-2.185

Table 8a. Identification for hovering rotor with rolled up wake

hovering rotor, rolled up wake
 nonrotating frame, 3 blades
 identification for all radial stations; six inflow modes
 identified equation

order = equation order
 wmax = identification frequency range
 weight = 16 for 0 to 1.5/rev,
 weight = 1 for 1.5 to wmax

wmax	order	inflow mode	poles		inflow mode	poles	
			real	imag		real	imag
4.5	6	1	-1.9144	4.9566	2	-0.3731	2.9479
			-1.9144	-4.9566		-0.3731	-2.9479
			-0.6658	2.9592		-0.2349	0.4294
			-0.6658	-2.9592		-0.2349	-0.4294
			-0.1071	0.0000		-7.9477	0.0000
			-7.6523	0.0000		-5.6843	0.0000
4.5	6	3	-0.3714	5.5955	4	-2.0528	8.6765
			-0.3714	-5.5955		-2.0528	-8.6765
			-0.4724	3.0474		-0.9566	3.1013
			-0.4724	-3.0474		-0.9566	-3.1013
			-8.5166	0.0000		-1.0952	0.0000
			-0.4045	0.0000		-7.5764	0.0000
4.5	6	5	-0.9612	1.2656	6	-0.7516	1.1121
			-0.9612	-1.2656		-0.7516	-1.1121
			-1.1263	3.7180		-0.2600	3.7486
			-1.1263	-3.7180		-0.2600	-3.7486
			-2.1830	8.7510		-1.0880	6.4135
			-2.1830	-8.7510		-1.0880	-6.4135

Table 8b. Concluded

hovering rotor
 nonrotating frame, 3 blades
 identification for all radial stations; six inflow modes
 identified equation

order = equation order
 wmax = identification frequency range
 weight = 16 for 0 to 1.5/rev,
 weight = 1 for 1.5 to wmax
 maximum = excluding 0.93R

wmax	order	inflow mode	rms system function error		
			for 0.93R	minimum	maximum
4.5	6	1	0.0140	0.0002	0.0014
		2	0.3500	0.0005	0.0144
		3	0.0282	0.0005	0.0086
		4	0.0340	0.0001	0.0024
		5	0.0606	0.0002	0.0065
		6	0.1736	0.0005	0.0200

Table 9. Flap motion of hovering rotor with rolled up wake

hovering rotor, rolled up wake
 nonrotating frame, 3 blades
 roots of coning mode

equivalent values, derived from
 real part of flap root:
 C = lift deficiency function
 dl/dT = derivative inflow with thrust
 = f / (mean inflow)

wake model	CT/s	inflow modes	flap root		natural freq	C	dl/dT	f
			real	imag				
uncoupled	0.08		-0.500	0.923	1.050			
dynamic	0.08	1	-0.492	0.958	1.077			
		2	-0.400	0.985	1.063			
		3	-0.424	0.986	1.073			
		4	-0.448	0.961	1.060			
		5	-0.448	0.943	1.044			
		6	-0.460	0.947	1.052			
static	0.08	6	-0.240	1.021	1.049	0.480	13.19	0.781
vortex theory (no wake geometry distortion)						0.544	9.86	0.583
momentum theory						0.693	4.93	0.292

Figure 1a. Impulse response of hovering rotor with undistorted wake

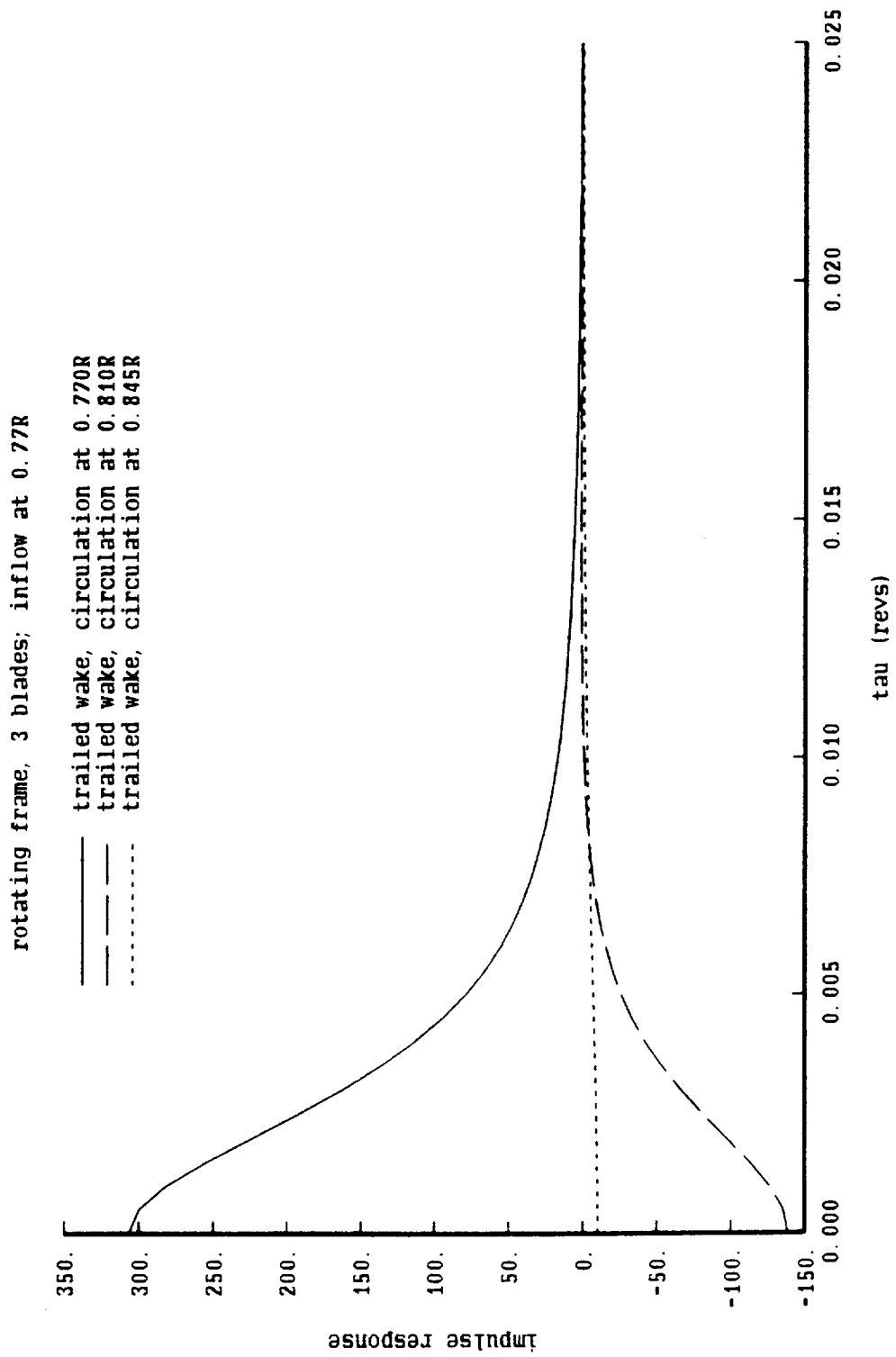


Figure 1b. Impulse response of hovering rotor with undistorted wake

rotating frame, 3 blades; inflow at 0.77R

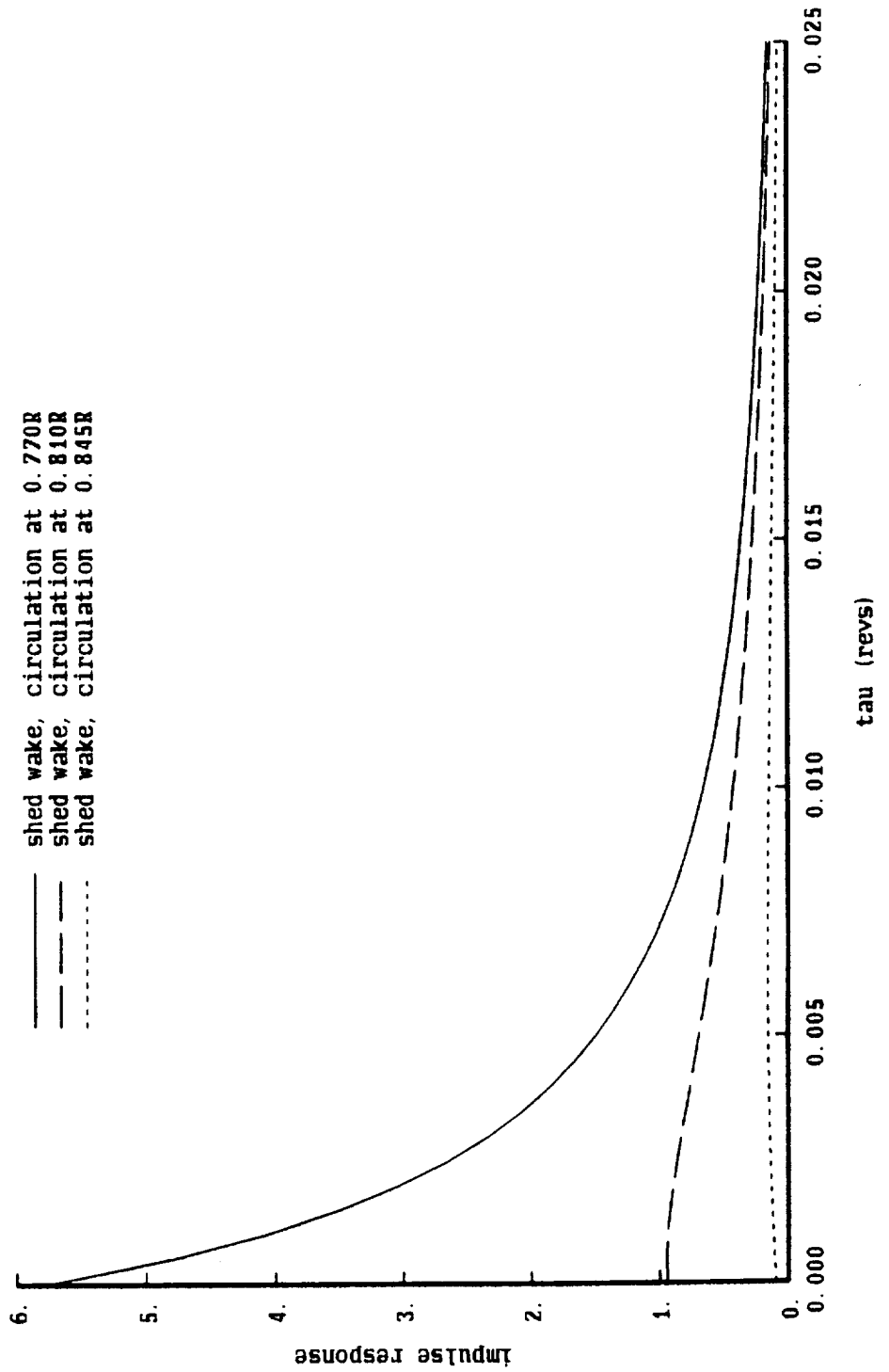


Figure 2a. Impulse response of hovering rotor with undistorted wake

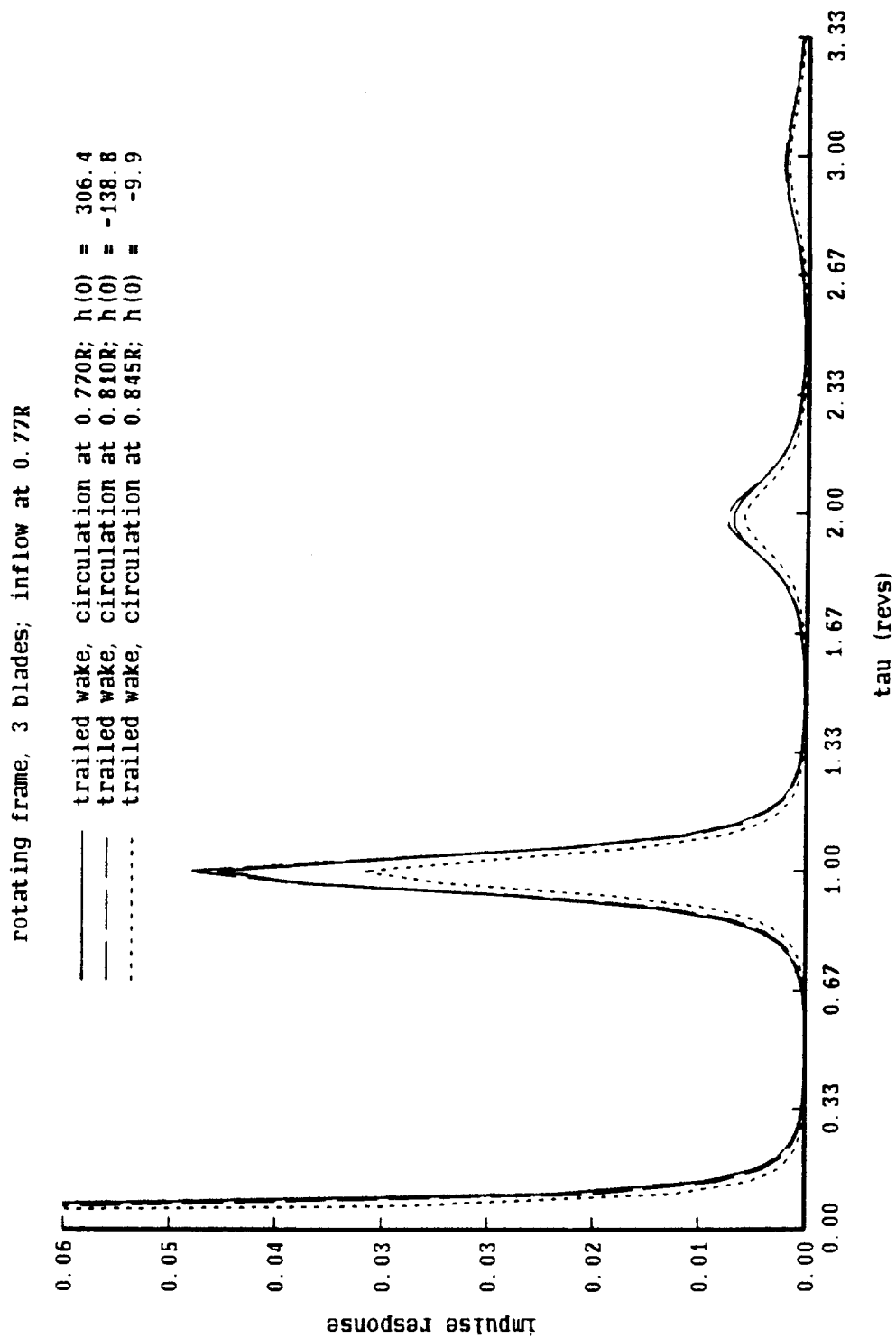


Figure 2b. Impulse response of hovering rotor with undistorted wake

rotating frame, 3 blades; inflow at 0.77R

— shed wake, circulation at 0.770R; $h(0) = 5.742$
 - - - shed wake, circulation at 0.810R; $h(0) = 0.937$
 ····· shed wake, circulation at 0.845R; $h(0) = 0.099$

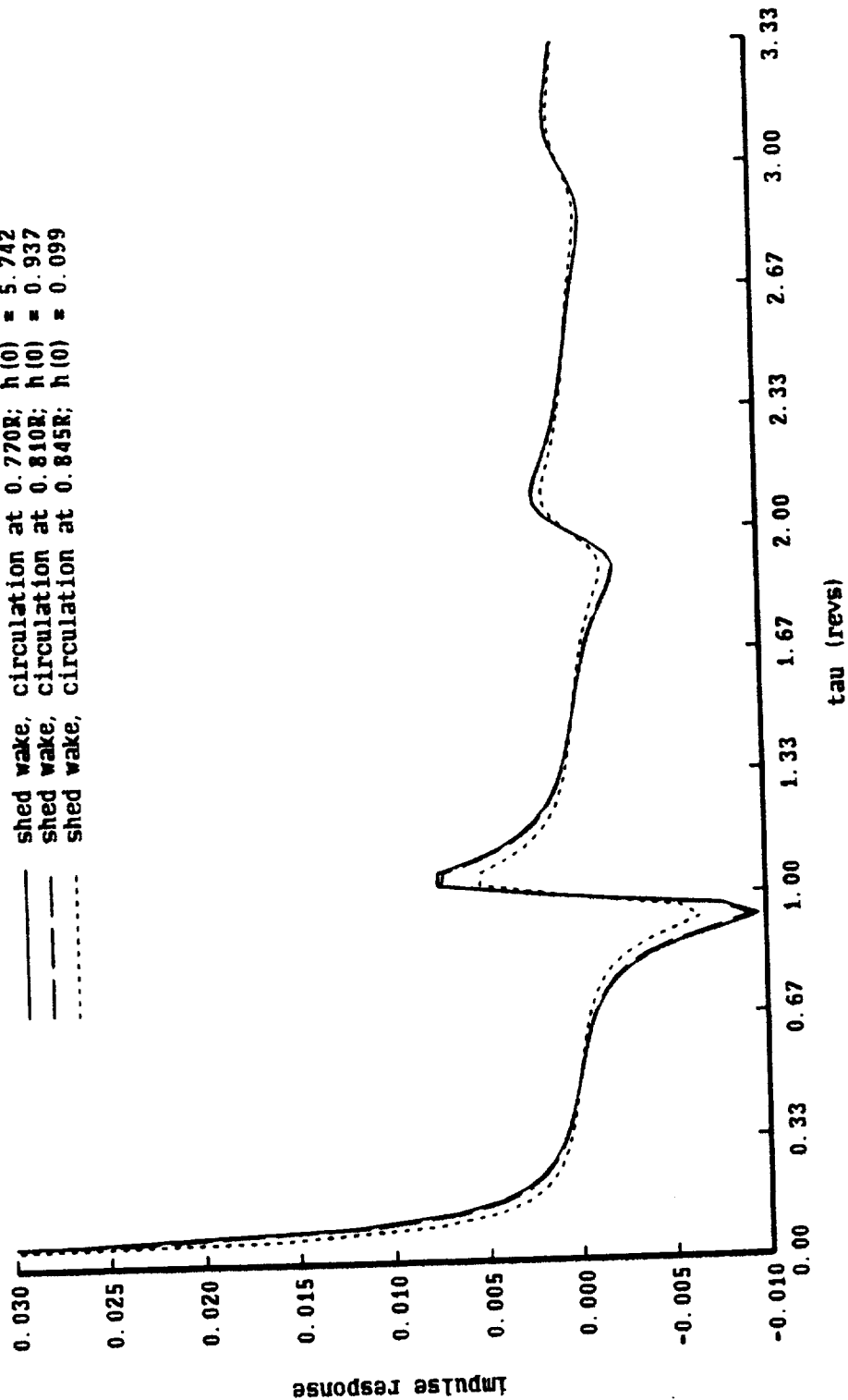


Figure 3a. Impulse response of hovering rotor with undistorted wake

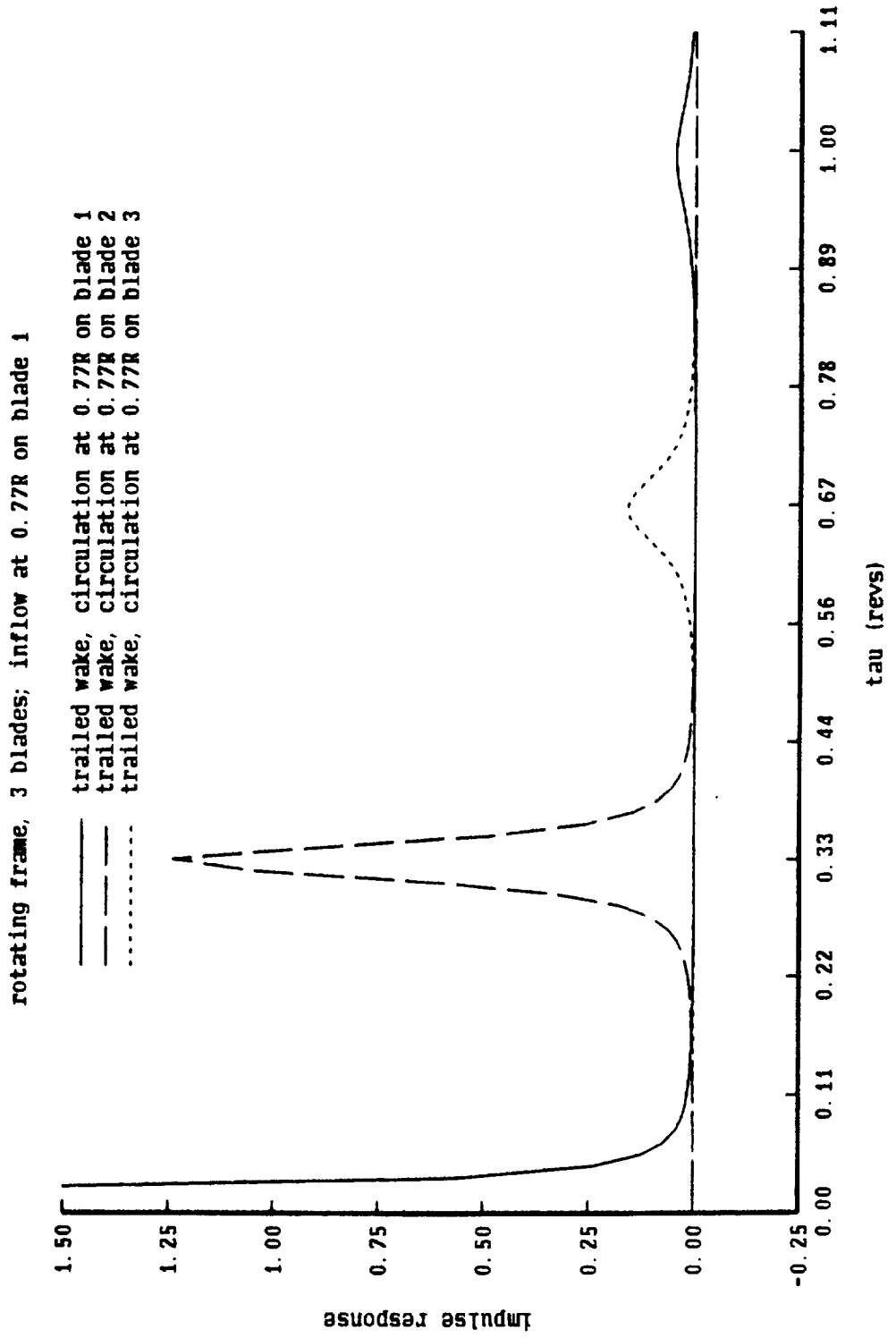


Figure 3b. Impulse response of hovering rotor with undistorted wake

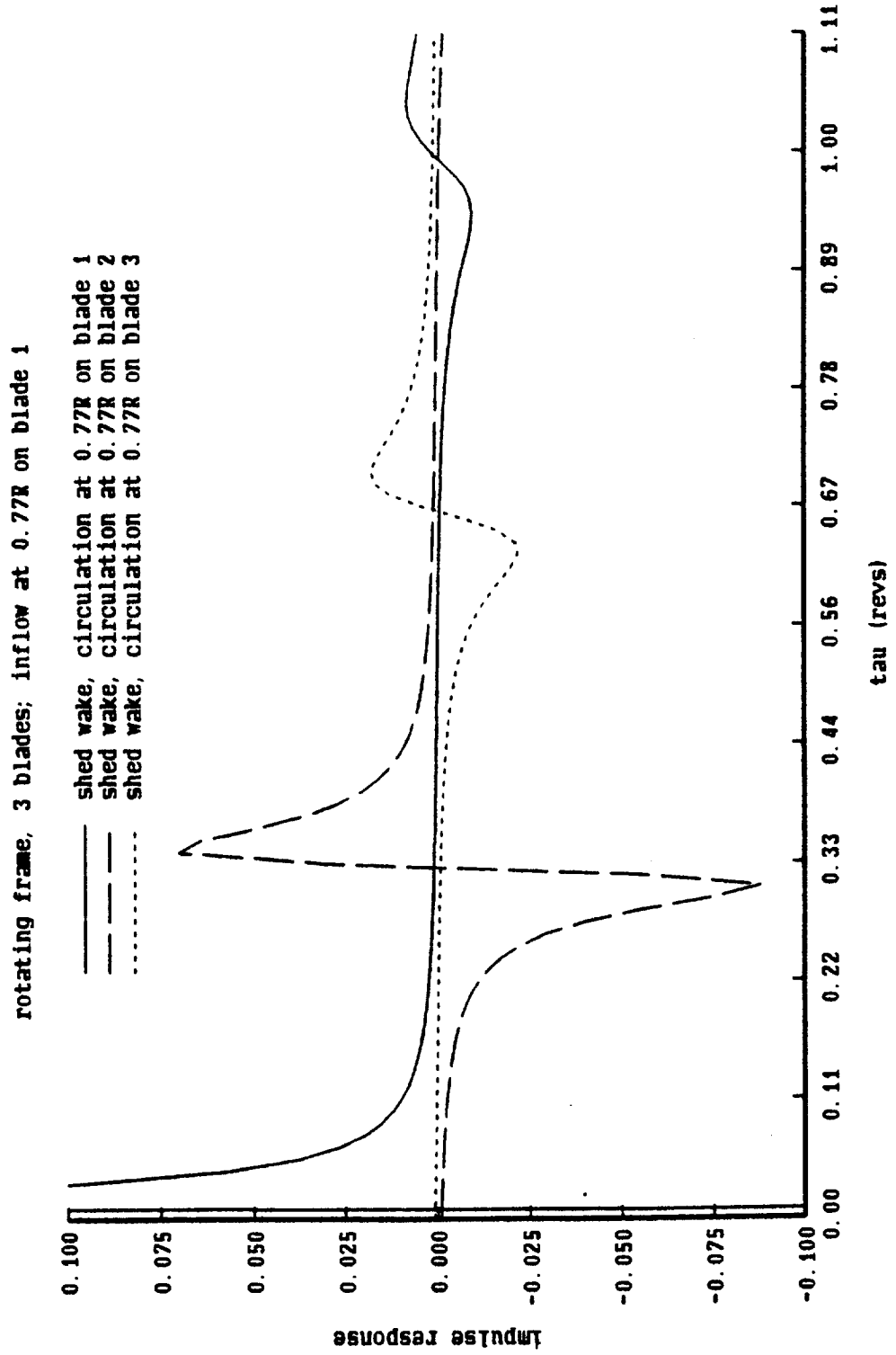


Figure 4a. Impulse response with model order reduction for inflow and circulation

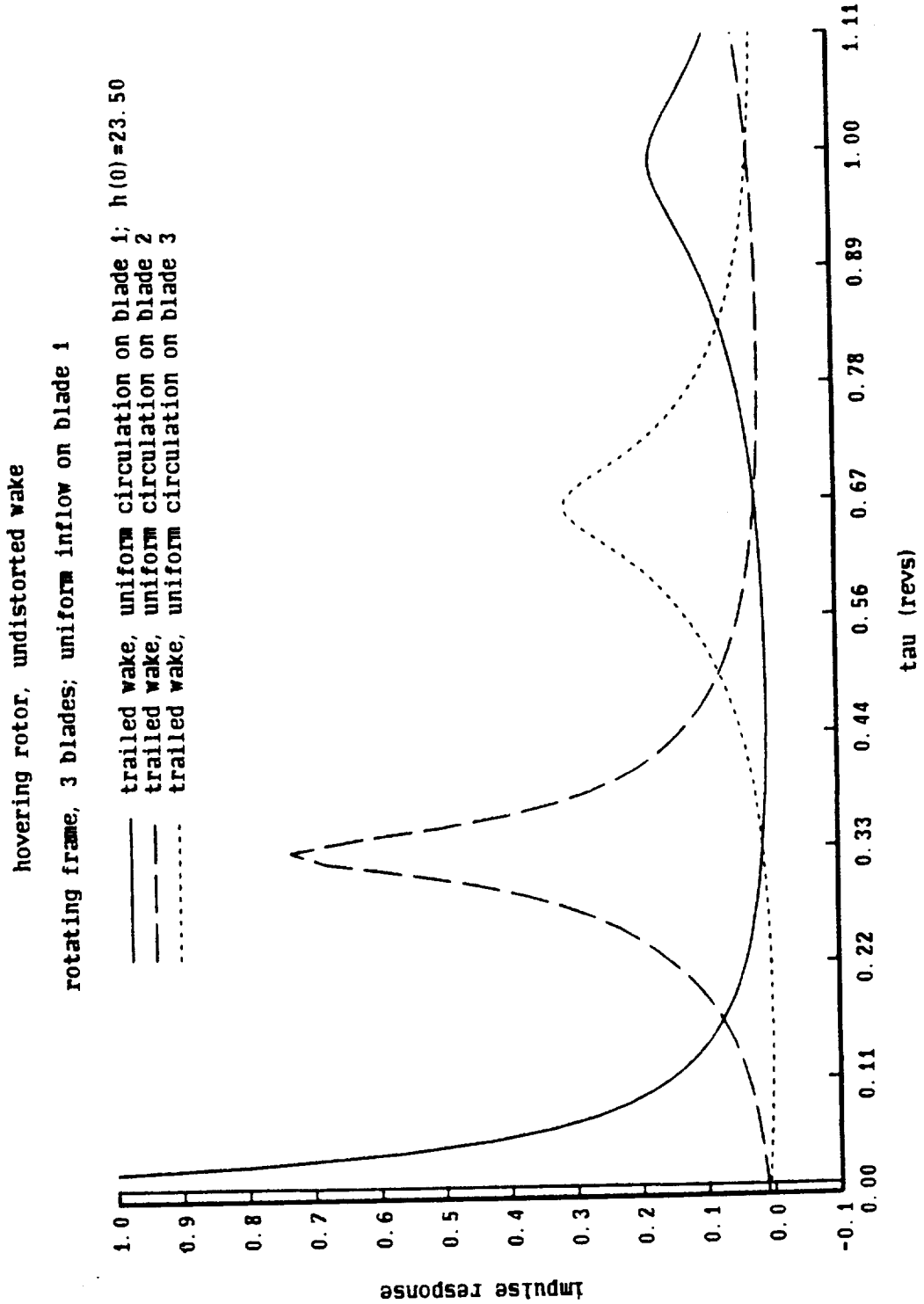


Figure 4b. Impulse response with model order reduction for inflow and circulation

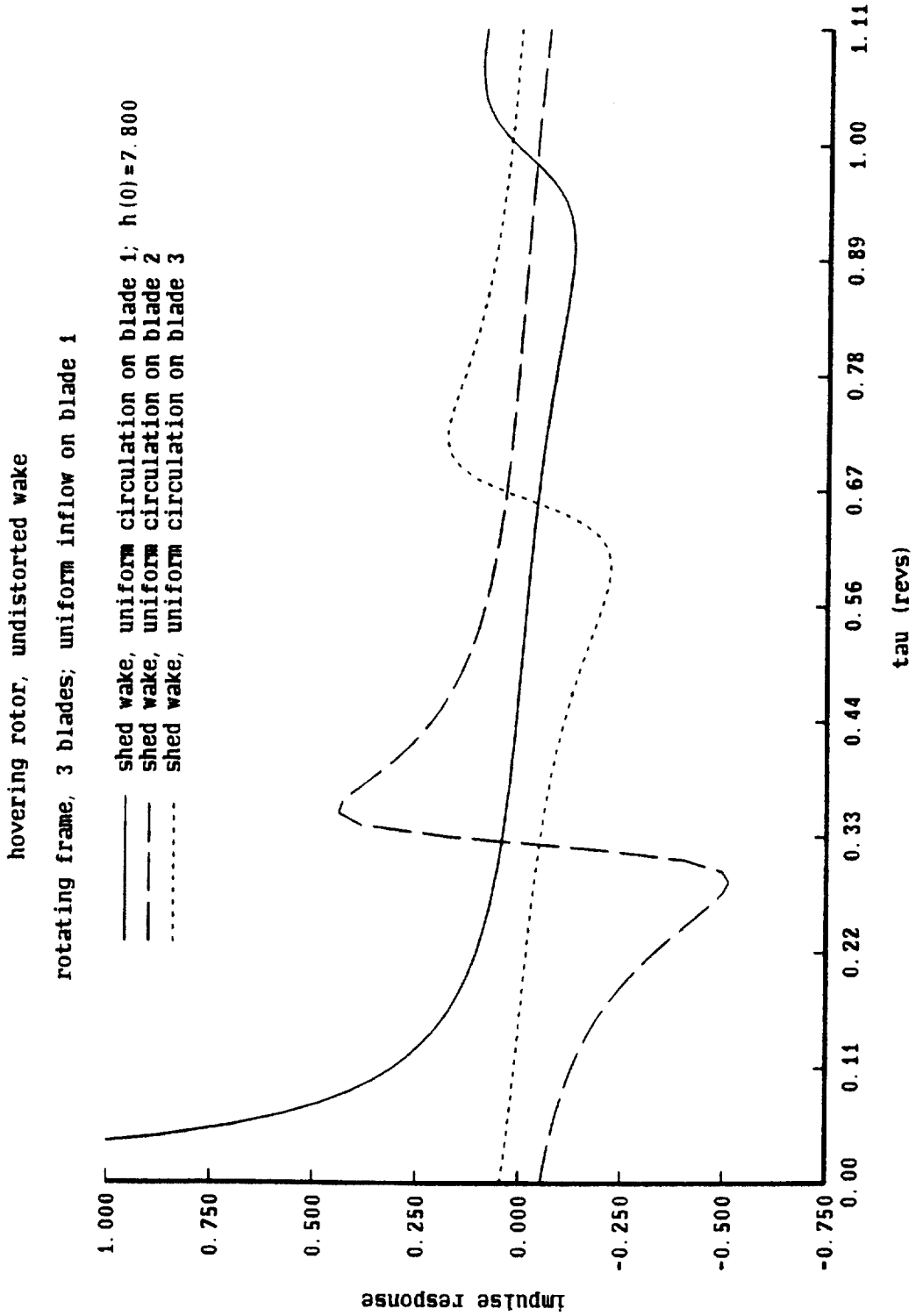


Figure 5a. Impulse response with model order reduction for inflow and circulation

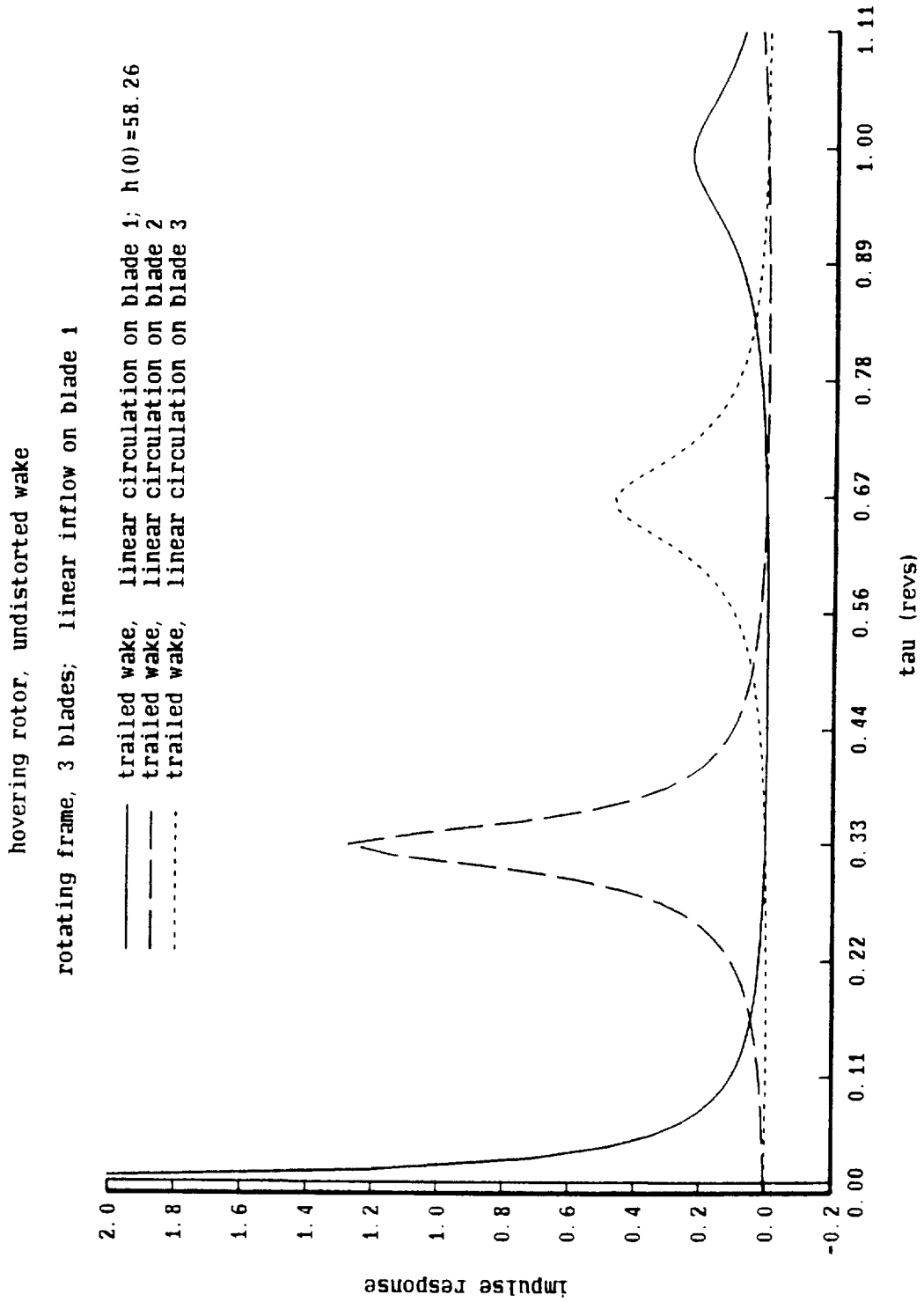


Figure 5b. Impulse response with model order reduction for inflow and circulation

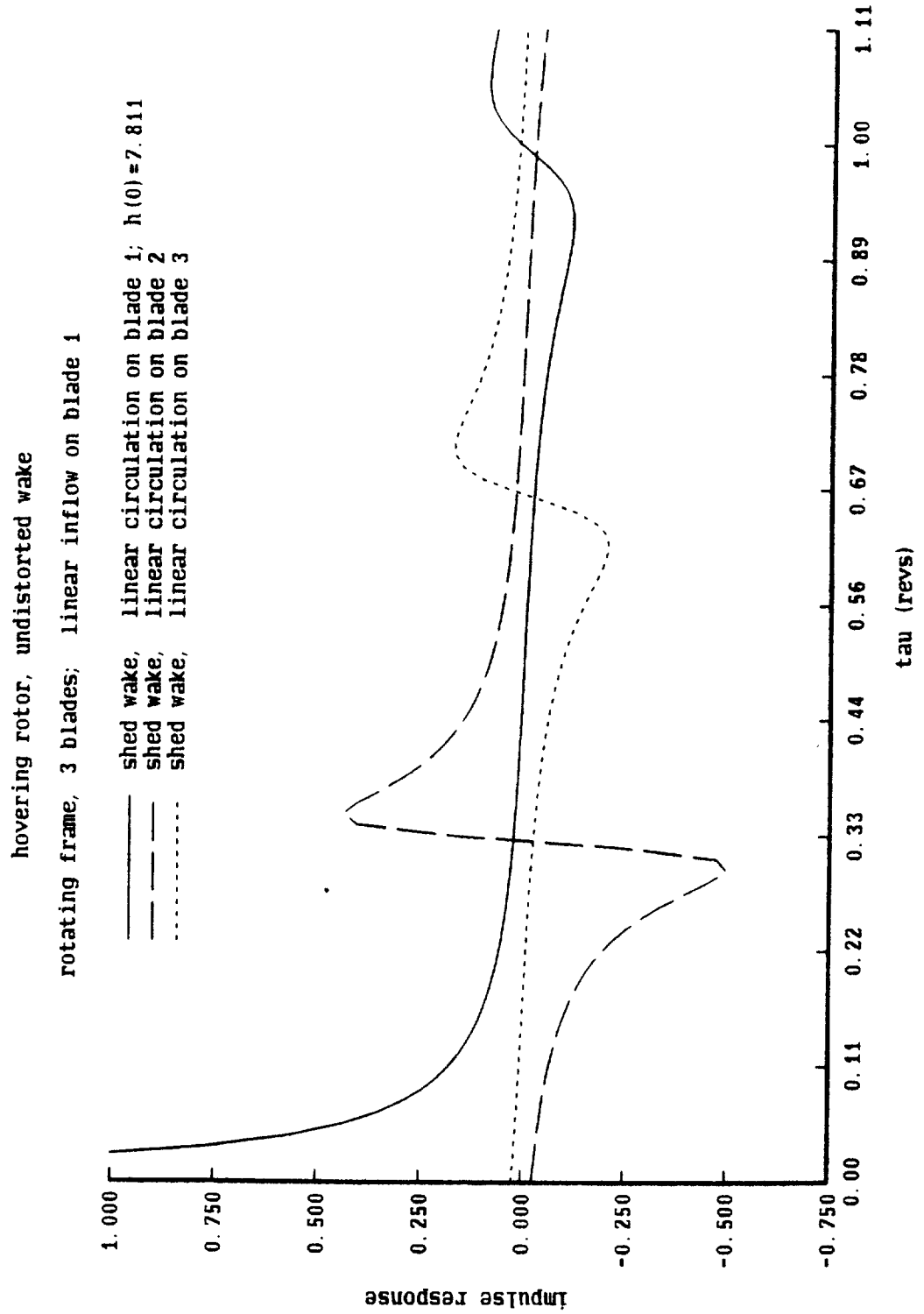


Figure 6a. Impulse response with multiblade coordinates

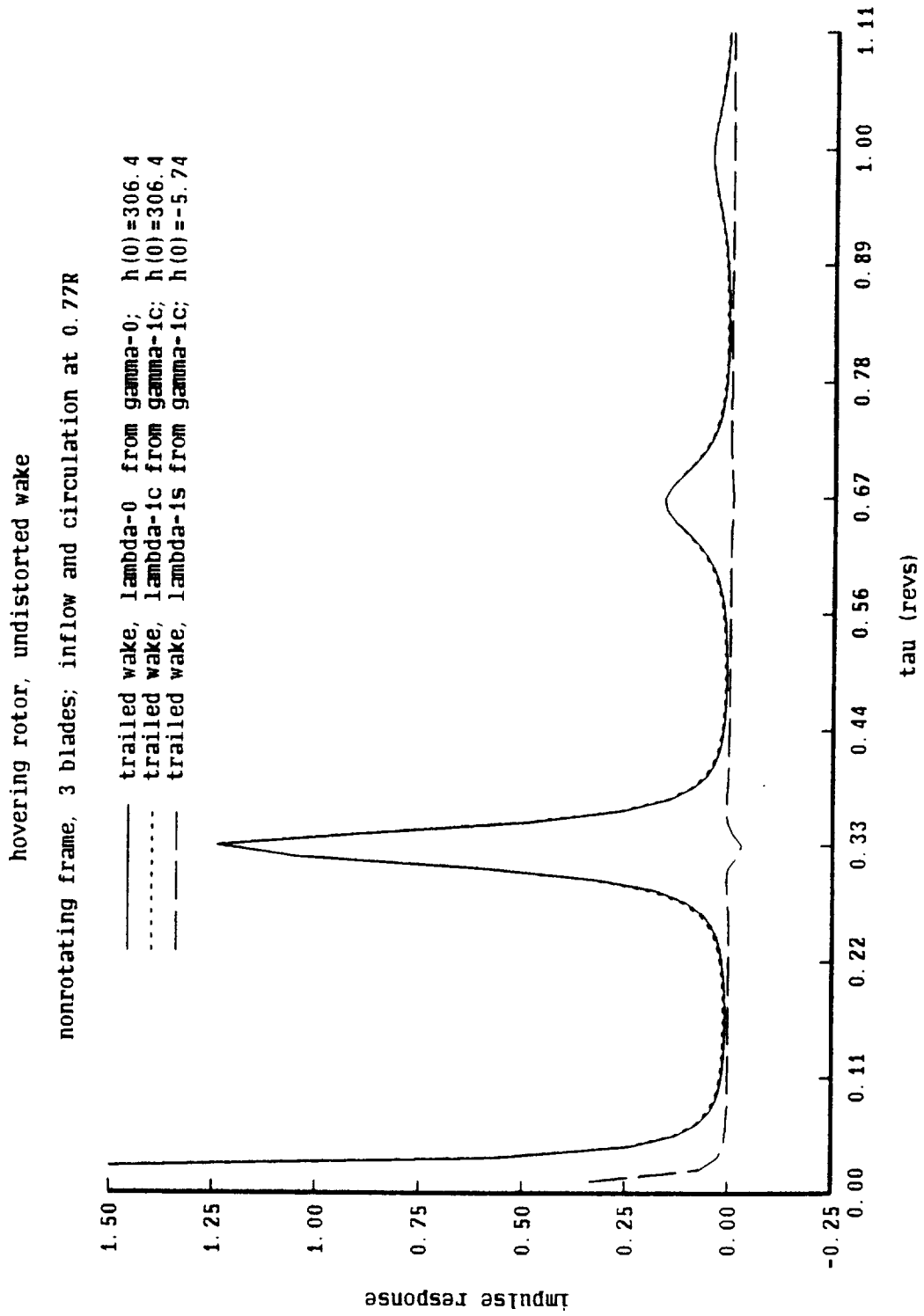


Figure 6b. Impulse response with multiblade coordinates

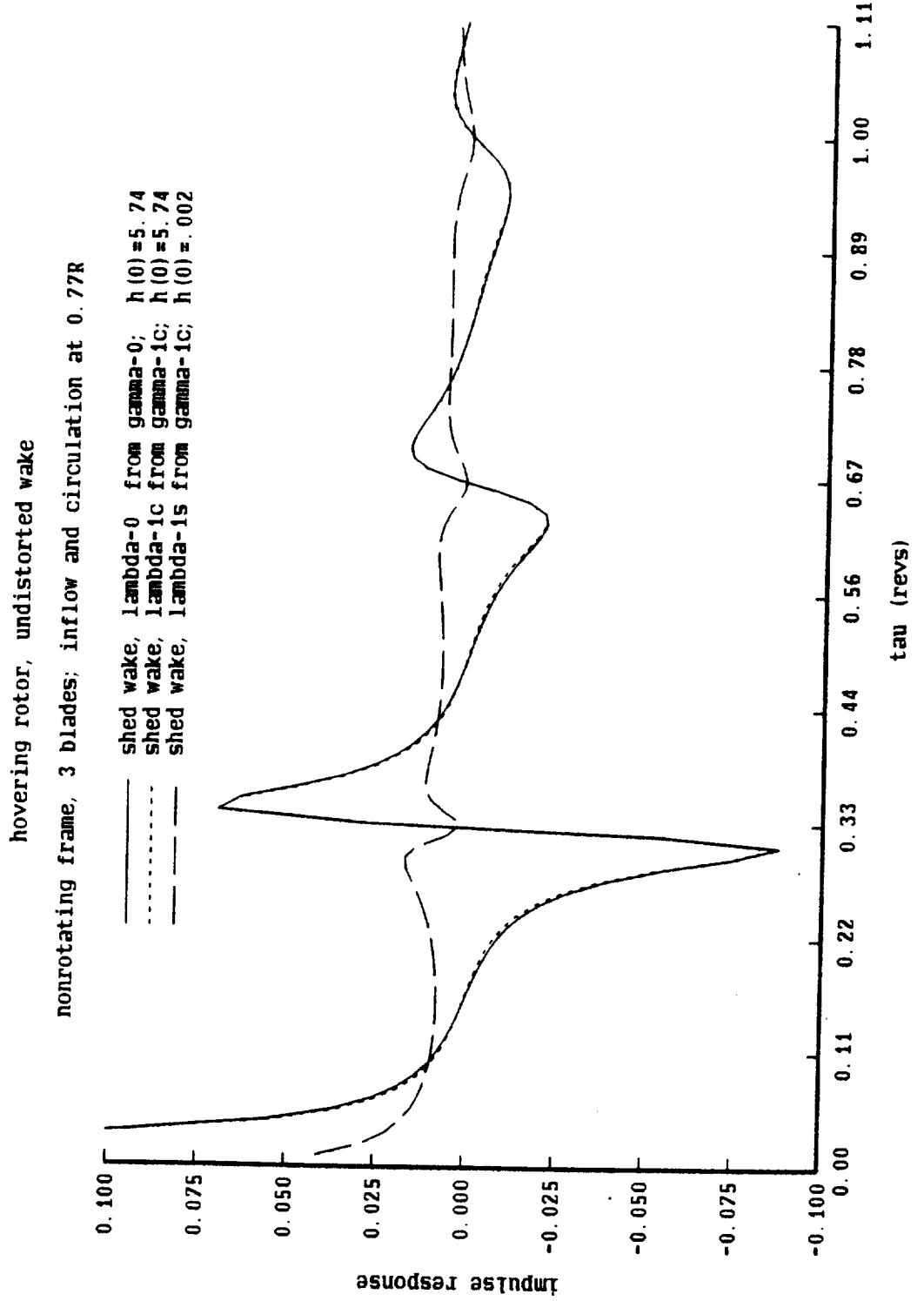


Figure 7a. Impulse response with multiblade coordinates

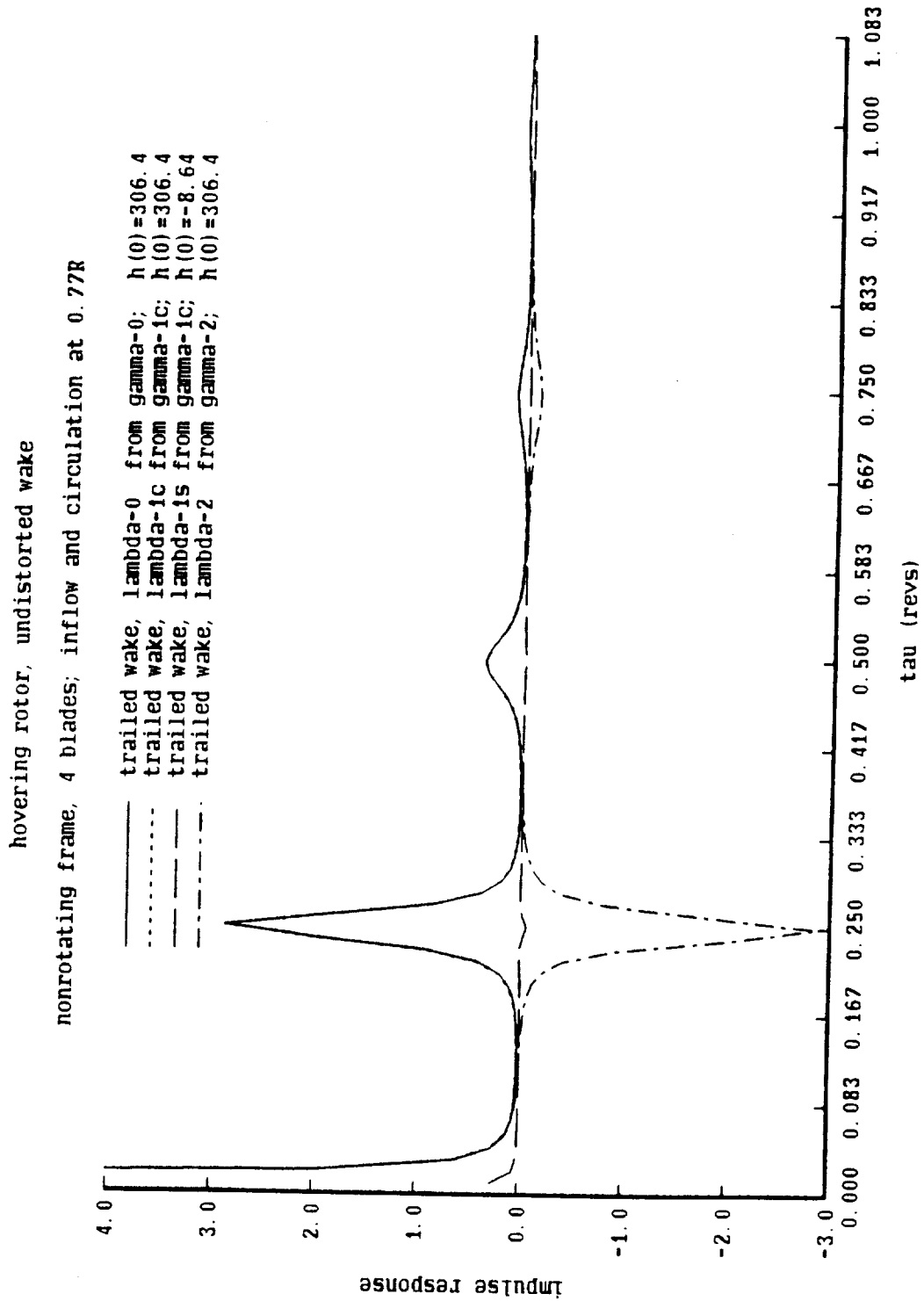


Figure 7b. Impulse response with multiblade coordinates

hovering rotor, undistorted wake

nonrotating frame, 4 blades; inflow and circulation at 0.77R

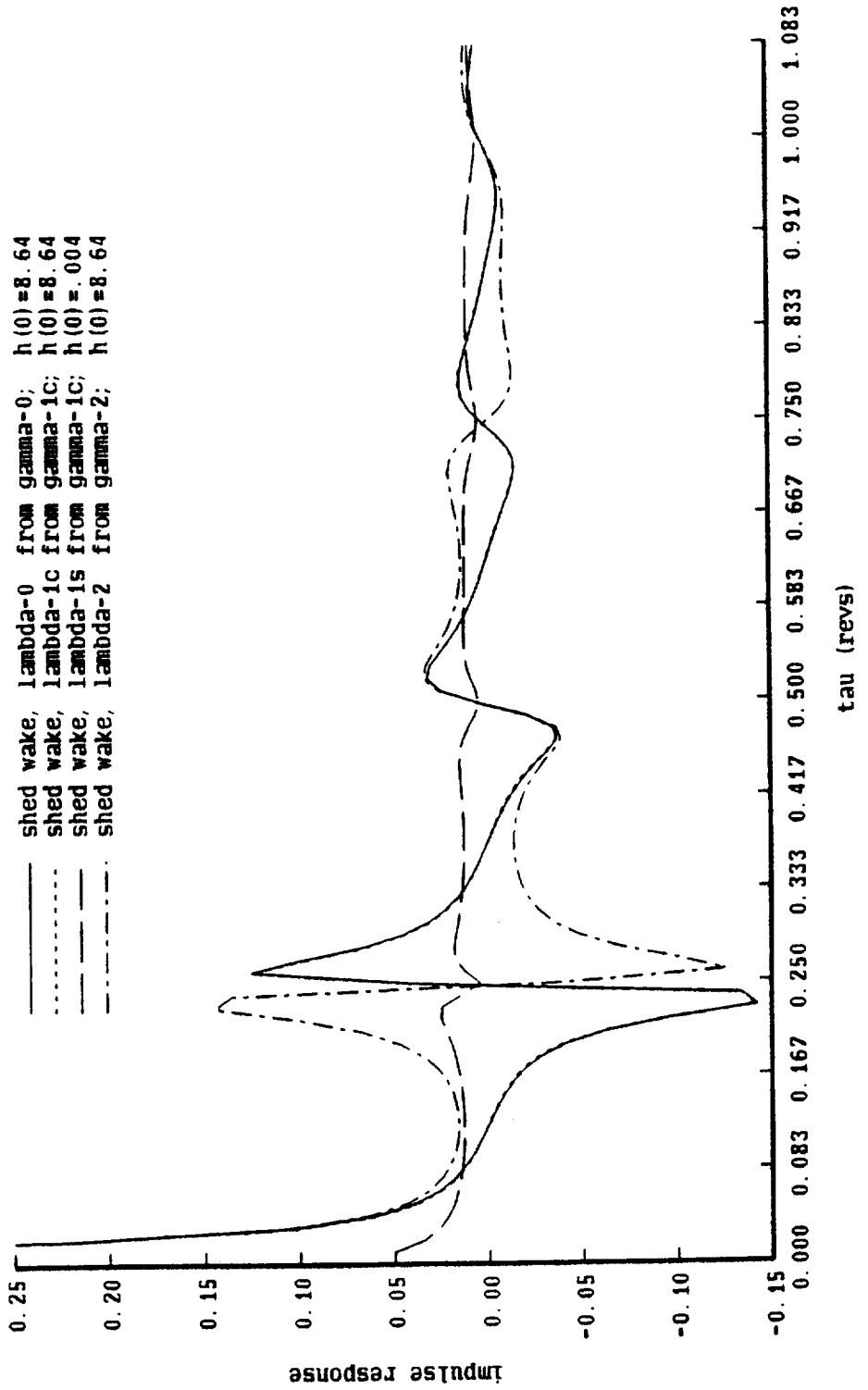


Figure 8a. Impulse response with model order reduction and multiblade coordinates

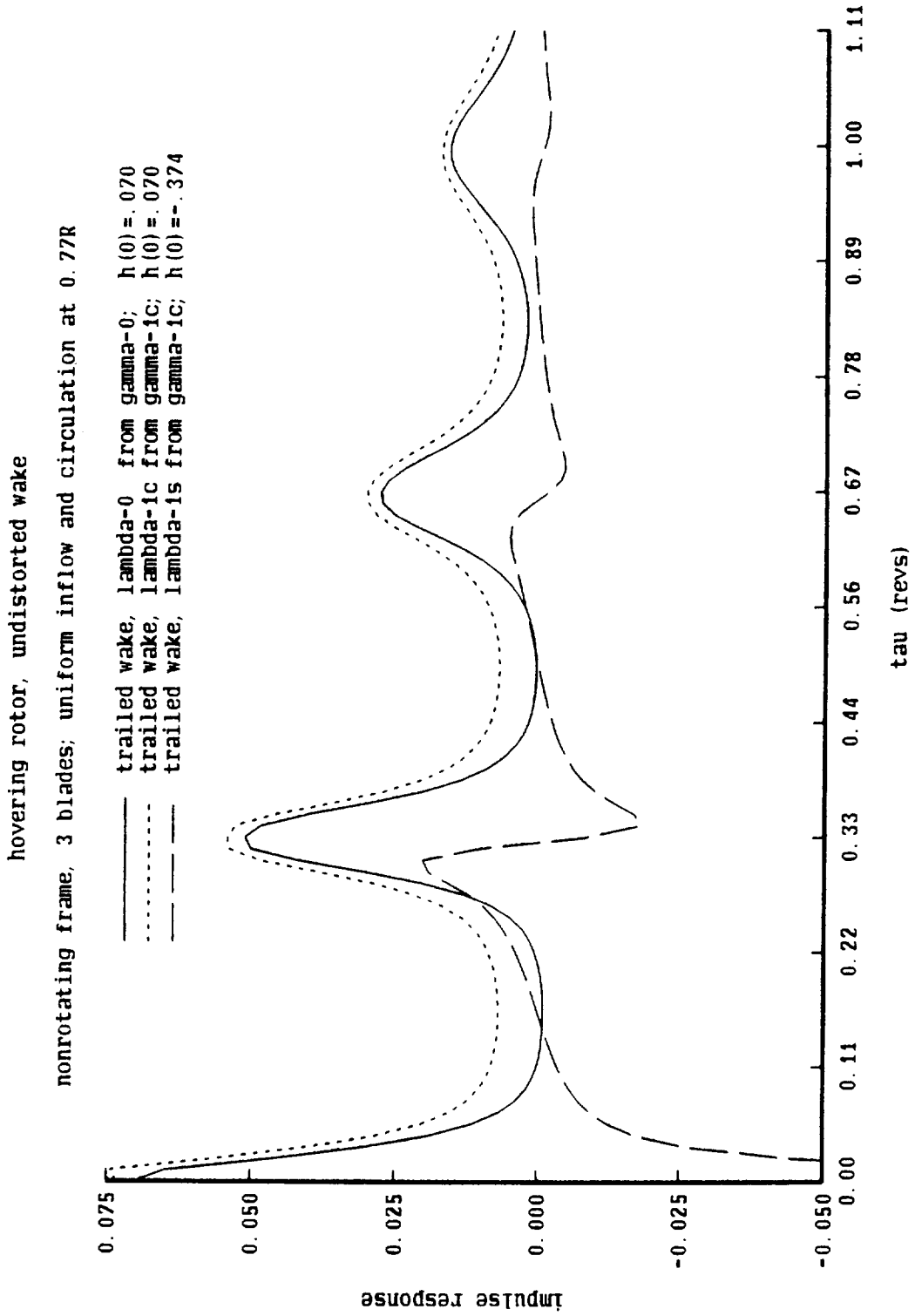


Figure 8b. Impulse response with model order reduction and multiblade coordinates

hovering rotor, undistorted wake

nonrotating frame, 3 blades; uniform inflow and circulation at 0.77R

— shed wake, lambda-0 from gamma-0; $h(0) = .374$
 - - - shed wake, lambda-1c from gamma-1c; $h(0) = .374$
 - - - shed wake, lambda-1s from gamma-1s; $h(0) = .002$

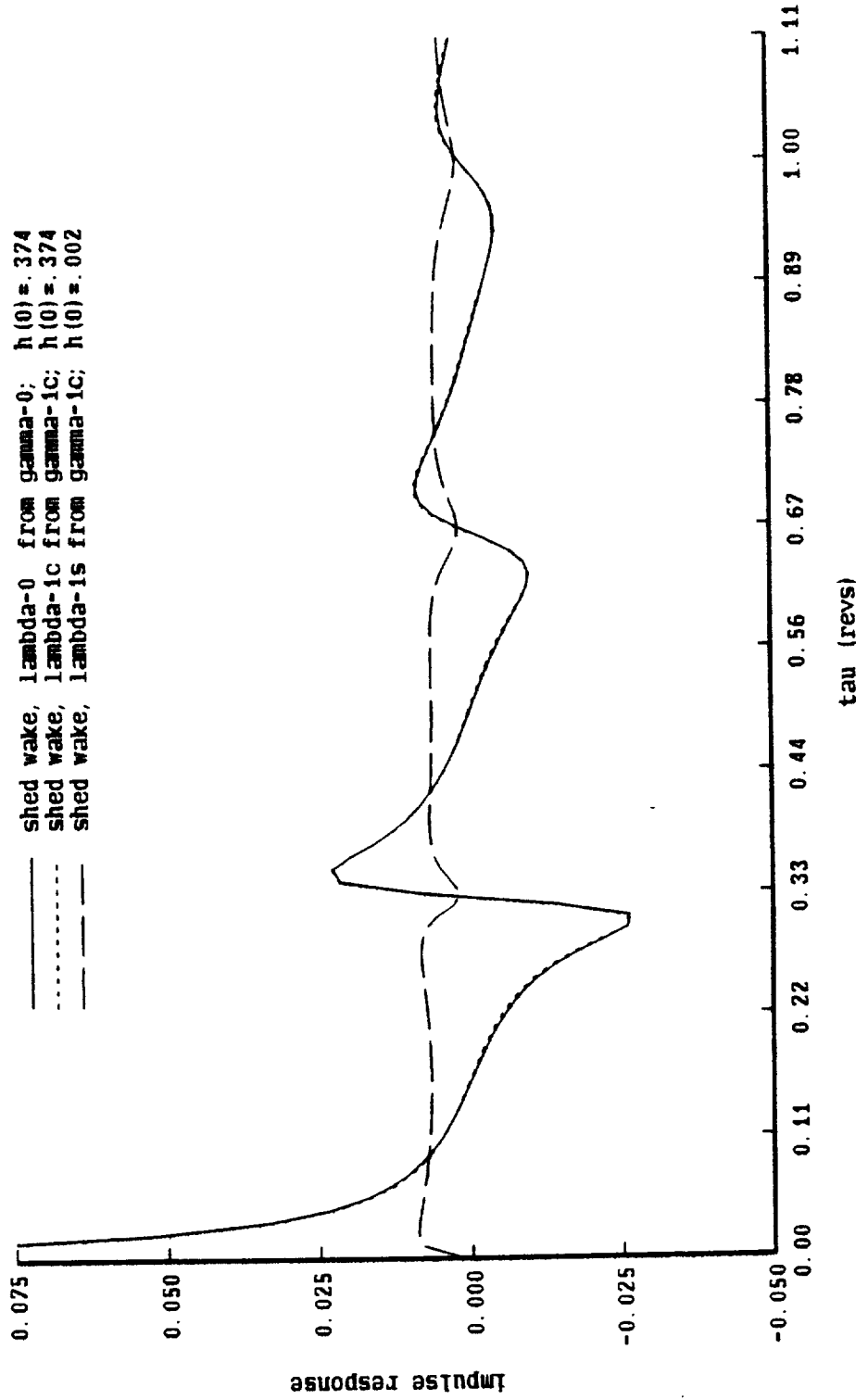


Figure 9a. Influence of sample rate on impulse response

hovering rotor, undistorted wake; 256 steps per rev

nonrotating frame, 3 blades; uniform inflow and circulation at 0.77R

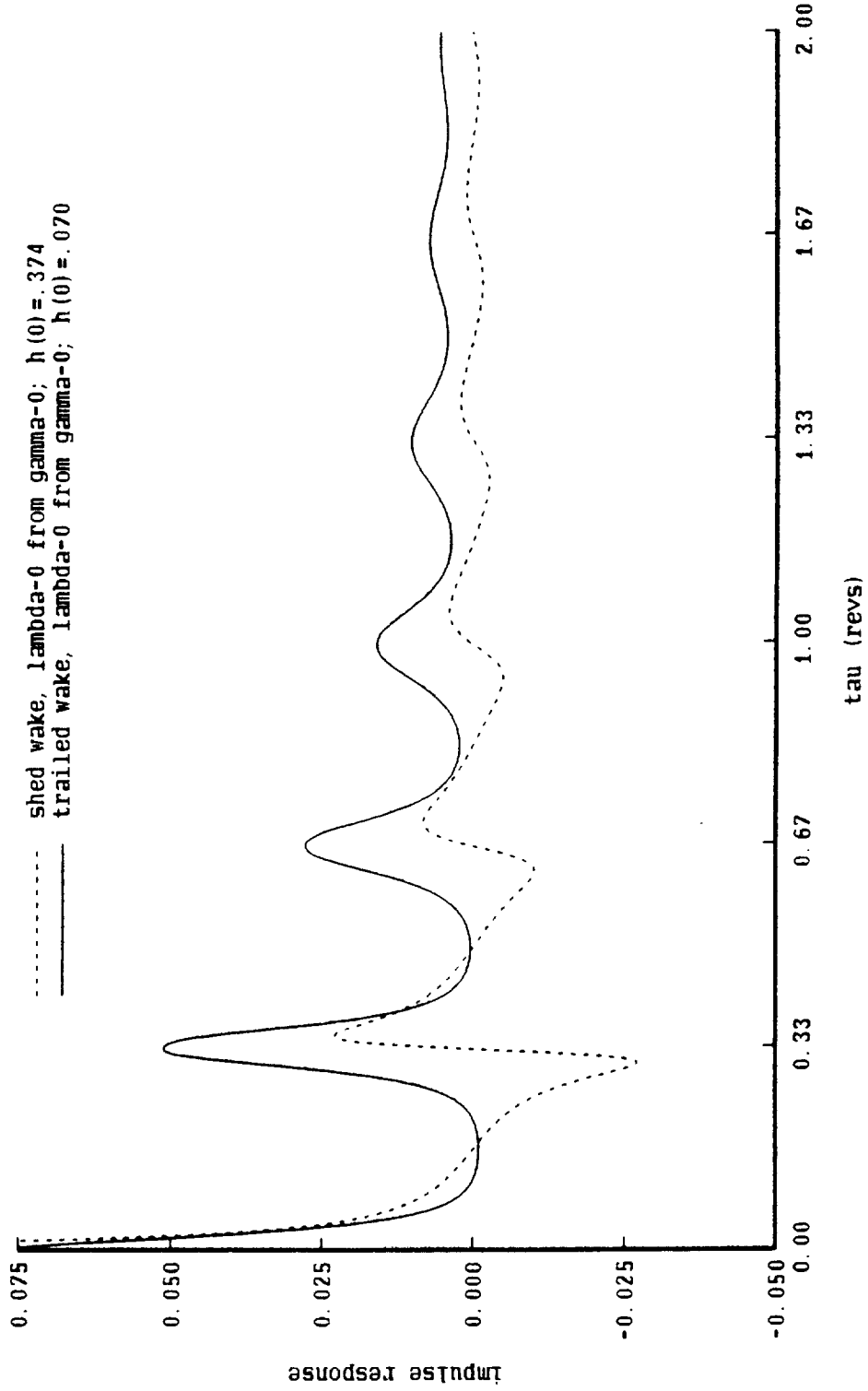


Figure 9b. Influence of sample rate on impulse response

hovering rotor, undistorted wake; 128 steps per rev

nonrotating frame, 3 blades; uniform inflow and circulation at 0.77R

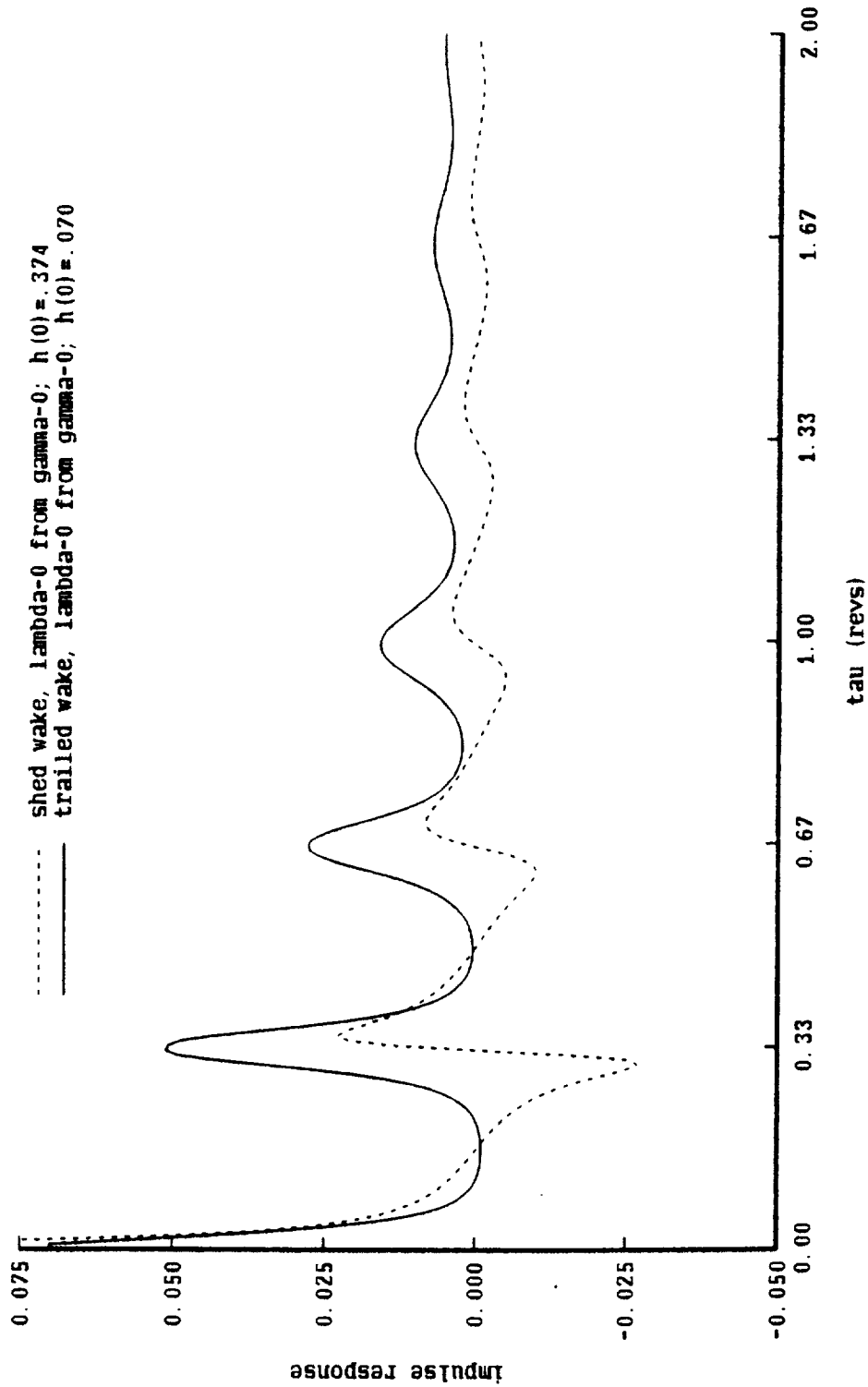


Figure 9c. Influence of sample rate on impulse response

hovering rotor, undistorted wake; 64 steps per rev

nonrotating frame, 3 blades; uniform inflow and circulation at 0.77R

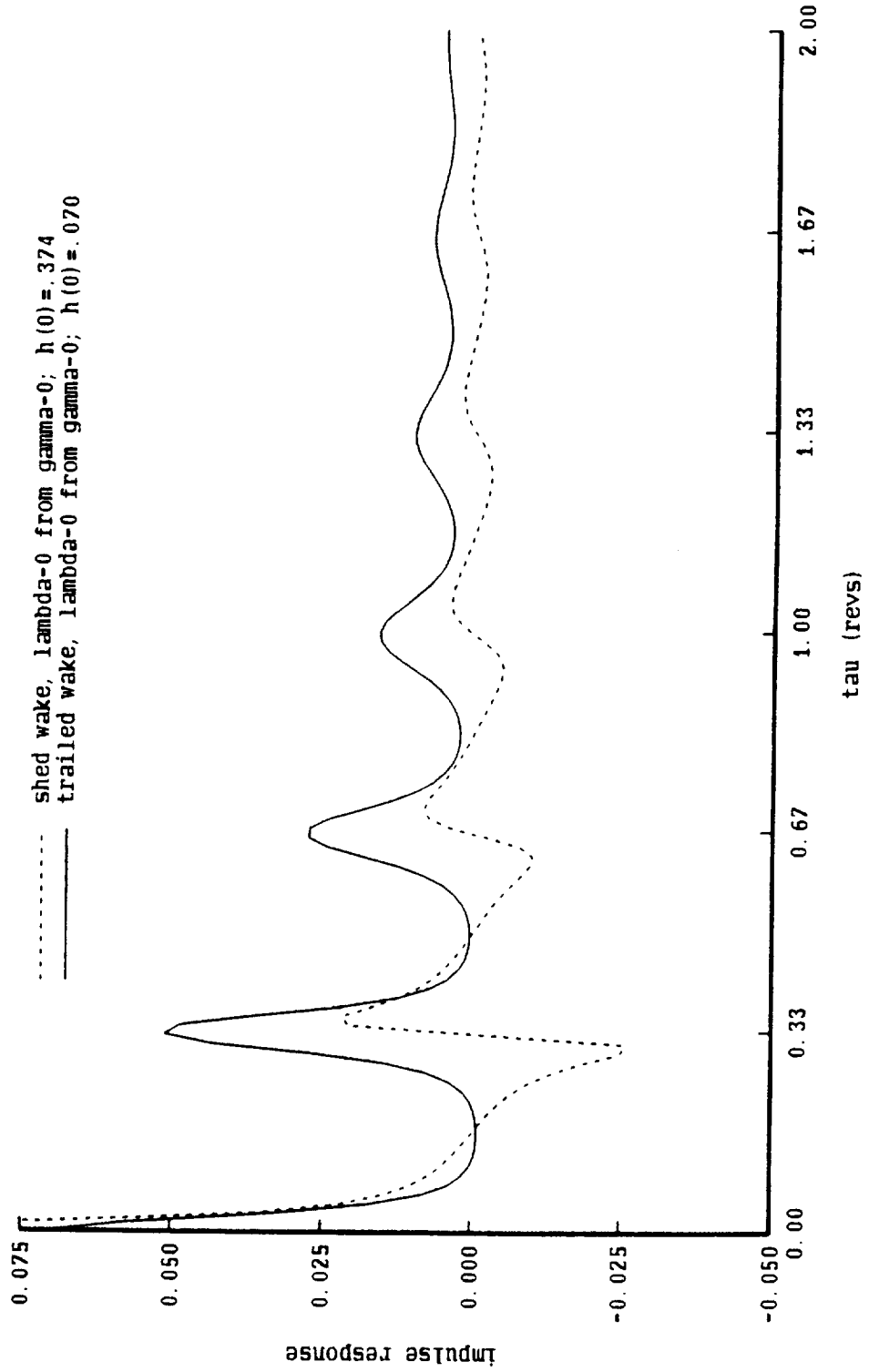


Figure 9d. Influence of sample rate on impulse response

hovering rotor, undistorted wake; 32 steps per rev
nonrotating frame, 3 blades; uniform inflow and circulation at 0.77R

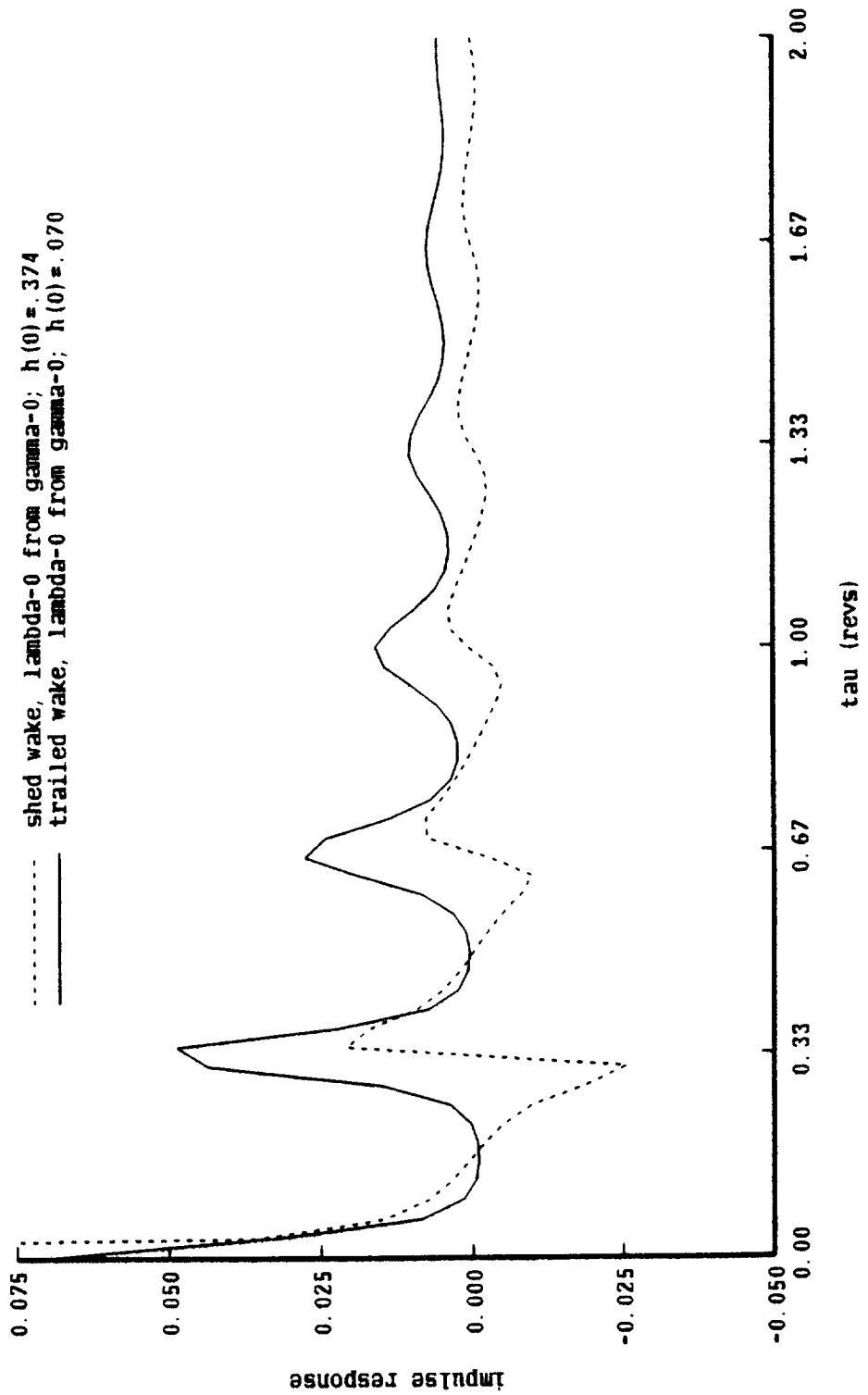


Figure 10a. System function of hovering rotor with undistorted wake

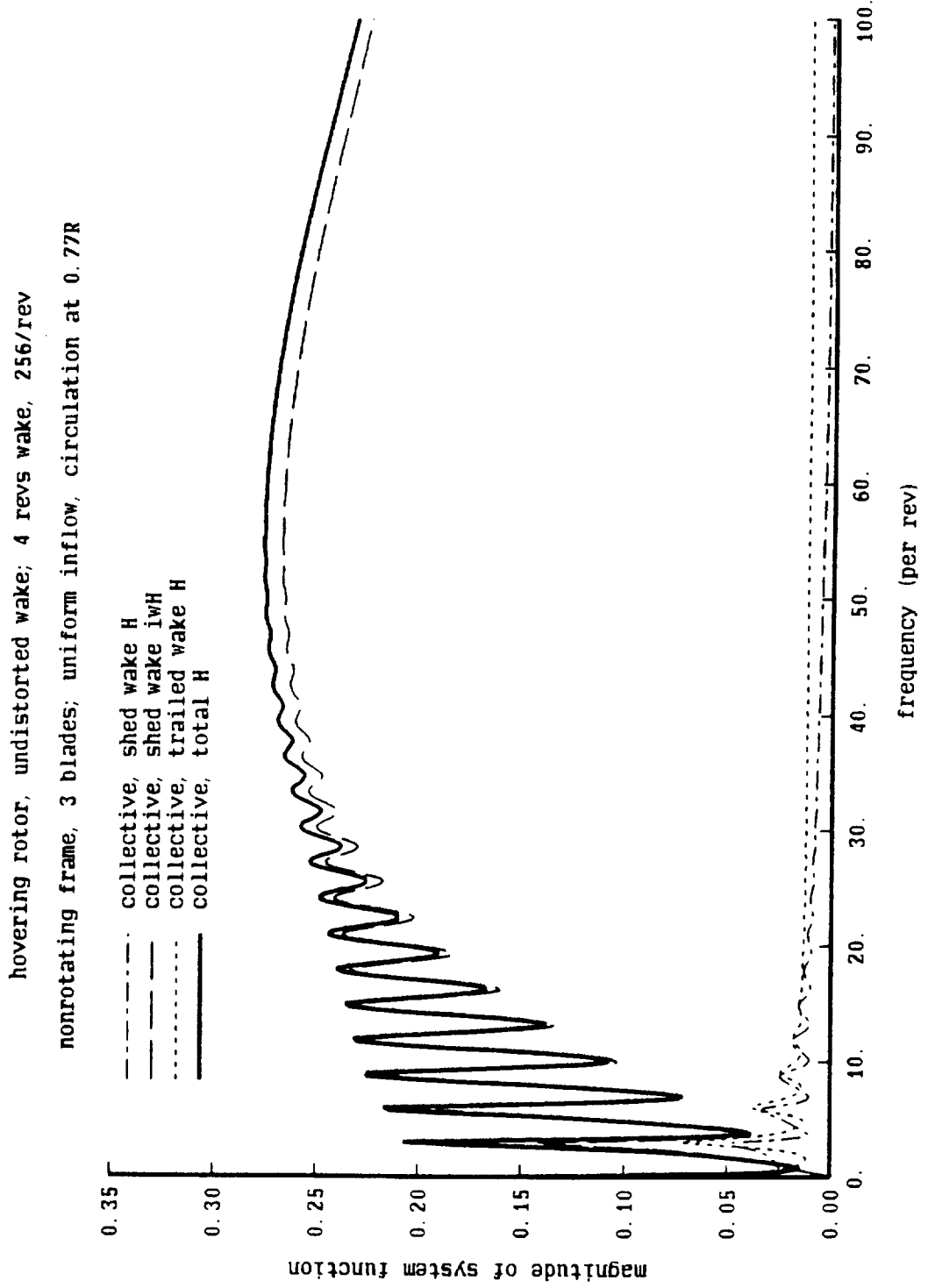


Figure 10b. System function of hovering rotor with undistorted wake

hovering rotor, undistorted wake; 4 revs wake, 256/rev
 nonrotating frame, 3 blades; uniform inflow, circulation at 0.77R

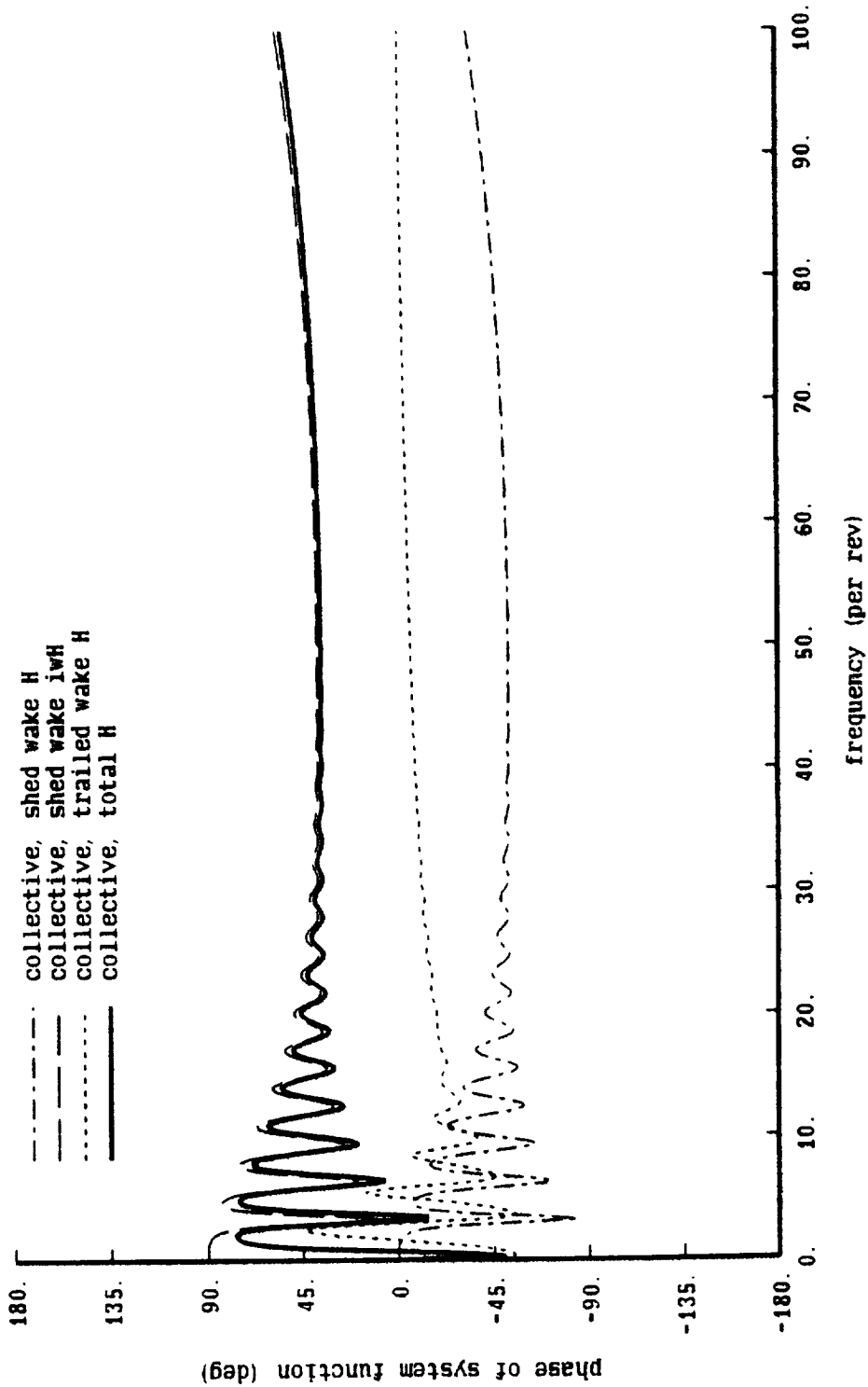


Figure 11a. System function of hovering rotor with undistorted wake

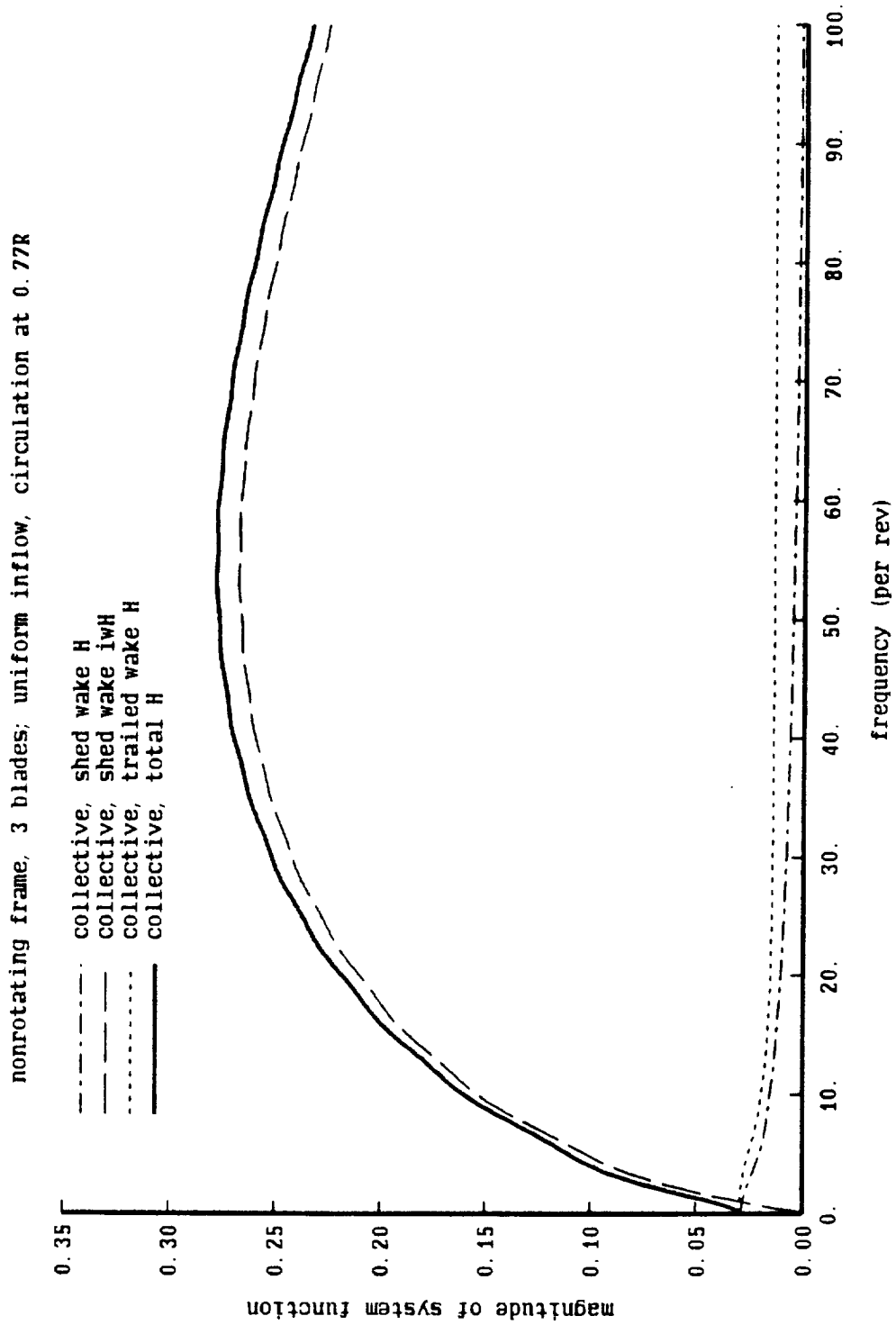


Figure 11b. System function of hovering rotor with undistorted wake

nonrotating frame, 3 blades; uniform inflow, circulation at 0.77R

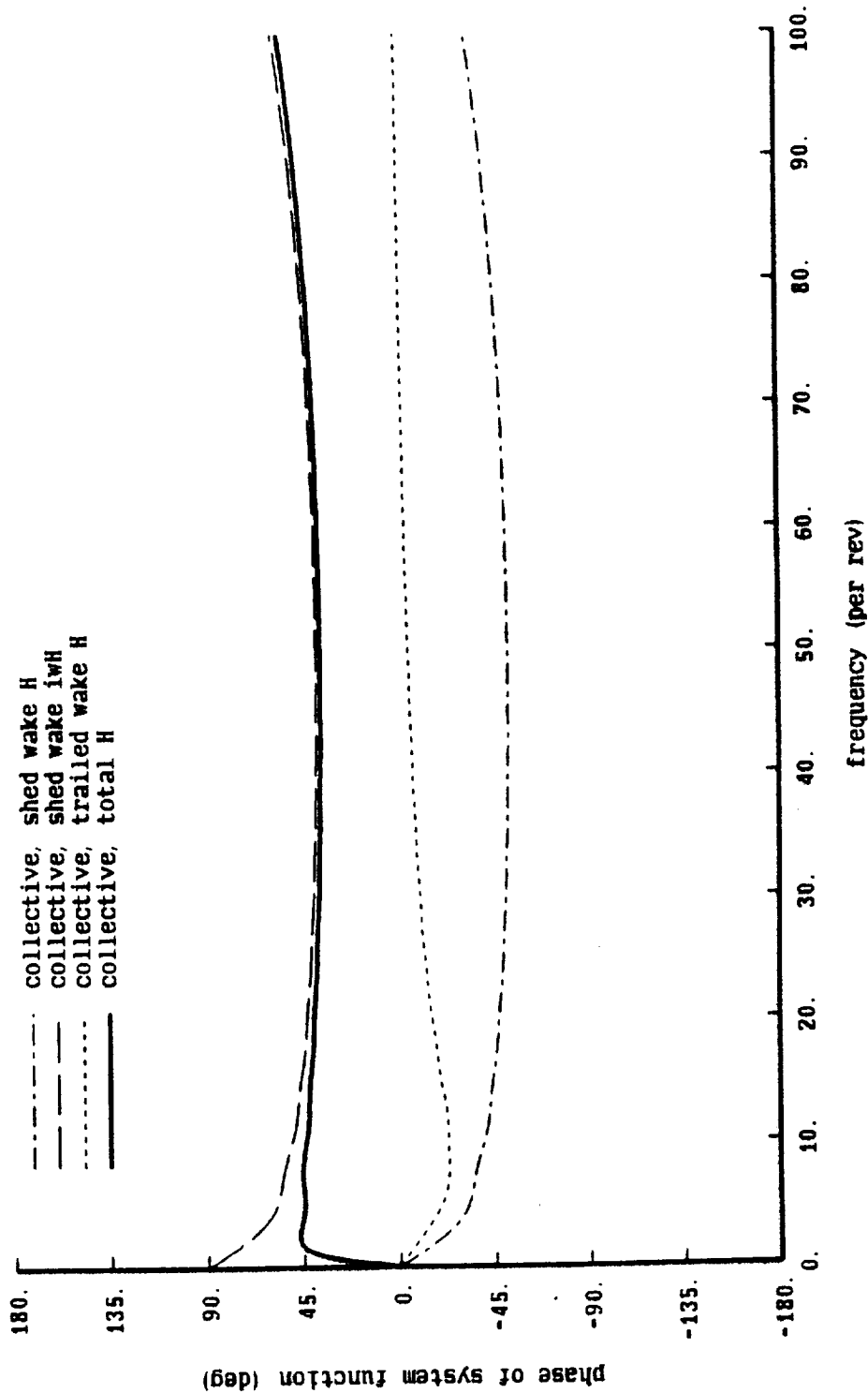


Figure 12a. Influence of sample rate on system function

hovering rotor, undistorted wake; 4 revs wake, 256/rev

nonrotating frame, 3 blades; uniform inflow, circulation at 0.77R

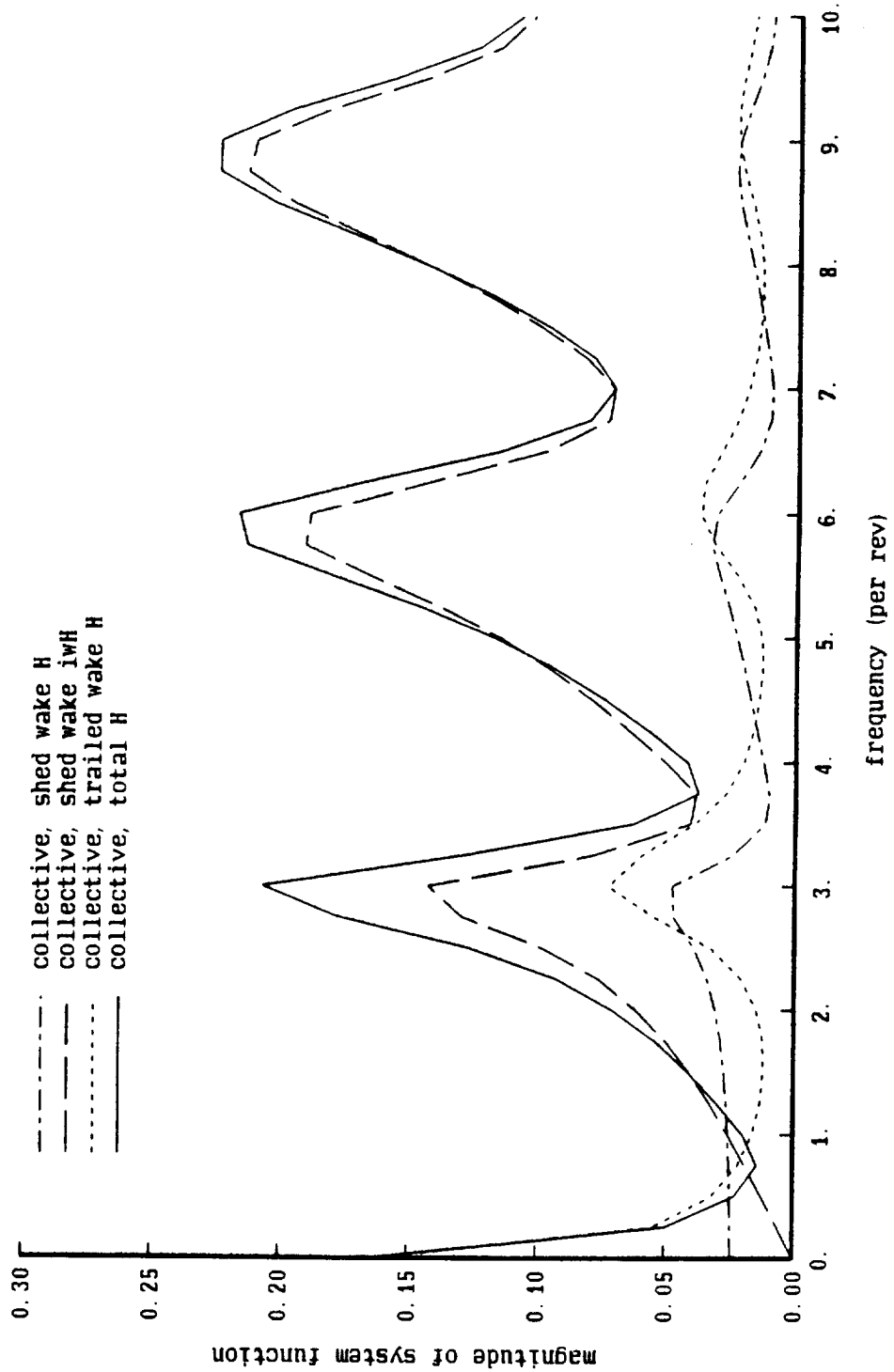


Figure 12b. Influence of sample rate on system function

hovering rotor, undistorted wake; 4 revs wake, 128/rev
 nonrotating frame, 3 blades; uniform inflow, circulation at 0.77R

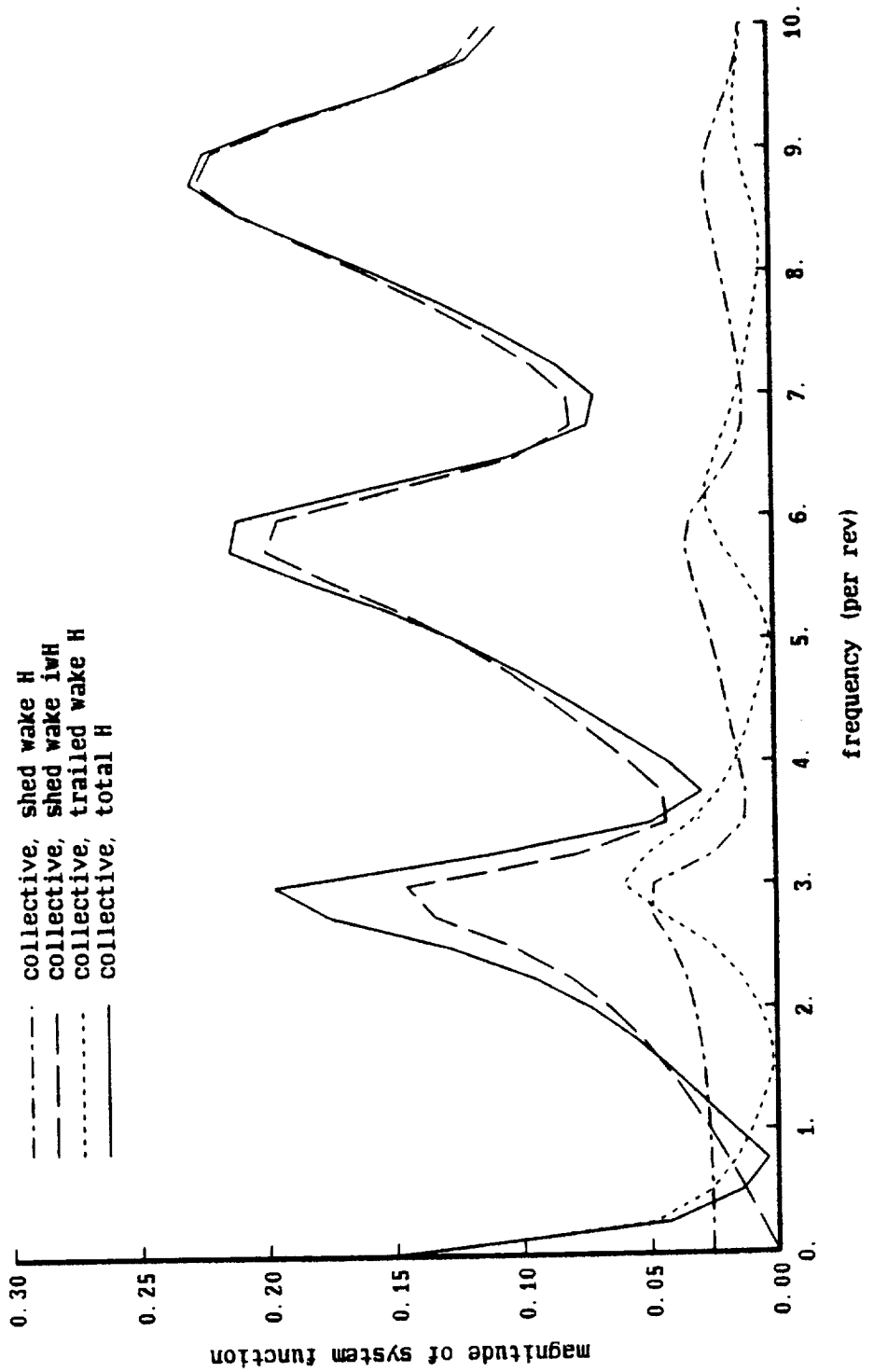


Figure 12c. Influence of sample rate on system function

hovering rotor, undistorted wake; 4 revs wake, 64/rev
 nonrotating frame, 3 blades; uniform inflow, circulation at 0.77R

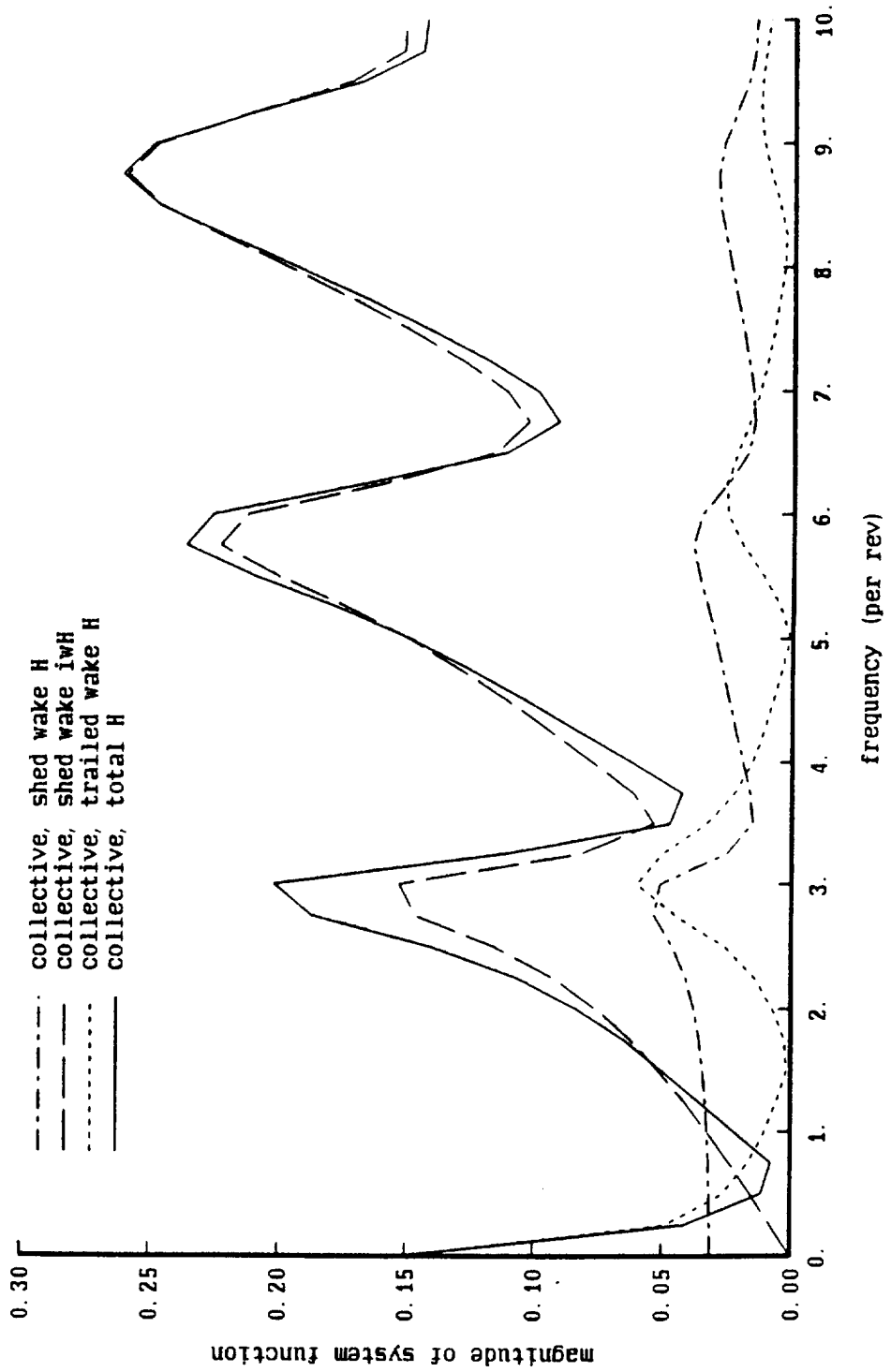


Figure 12d. Influence of sample rate on system function

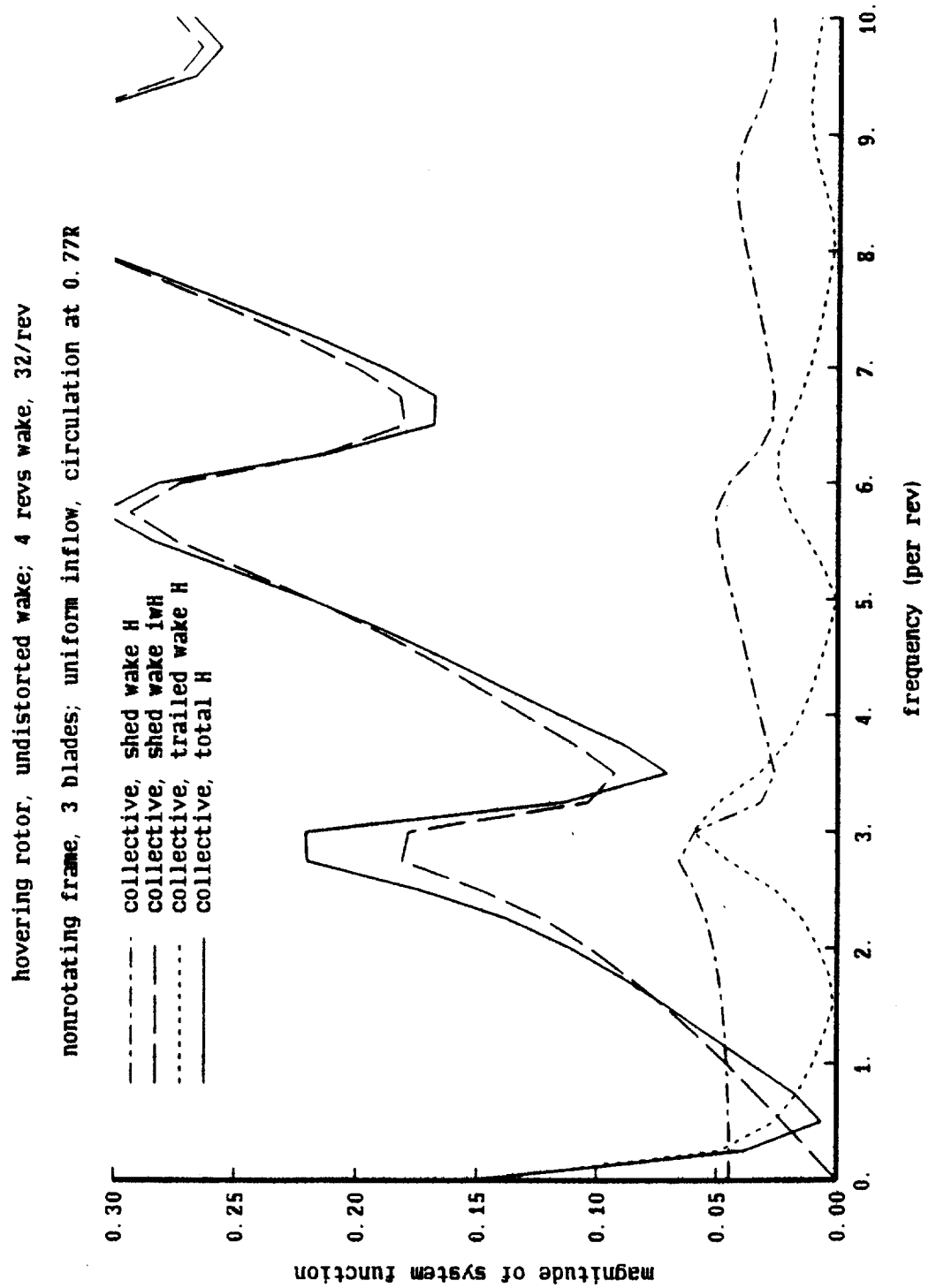


Figure 12e. Influence of sample rate on system function

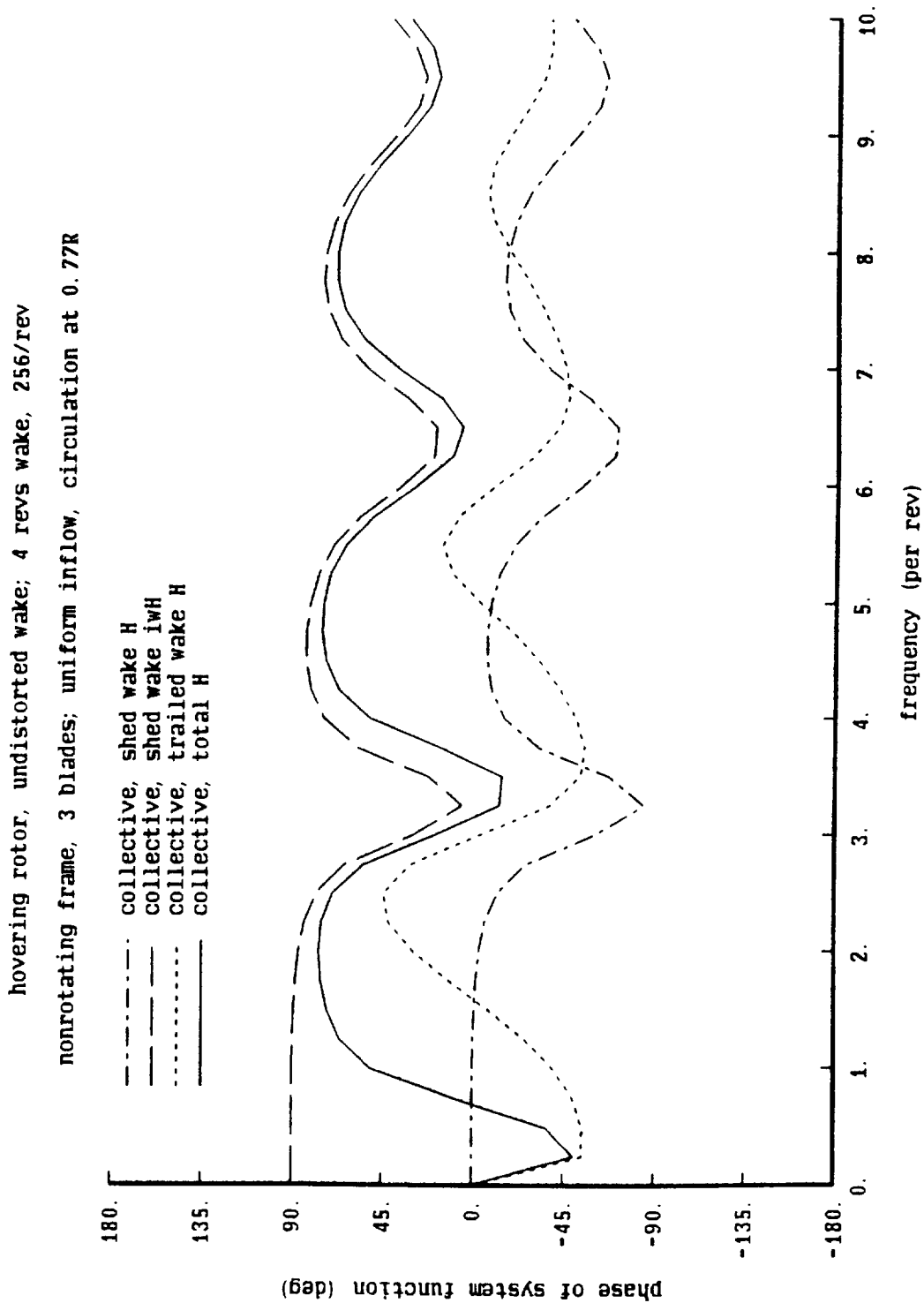


Figure 12f. Influence of sample rate on system function

hovering rotor, undistorted wake; 4 revs/wake, 128/rev

nonrotating frame, 3 blades; uniform inflow, circulation at 0.77R

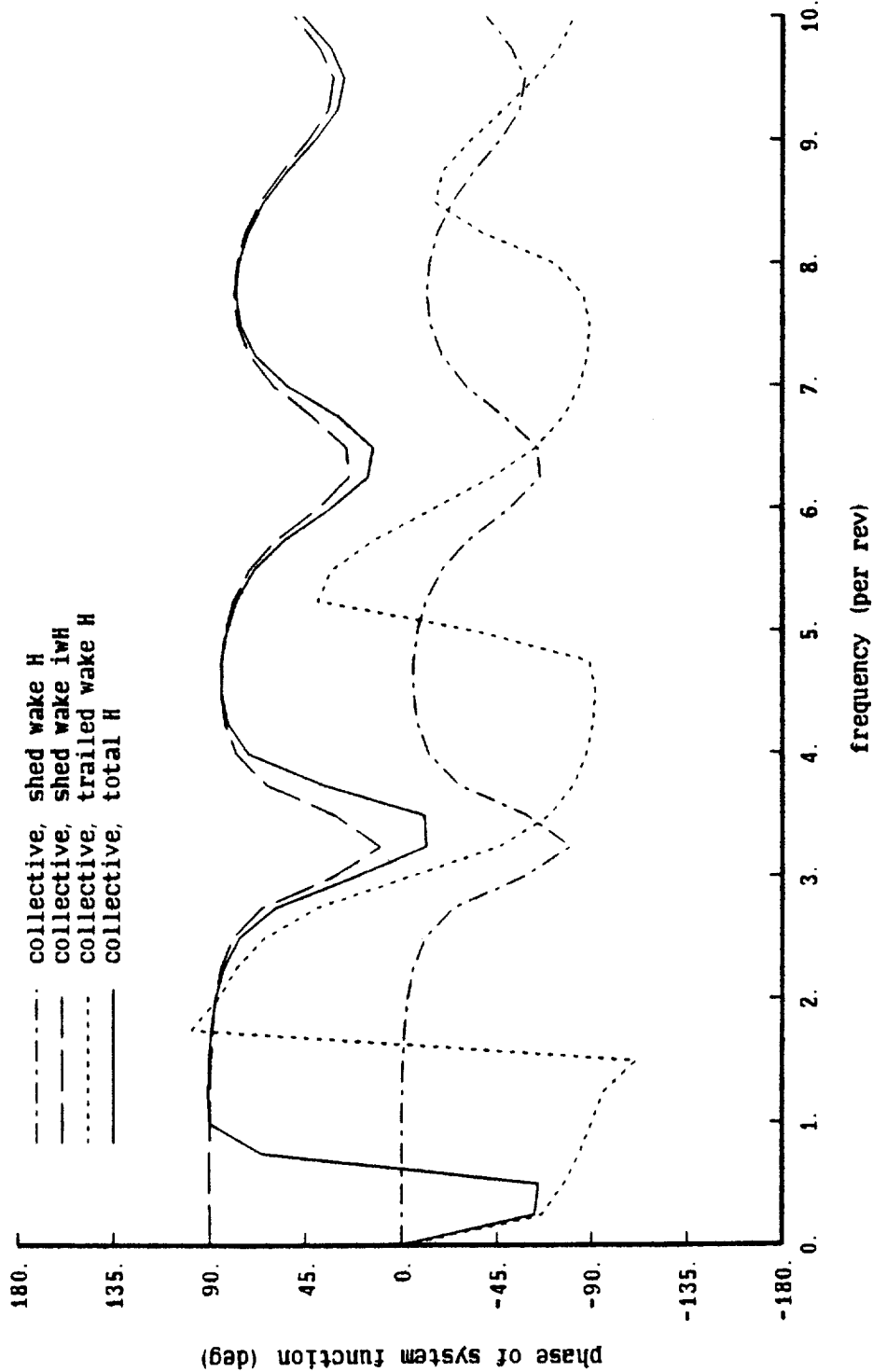


Figure 12g. Influence of sample rate on system function

hovering rotor, undistorted wake; 4 revs wake, 64/rev
 nonrotating frame, 3 blades; uniform inflow, circulation at 0.77R

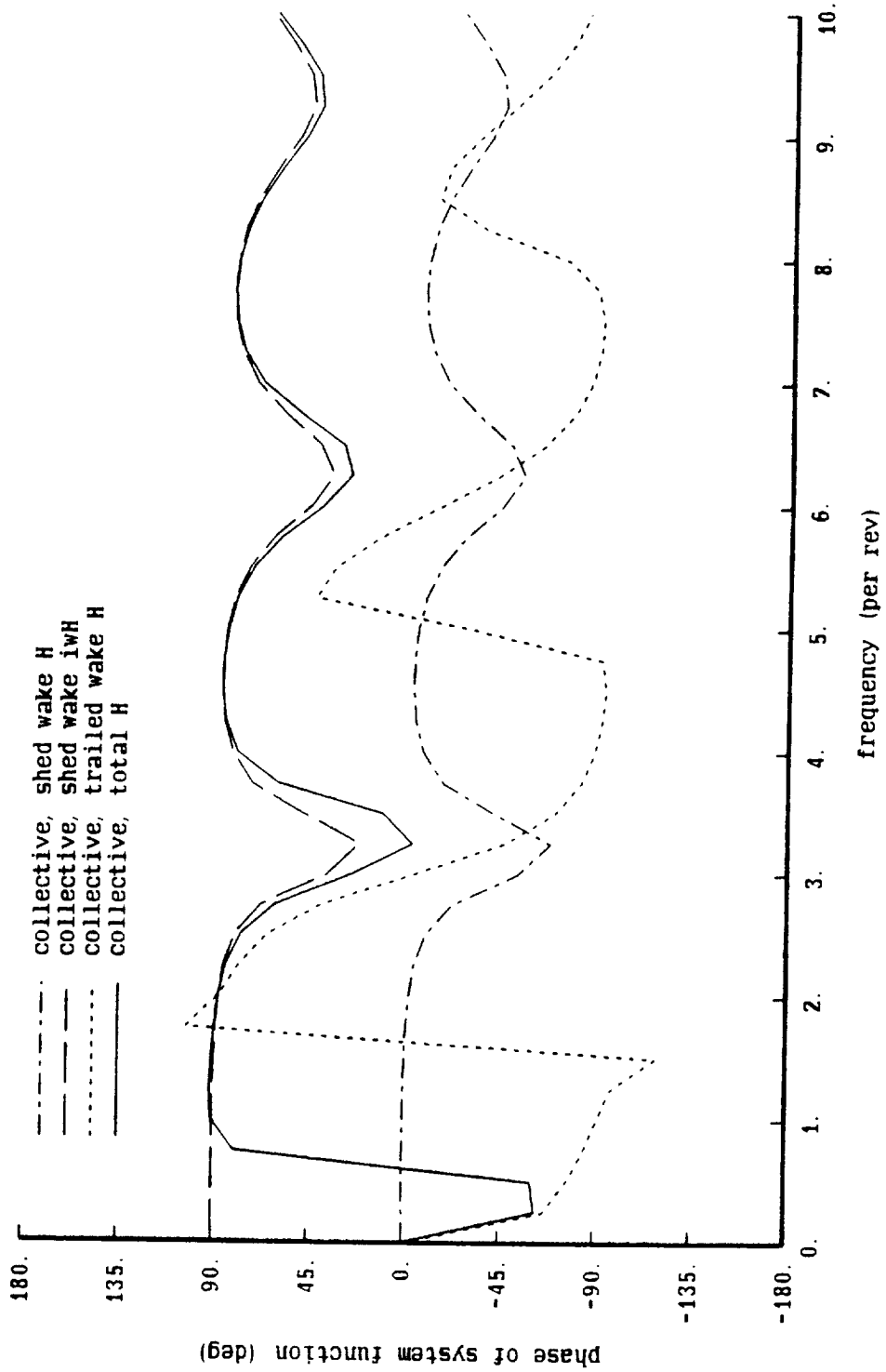


Figure 12h. Influence of sample rate on system function

hovering rotor, undistorted wake; 4 revs wake, 32/rev
 nonrotating frame, 3 blades; uniform inflow, circulation at 0.77R

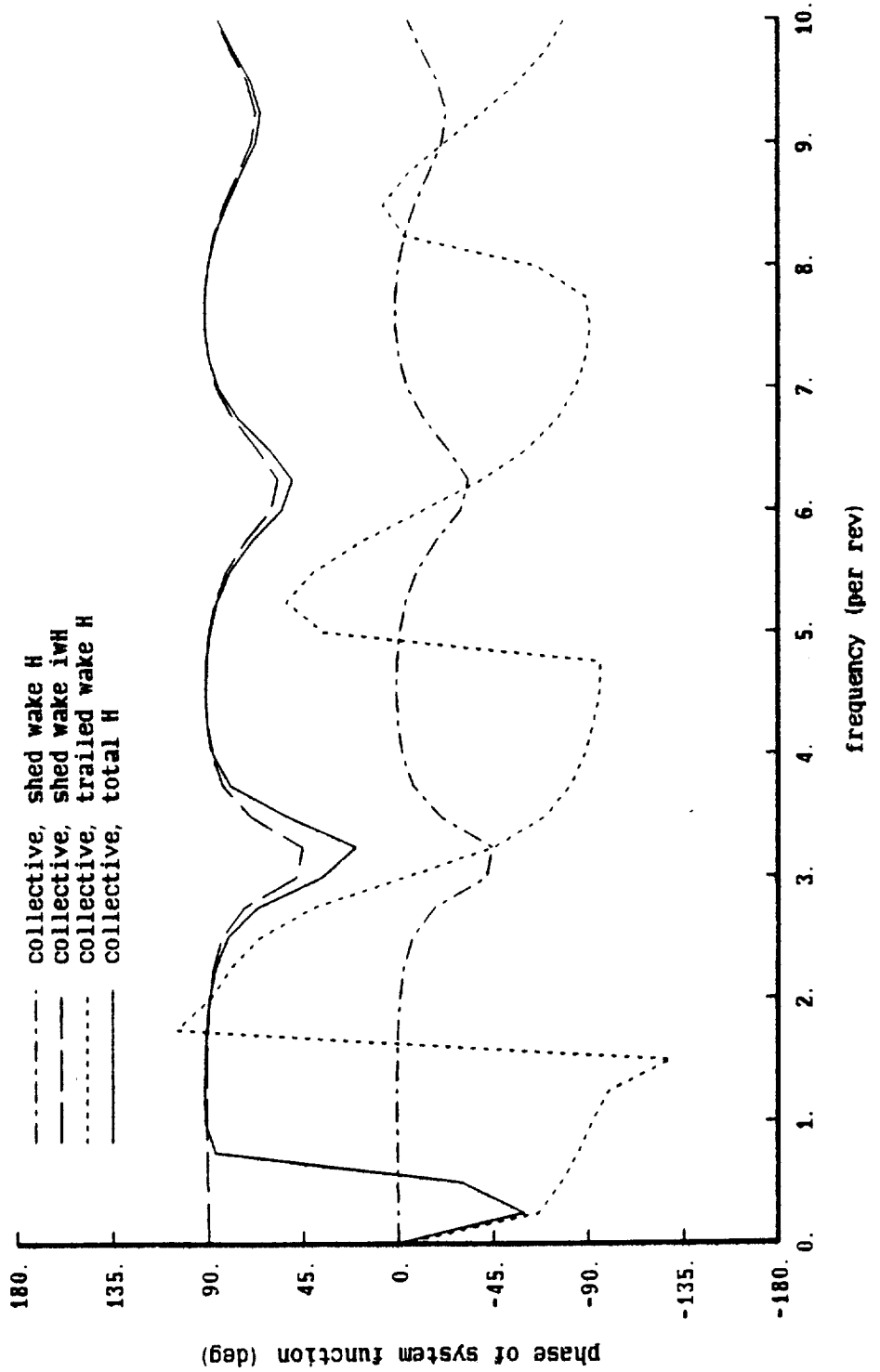


Figure 13a. Influence of sample length on system function

hovering rotor, undistorted wake; 8 revs wake, 128/rev

nonrotating frame, 3 blades; uniform inflow, circulation at 0.77R

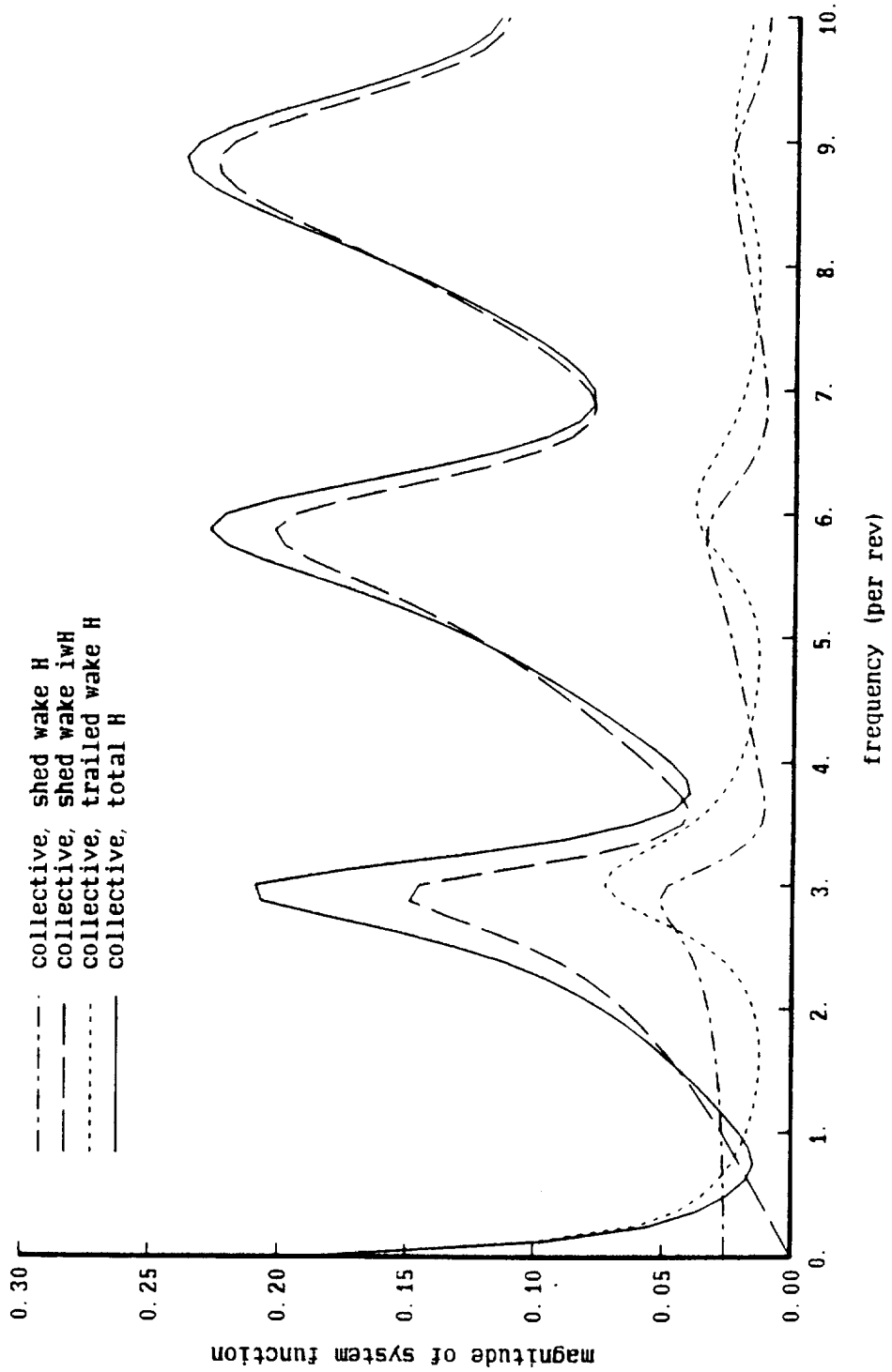


Figure 13b. Influence of sample length on system function

hovering rotor, undistorted wake; 8 revs wake, 128/rev
 nonrotating frame, 3 blades; uniform inflow, circulation at 0.77R

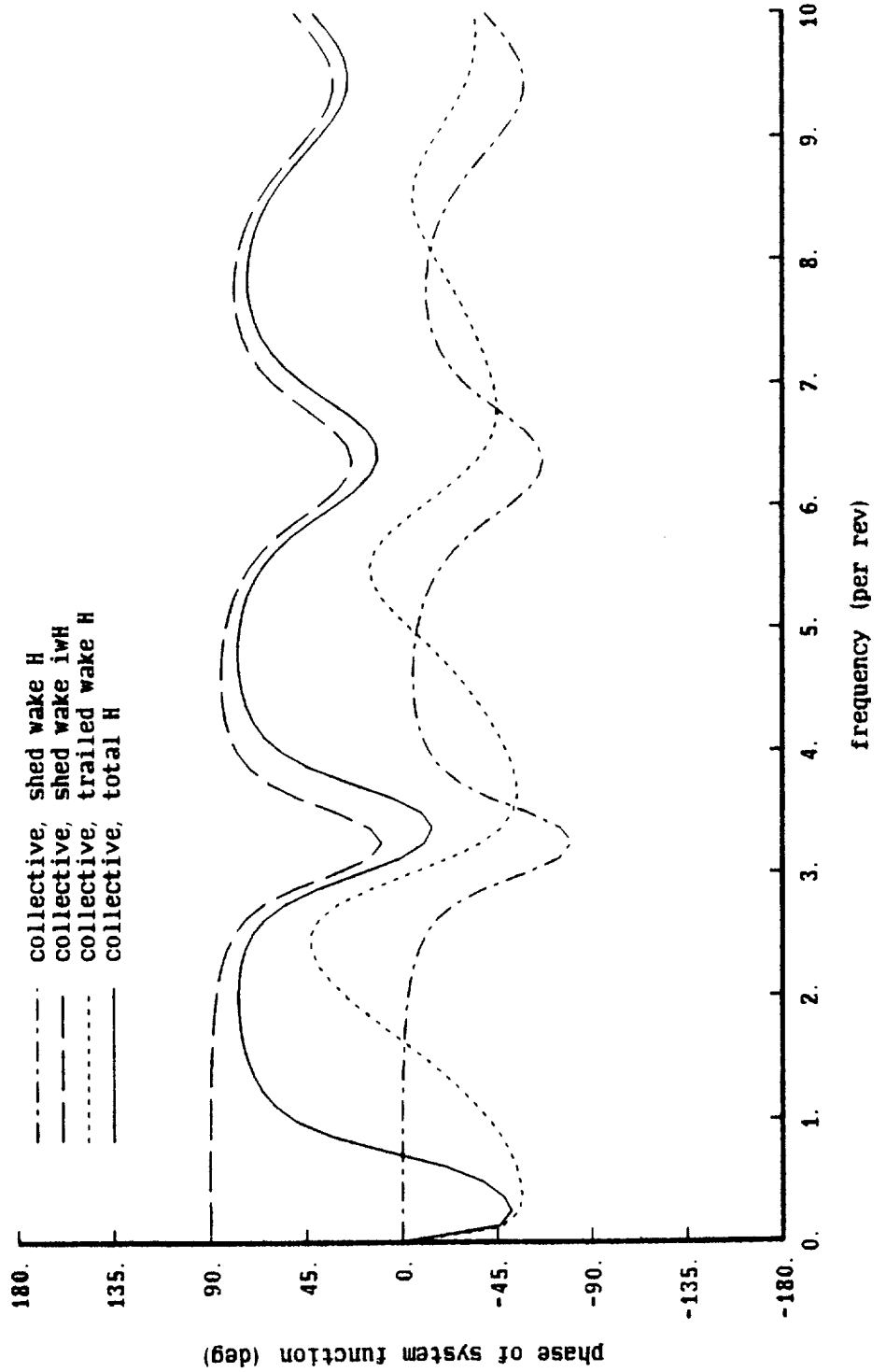


Figure 14a. Inflow response to thrust

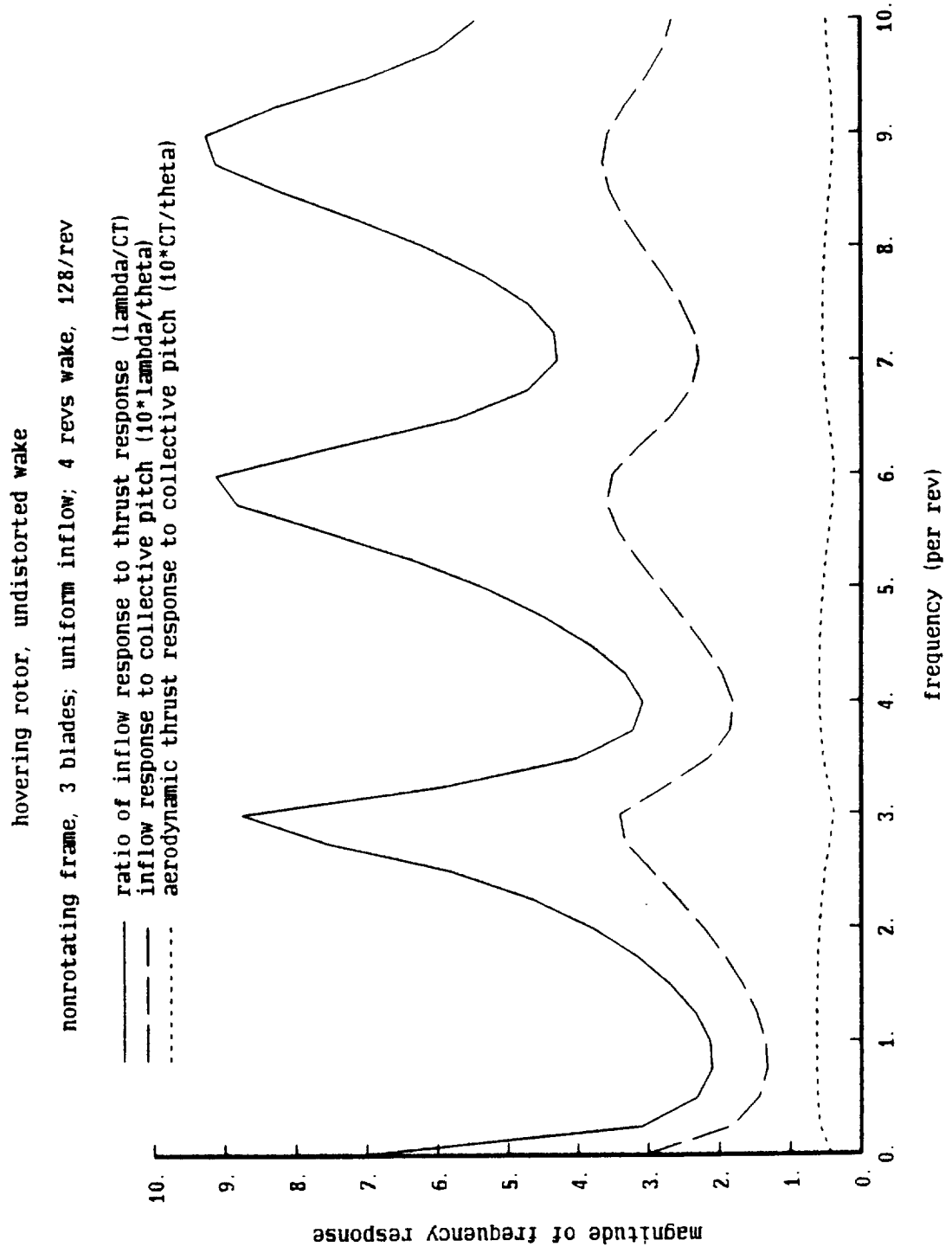


Figure 14b. Inflow response to thrust

hovering rotor, undistorted wake

nonrotating frame, 3 blades; uniform inflow; 4 revs wake, 128/rev

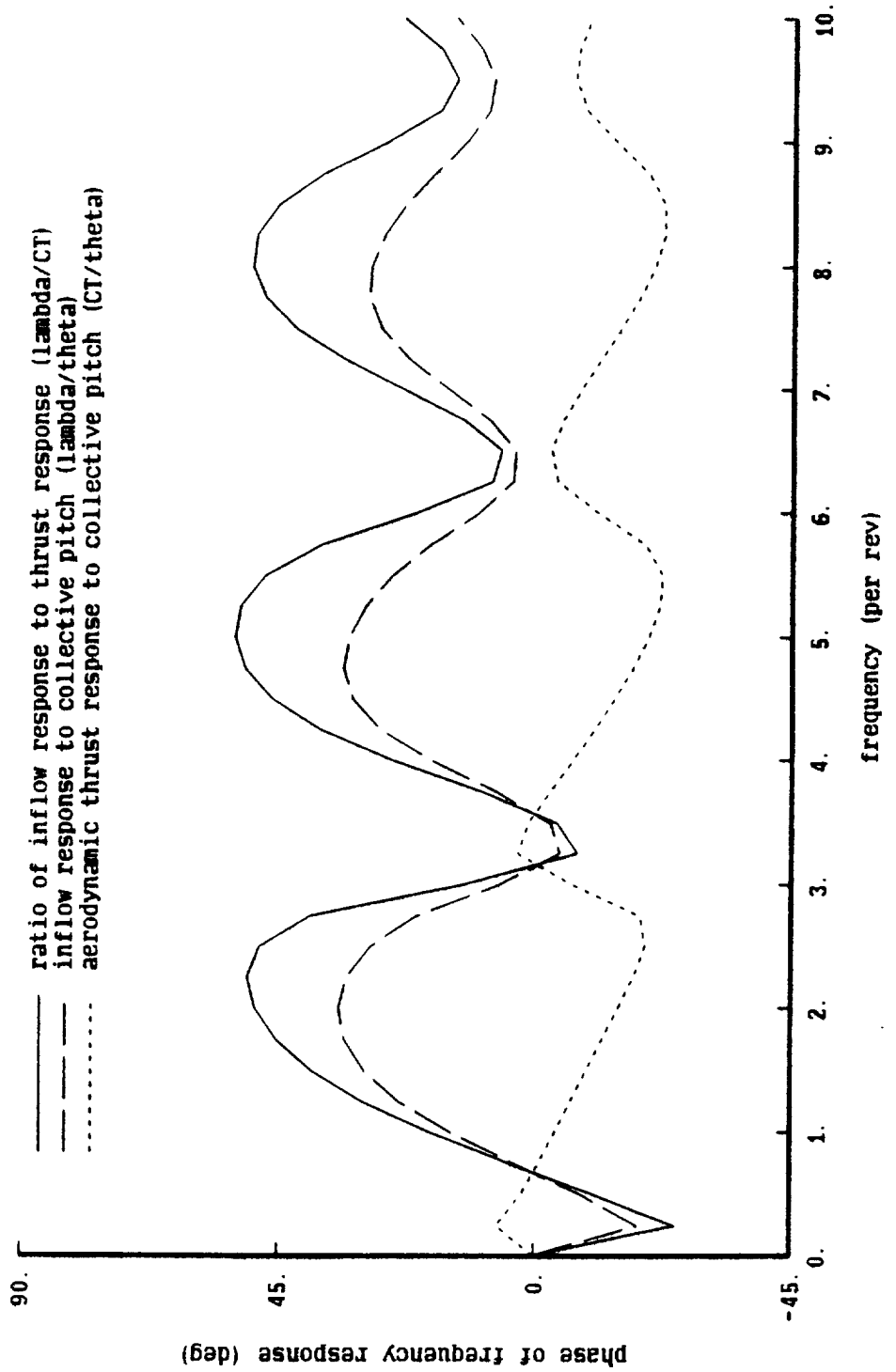


Figure 15a. Inflow response to thrust

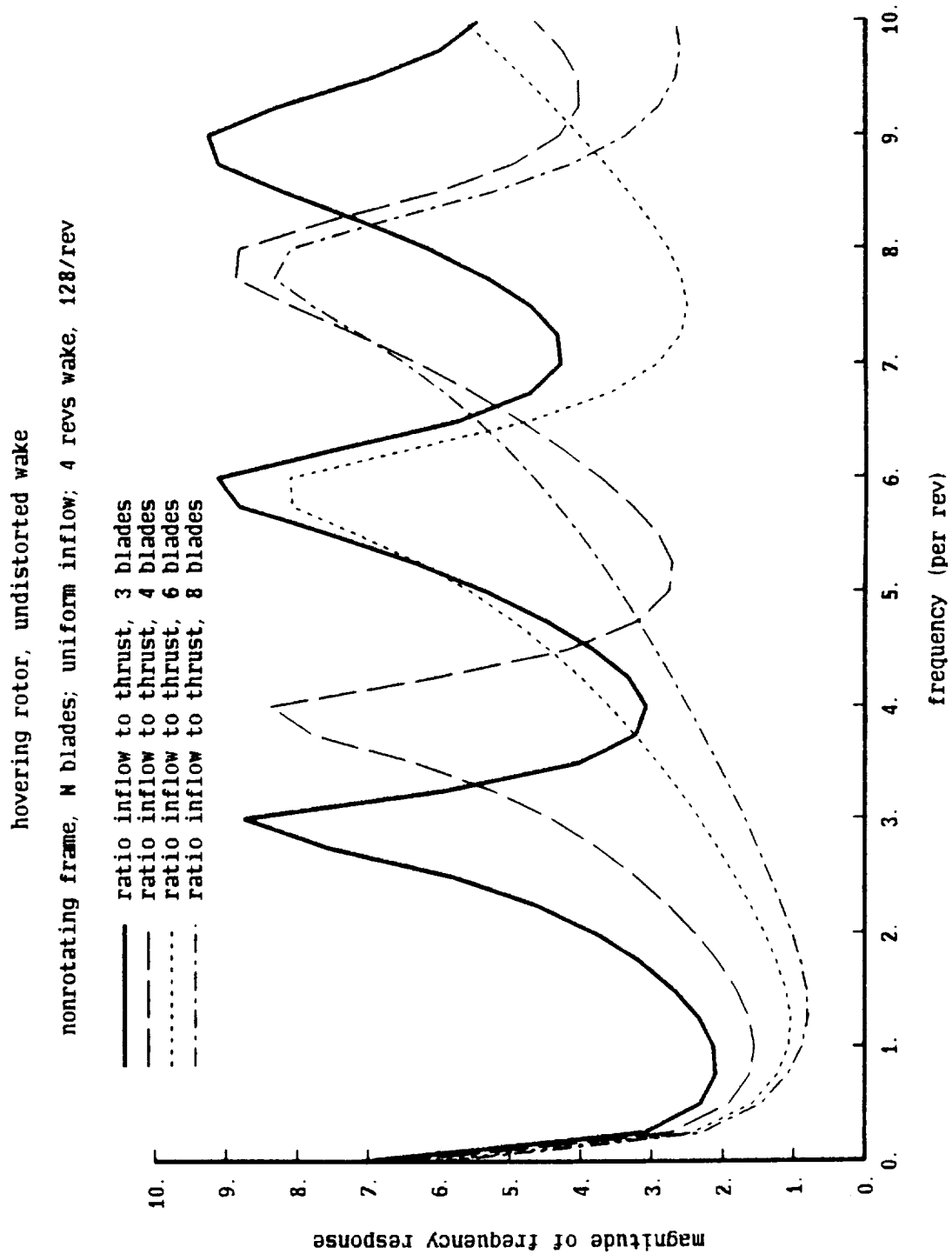


Figure 15b. Inflow response to thrust

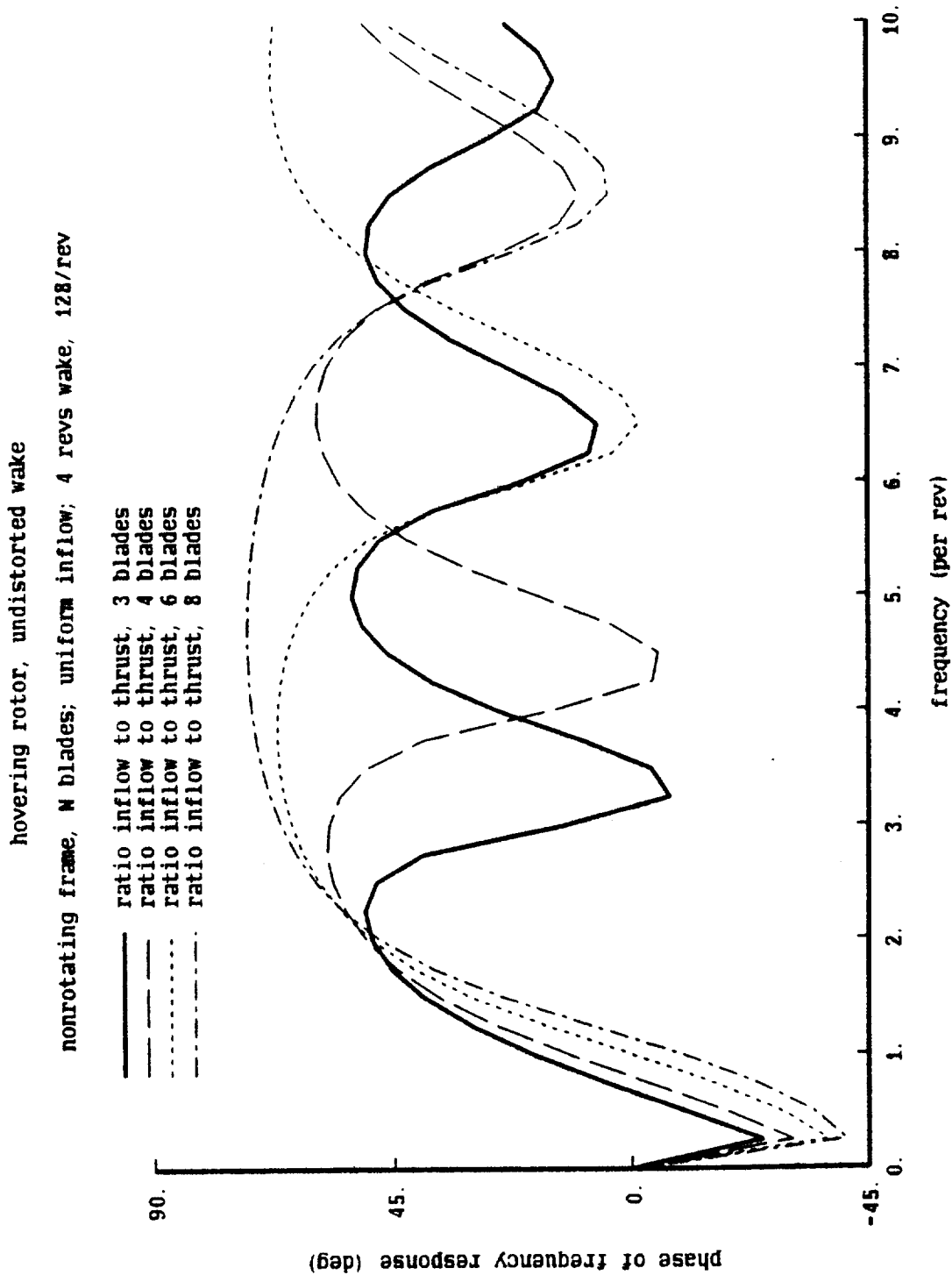


Figure 16a. System function of hovering rotor with undistorted wake

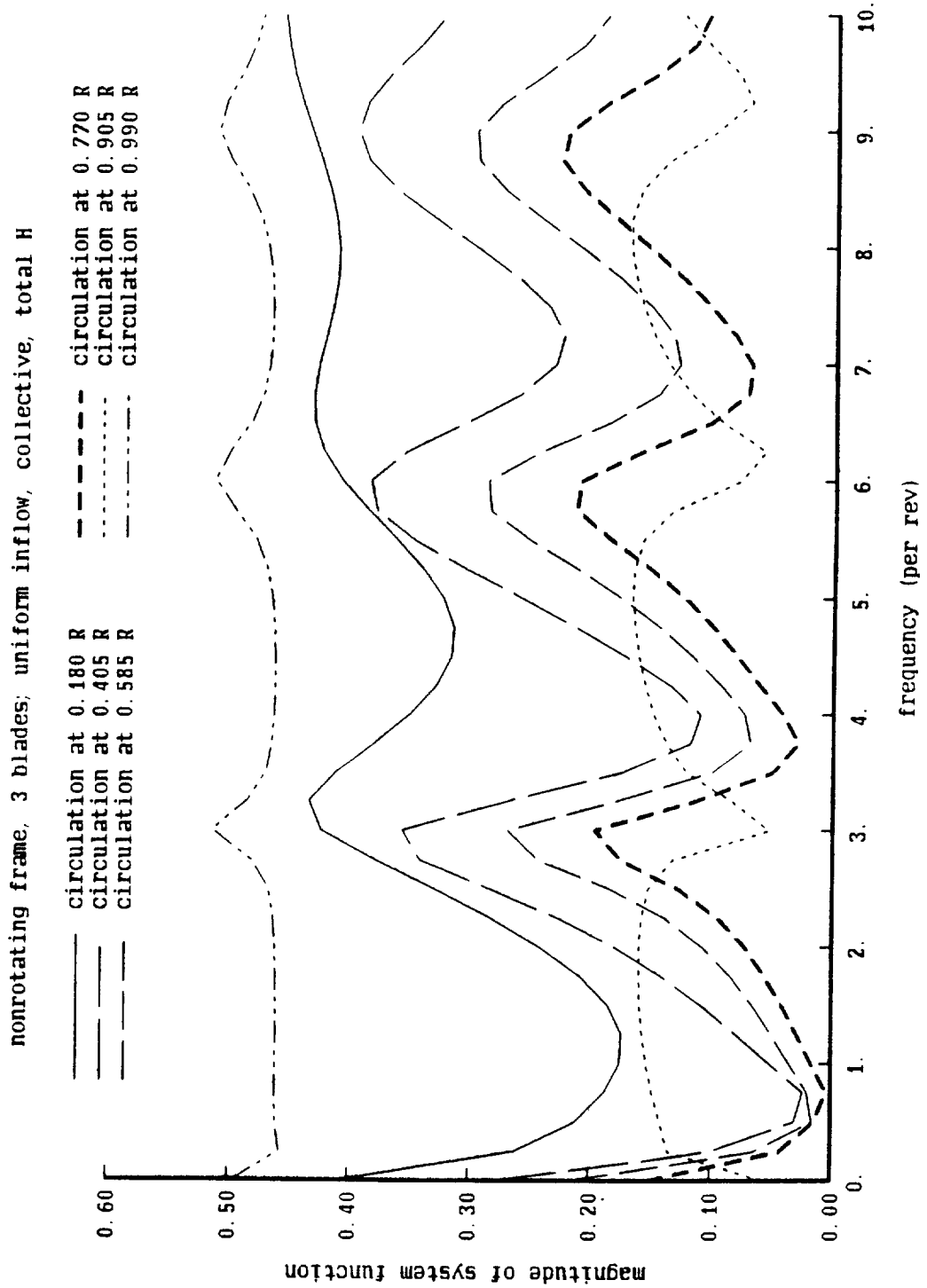


Figure 16b. System function of hovering rotor with undistorted wake

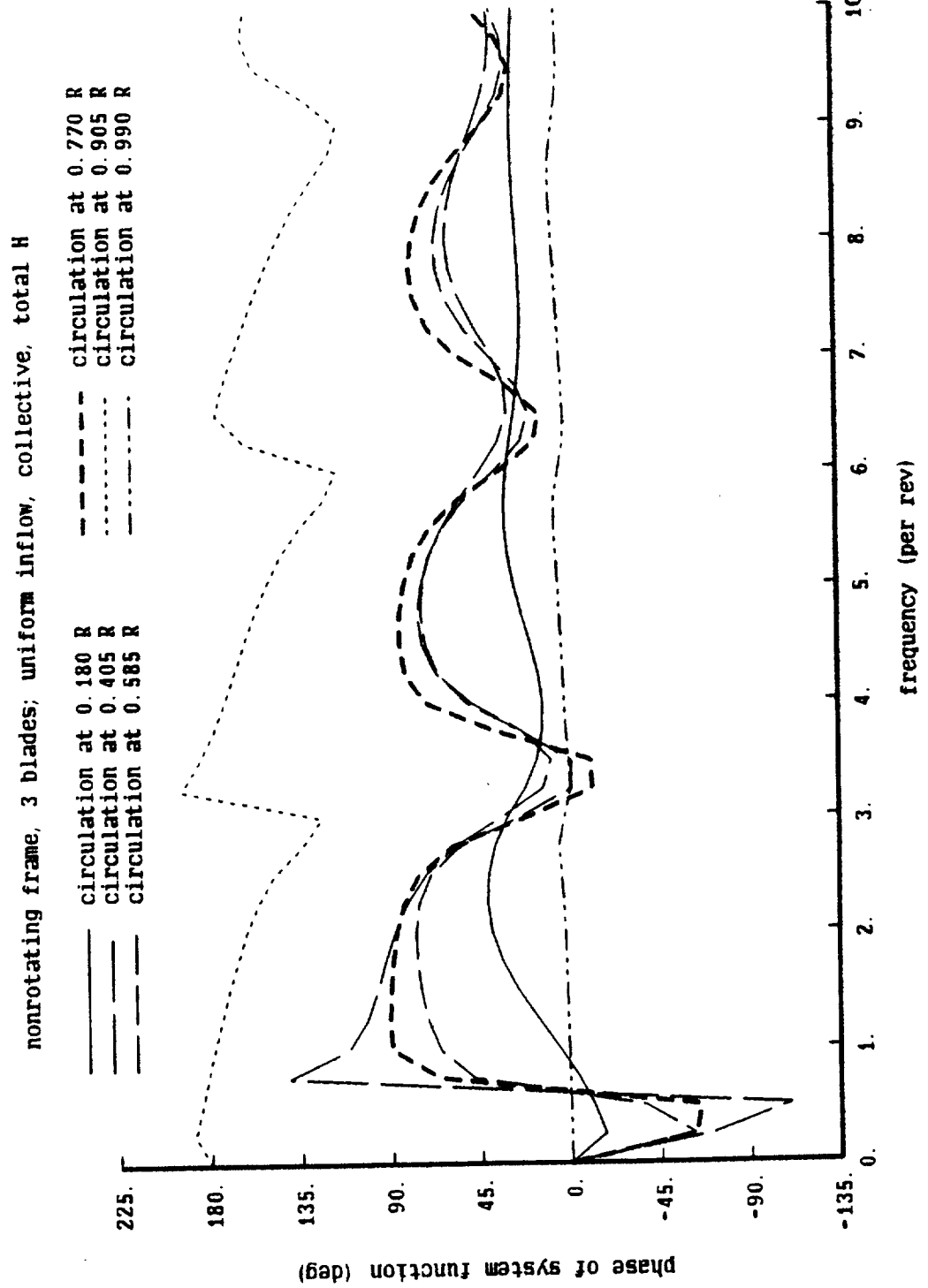


Figure 17. Impulse response function of hovering rotor with undistorted wake

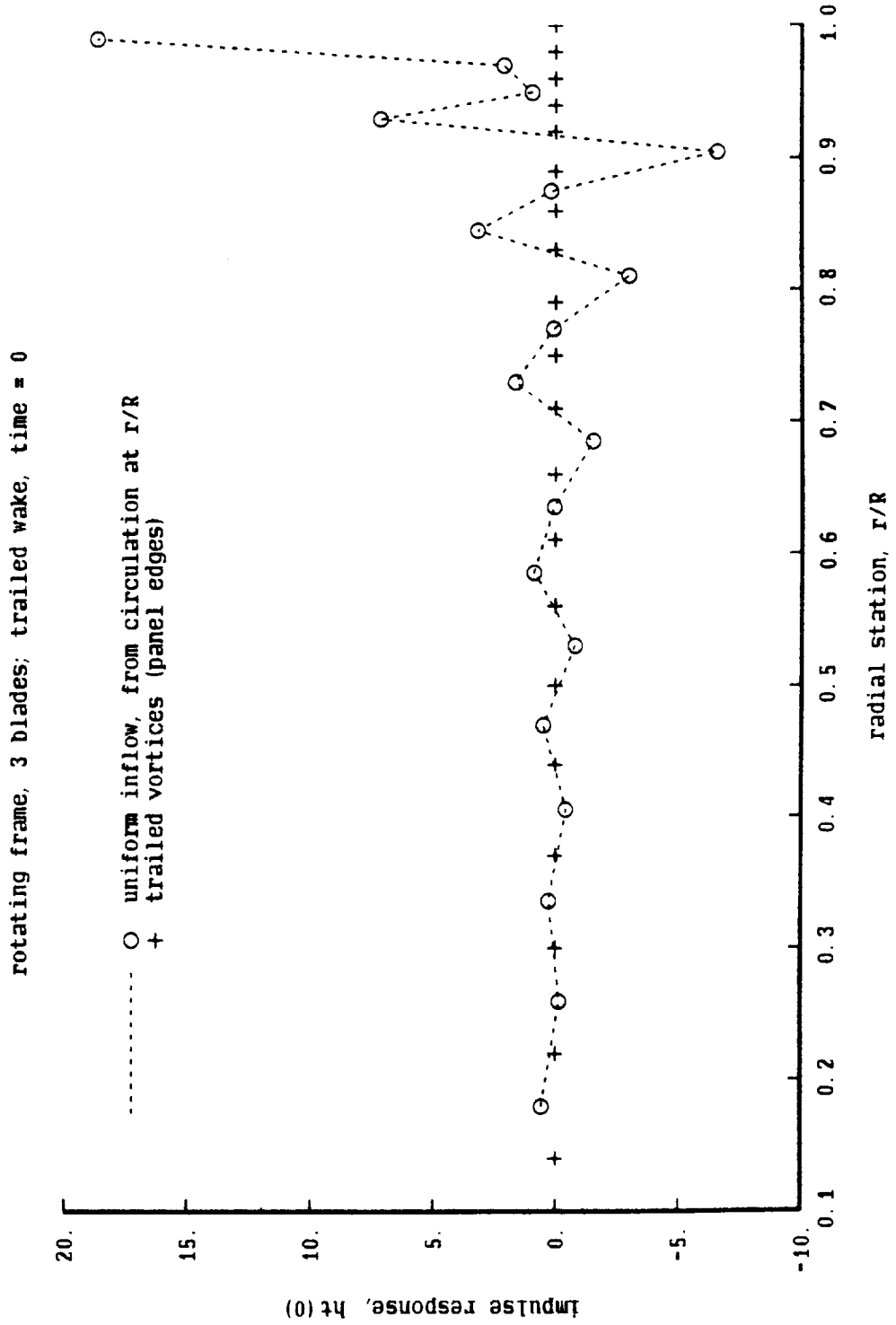


Figure 18a. Influence of frequency range on identification

nonrotating frame, 3 blades; uniform inflow, circulation at 0.77R

identification frequency range = 2/rev

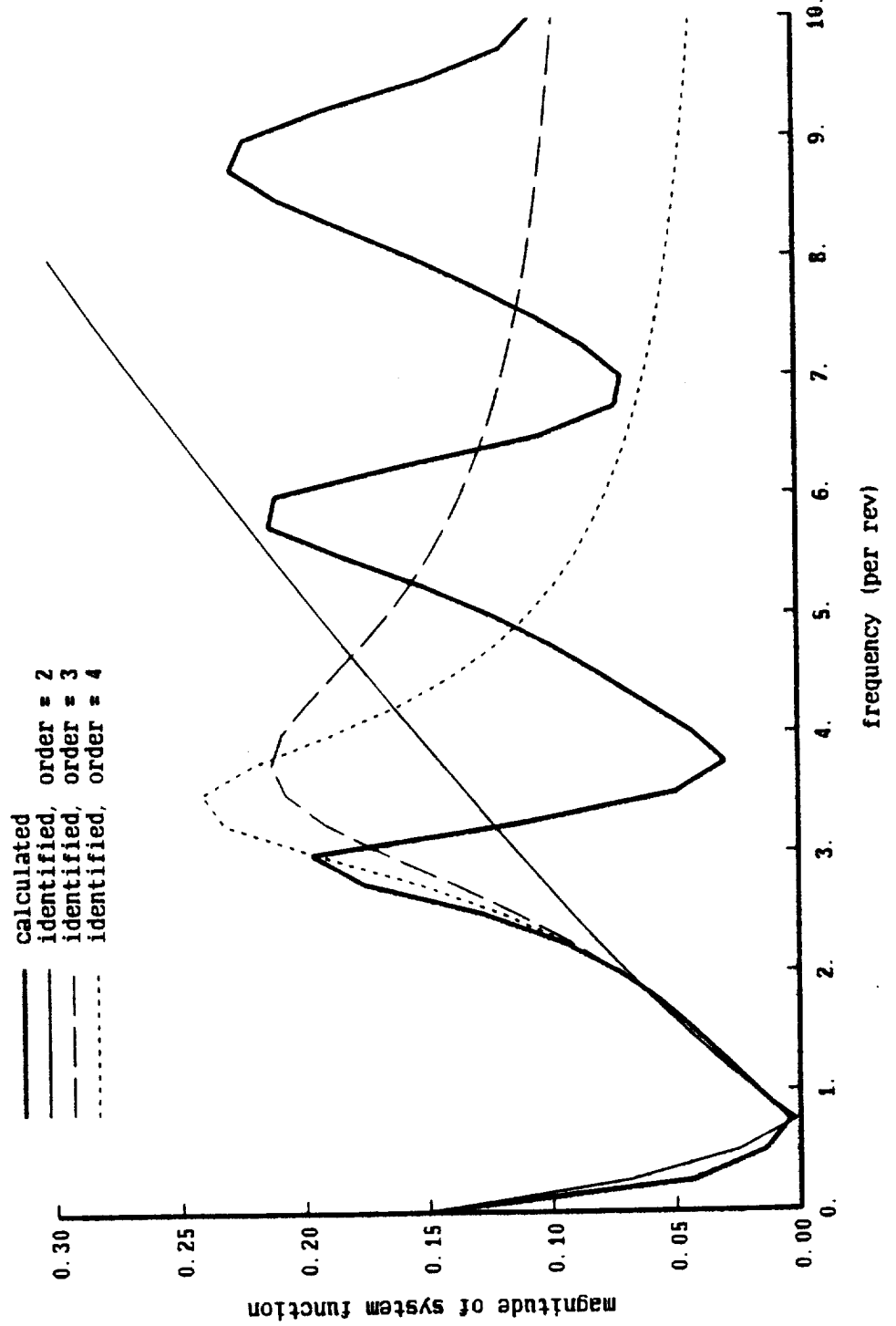


Figure 18b. Influence of frequency range on identification

nonrotating frame, 3 blades; uniform inflow, circulation at 0.77R

identification frequency range = 2/rev

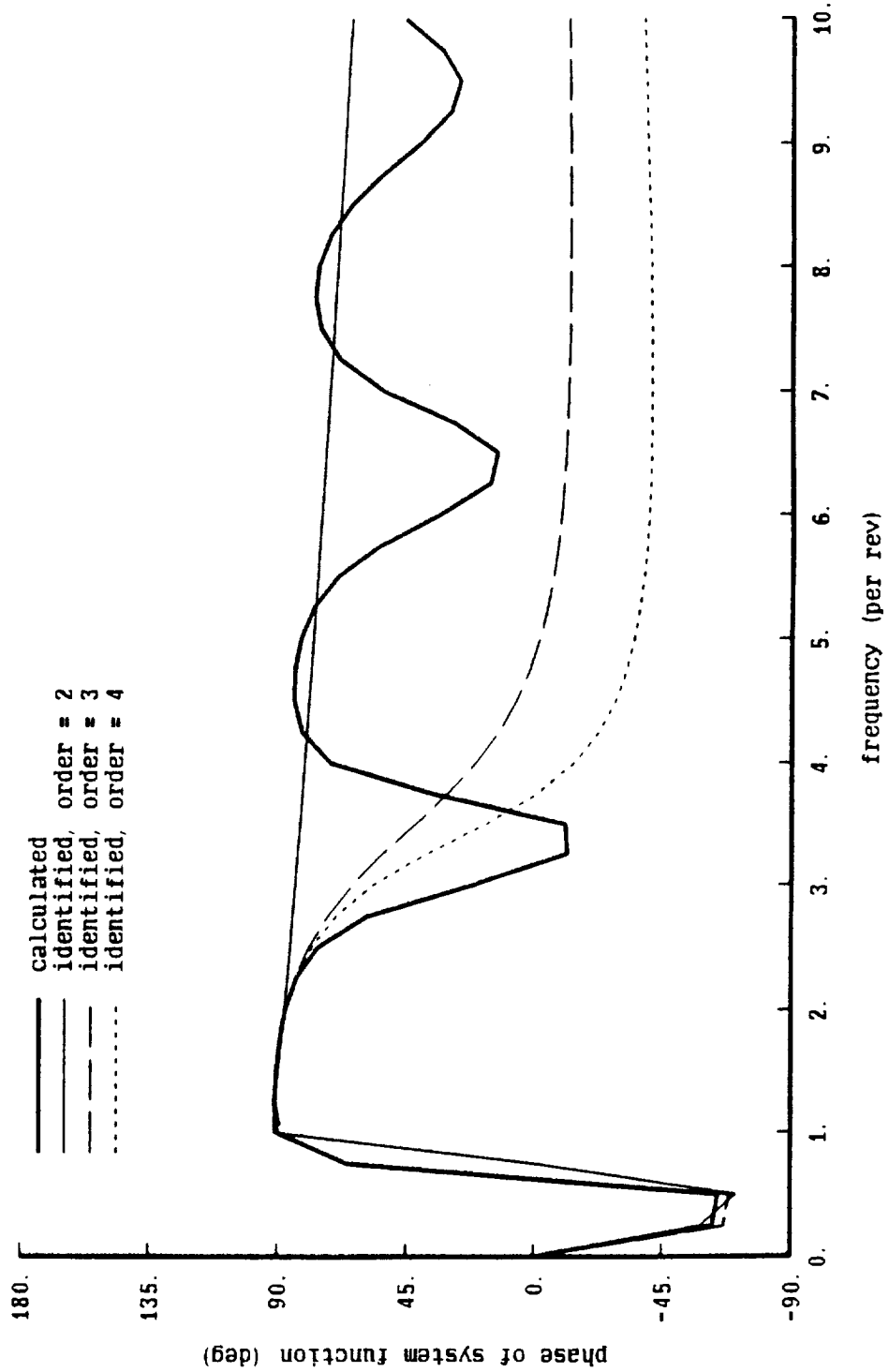


Figure 18c. Influence of frequency range on identification

nonrotating frame, 3 blades; uniform inflow, circulation at 0.77R

identification frequency range = 4.5/rev

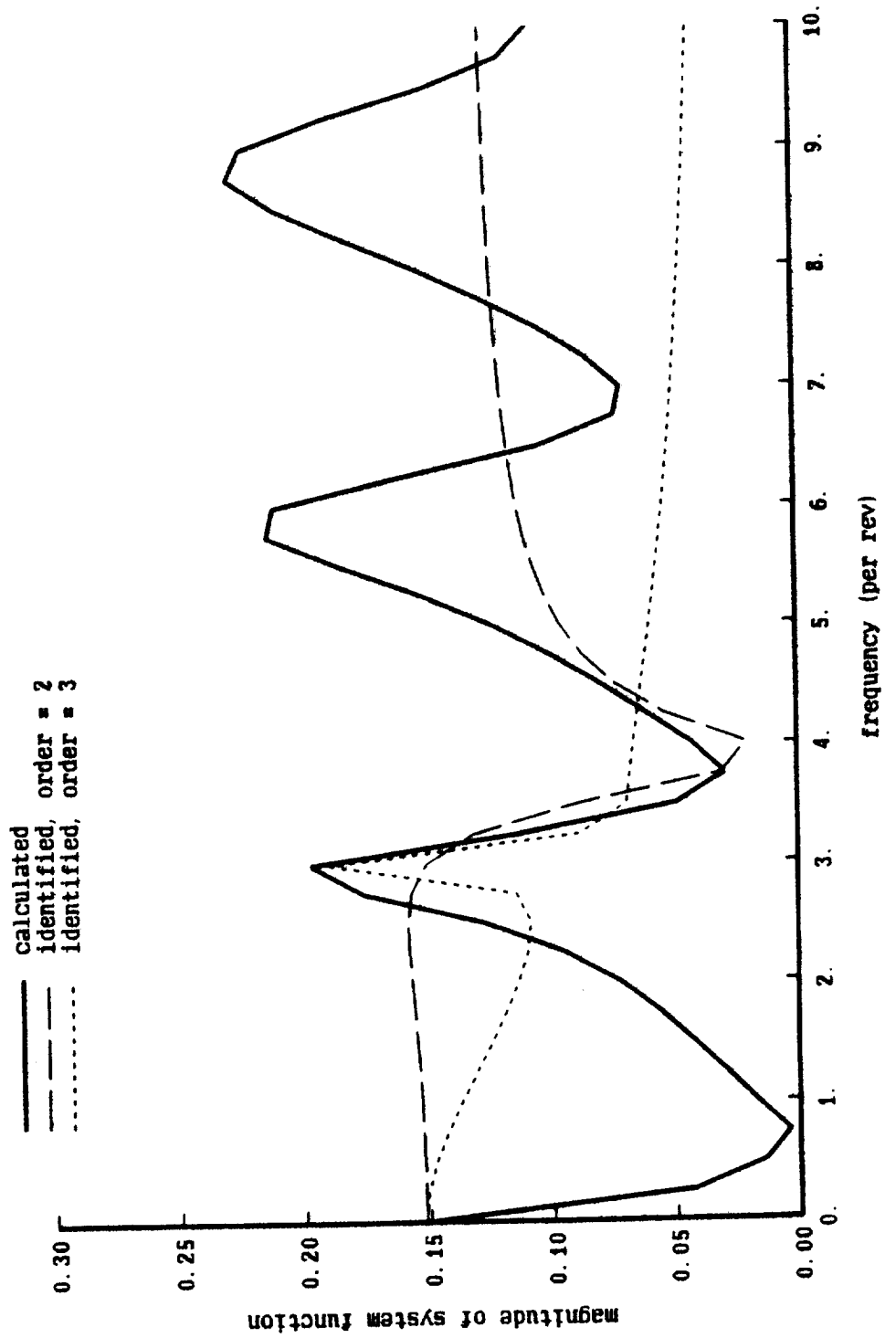


Figure 18d. Influence of frequency range on identification

nonrotating frame, 3 blades; uniform inflow, circulation at 0.77R

identification frequency range = 4.5/rev

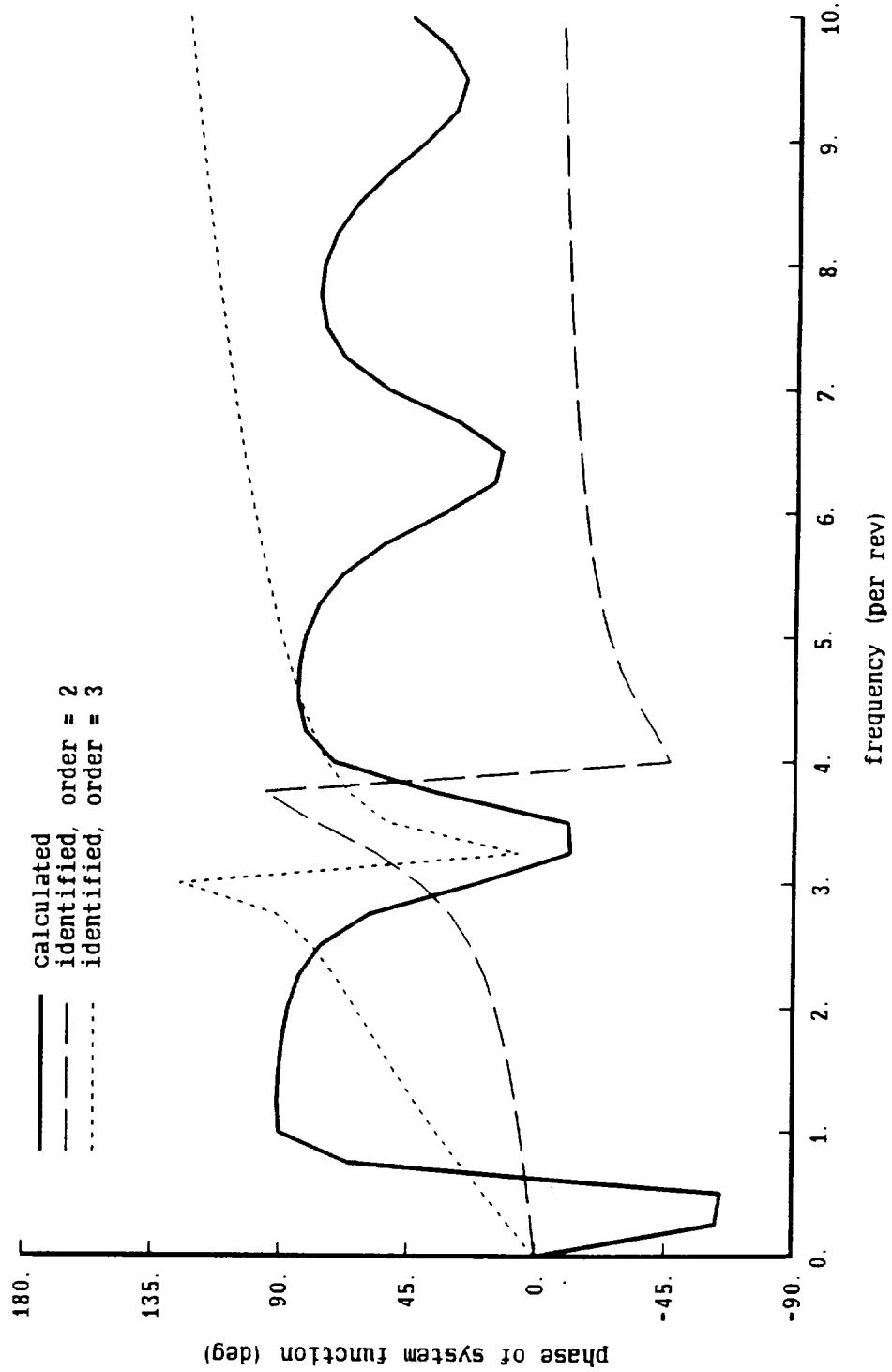


Figure 18e. Influence of frequency range on identification

nonrotating frame, 3 blades; uniform inflow, circulation at 0.77R

identification frequency range = 4.5/rev

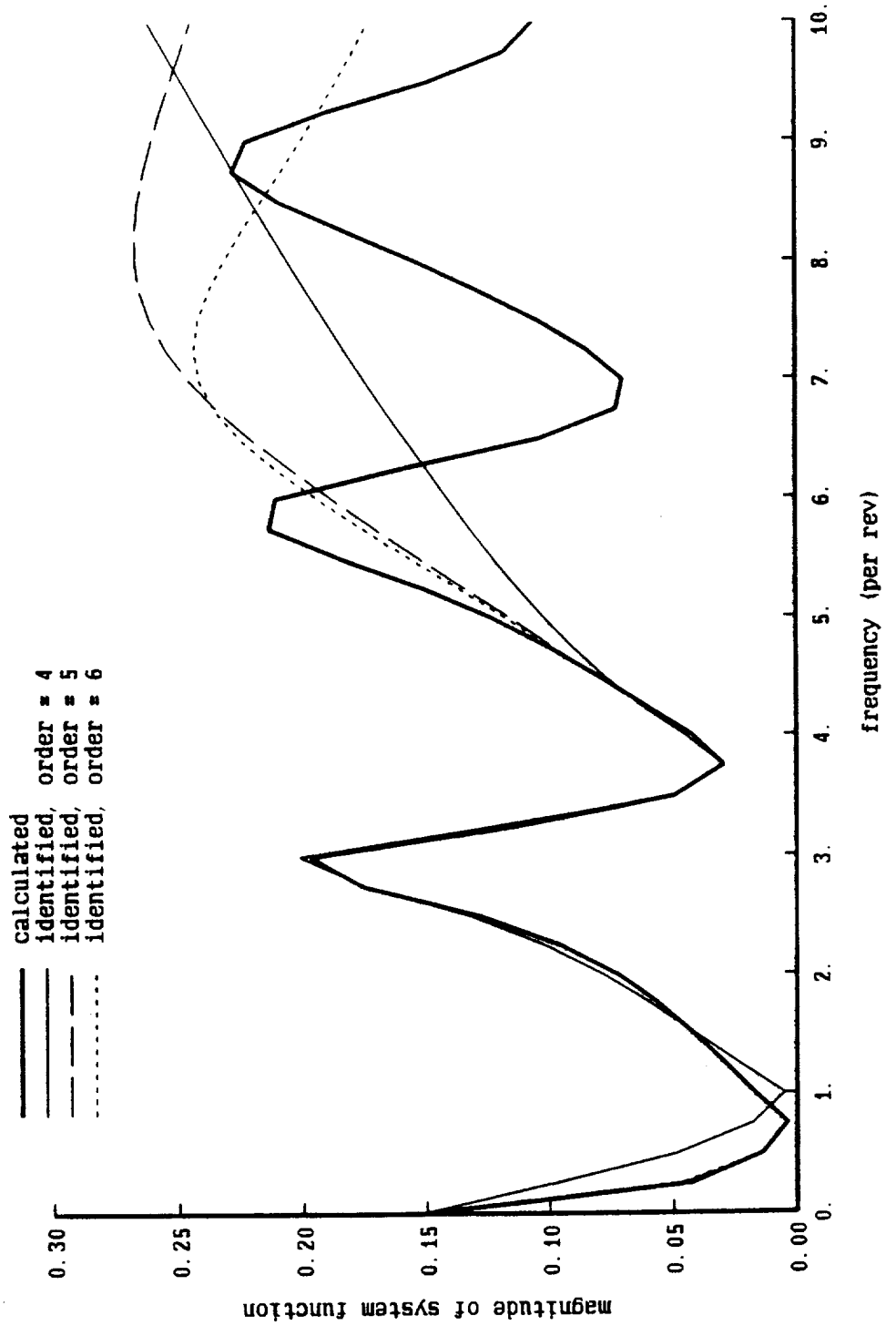


Figure 18f. Influence of frequency range on identification

nonrotating frame, 3 blades; uniform inflow, circulation at 0.77R

identification frequency range = 4.5/rev

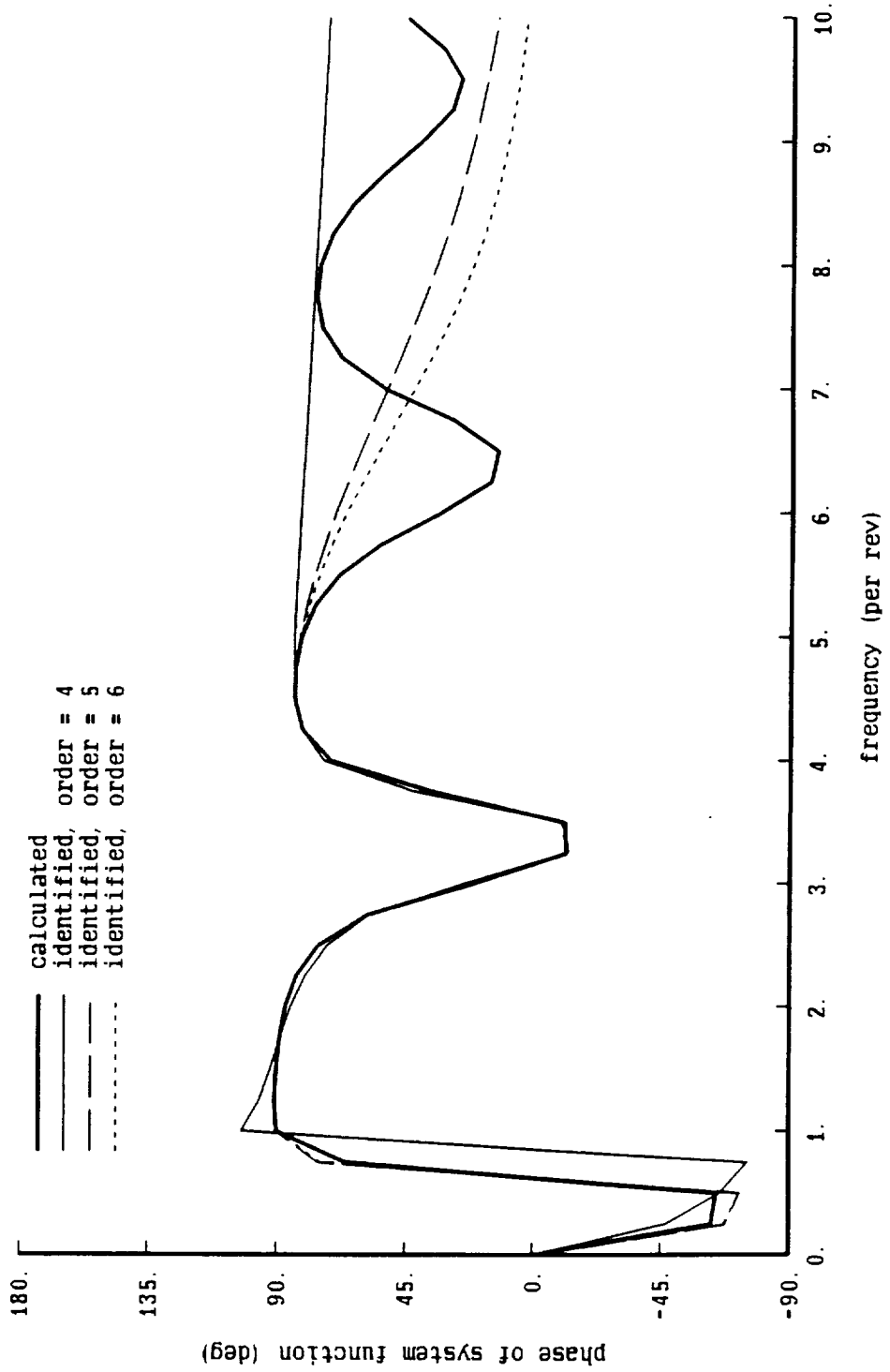


Figure 18g. Influence of frequency range on identification

nonrotating frame, 3 blades; uniform inflow, circulation at 0.77R

identification frequency range = 7.5/rev

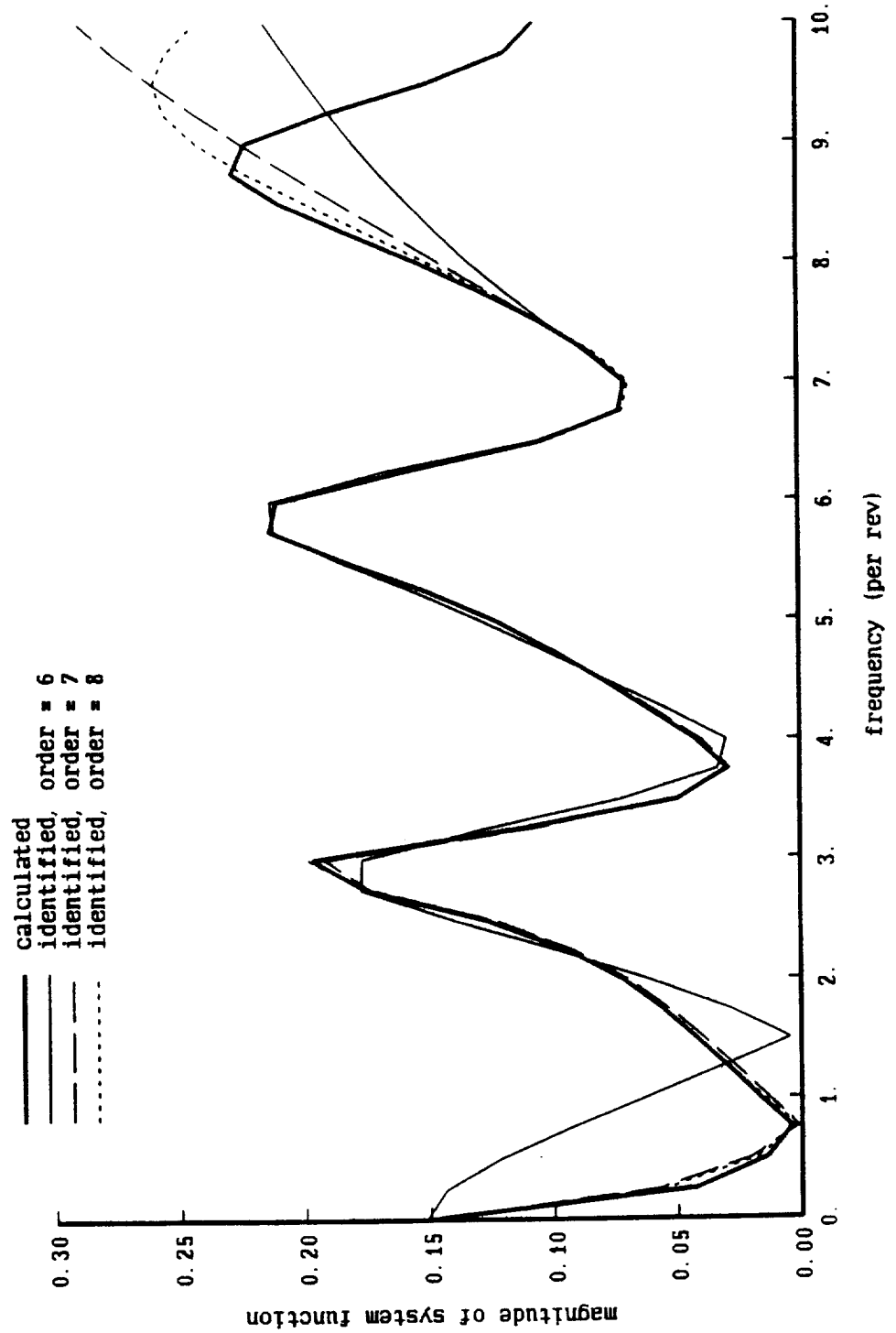


Figure 18h. Influence of frequency range on identification

nonrotating frame, 3 blades; uniform inflow, circulation at 0.77R

identification frequency range = 7.5/rev

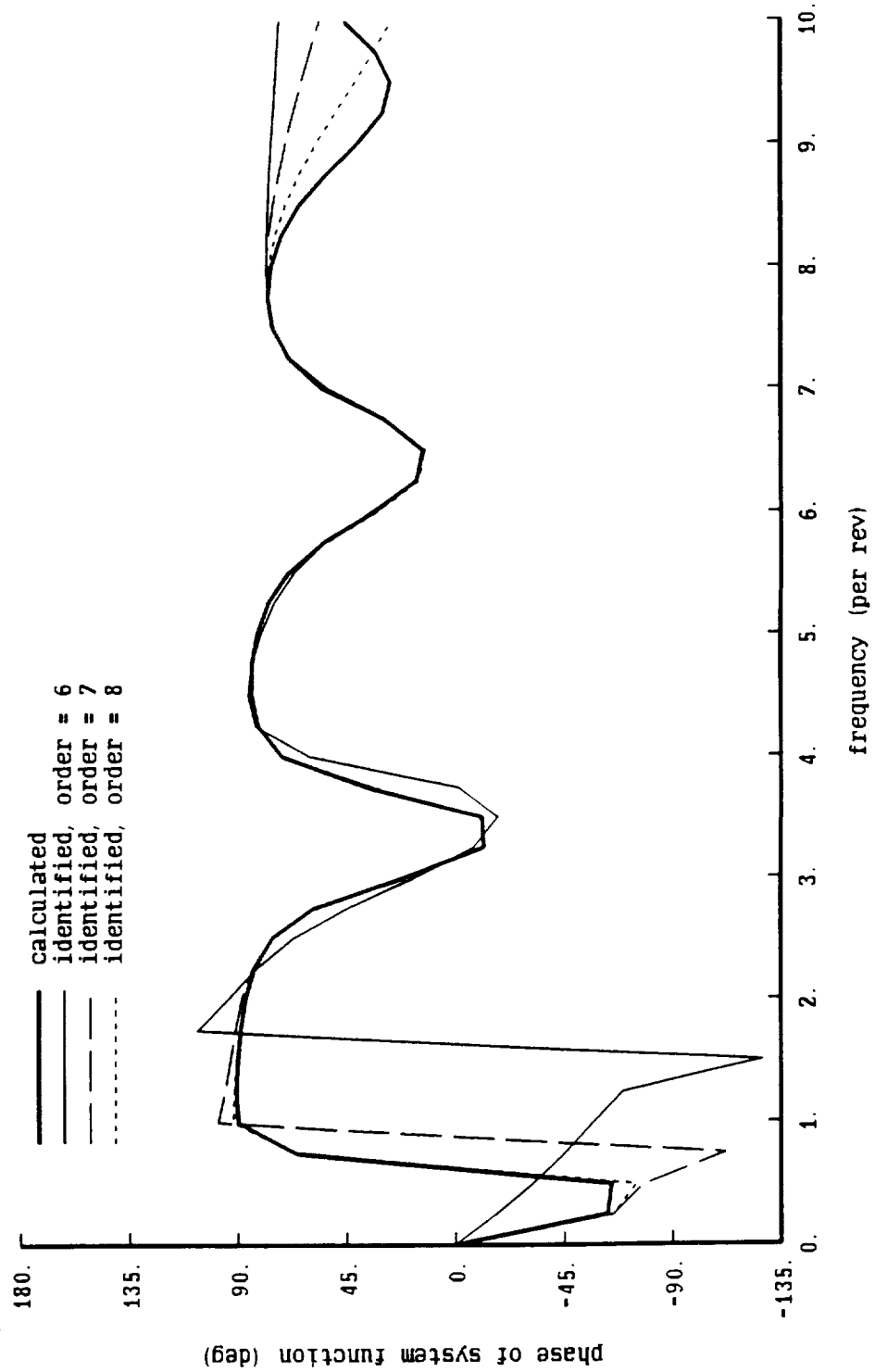


Figure 19a. Influence of frequency range on identification

nonrotating frame, 3 blades; uniform inflow, circulation at 0.77R

identification for all radial stations; frequency range = 2/rev

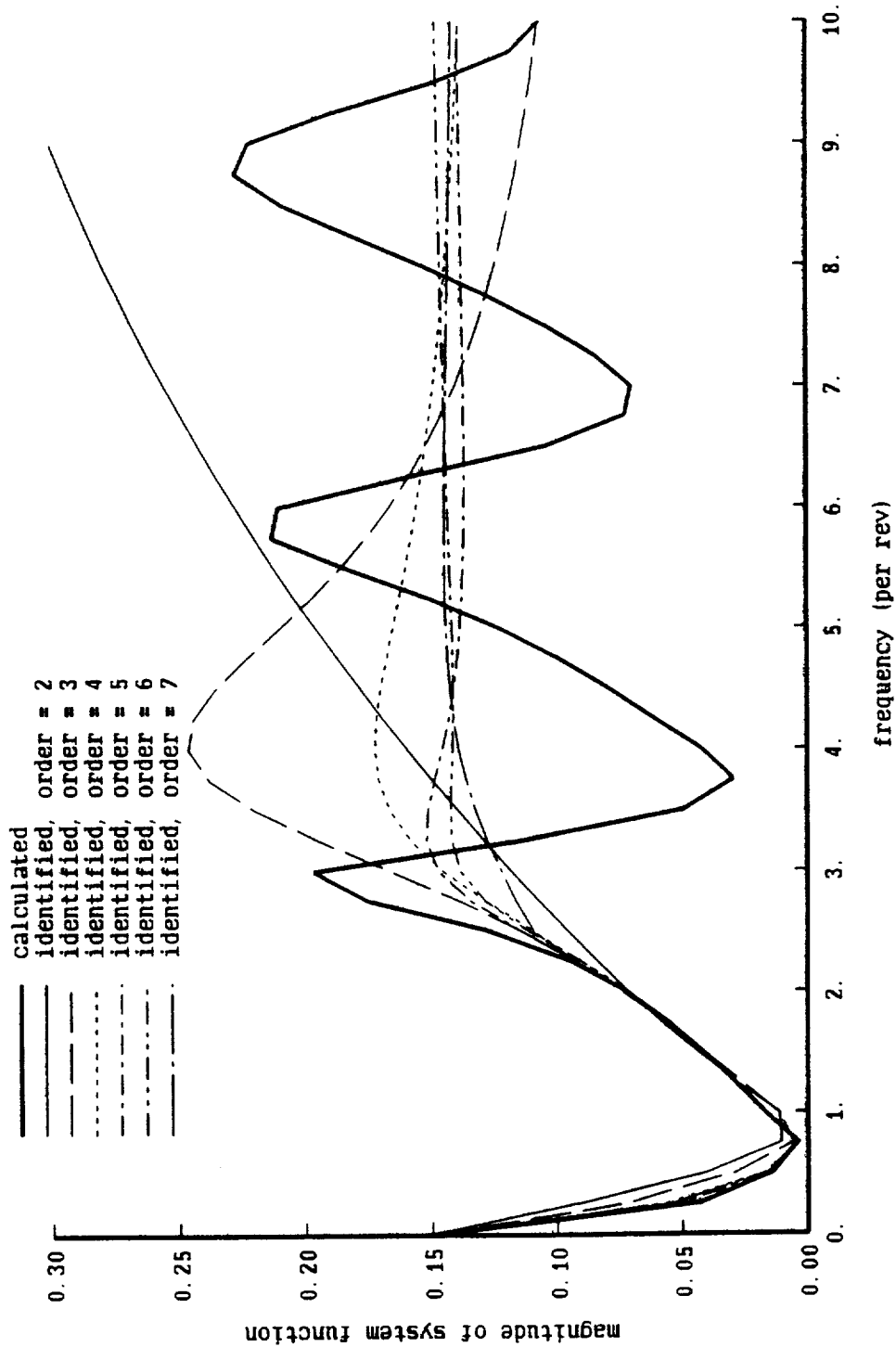


Figure 19b. Influence of frequency range on identification

nonrotating frame, 3 blades; uniform inflow, circulation at 0.77R
 identification for all radial stations; frequency range = 2/rev

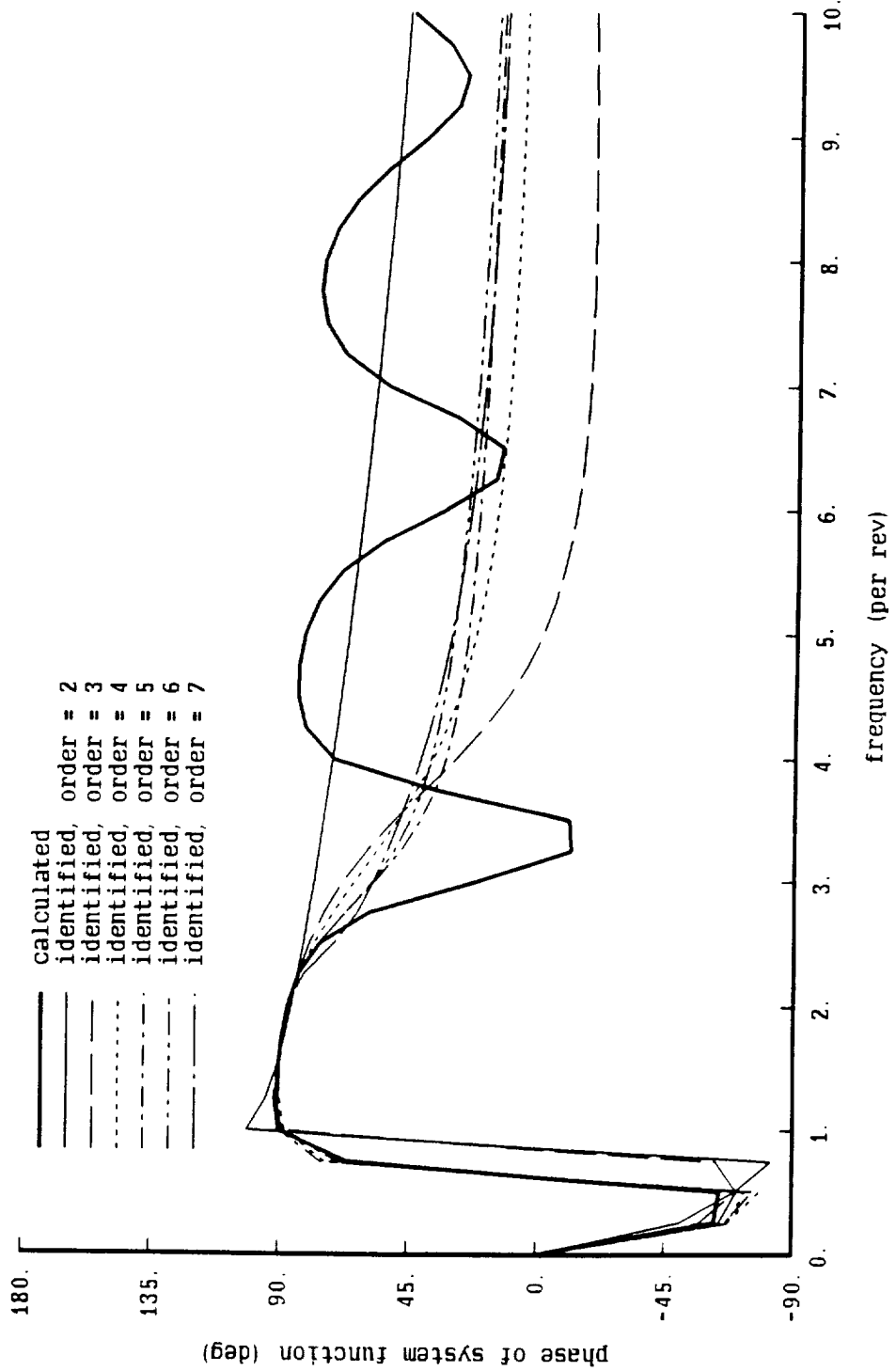


Figure 19c. Influence of frequency range on identification

nonrotating frame, 3 blades; uniform inflow, circulation at 0.77R
 identification for all radial stations; frequency range = 4.5/rev

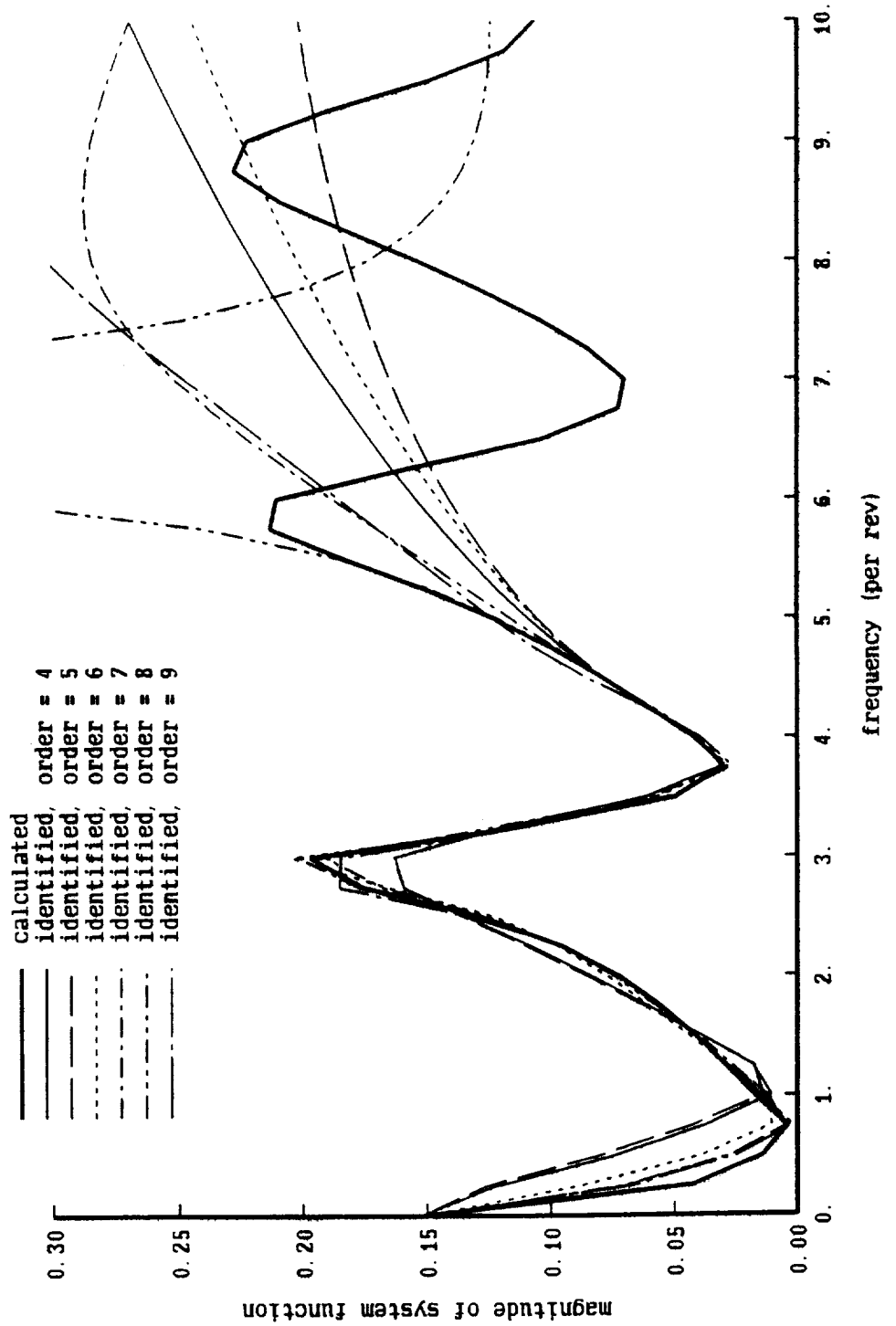


Figure 19d. Influence of frequency range on identification

nonrotating frame, 3 blades; uniform inflow, circulation at 0.77R
 identification for all radial stations; frequency range = 4.5/rev

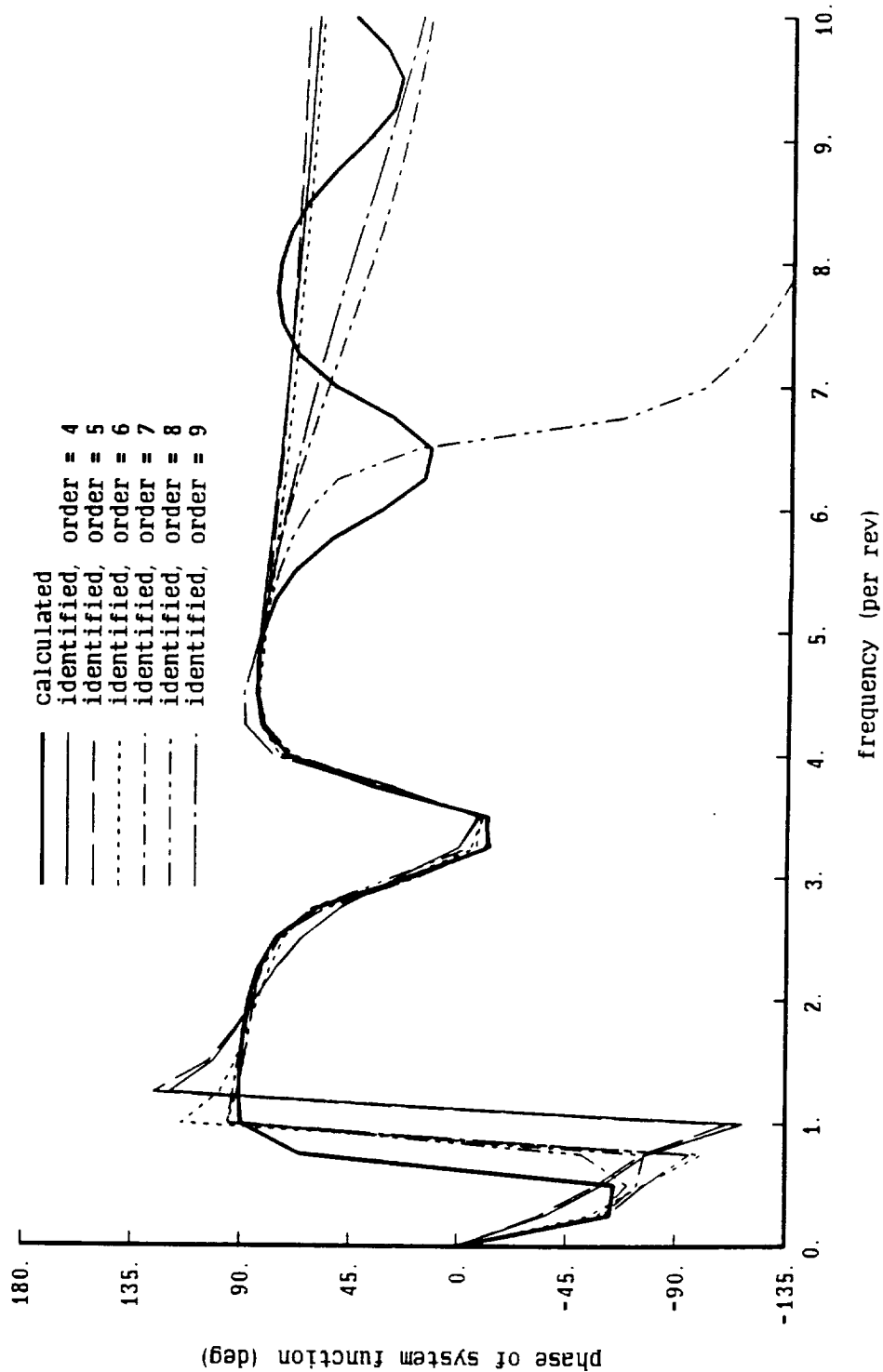


Figure 19e. Influence of frequency range on identification

nonrotating frame, 3 blades; uniform inflow, circulation at 0.77R

identification for all radial stations; frequency range = 7.5/rev

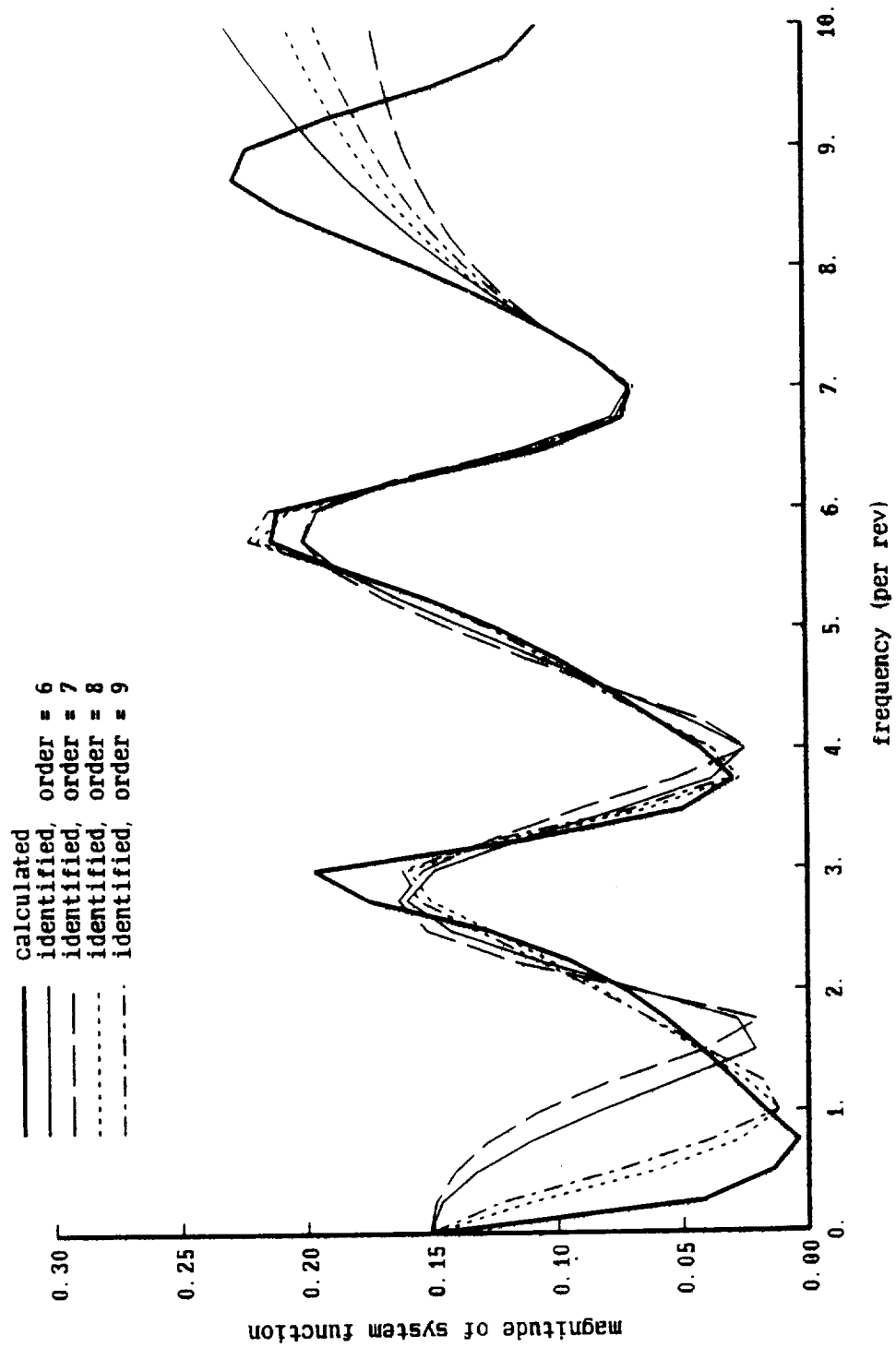


Figure 19f. Influence of frequency range on identification

nonrotating frame, 3 blades; uniform inflow, circulation at 0.77R
identification for all radial stations; frequency range = 7.5/rev

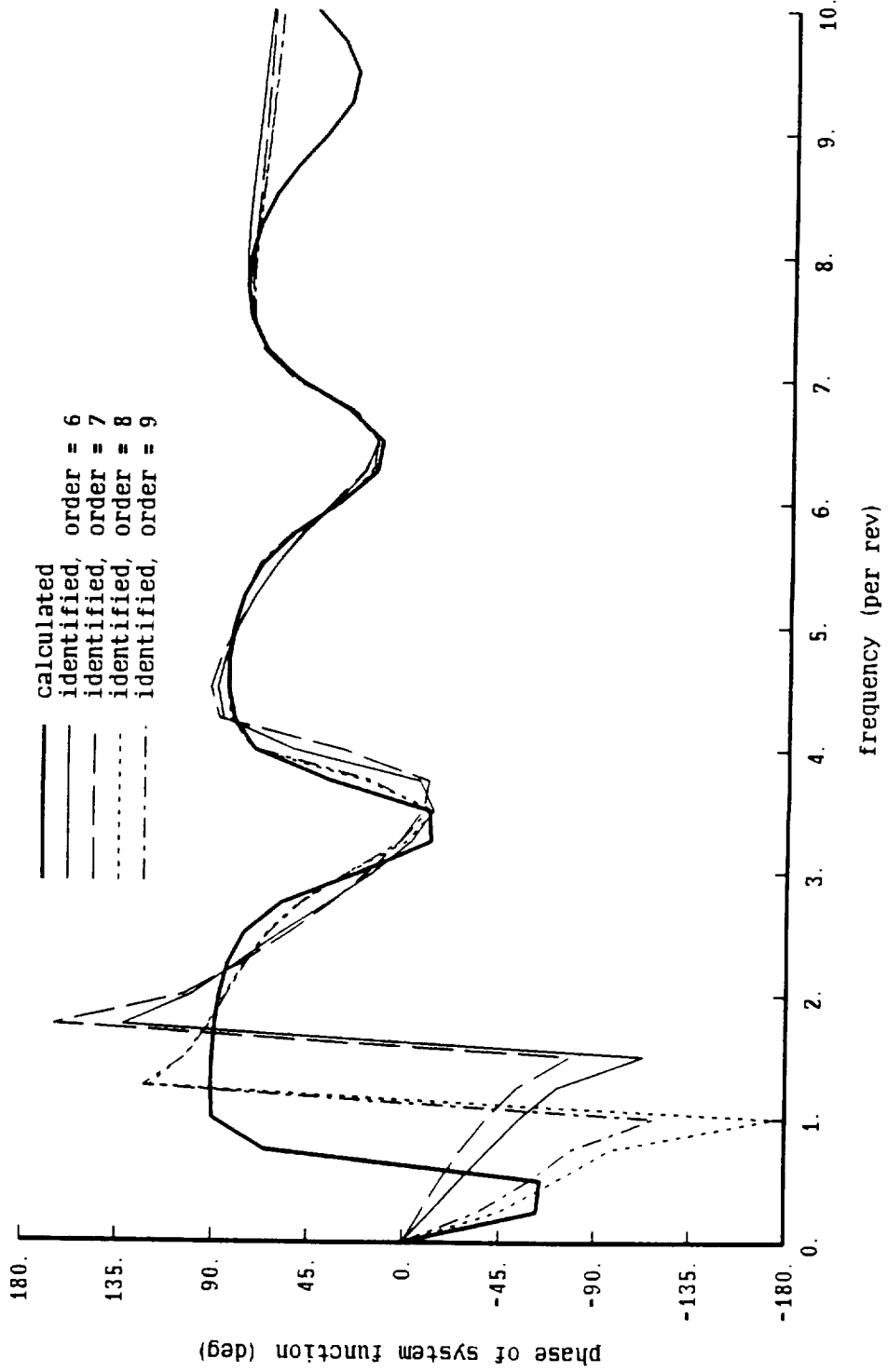


Figure 20a. Influence of of order and weight on identification

nonrotating frame, 3 blades; uniform inflow, circulation at 0.77R

ident for all radial stations; freq range = 0-1.5 (wt=4), 1.5-4.5 (wt=1)

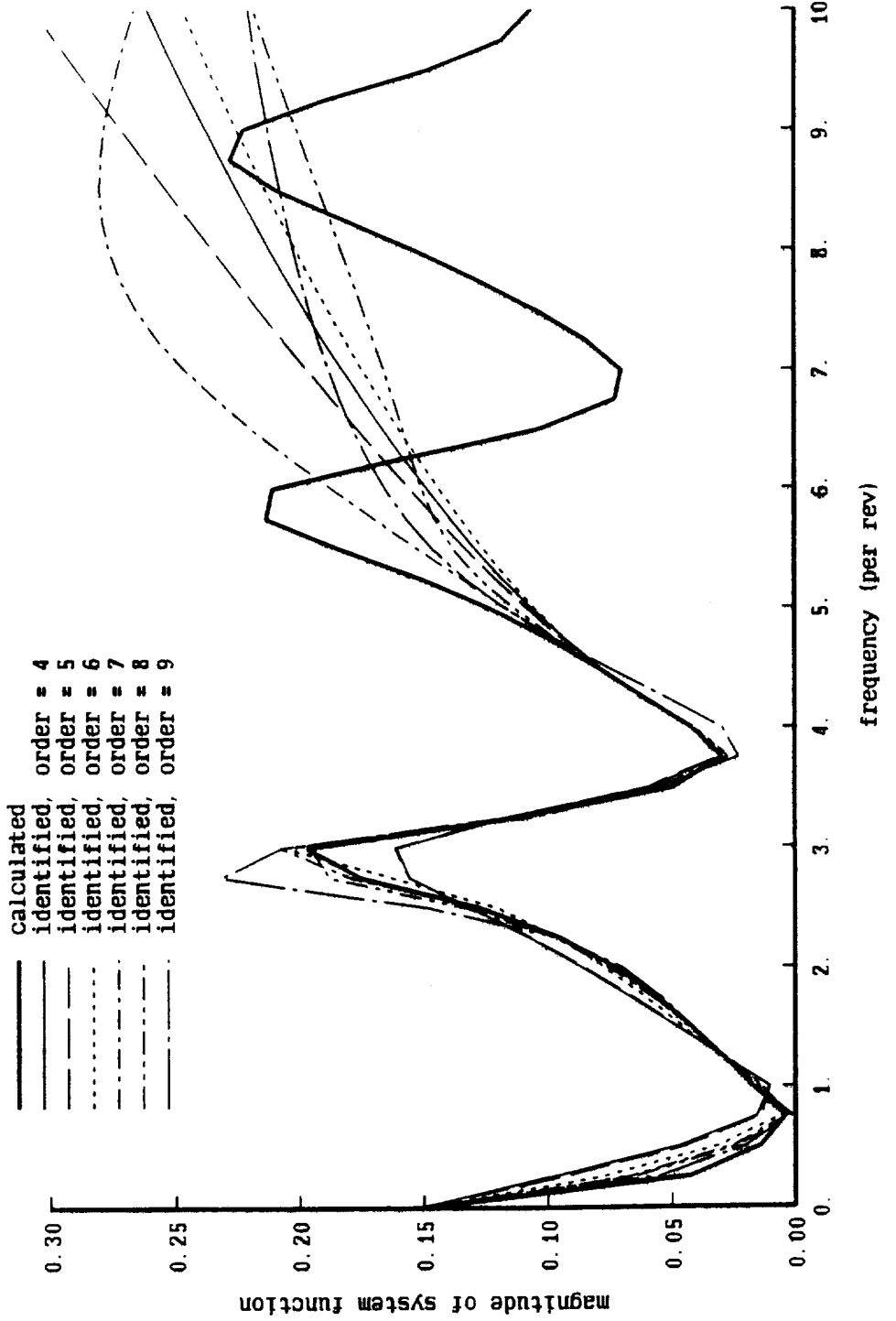


Figure 20b. Influence of of order and weight on identification

nonrotating frame, 3 blades; uniform inflow, circulation at 0.77R

ident for all radial stations; freq range = 0-10 (wt=4), 1.5-4.5 (wt=1)

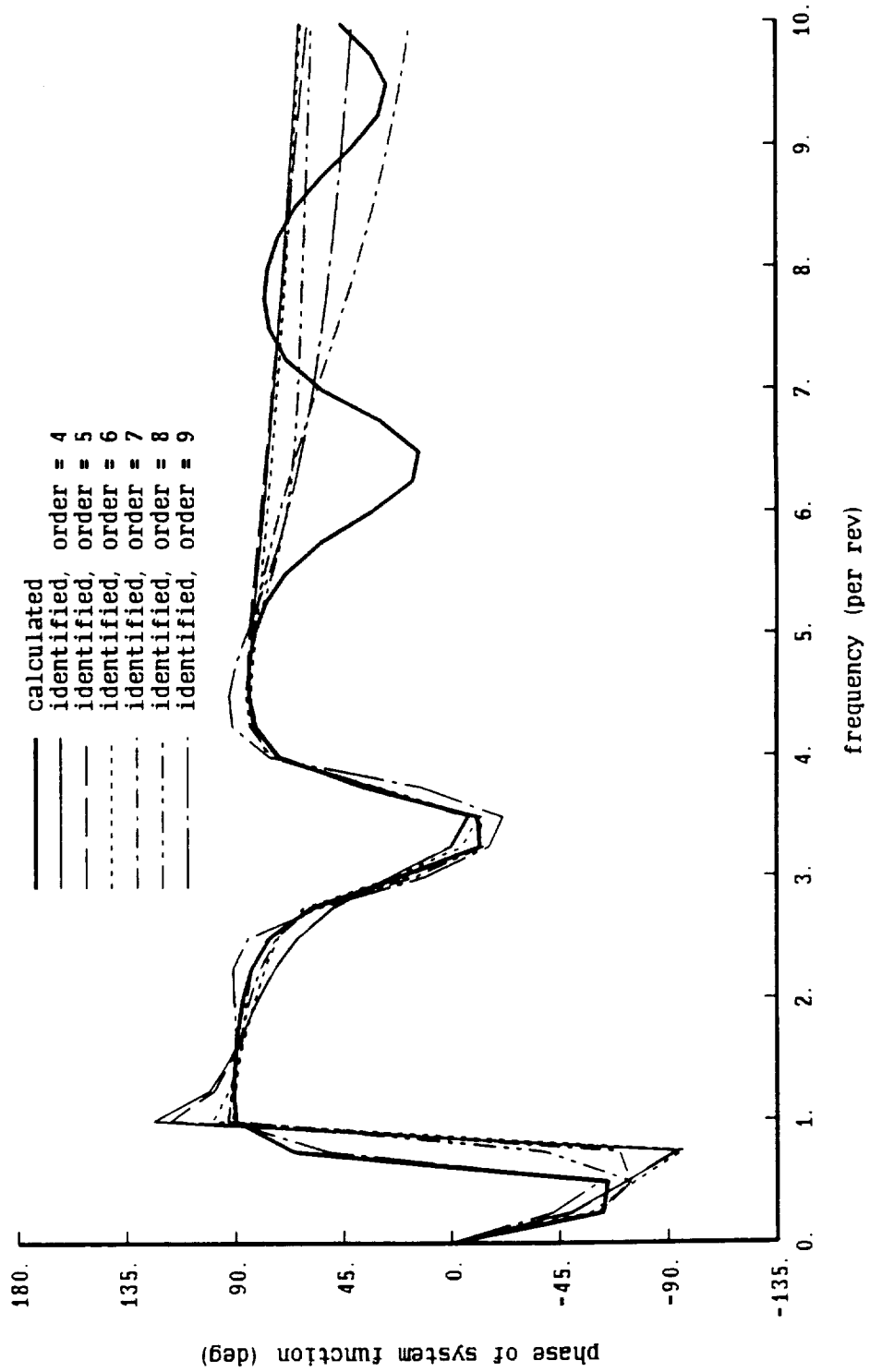


Figure 20c. Influence of of order and weight on identification

nonrotating frame, 3 blades; uniform inflow, circulation at 0.77R
 ident for all radial stations; freq range = 0-1.5 (wt=16), 1.5-4.5 (wt=1)

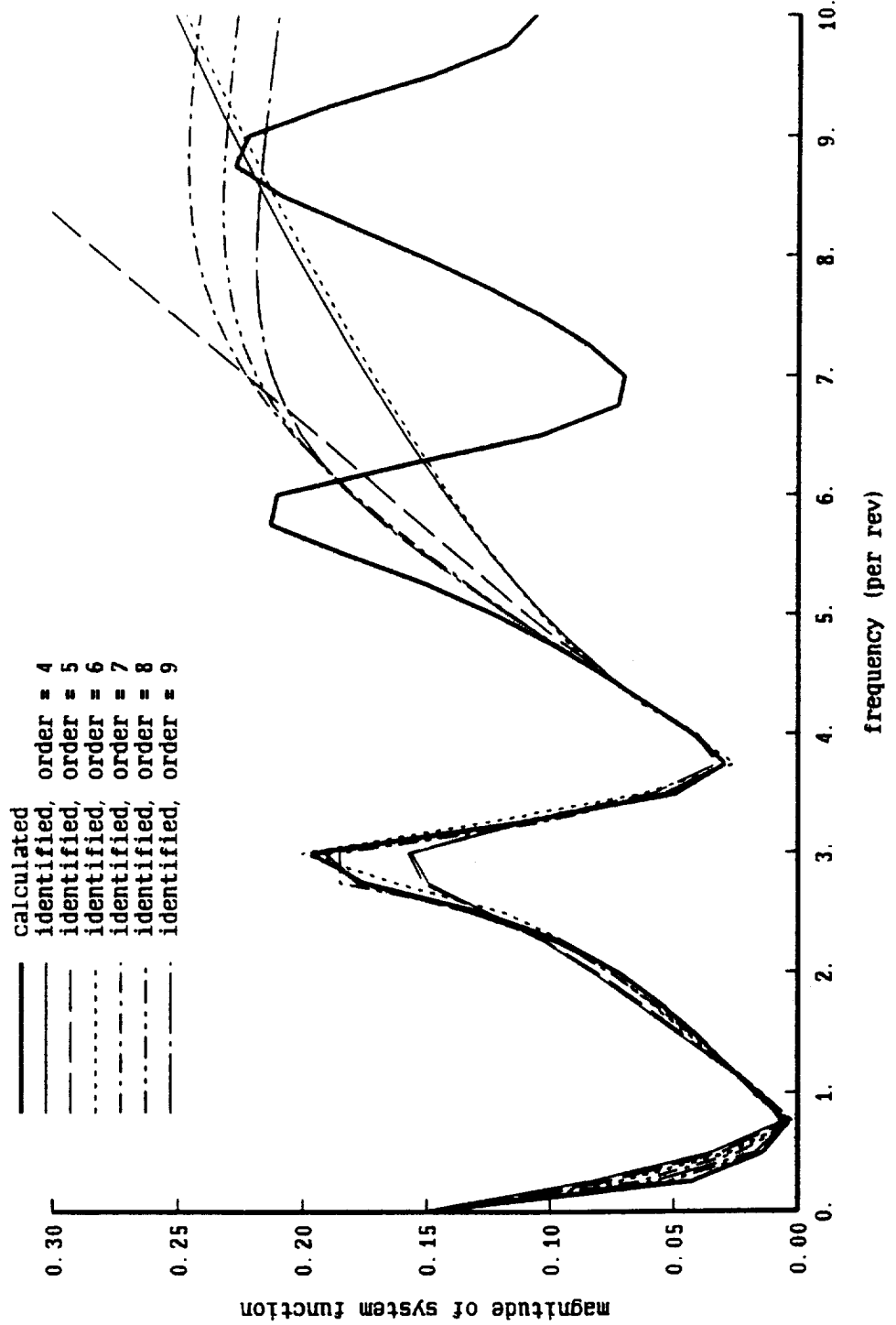


Figure 20d. Influence of of order and weight on identification

nonrotating frame, 3 blades; uniform inflow, circulation at 0.77R
 ident for all radial stations; freq range = 0-1.5 (wt=16), 1.5-4.5 (wt=1)

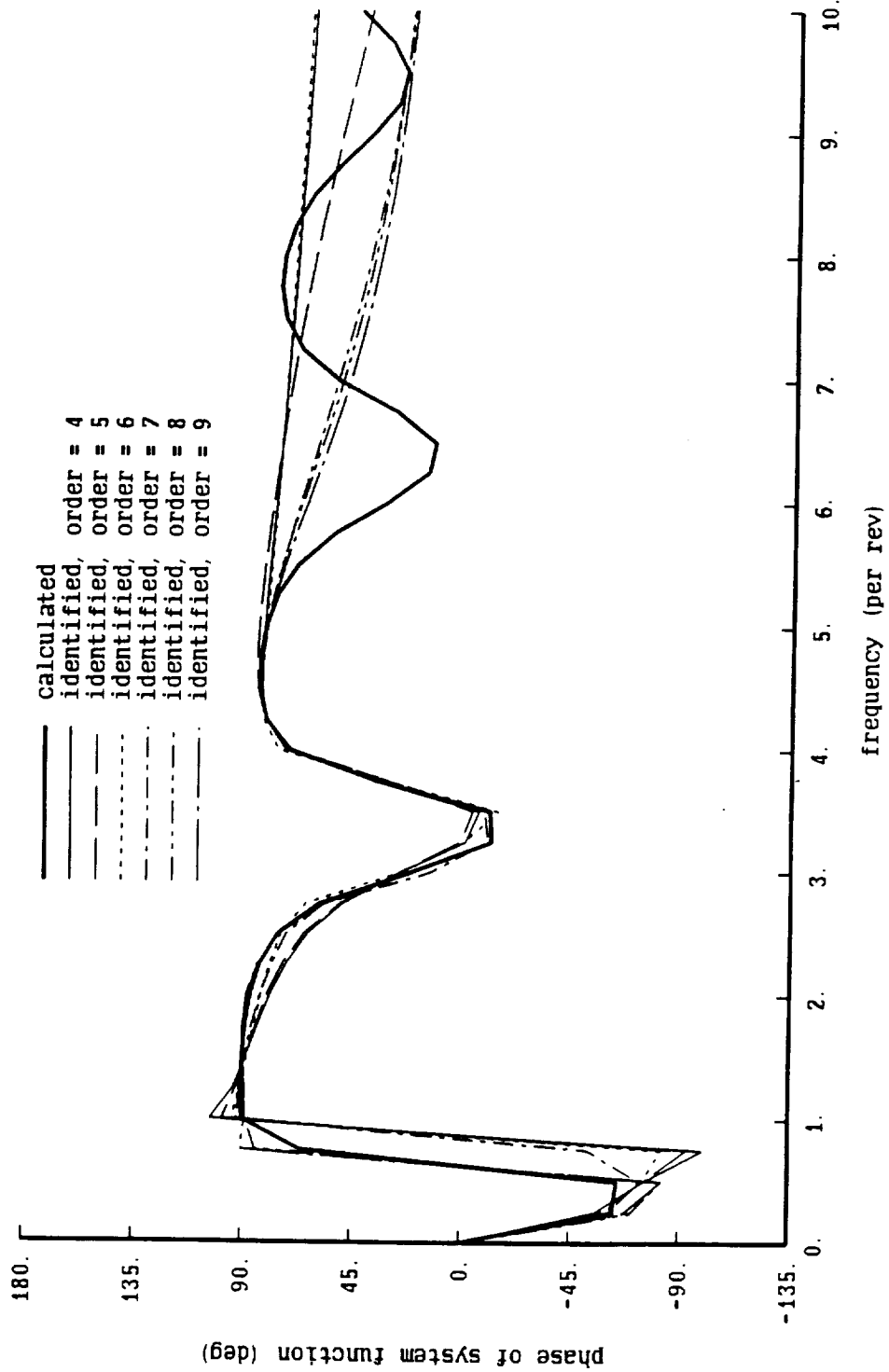


Figure 21a. System function of hovering rotor with undistorted wake

nonrotating frame, 3 blades; uniform inflow, collective, total H

- circulation at 0.77 R; first inflow mode
- - - circulation at 0.77 R; second inflow mode
- circulation at 0.77 R; third inflow mode

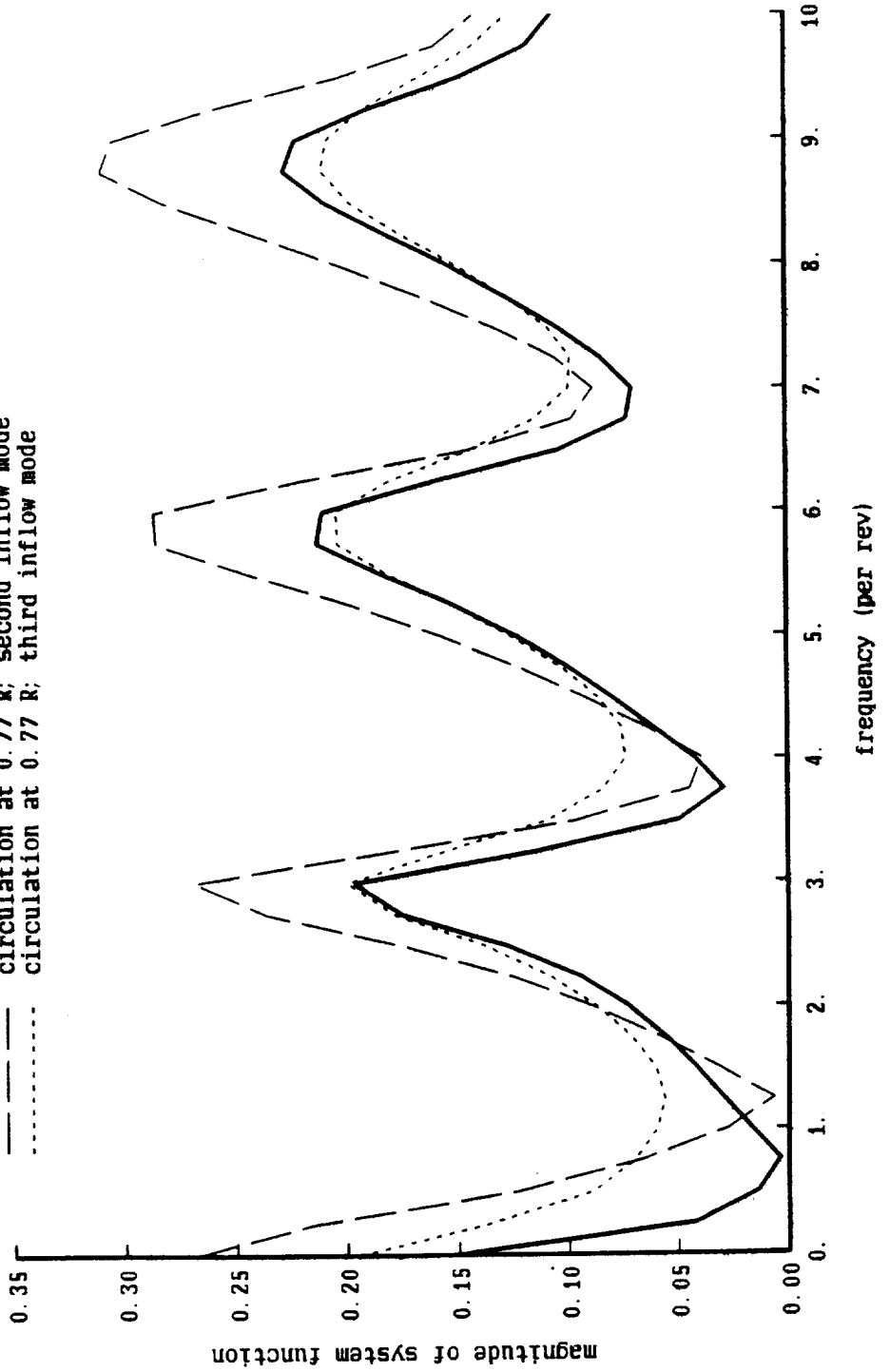


Figure 21b. System function of hovering rotor with undistorted wake

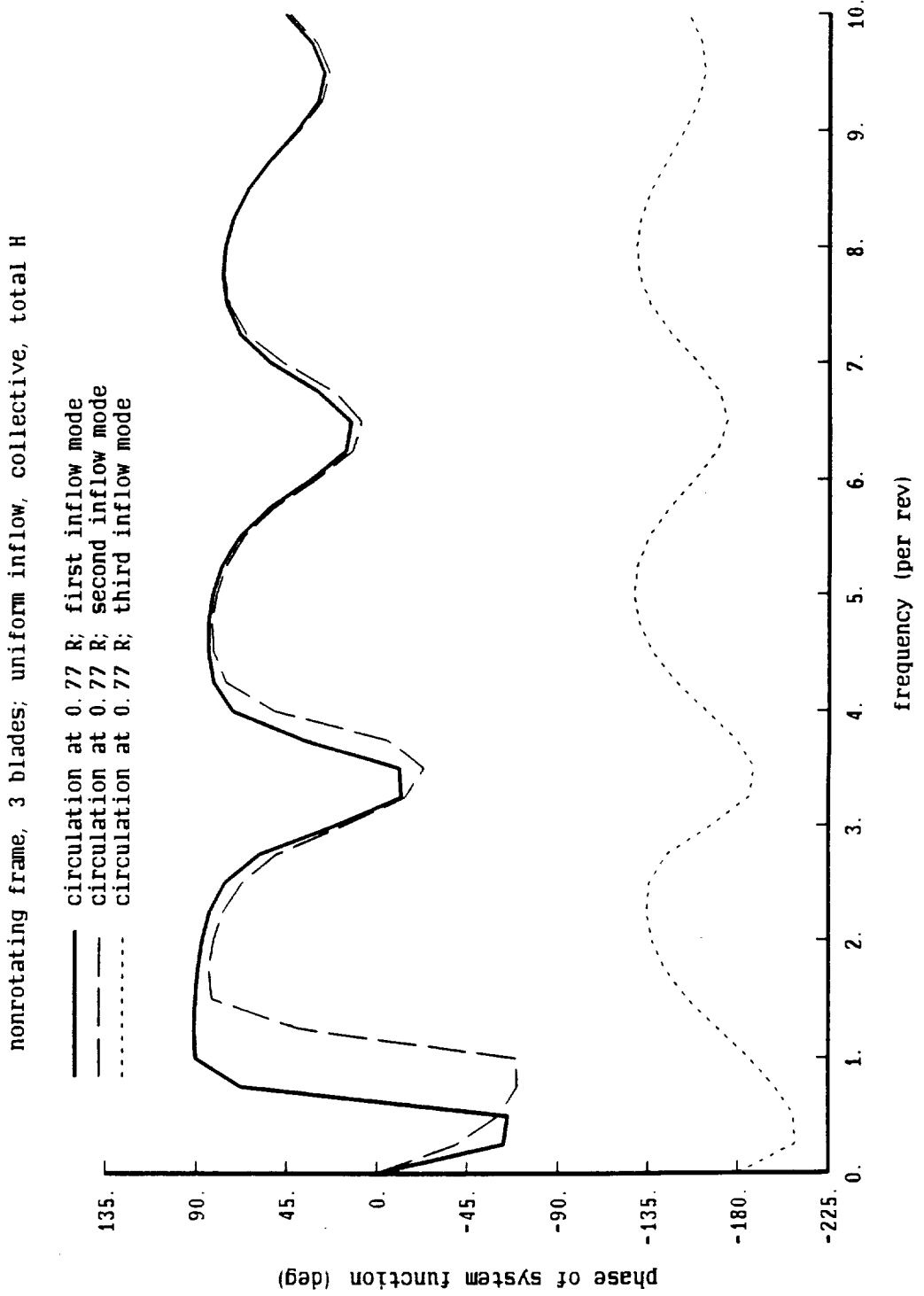


Figure 22a. Influence of of order and weight on identification

nonrotating frame, 3 blades; uniform inflow, circulation at 0.77R
 ident for all radial stations, three inflow modes; frequency range = 4.5/rev

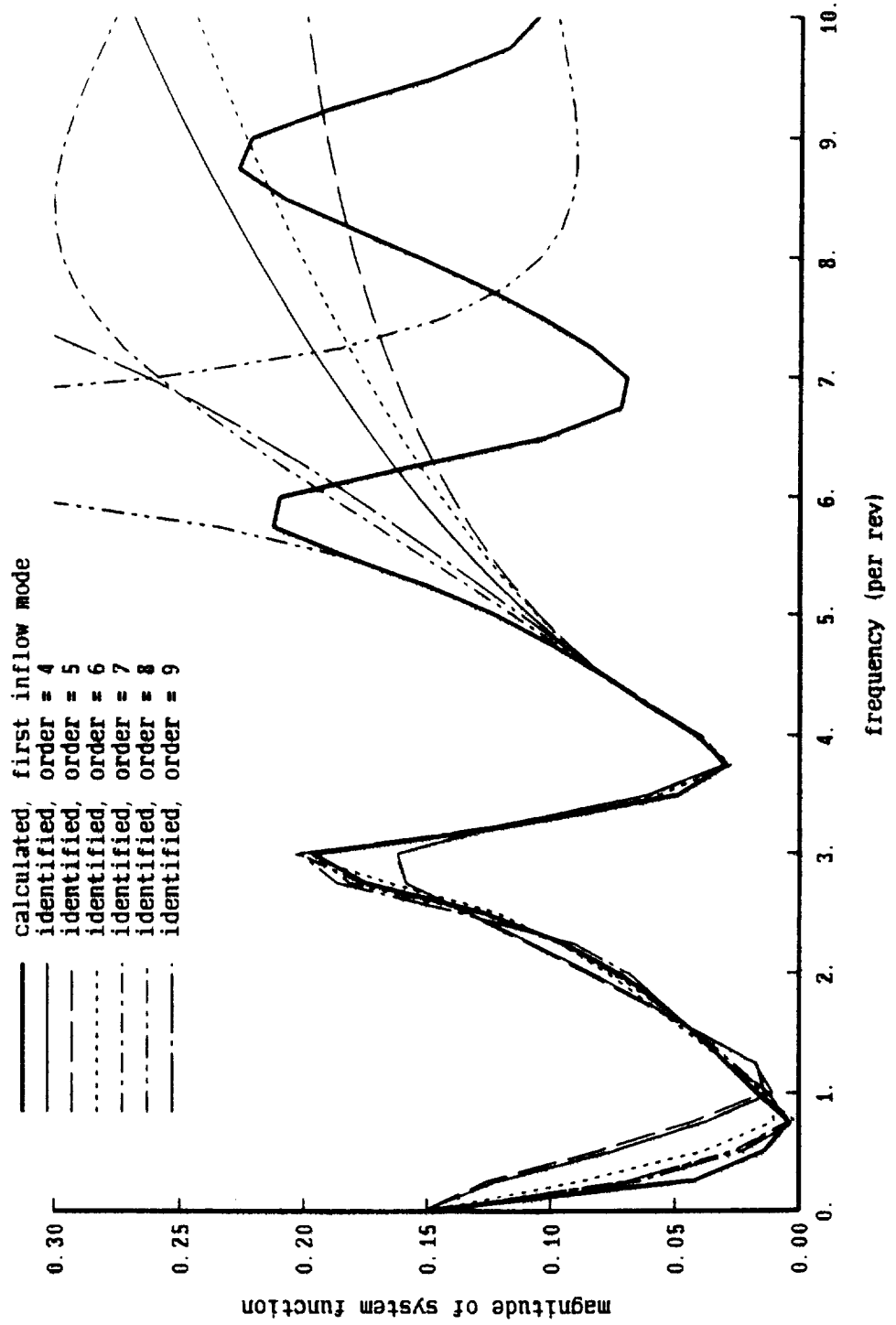


Figure 22b. Influence of of order and weight on identification

nonrotating frame, 3 blades; uniform inflow, circulation at 0.77R

ident for all radial stations, three inflow modes; frequency range = 4.5/rev

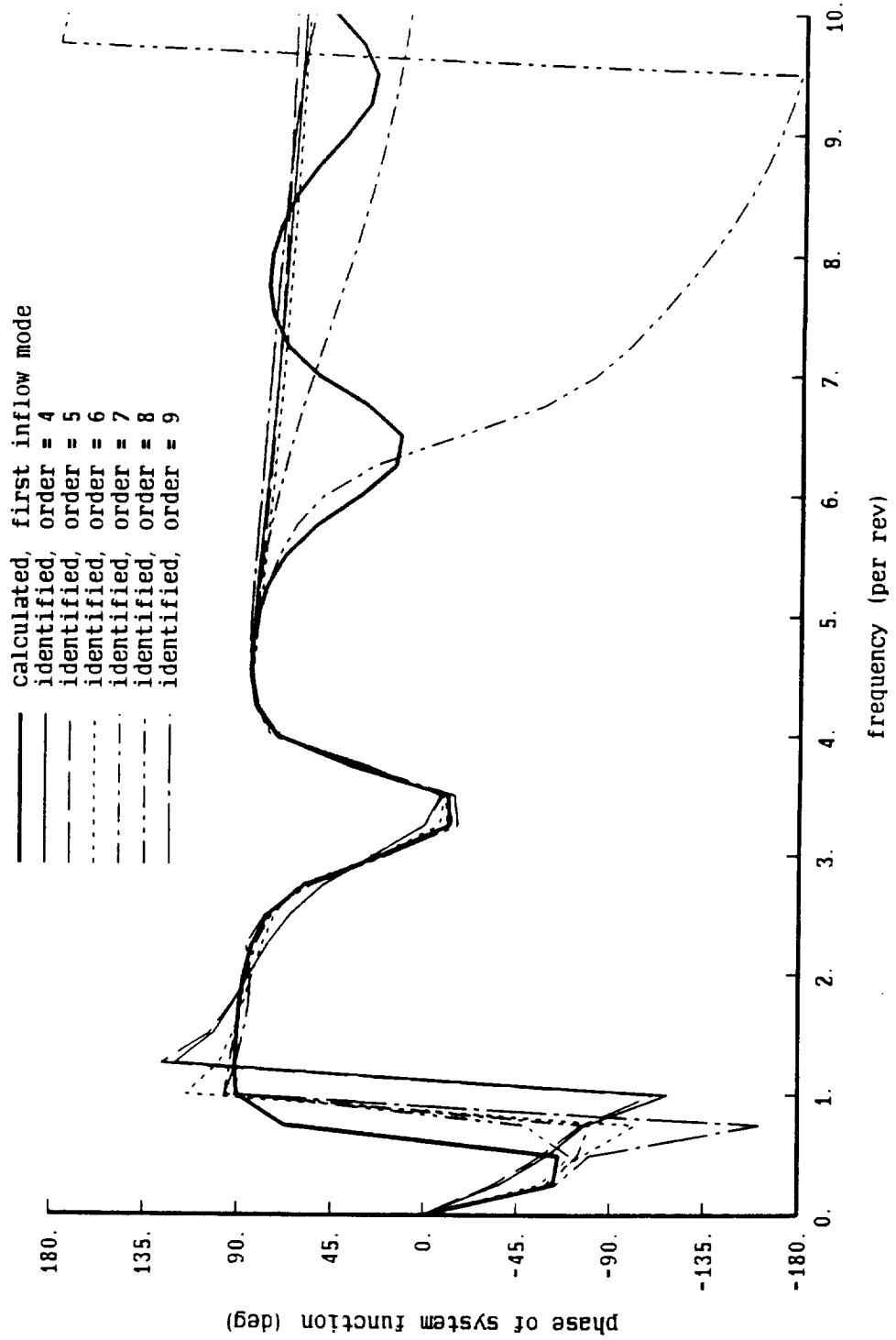


Figure 22c. Influence of of order and weight on identification

nonrotating frame, 3 blades; uniform inflow, circulation at 0.77R

ident for all radial stations, three inflow modes; frequency range = 4.5/rev

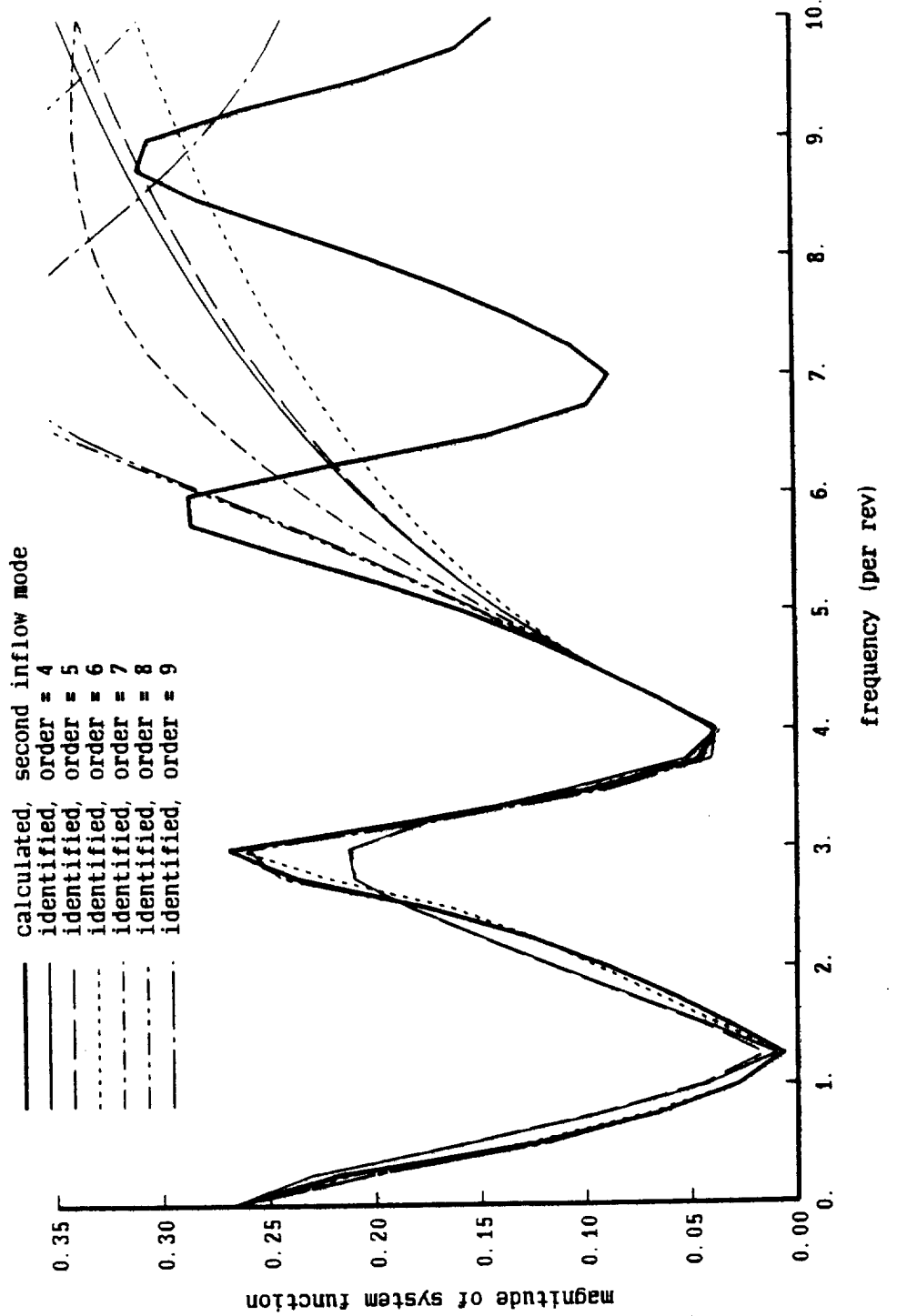


Figure 22d. Influence of of order and weight on identification

nonrotating frame, 3 blades; uniform inflow, circulation at 0.77R

ident for all radial stations, three inflow modes; frequency range = 4.5/rev

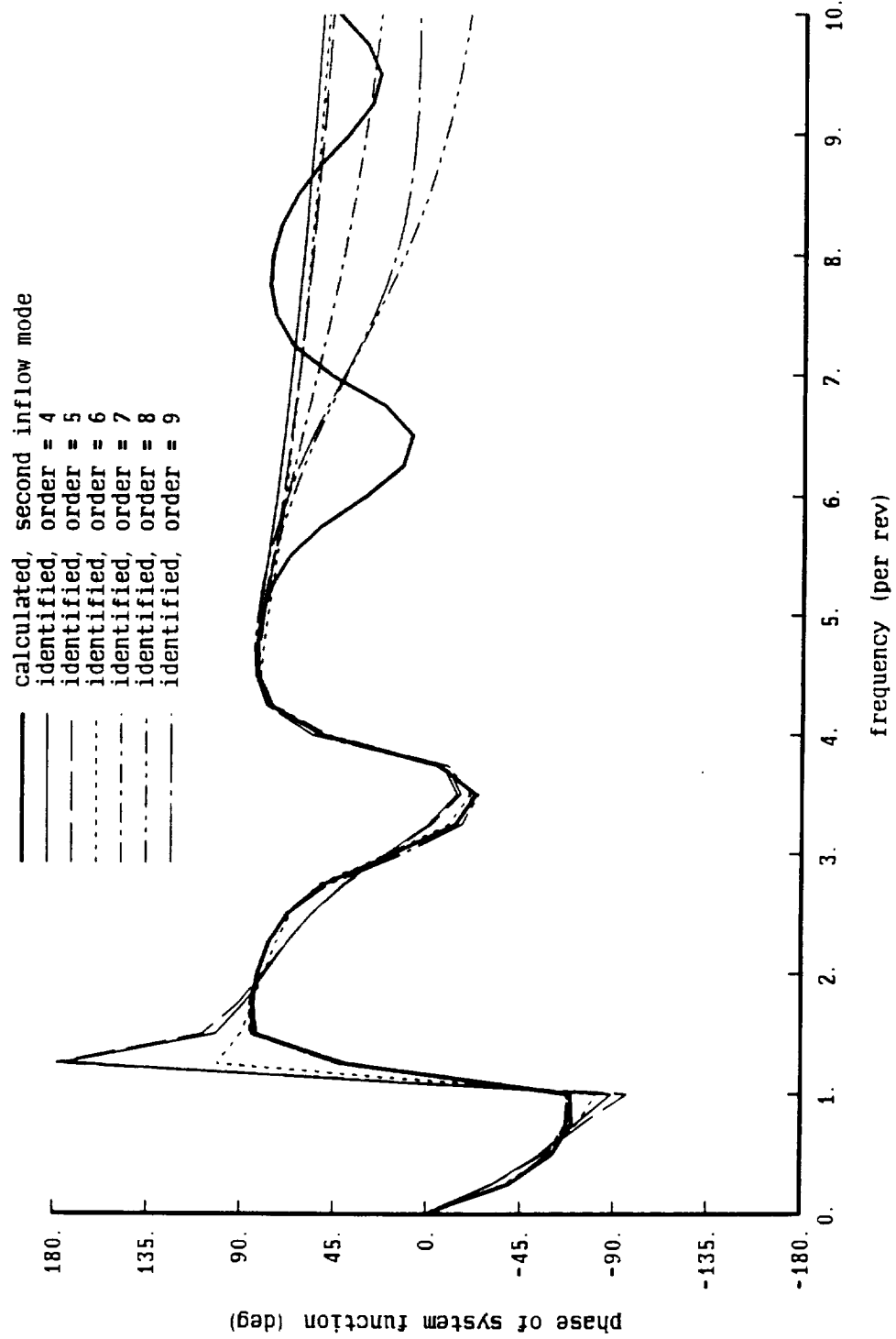


Figure 22e. Influence of of order and weight on identification

nonrotating frame, 3 blades; uniform inflow, circulation at 0.77R

ident for all radial stations, three inflow modes; frequency range = 4.5/rev

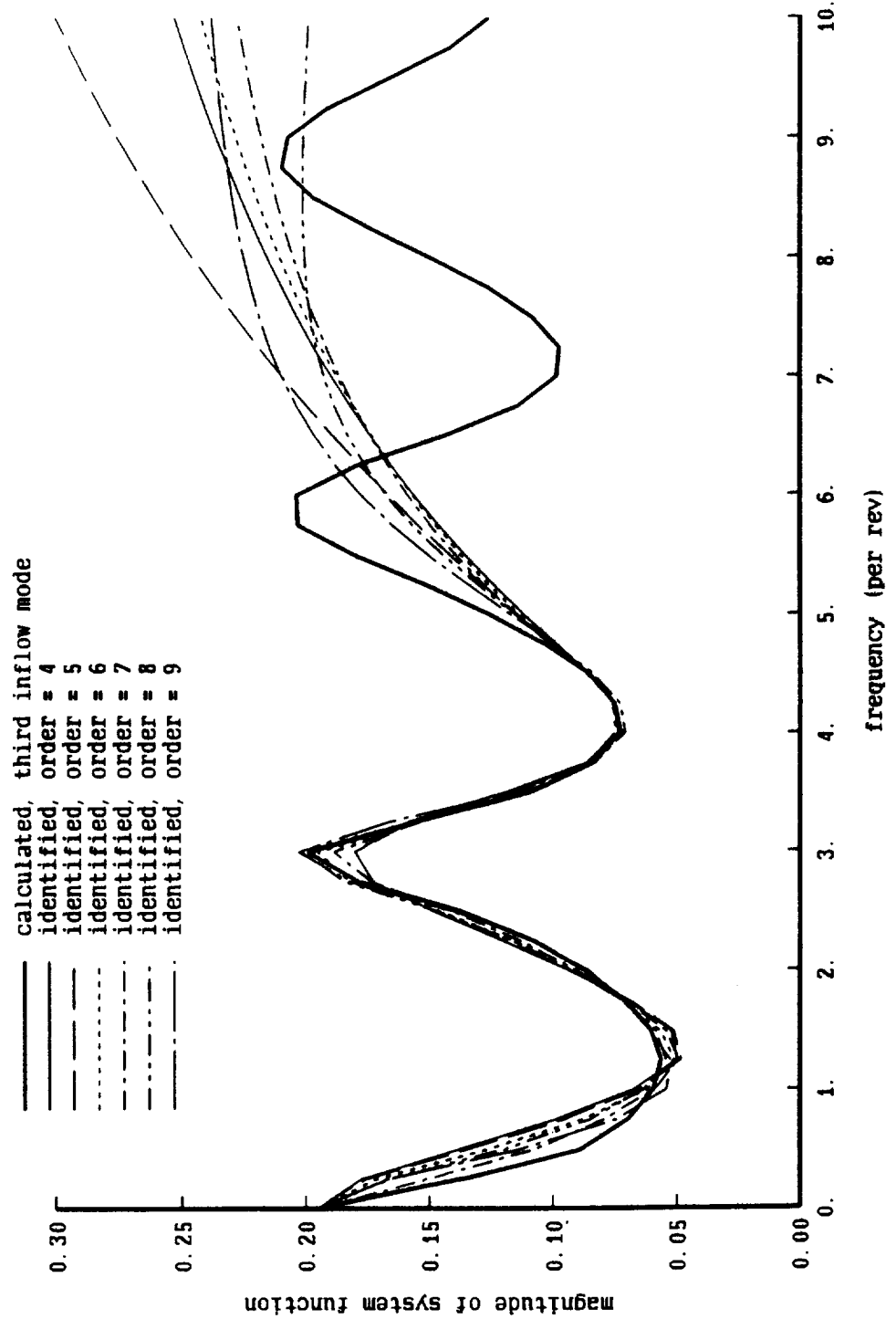


Figure 22f. Influence of order and weight on identification

nonrotating frame, 3 blades; uniform inflow, circulation at 0.77R

ident for all radial stations, three inflow modes; frequency range = 4.5/rev

- calculated, third inflow mode
- identified, order = 4
- identified, order = 5
- identified, order = 6
- identified, order = 7
- identified, order = 8
- identified, order = 9

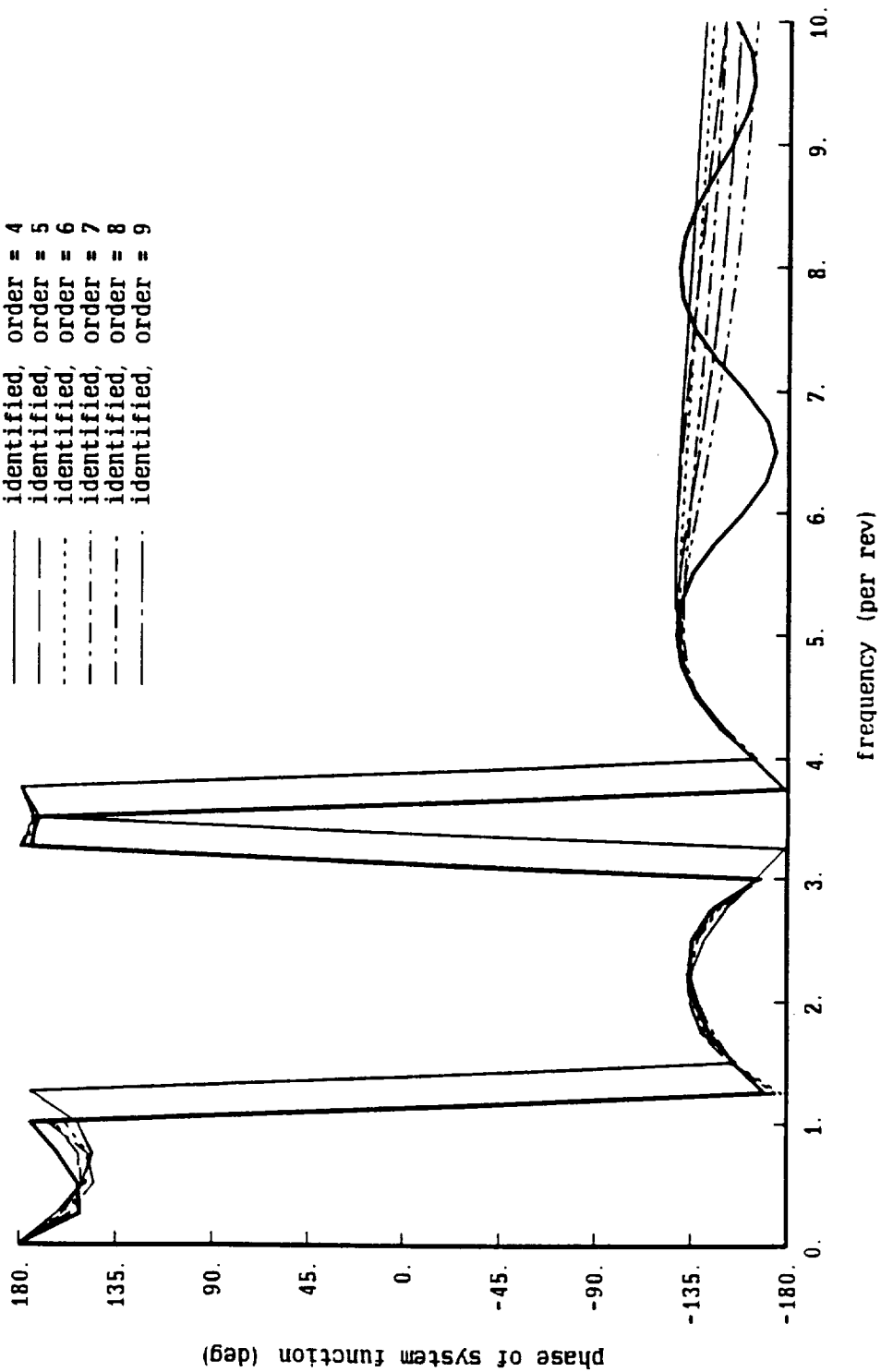


Figure 22g. Influence of of order and weight on identification

nonrotating frame, 3 blades; uniform inflow, circulation at 0.77R
 all radial stations, three inflow modes; freq = 1-1.5 (wt=16), 1.5-4.5 (wt=1)

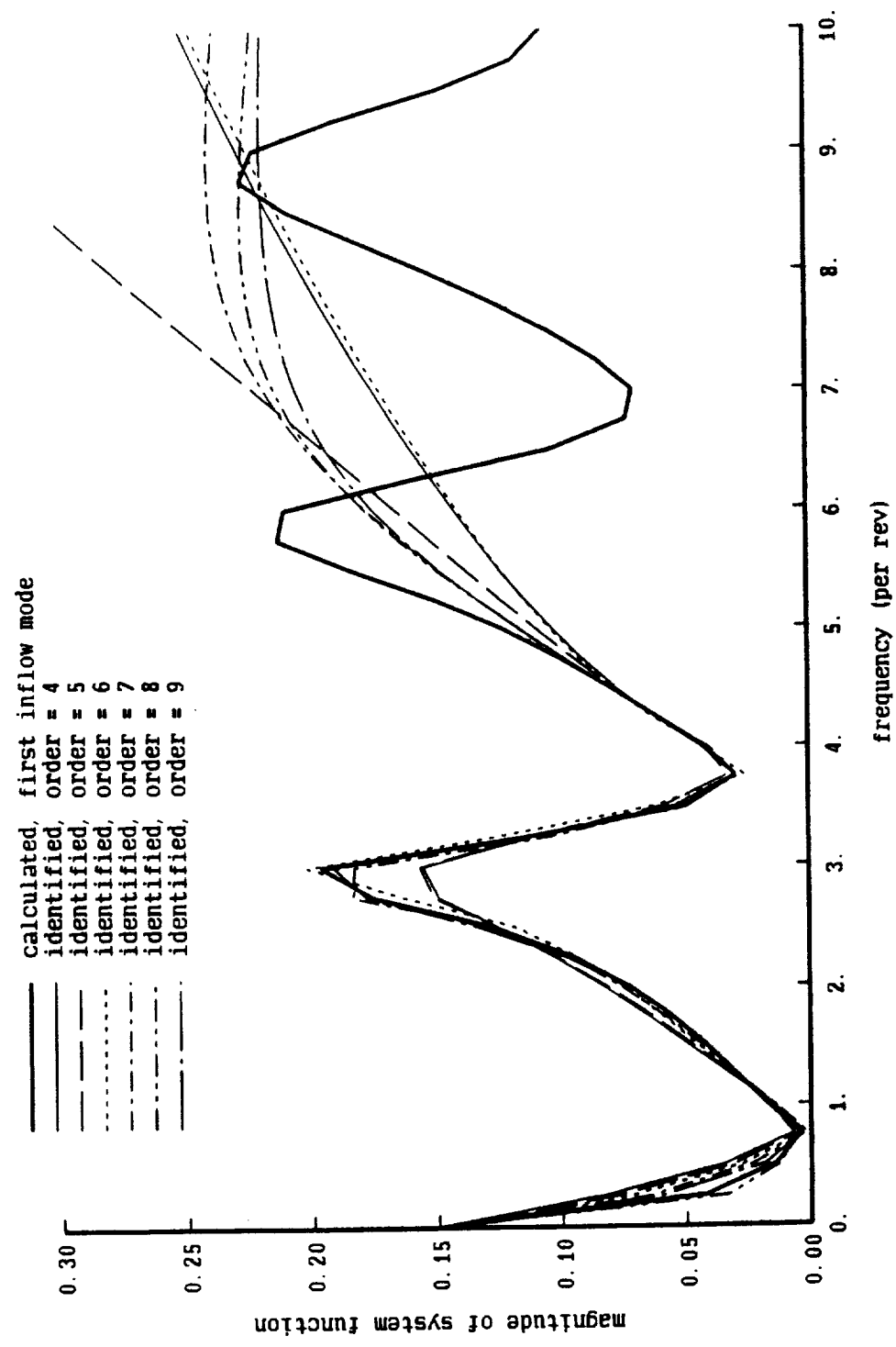


Figure 22h. Influence of of order and weight on identification

nonrotating frame, 3 blades; uniform inflow, circulation at 0.77R

all radial stations, three inflow modes; freq = 0-1.5 (wt=16), 1.5-4.5 (wt=1)

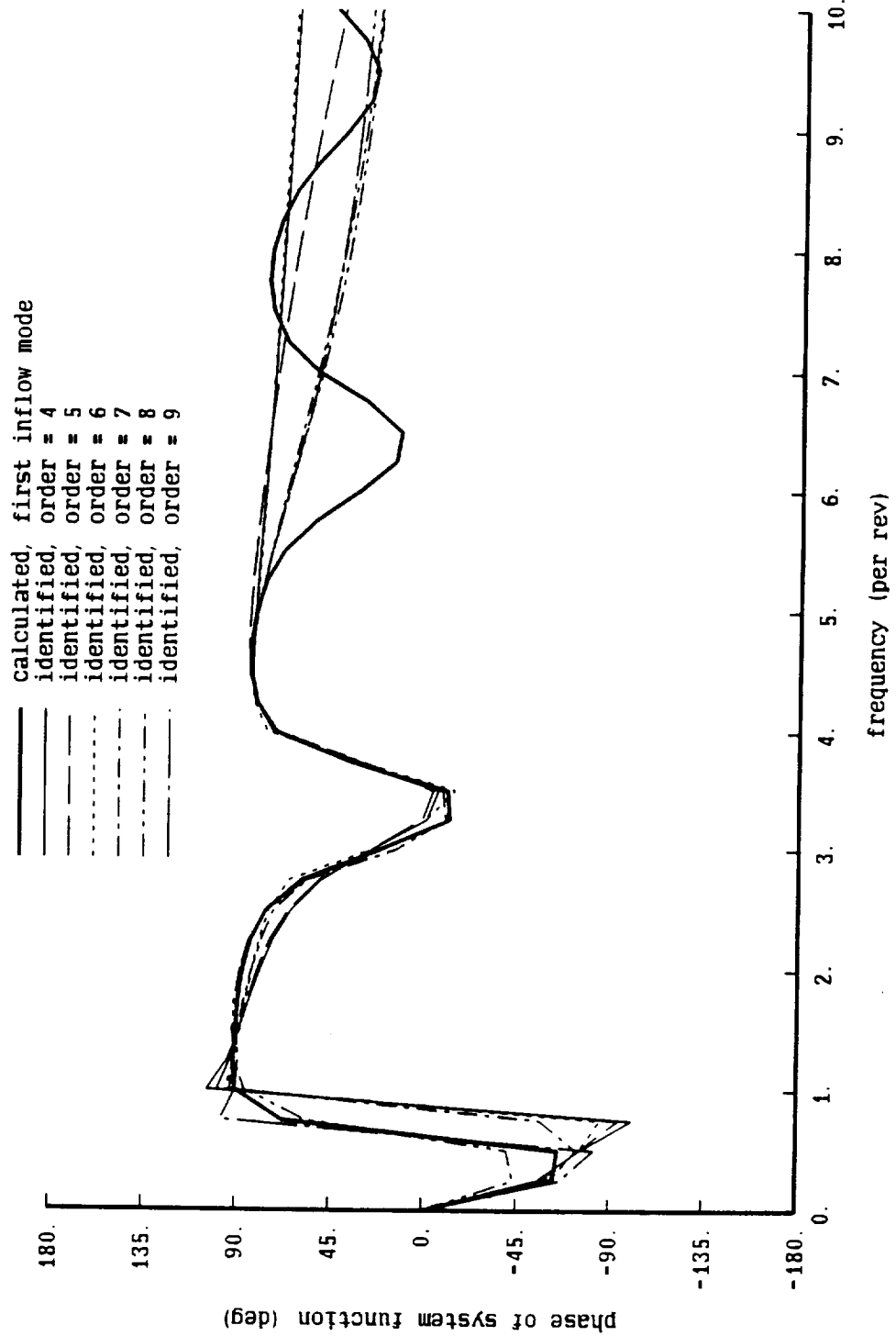


Figure 22i. Influence of of order and weight on identification

nonrotating frame, 3 blades; uniform inflow, circulation at 0.77R

all radial stations, three inflow modes; freq = 1-1.5 (wt=16), 1.5-4.5 (wt=1)

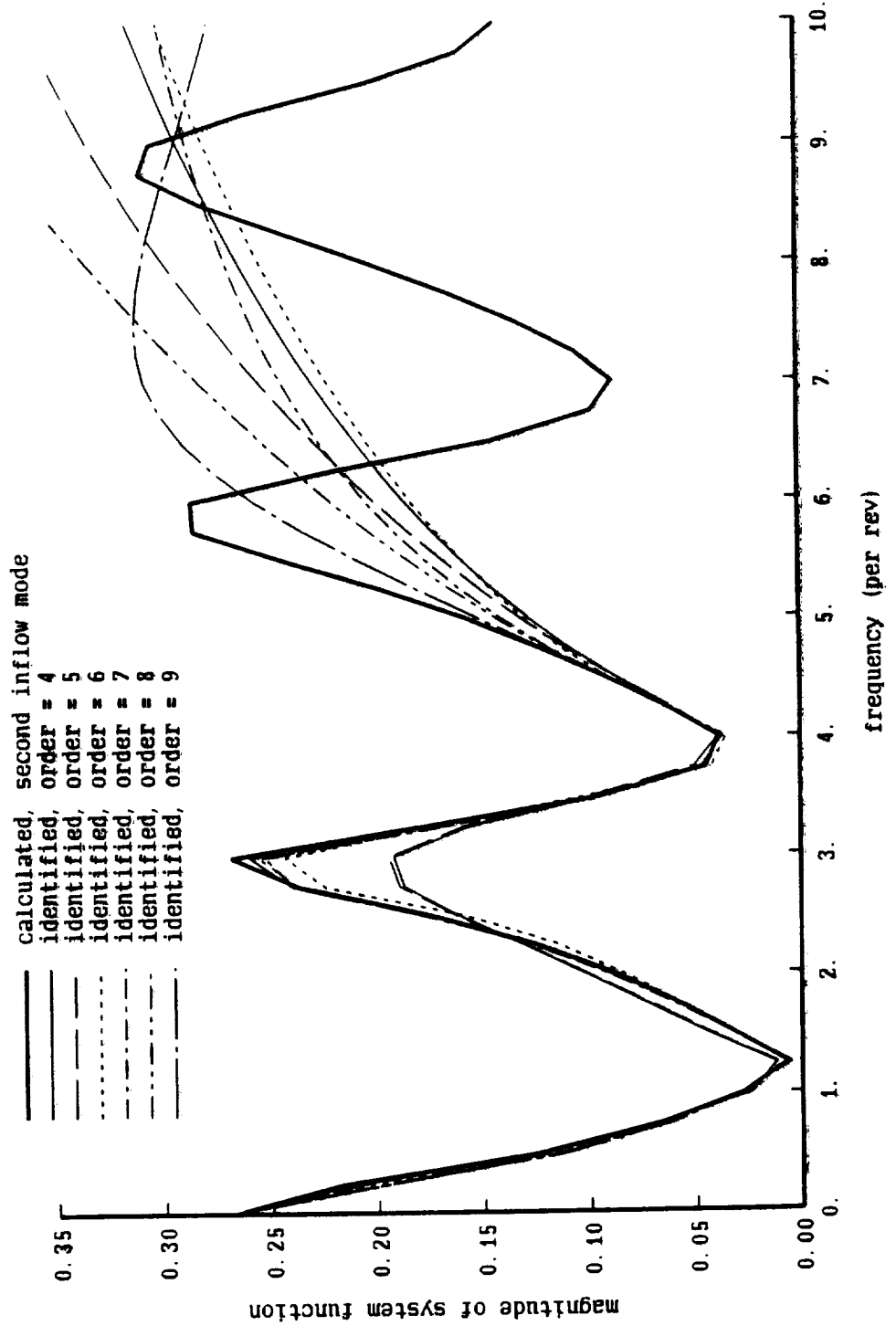


Figure 22j. Influence of of order and weight on identification

nonrotating frame, 3 blades; uniform inflow, circulation at 0.77R
 all radial stations, three inflow modes; freq = 0-1.5 (wt=16), 1.5-4.5 (wt=1)

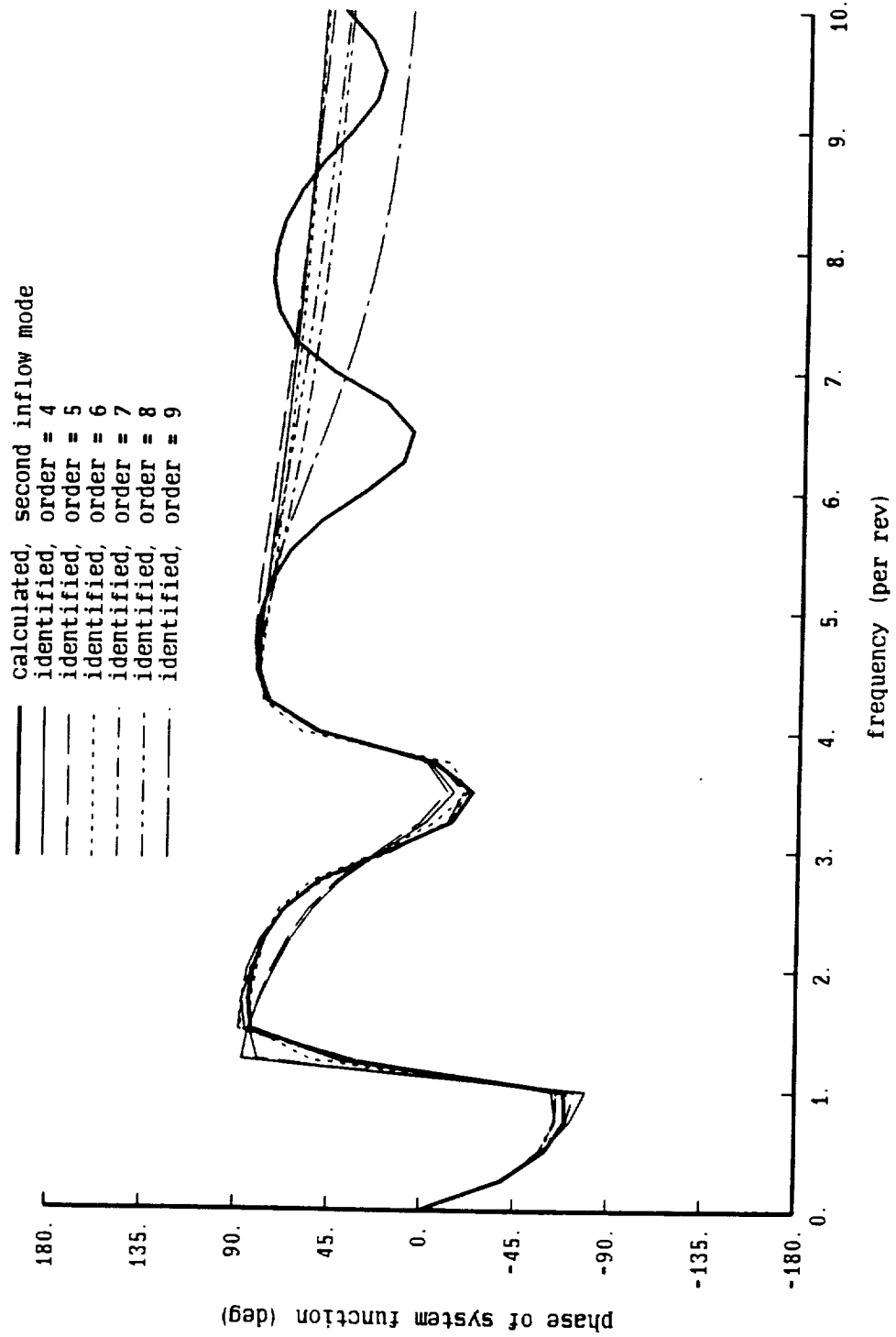


Figure 22k. Influence of of order and weight on identification

nonrotating frame, 3 blades; uniform inflow, circulation at 0.77R

all radial stations, three inflow modes; freq = 1-1.5 (wt=16), 1.5-4.5 (wt=1)

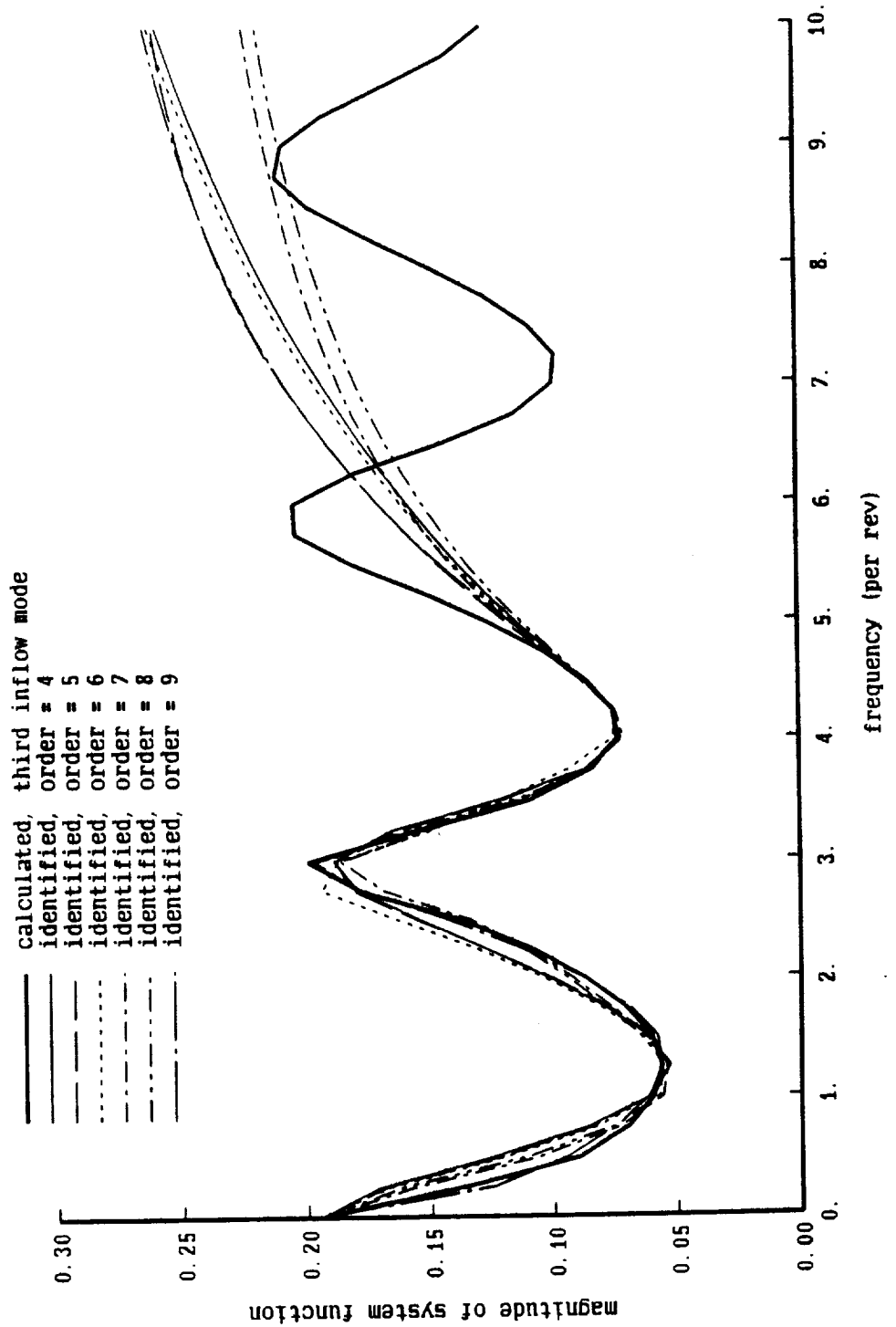


Figure 221. Influence of of order and weight on identification

nonrotating frame, 3 blades; uniform inflow, circulation at 0.77R

all radial stations, three inflow modes; freq = 0-1.5 (wt=16), 1.5-4.5 (wt=1)

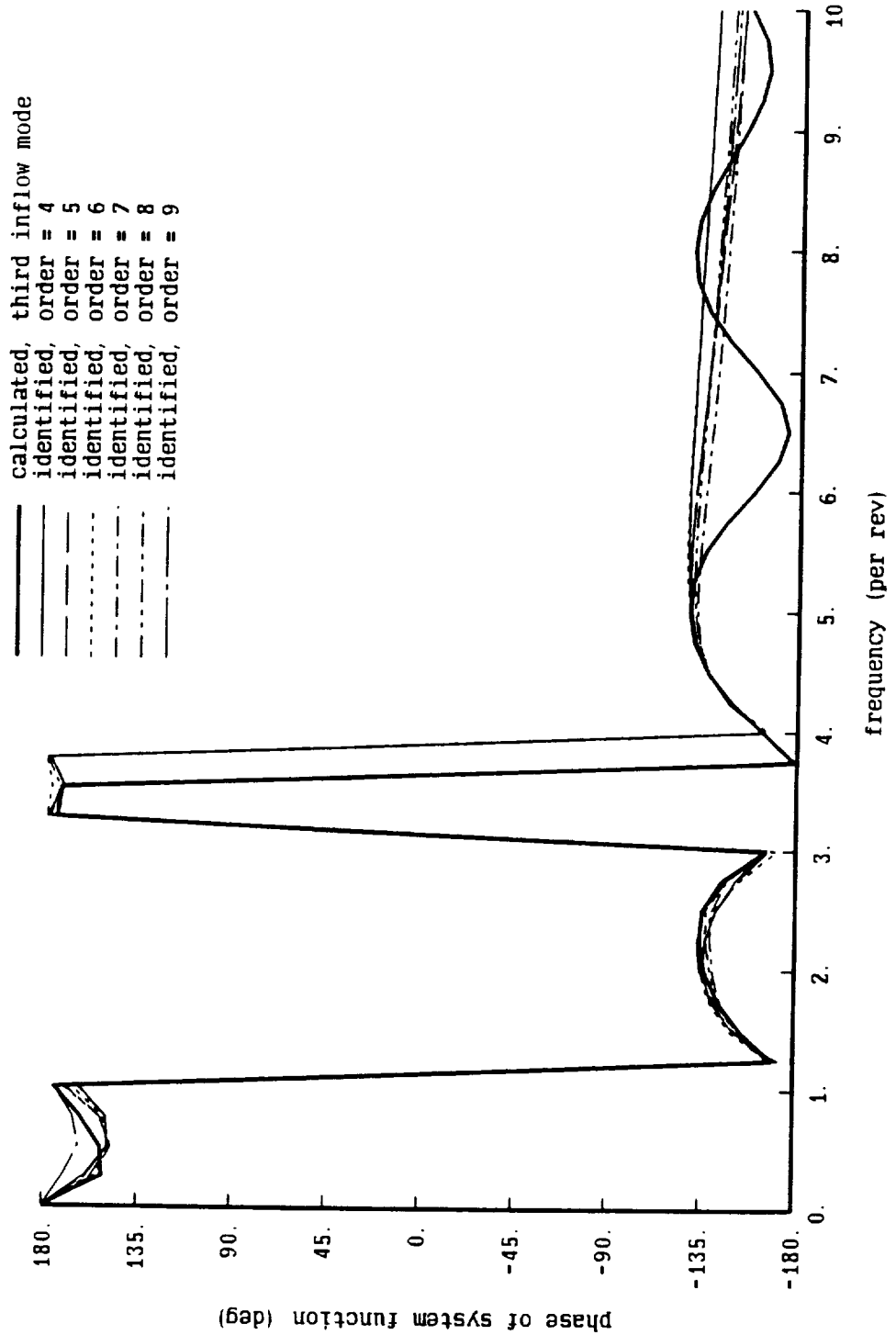


Figure 23a. System function of hovering rotor with undistorted wake

nonrotating frame, 3 blades, $CT/\sigma = 0.08$; circulation at 0.77R

six inflow modes, order = 6; frequency range = 0-1.5 (wt=16), 1.5-4.5 (wt=1)

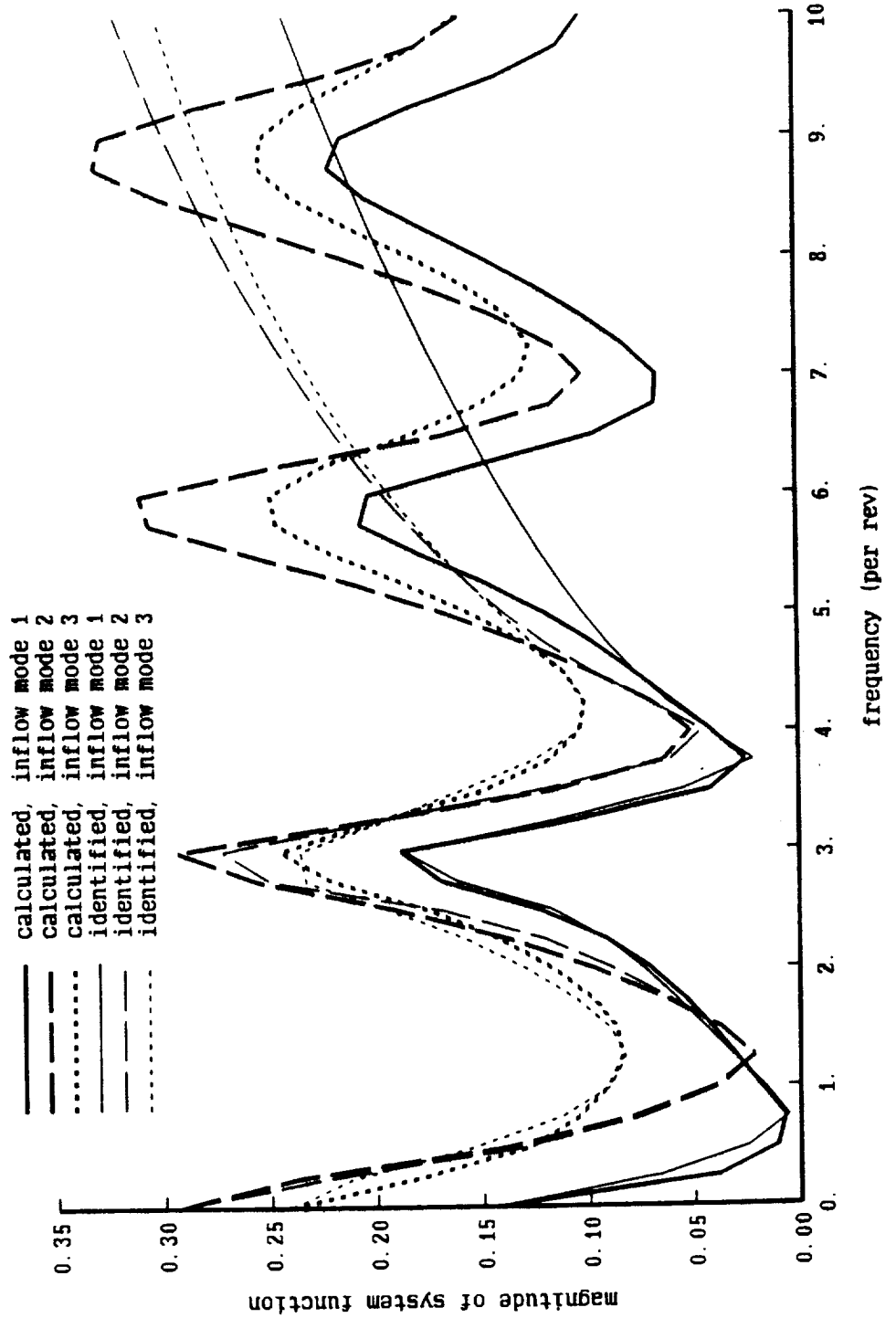


Figure 23b. System function of hovering rotor with undistorted wake

nonrotating frame, 3 blades, $CT/\sigma = 0.08$; circulation at $0.77R$

six inflow modes, order = 6; frequency range = 0-1.5 (wt=16), 1.5-4.5 (wt=1)

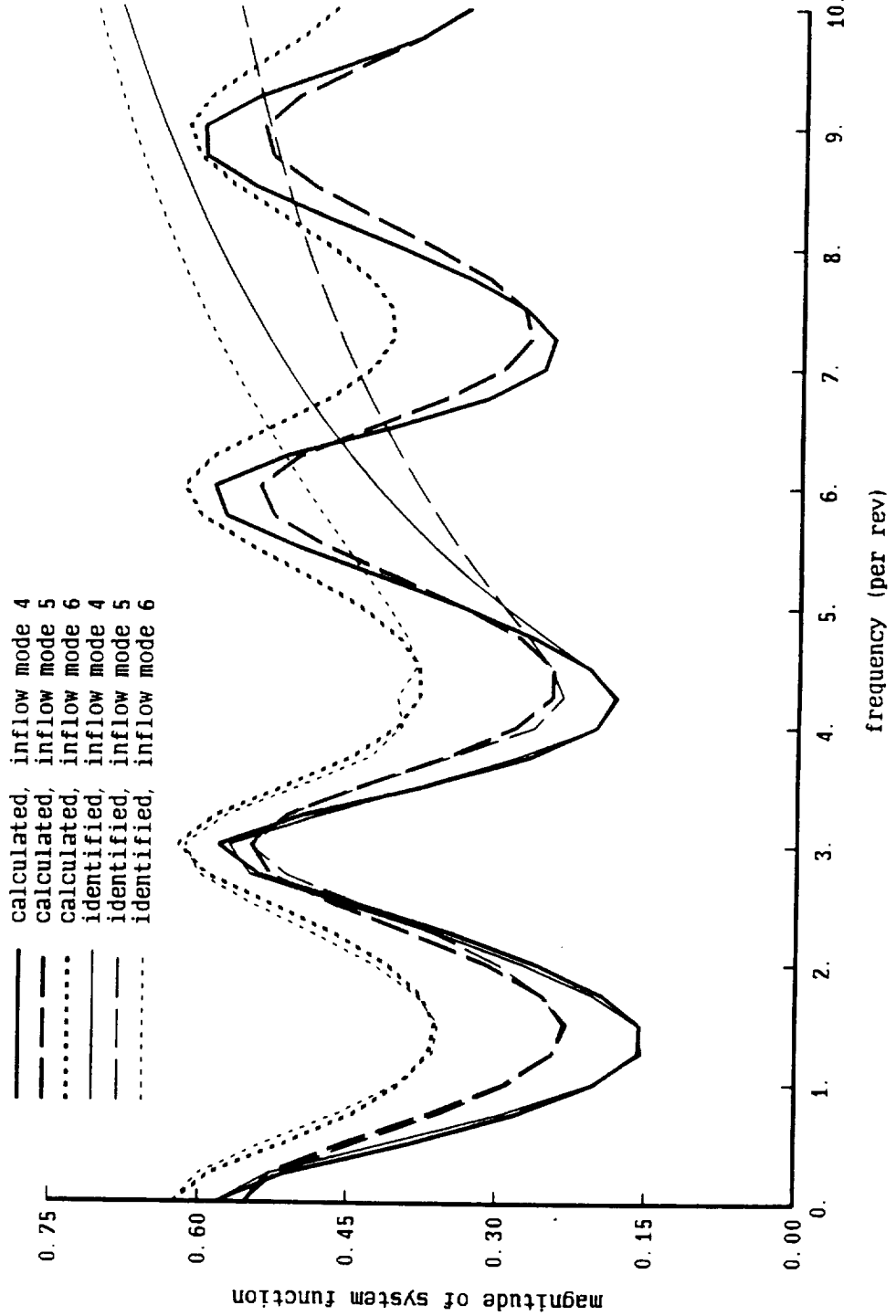


Figure 23c. System function of hovering rotor with undistorted wake

nonrotating frame, 3 blades, $CT/\sigma = 0.08$; circulation at 0.77R

six inflow modes, order = 6; frequency range = 0-1.5 (wt=16), 1.5-4.5 (wt=1)

- calculated, inflow mode 1
- - - calculated, inflow mode 2
- calculated, inflow mode 3
- identified, inflow mode 1
- - - identified, inflow mode 2
- identified, inflow mode 3

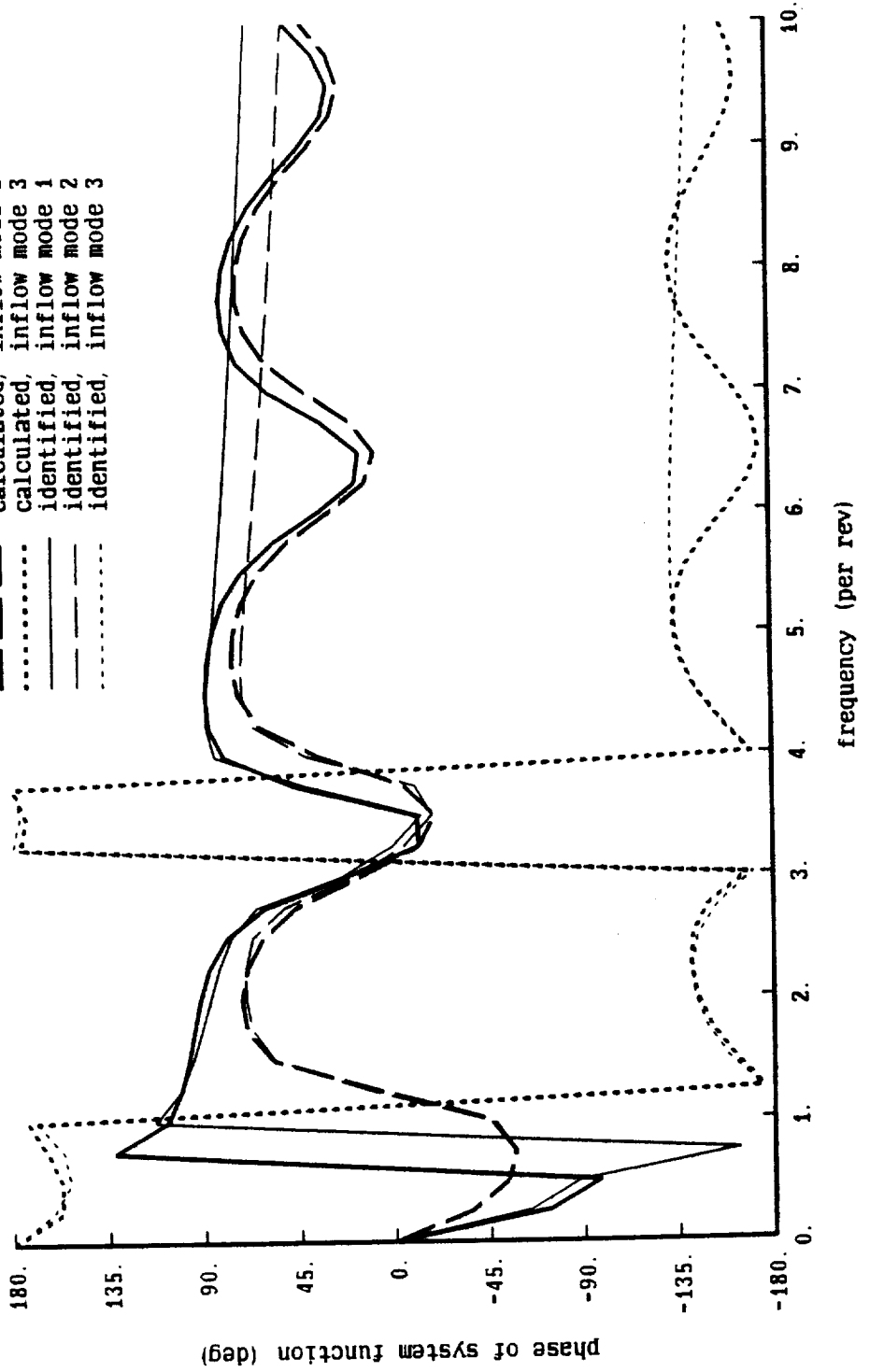


Figure 23d. System function of hovering rotor with undistorted wake

nonrotating frame, 3 blades, $CT/\sigma = 0.08$; circulation at 0.77R

six inflow modes, order = 6; frequency range = 0-1.5 (wt=16), 1.5-4.5 (wt=1)

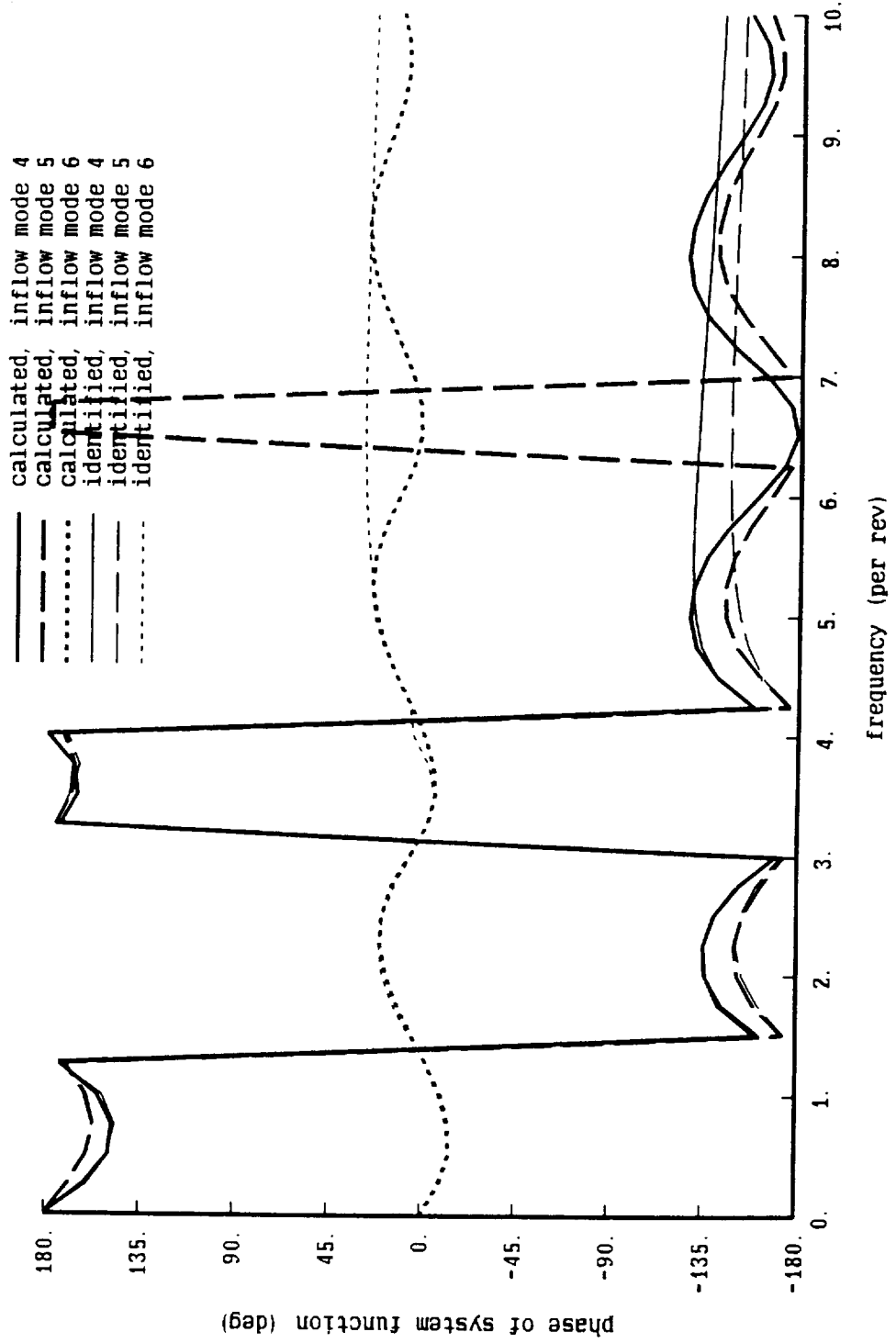


Figure 24a. System function of hovering rotor with undistorted wake

nonrotating frame, 3 blades, $CT/\sigma = 0.02$; circulation at 0.77R

six inflow modes, order = 6; frequency range = 0-1.5 (wt=16), 1.5-4.5 (wt=1)

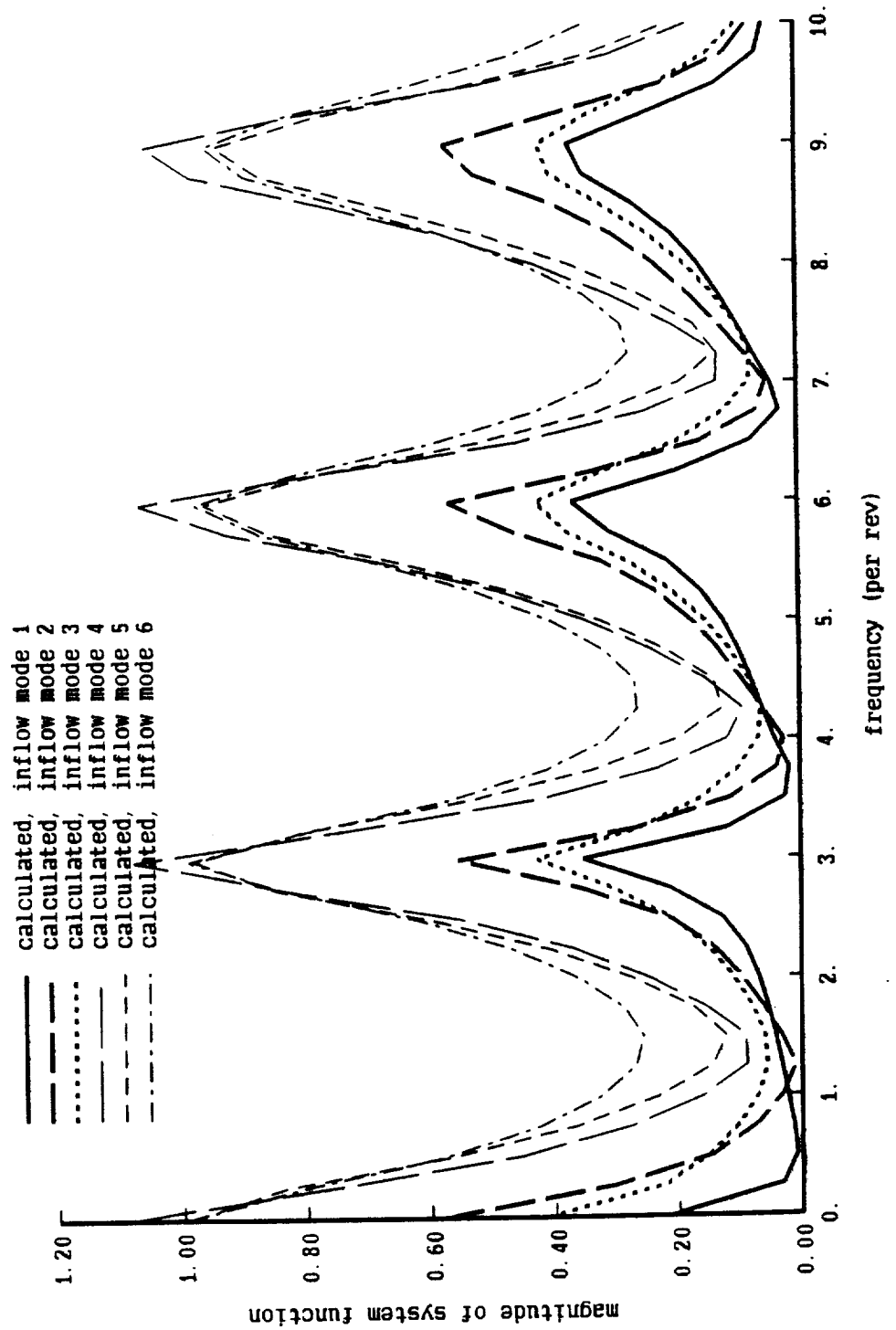


Figure 24b. System function of hovering rotor with undistorted wake

nonrotating frame, 3 blades, $CT/\sigma = 0.02$; circulation at 0.77R

six inflow modes, order = 6; frequency range = 0-1.5 (wt=16), 1.5-4.5 (wt=1)

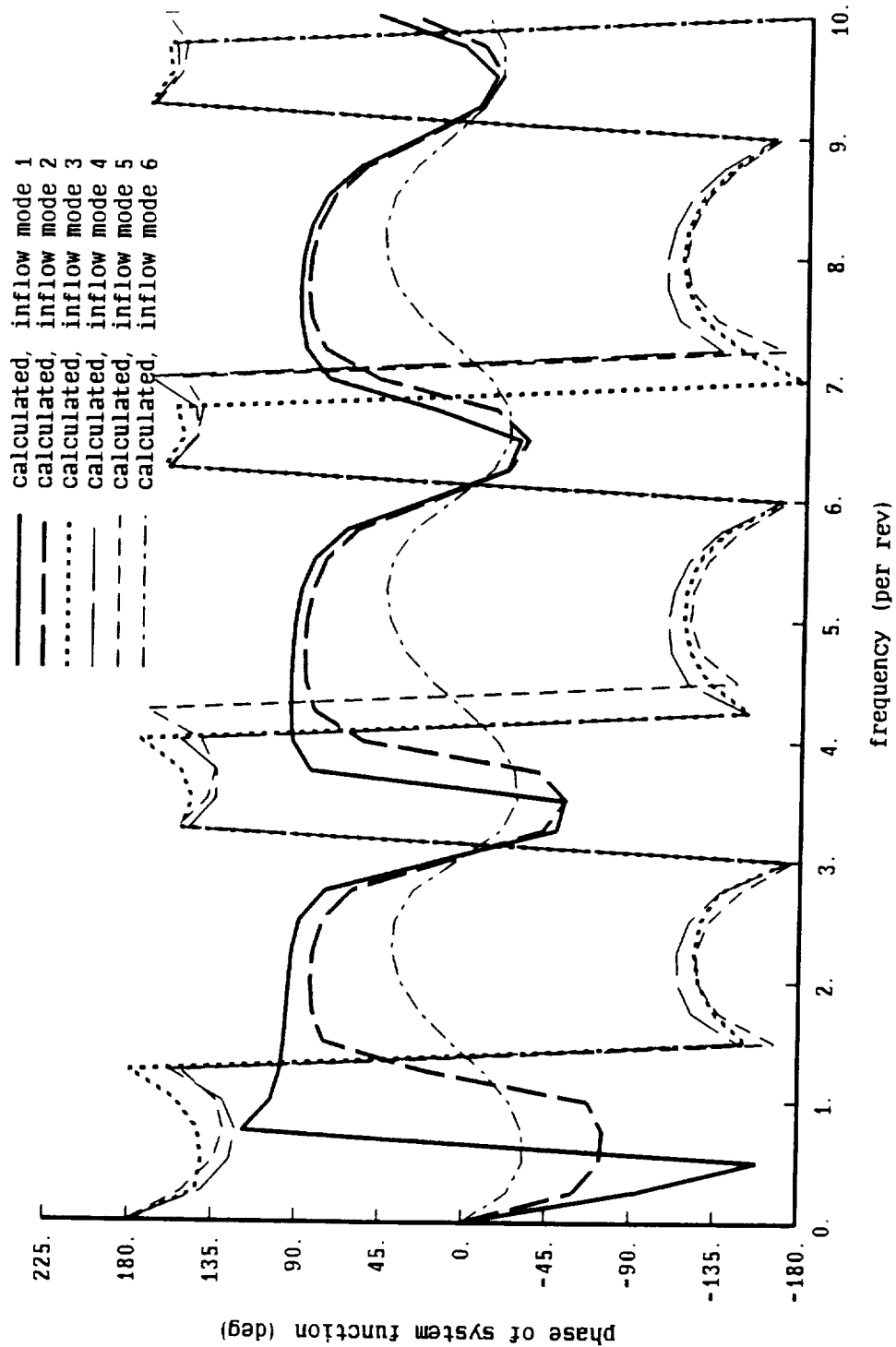


Figure 25a. Flap and wake roots of hovering rotor with undistorted wake

collective modes; 3 blades, $CT/\sigma = 0.08$

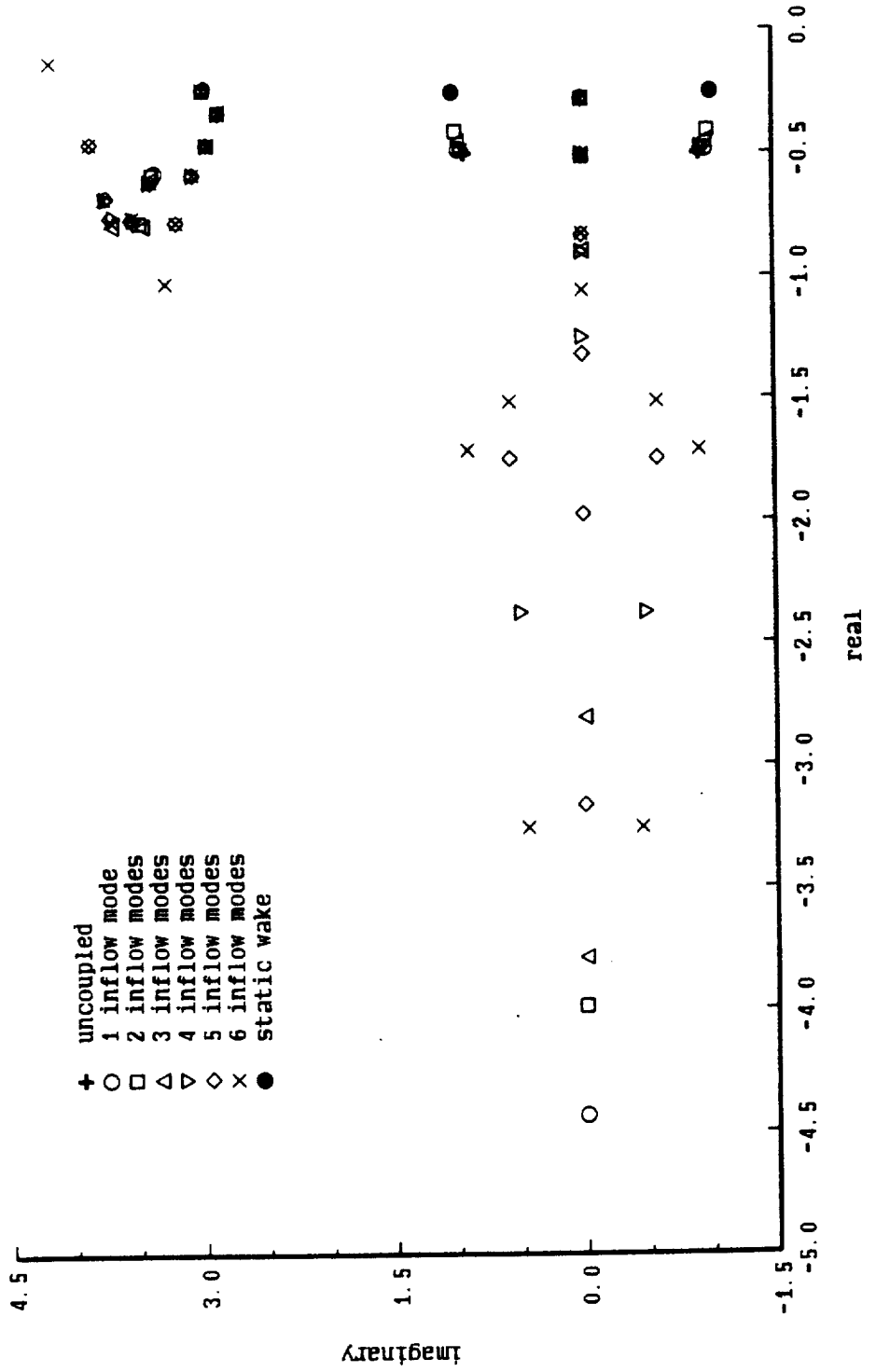


Figure 25b. Flap and wake roots of hovering rotor with undistorted wake

collective modes; 3 blades, $CT/\sigma = 0.08$

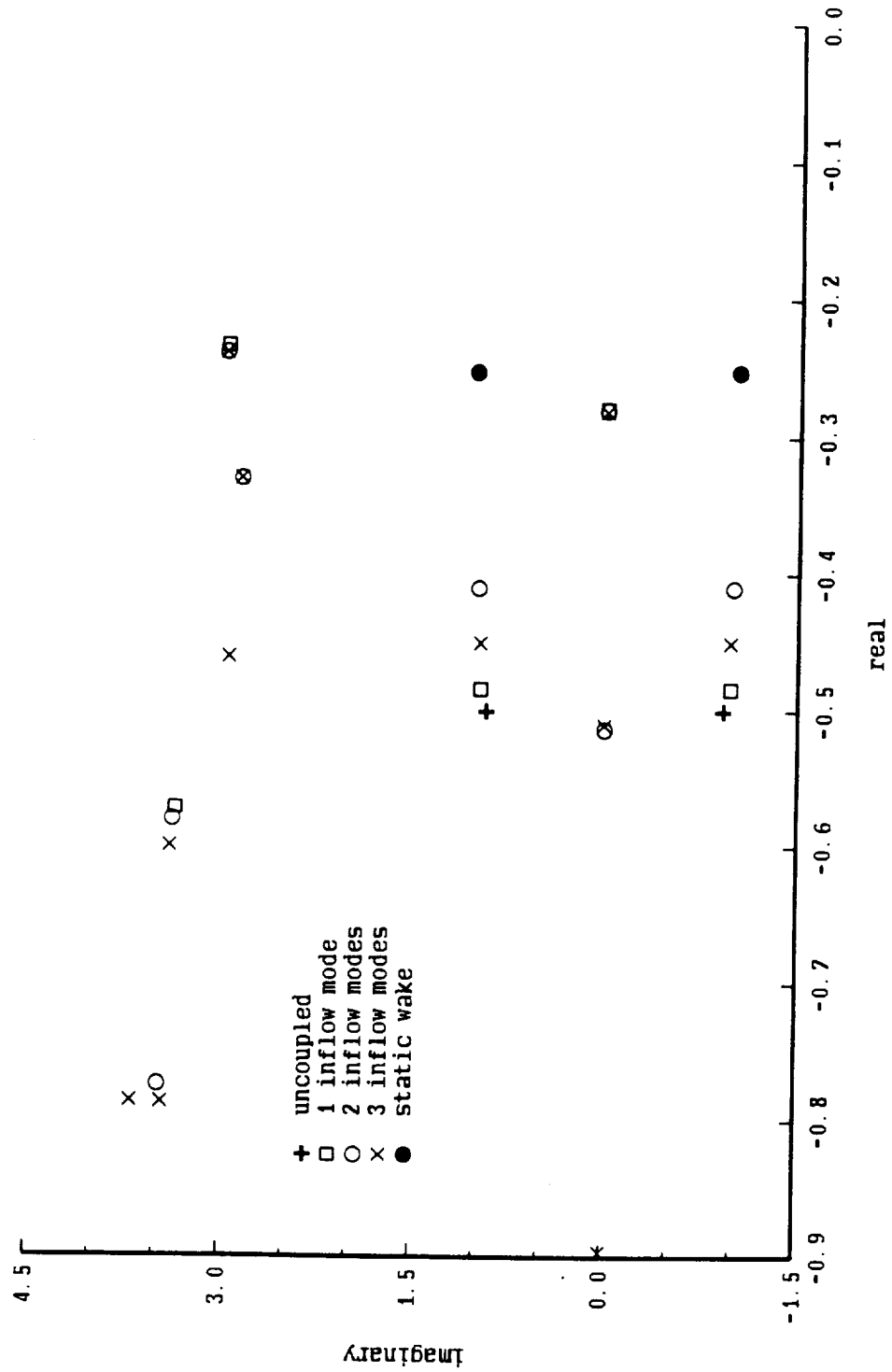


Figure 25d. Flap and wake roots of hovering rotor with undistorted wake

collective modes; 3 blades, $CT/\sigma = 0.02$

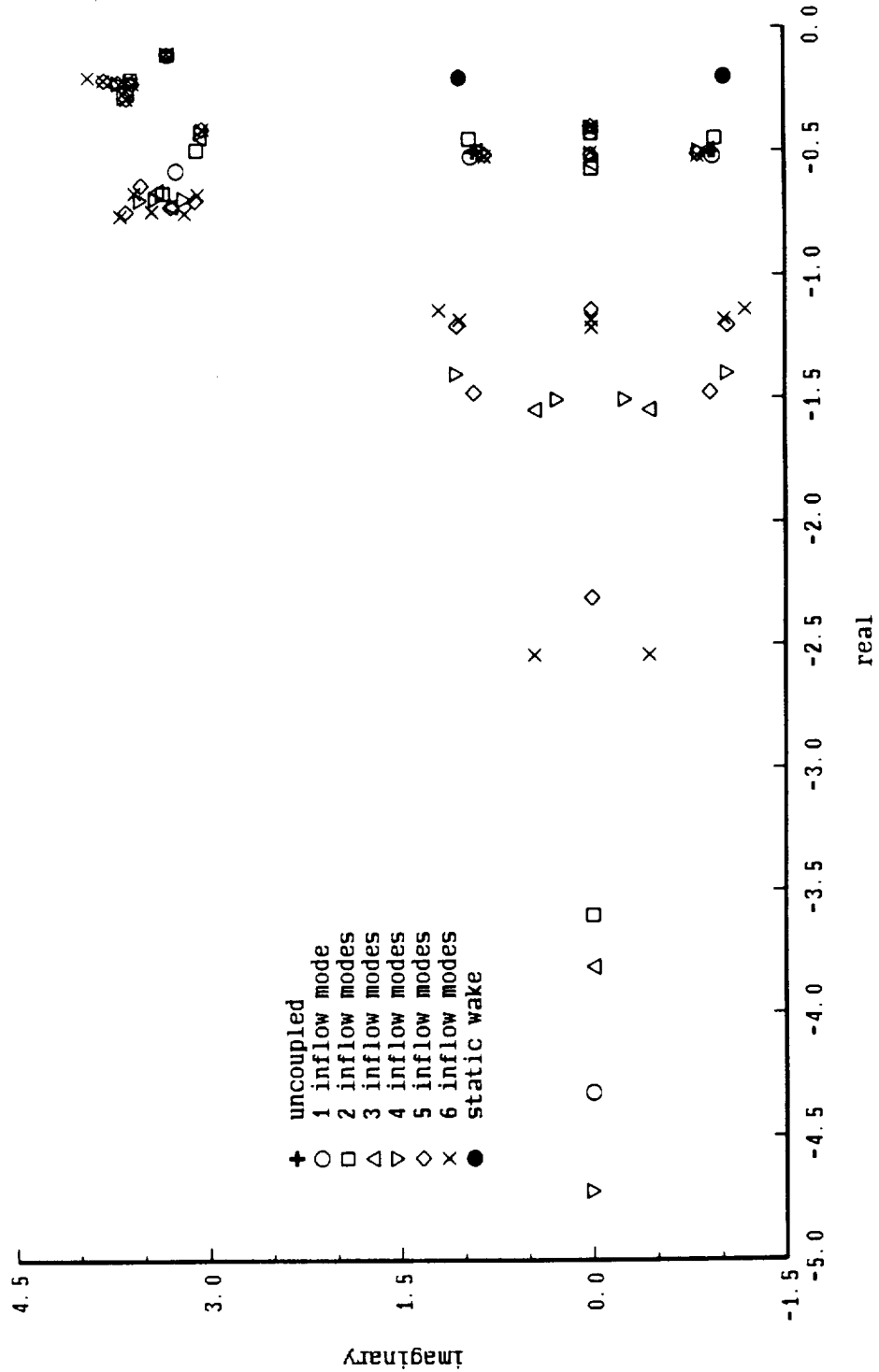


Figure 26a. Flap motion of hovering rotor with undistorted wake

3 blades, $CT/\sigma = 0.08$; coning response to collective pitch

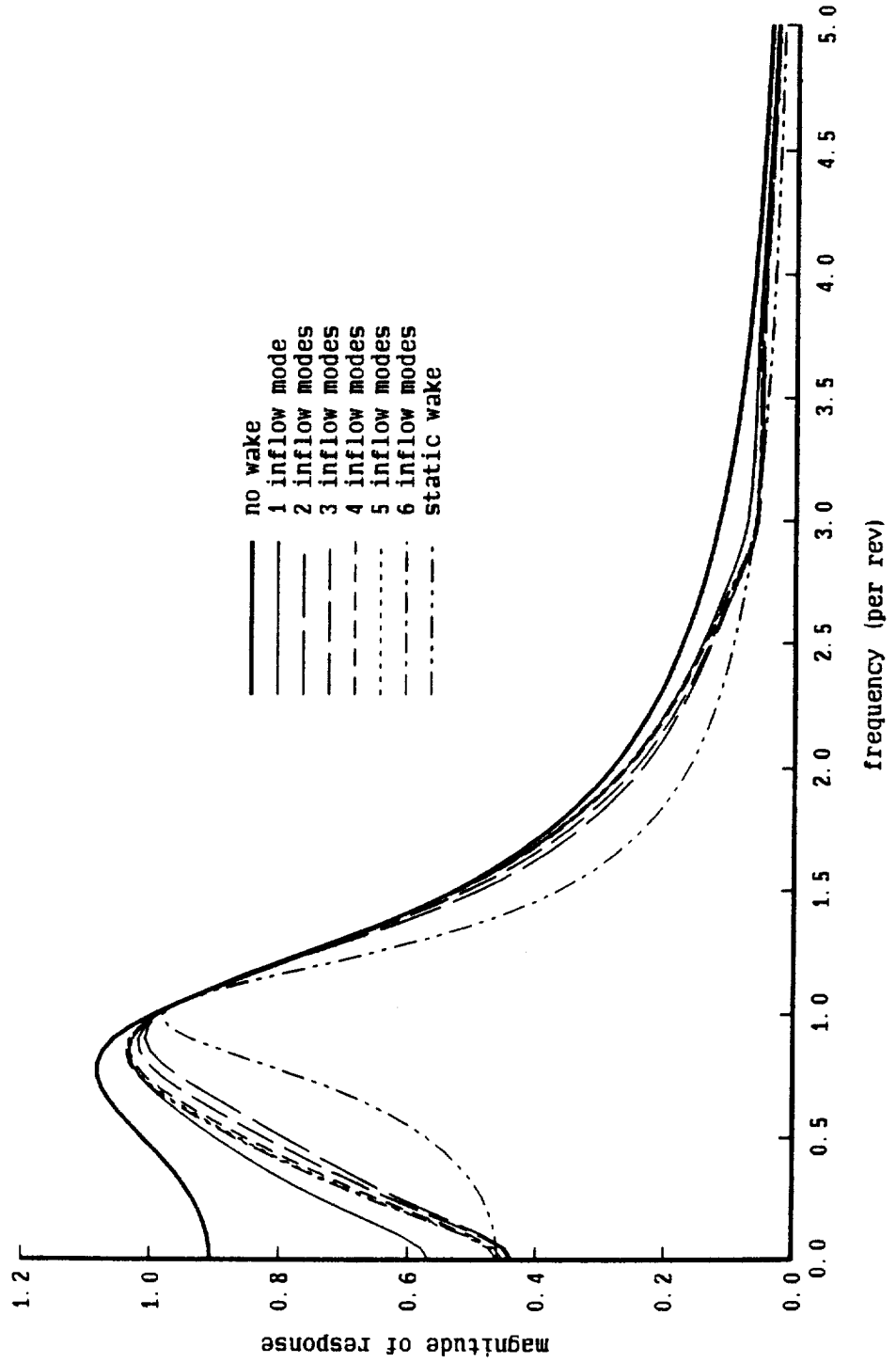


Figure 26b. Flap motion of hovering rotor with undistorted wake

3 blades, $CT/\sigma = 0.08$; coning response to collective pitch

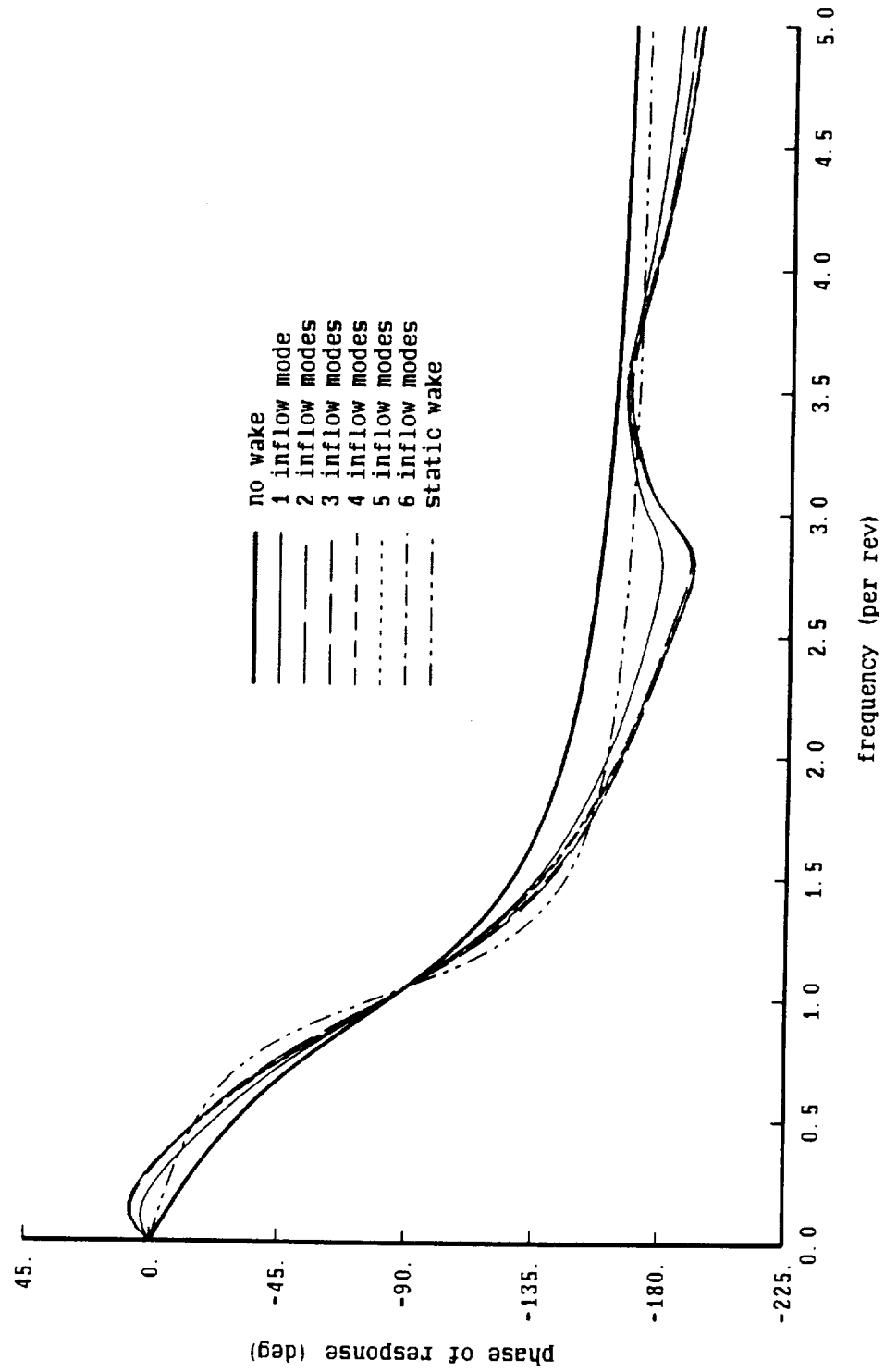


Figure 26c. Flap motion of hovering rotor with undistorted wake

3 blades, $CT/\sigma = 0.08$; coning response to vertical hub velocity

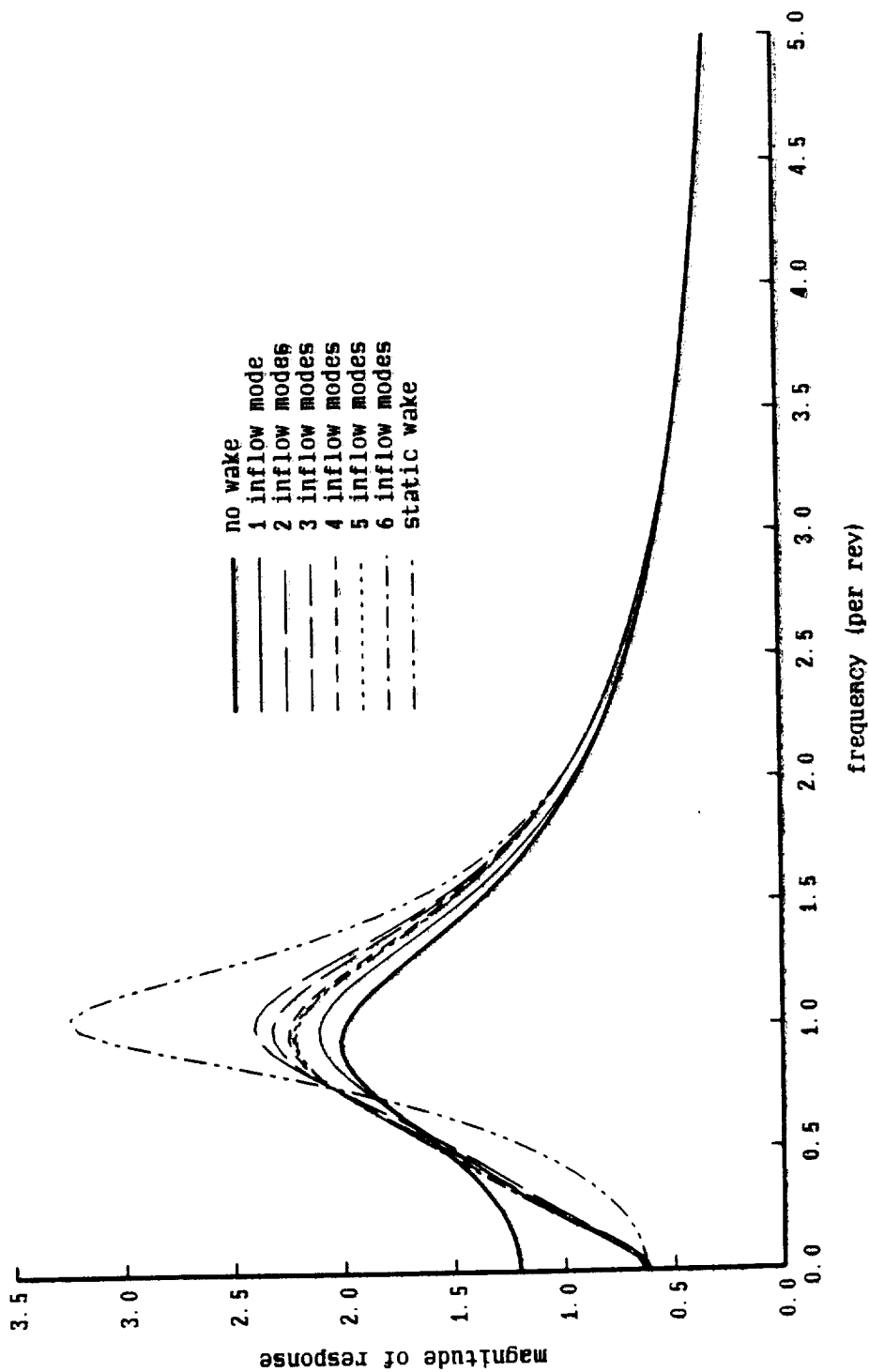


Figure 26d. Flap motion of hovering rotor with undistorted wake

3 blades, $CT/\sigma = 0.08$; coning response to vertical hub velocity

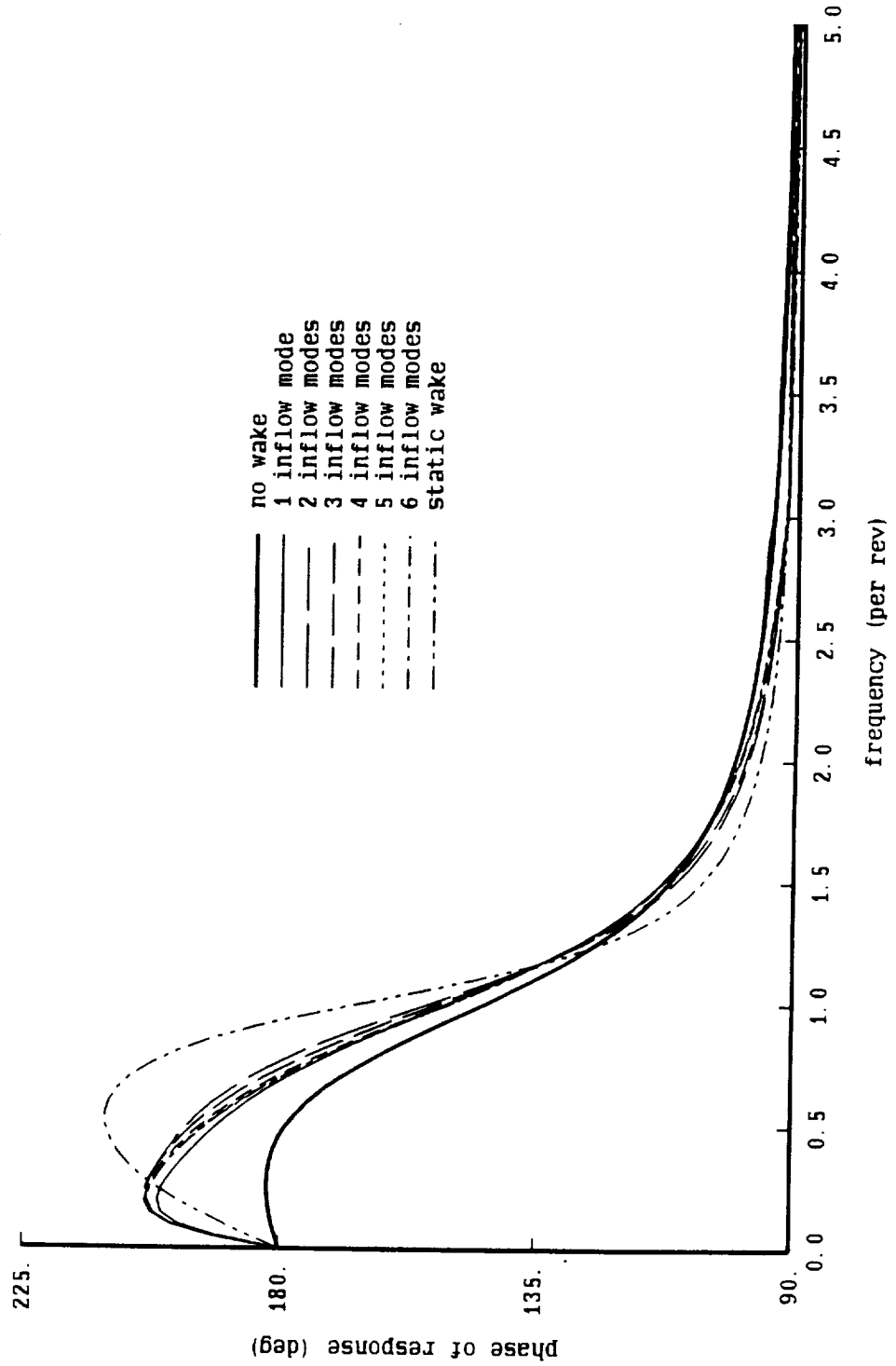


Figure 26e. Flap motion of hovering rotor with undistorted wake

3 blades, $CT/\sigma = 0.02$; coning response to collective pitch

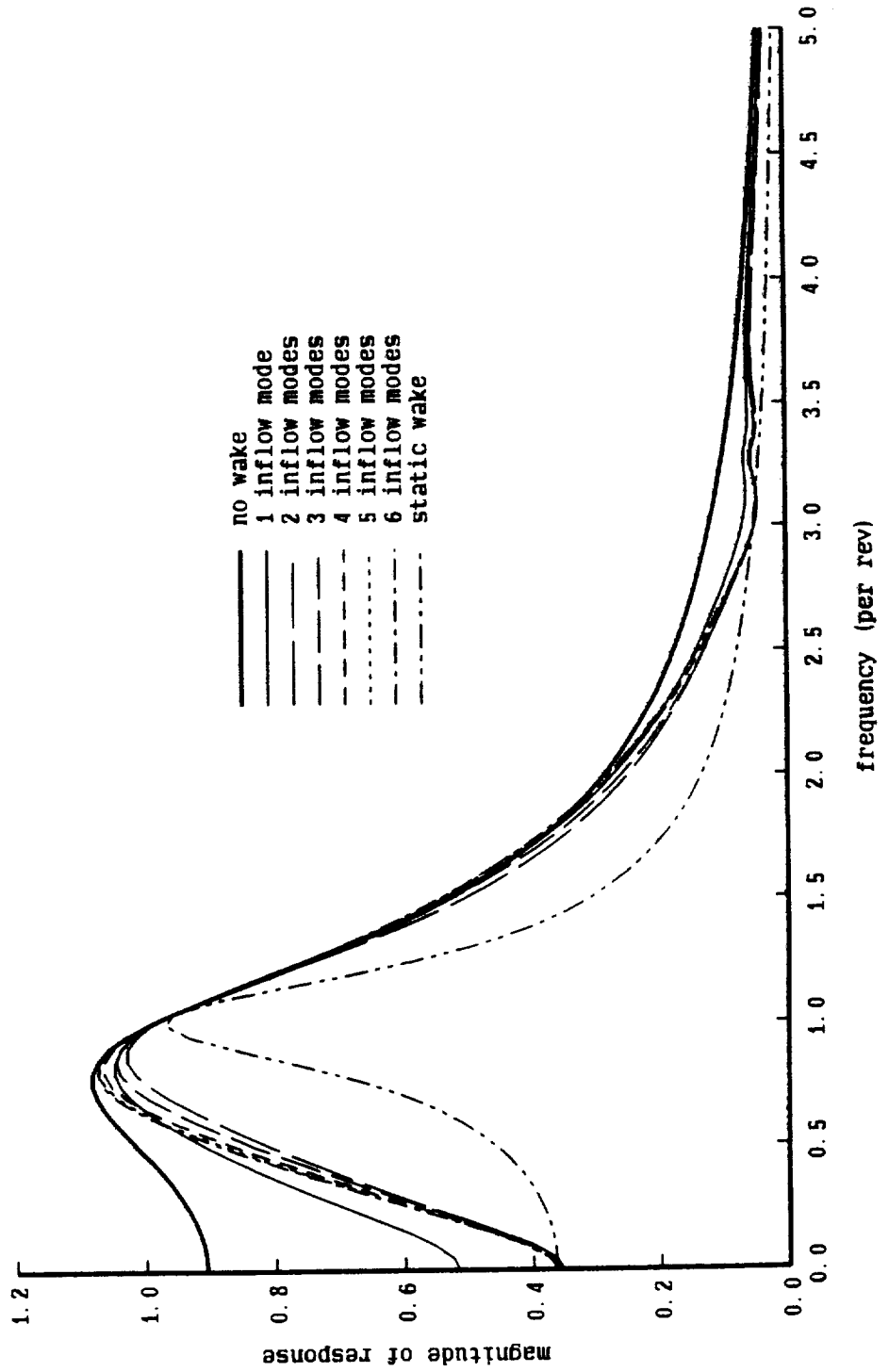


Figure 26f. Flap motion of hovering rotor with undistorted wake

3 blades, $CT/\sigma = 0.02$; coning response to collective pitch

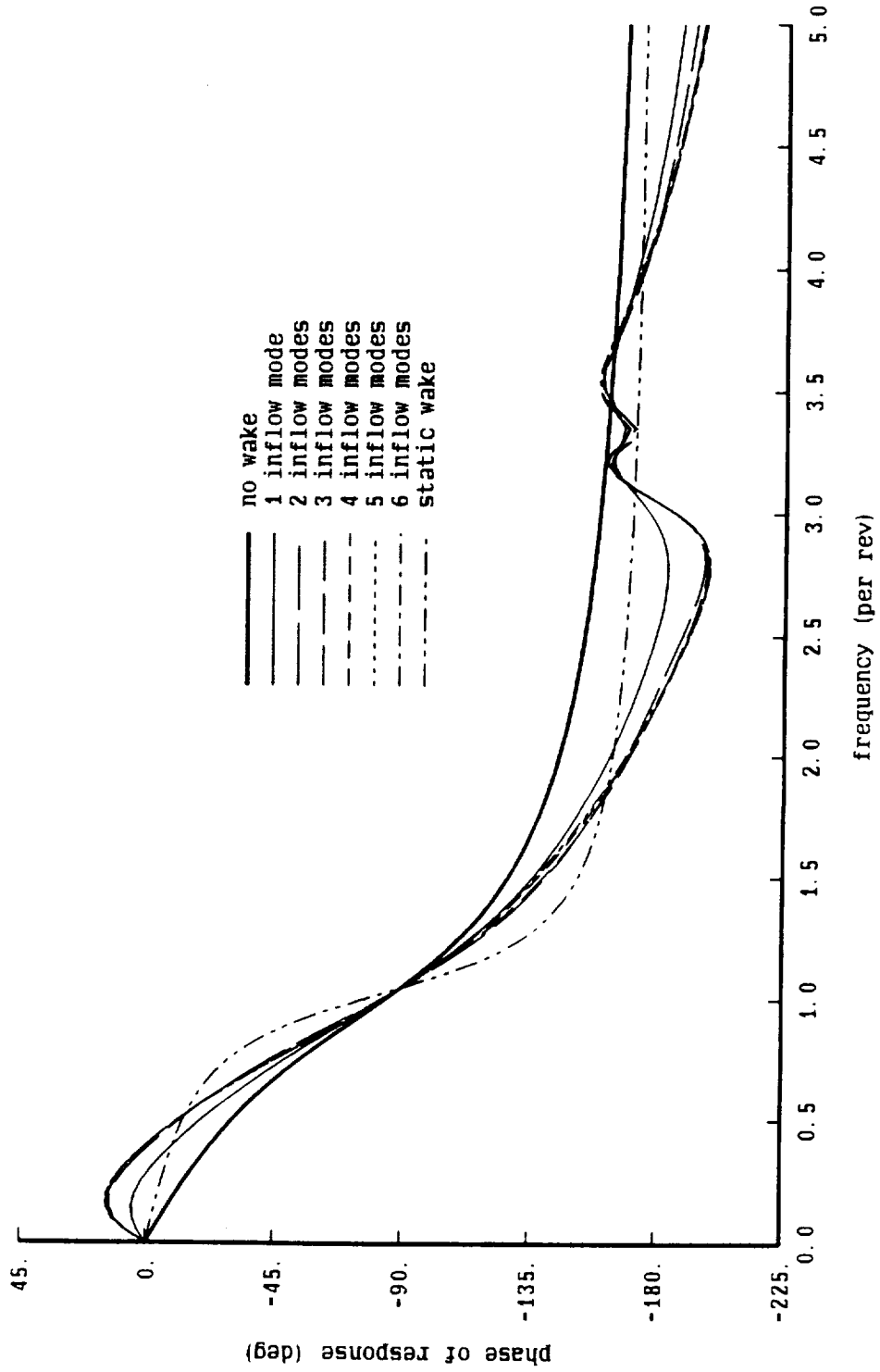


Figure 26g. Flap motion of hovering rotor with undistorted wake

3 blades, $CT/\sigma = 0.02$; coning response to vertical hub velocity

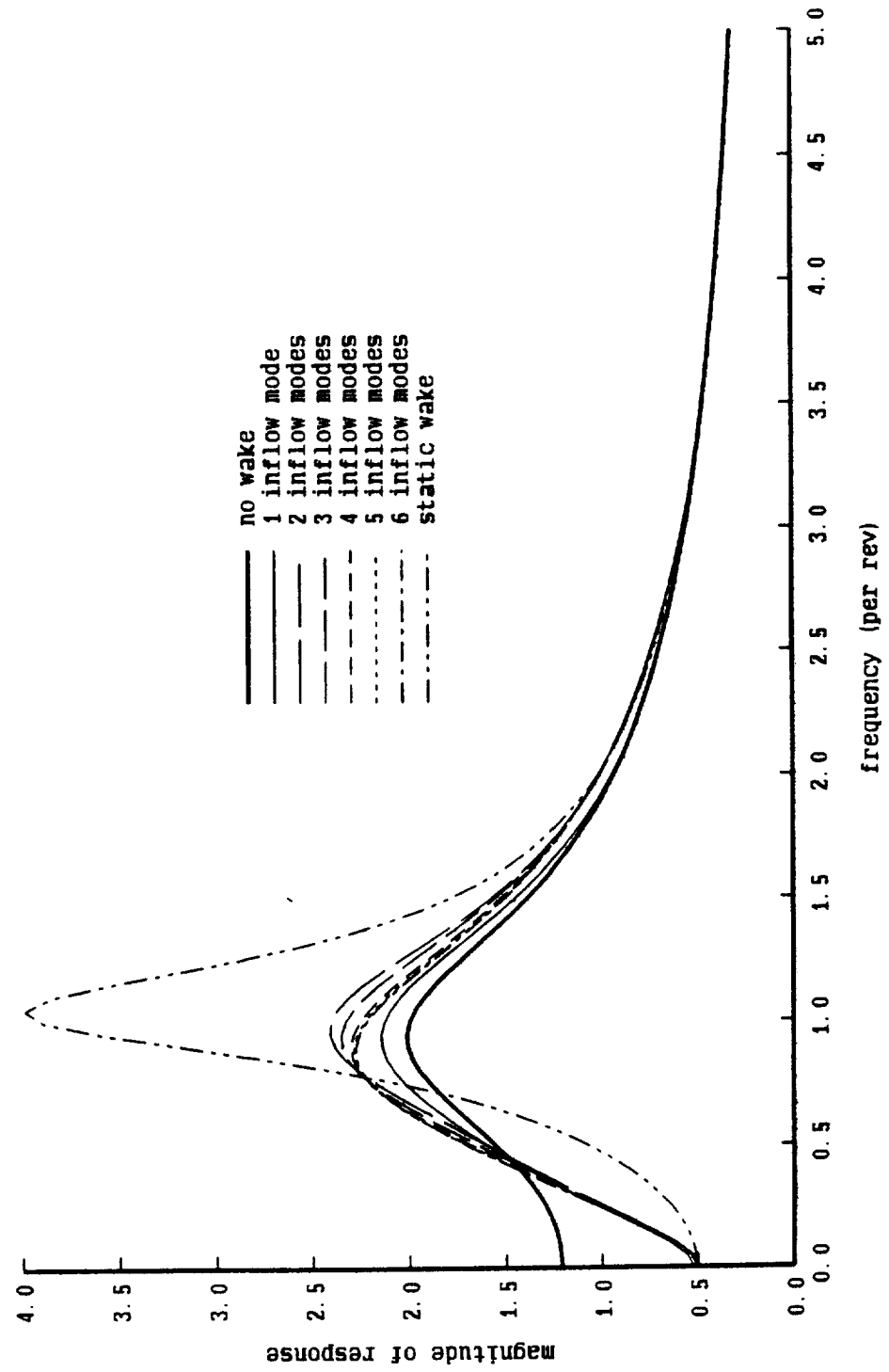


Figure 26h. Flap motion of hovering rotor with undistorted wake

3 blades, $CT/\sigma = 0.02$; coning response to vertical hub velocity

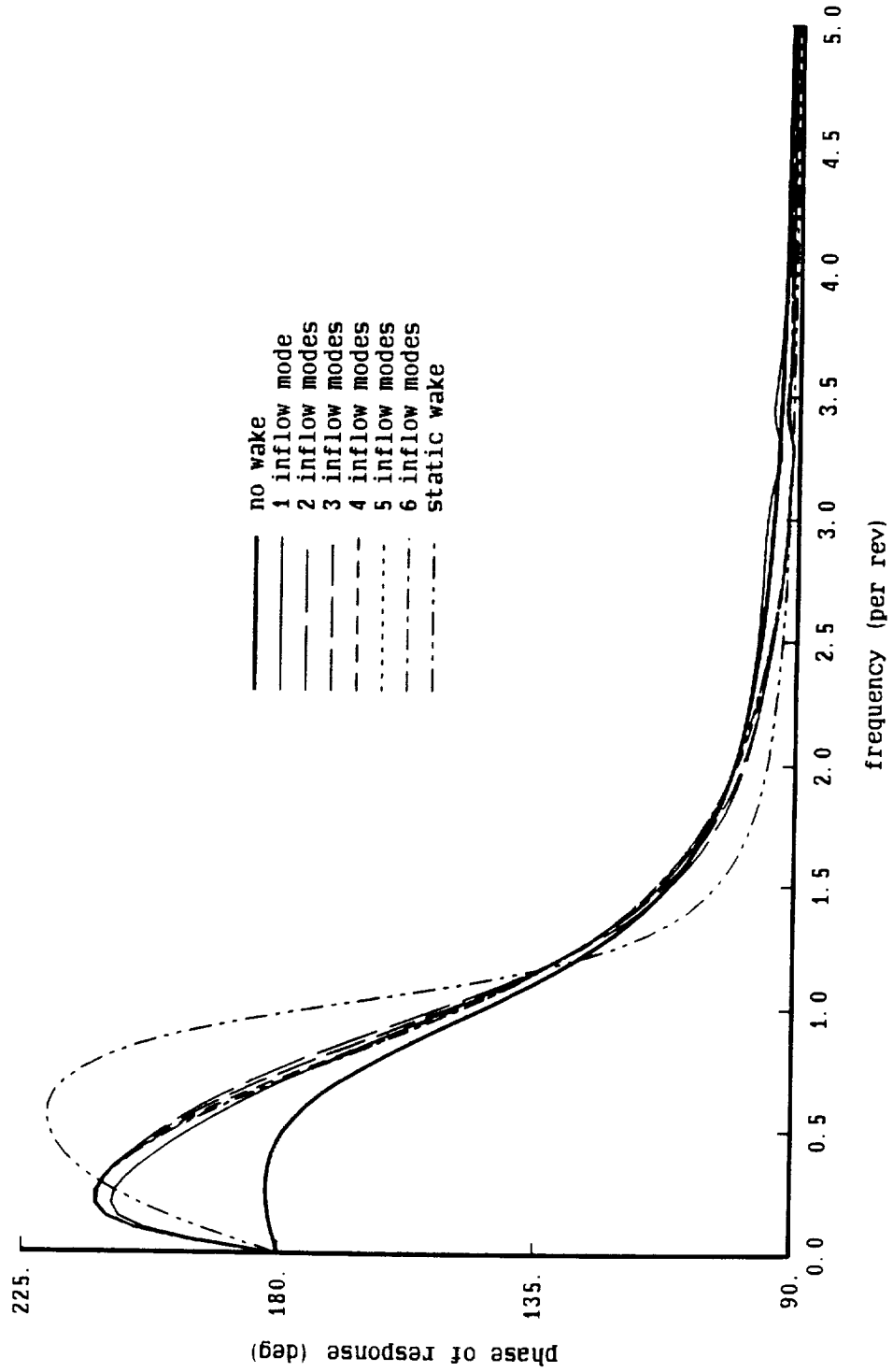


Figure 27a. Flap-pitch motion of hovering rotor with undistorted wake

3 blades, $CT/\sigma = 0.08$; flap/pitch: flap response to collective

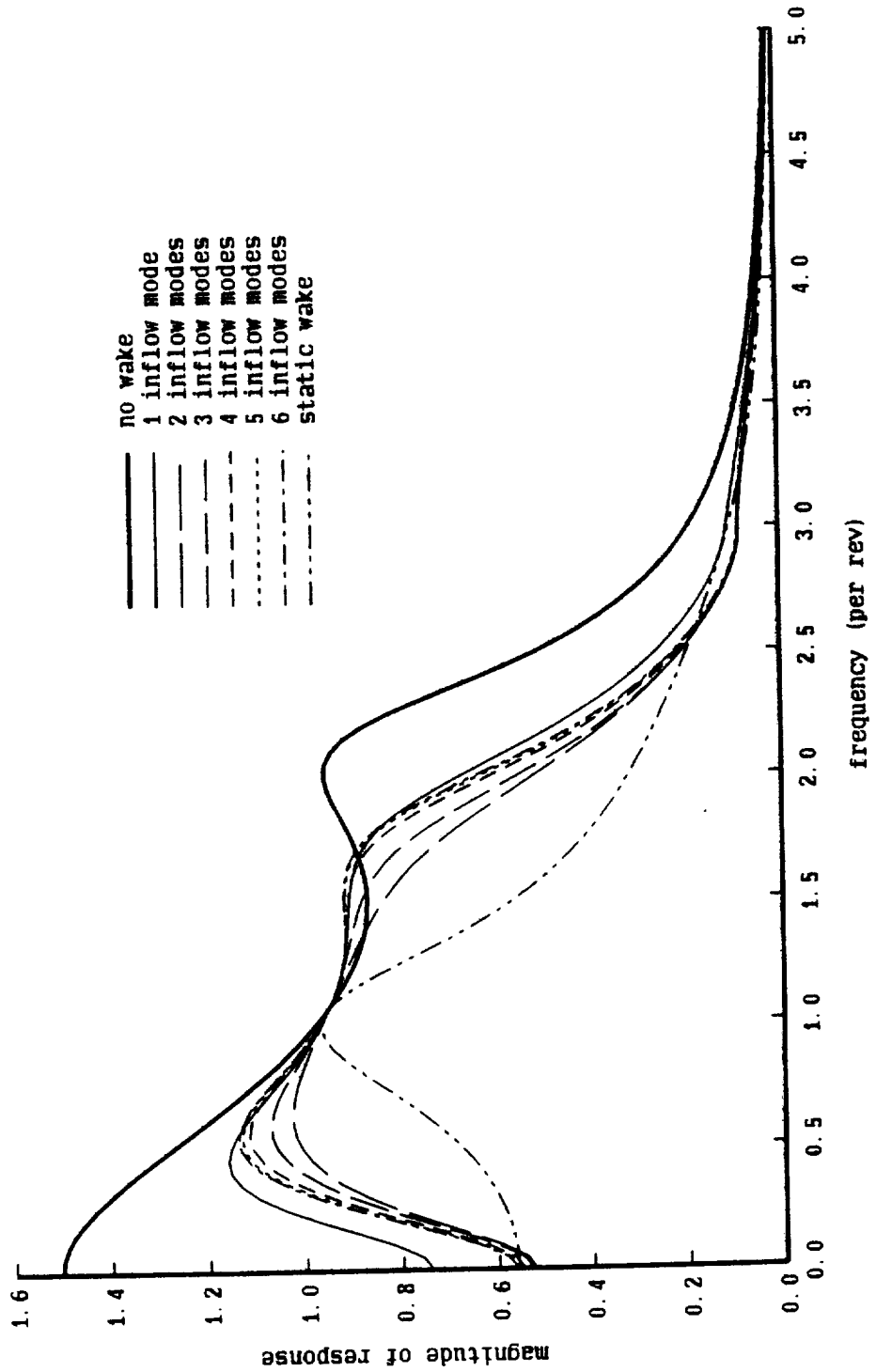


Figure 27b. Flap-pitch motion of hovering rotor with undistorted wake

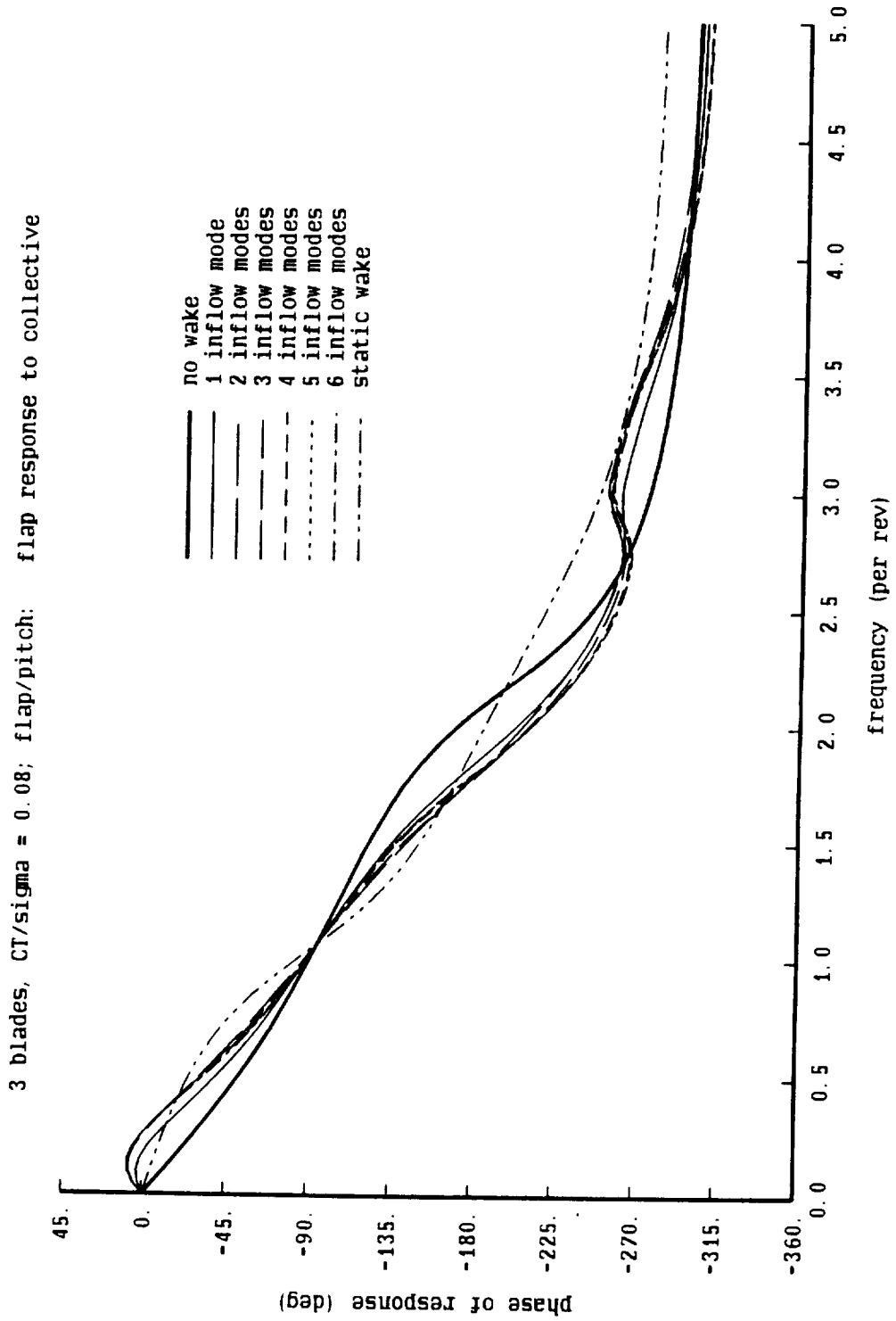


Figure 27c. Flap-pitch motion of hovering rotor with undistorted wake

3 blades, $CT/\sigma = 0.08$; flap/pitch: pitch response to collective

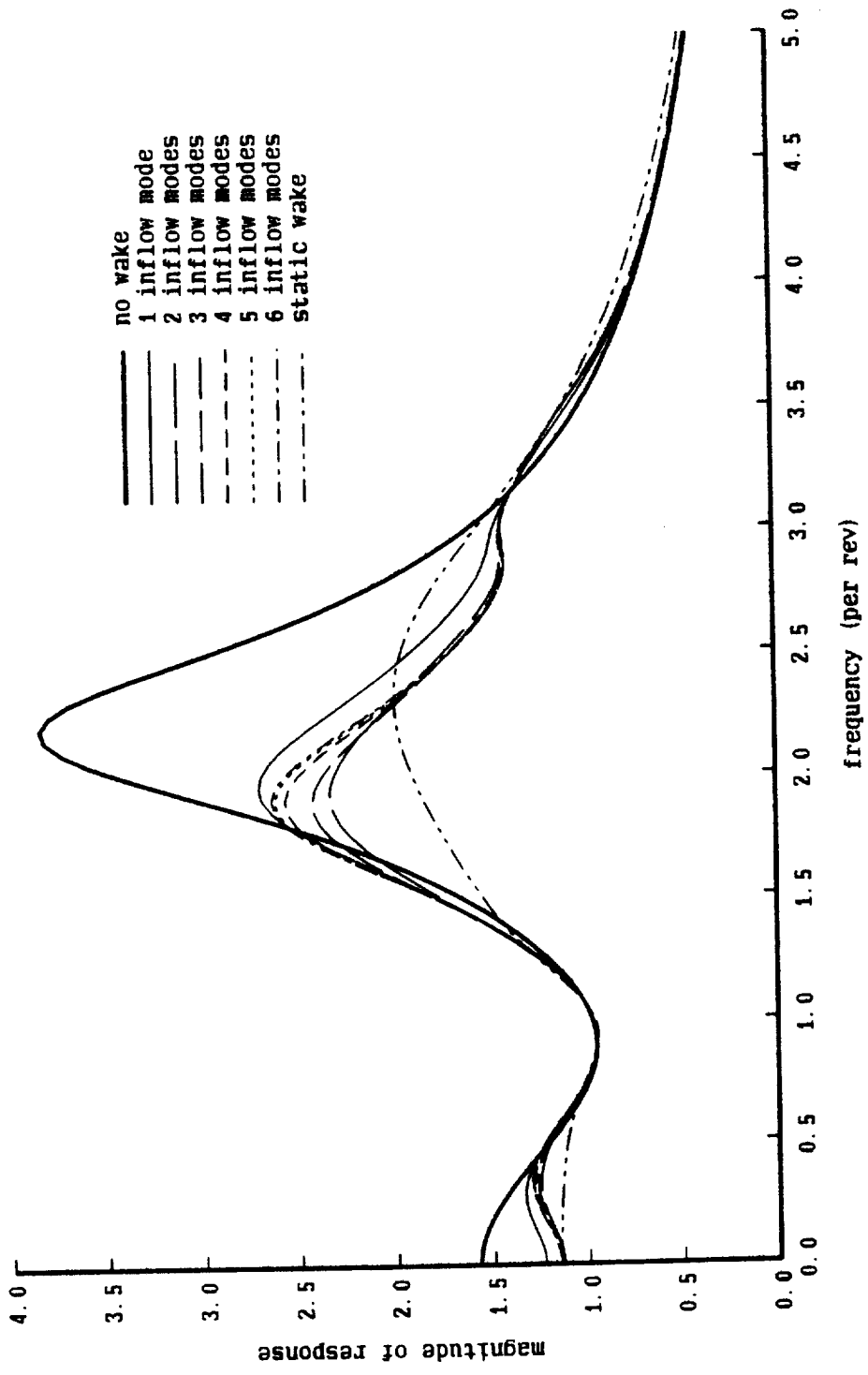


Figure 27d. Flap-pitch motion of hovering rotor with undistorted wake

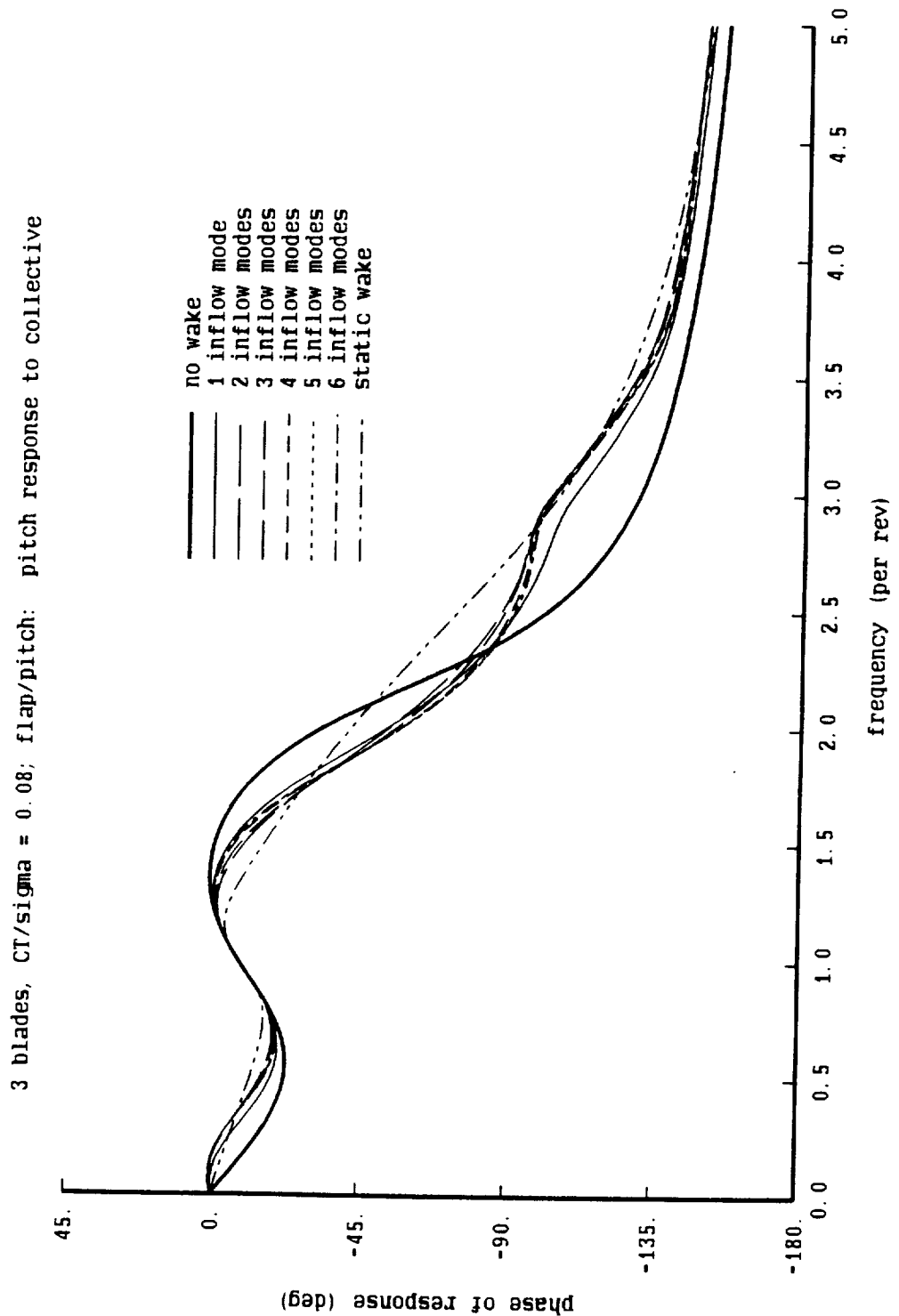


Figure 27e. Flap-pitch motion of hovering rotor with undistorted wake

3 blades, $CT/\sigma = 0.02$; flap/pitch: flap response to collective

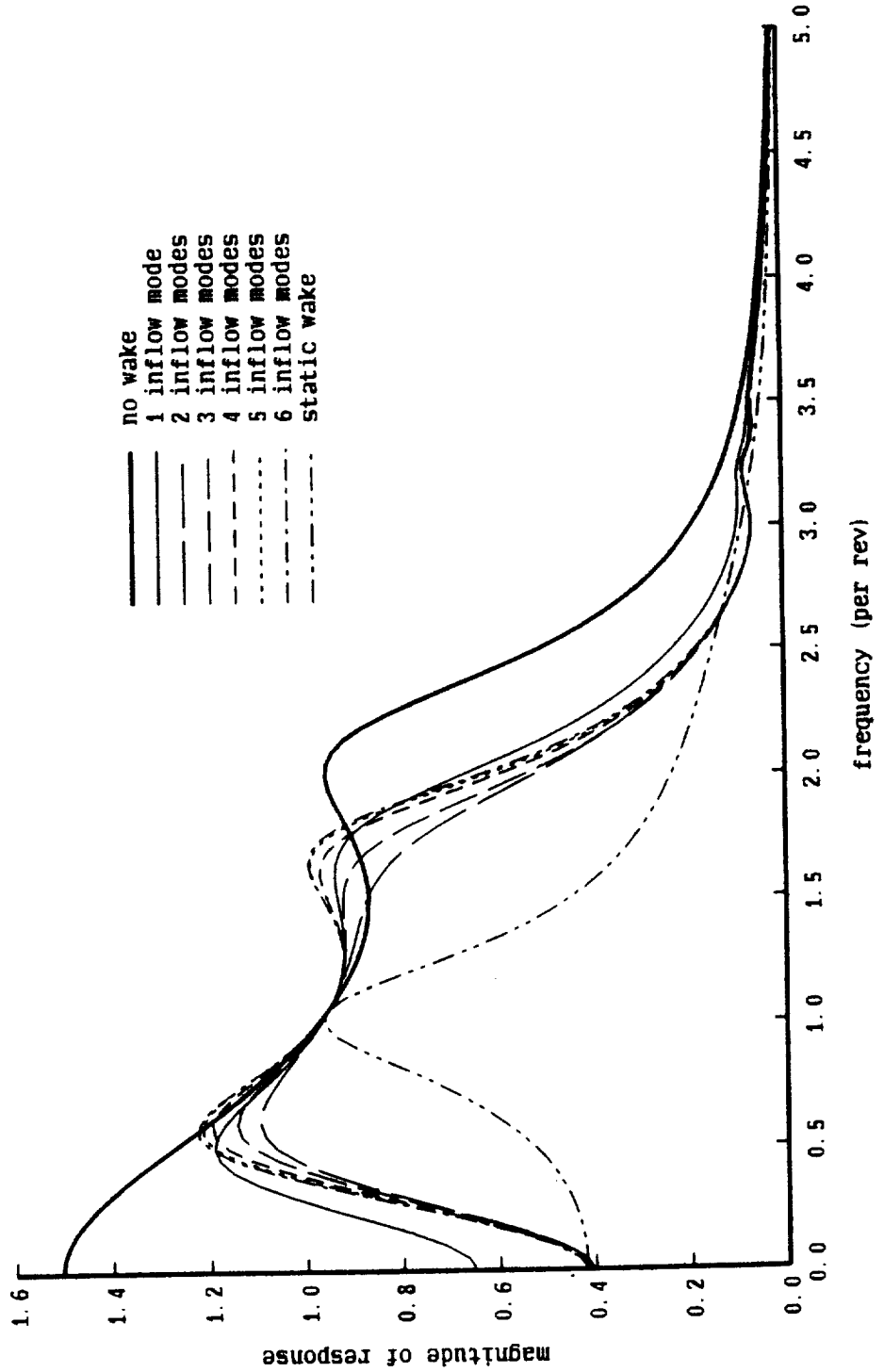


Figure 27f. Flap-pitch motion of hovering rotor with undistorted wake

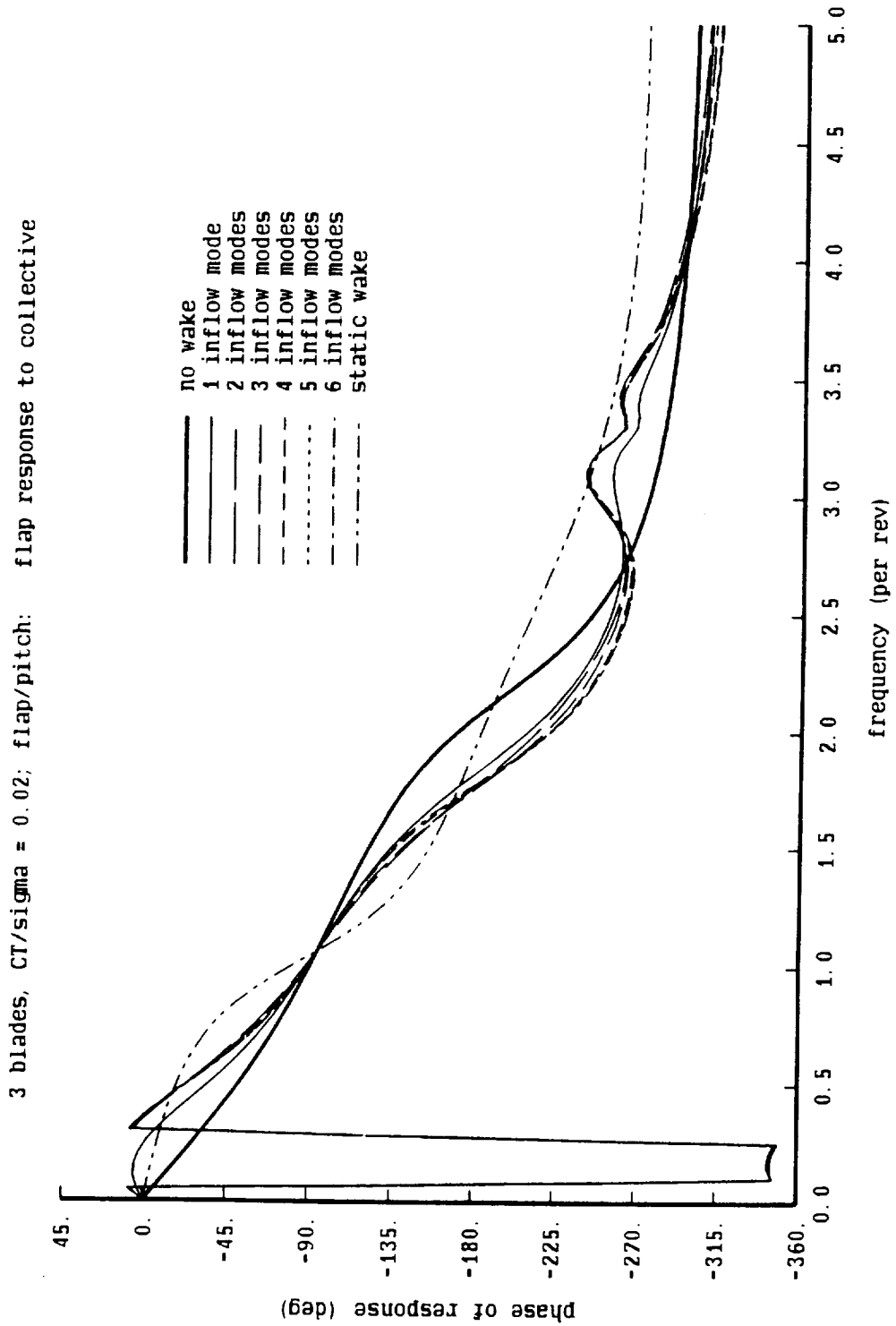


Figure 27g. Flap-pitch motion of hovering rotor with undistorted wake

3 blades, $CT/\sigma = 0.02$; flap/pitch: pitch response to collective

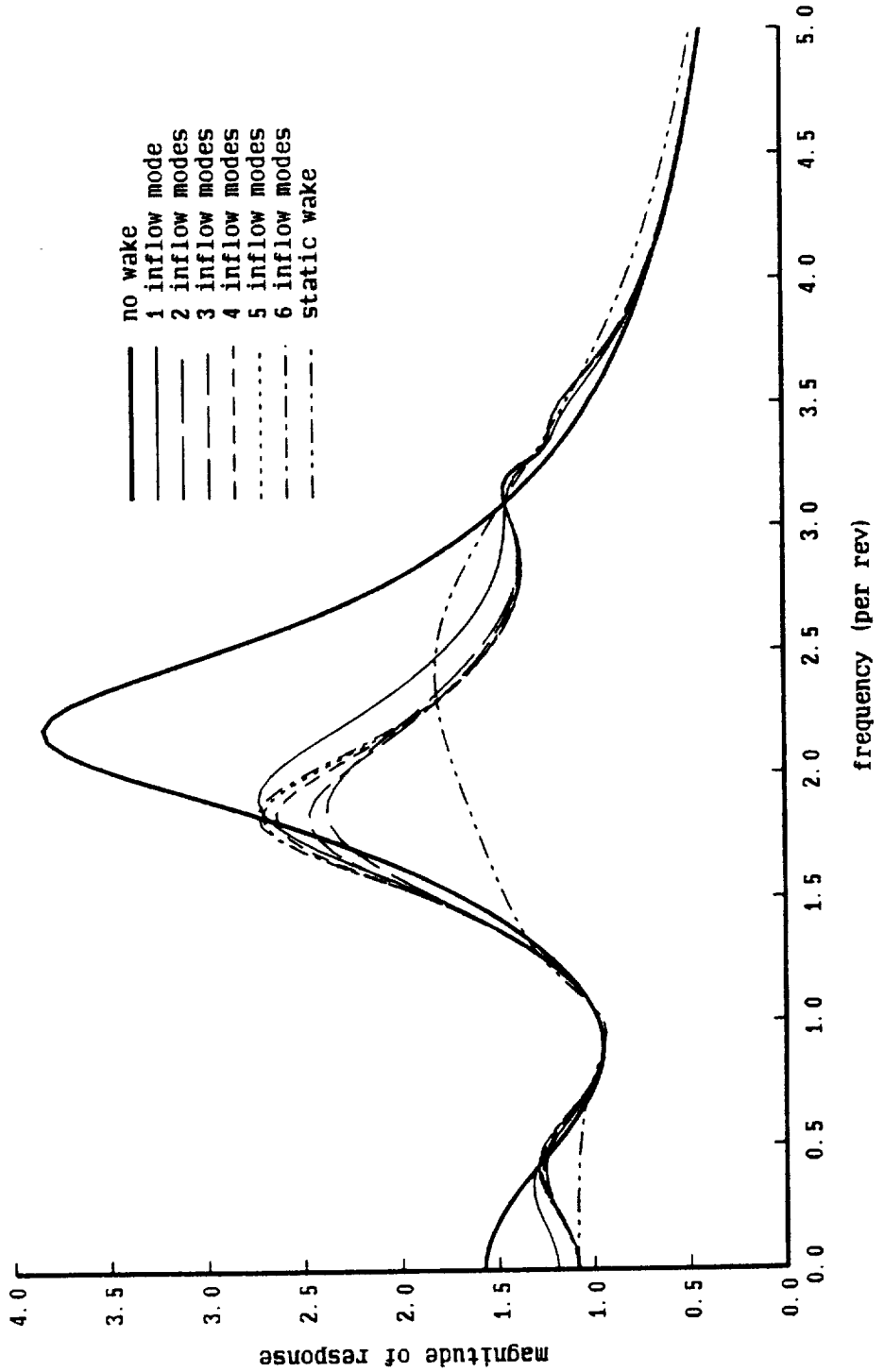


Figure 27h. Flap-pitch motion of hovering rotor with undistorted wake

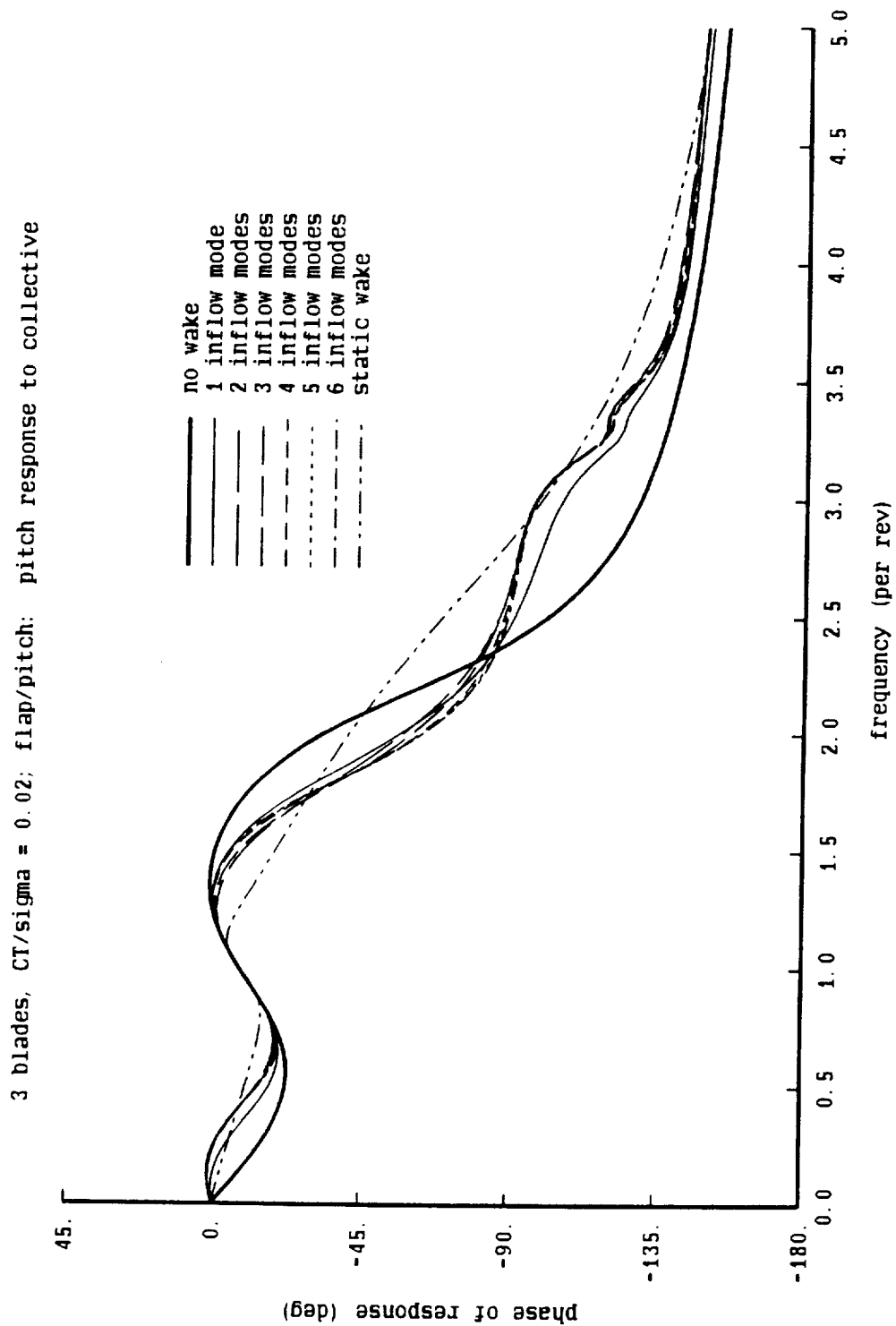


Figure 28a. Inflow response during flap motion; hovering rotor with undistorted wake

hovering rotor, undistorted wake; frequency = 0.0/rev
 3 blades, $CT/\sigma = 0.08$; inflow response to collective pitch

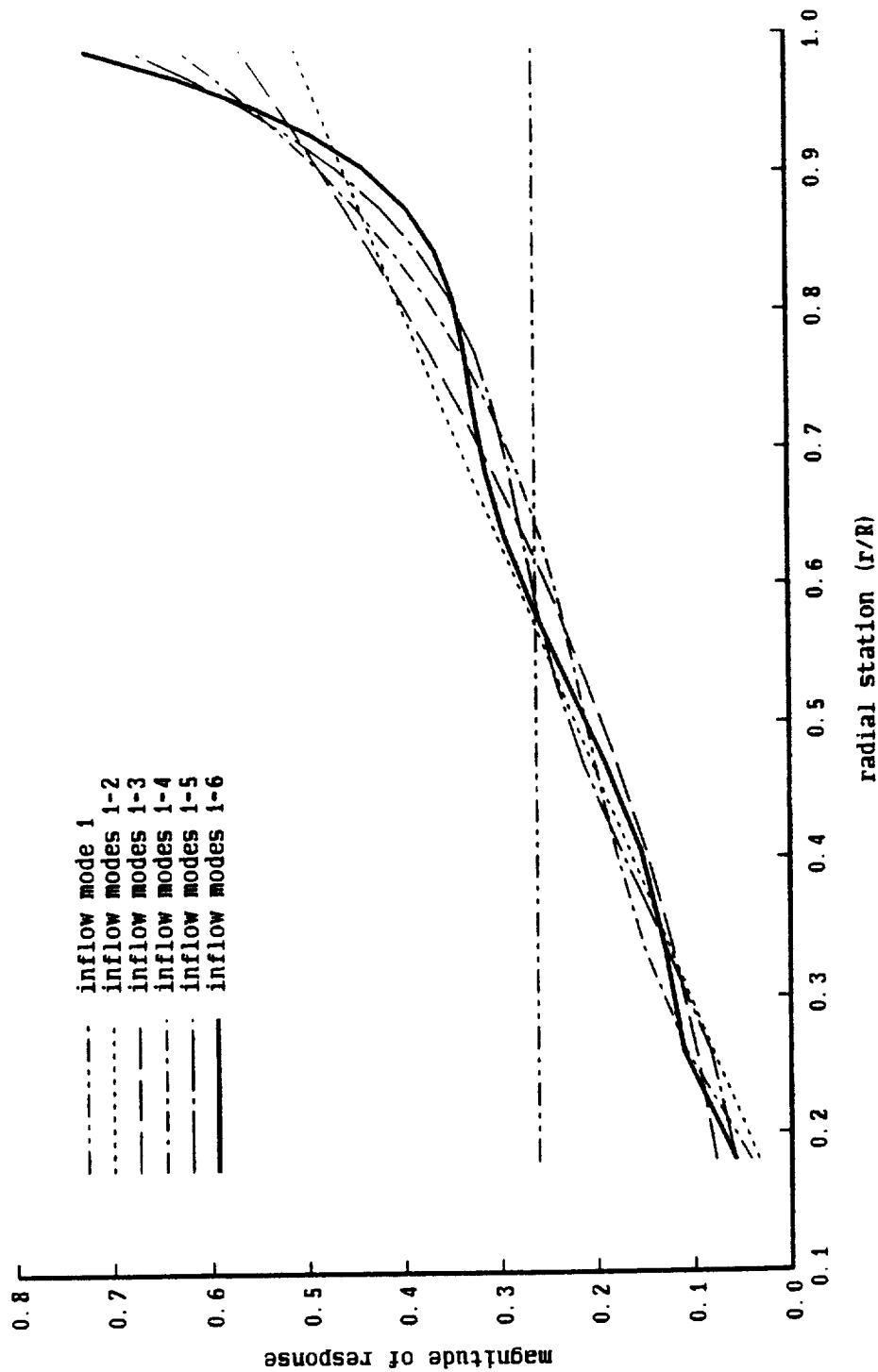


Figure 28b. Inflow response during flap motion; hovering rotor with undistorted wake

hovering rotor, undistorted wake; frequency = 0.40/rev

3 blades, $CT/\sigma = 0.08$; inflow response to collective pitch

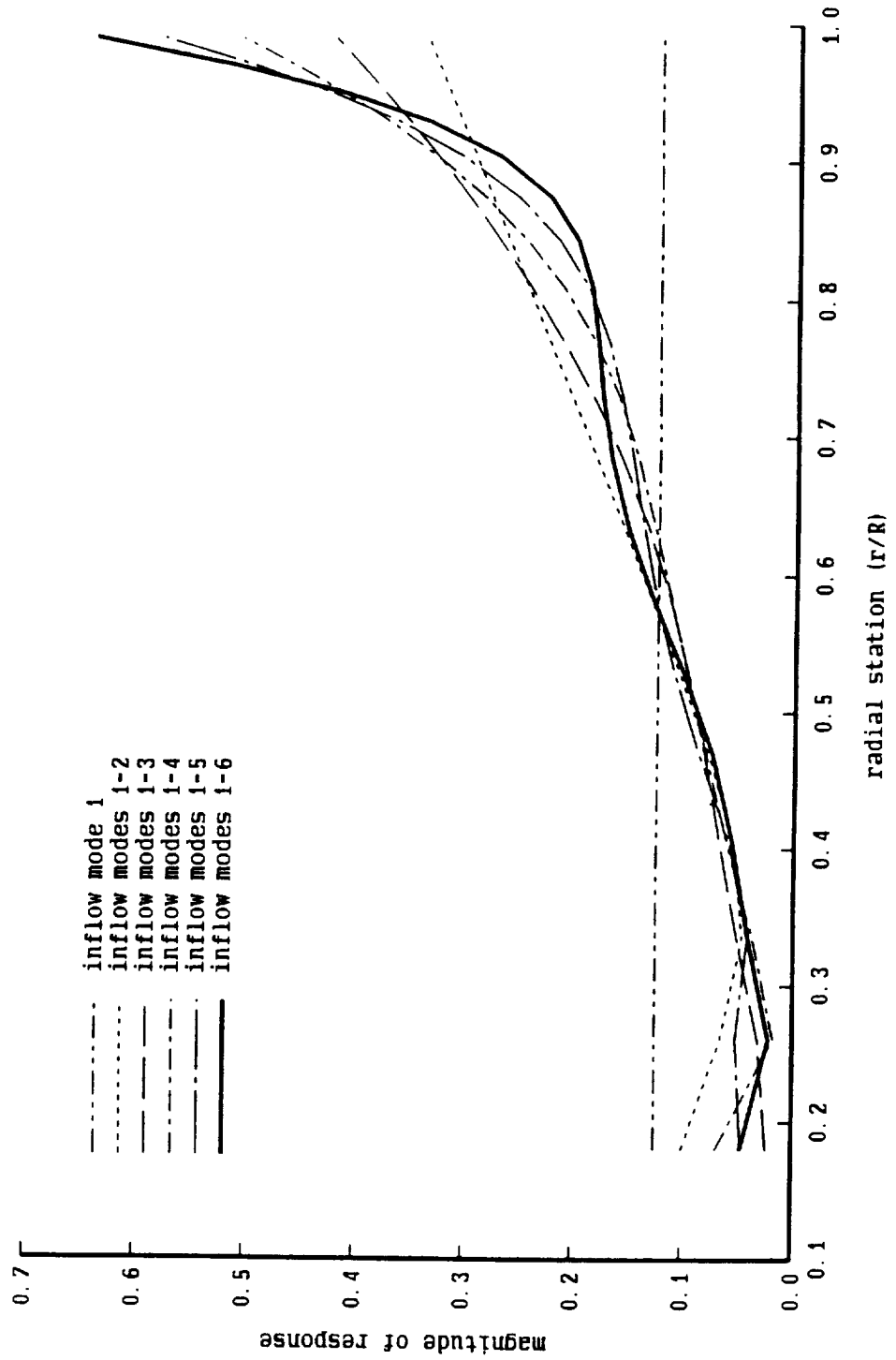


Figure 28c. Inflow response during flap motion; hovering rotor with undistorted wake

hovering rotor, undistorted wake; frequency = 2.25/rev
 3 blades, $CT/\sigma = 0.08$; inflow response to collective pitch

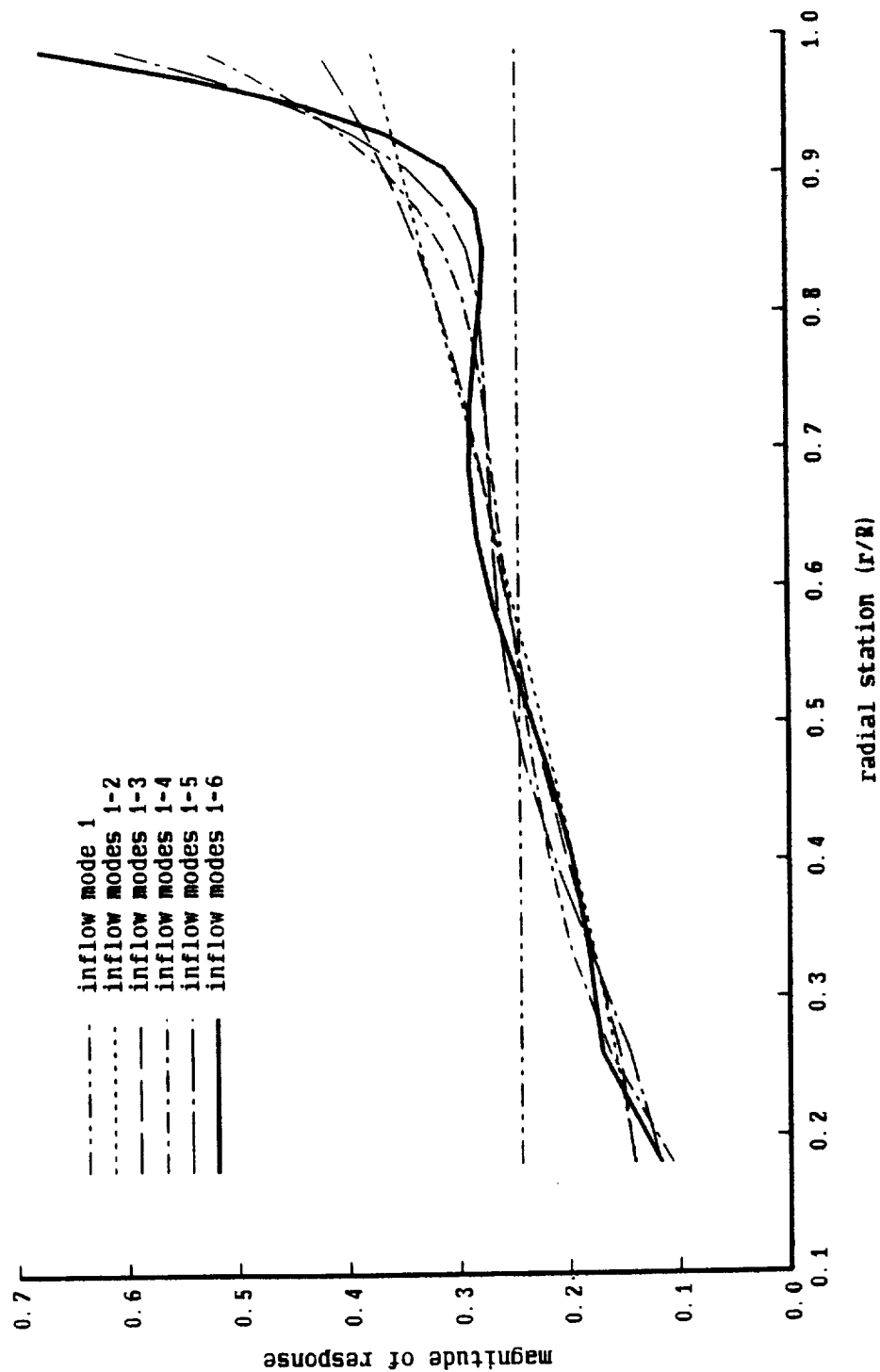


Figure 28d. Inflow response during flap motion; hovering rotor with undistorted wake

hovering rotor, undistorted wake; frequency = 0.40/rev

3 blades, $CT/\sigma = 0.08$; inflow response to collective pitch

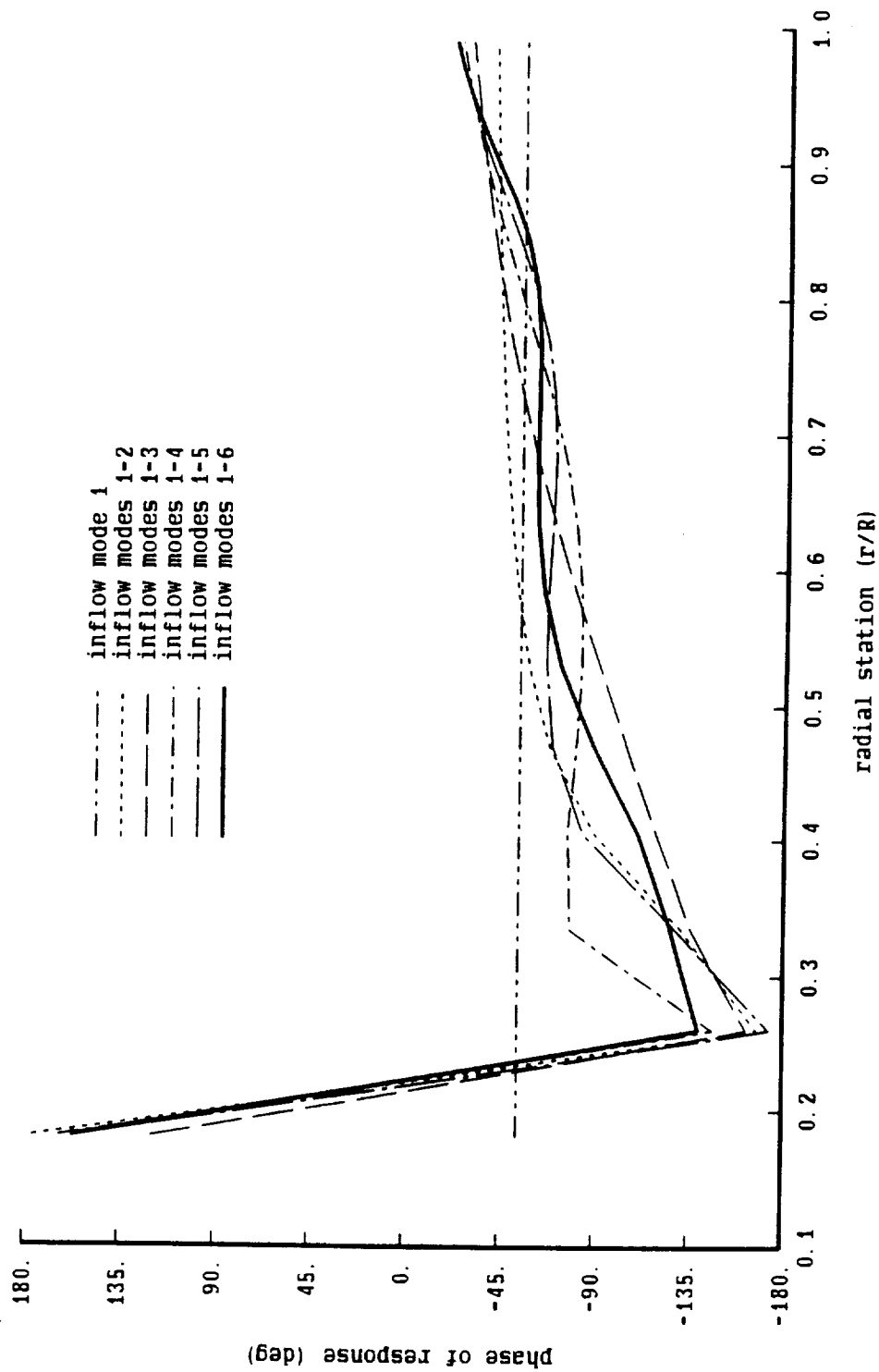


Figure 28e. Inflow response during flap motion; hovering rotor with undistorted wake

hovering rotor, undistorted wake; frequency = 2.25/rev
 3 blades, $CT/\sigma = 0.08$; inflow response to collective pitch

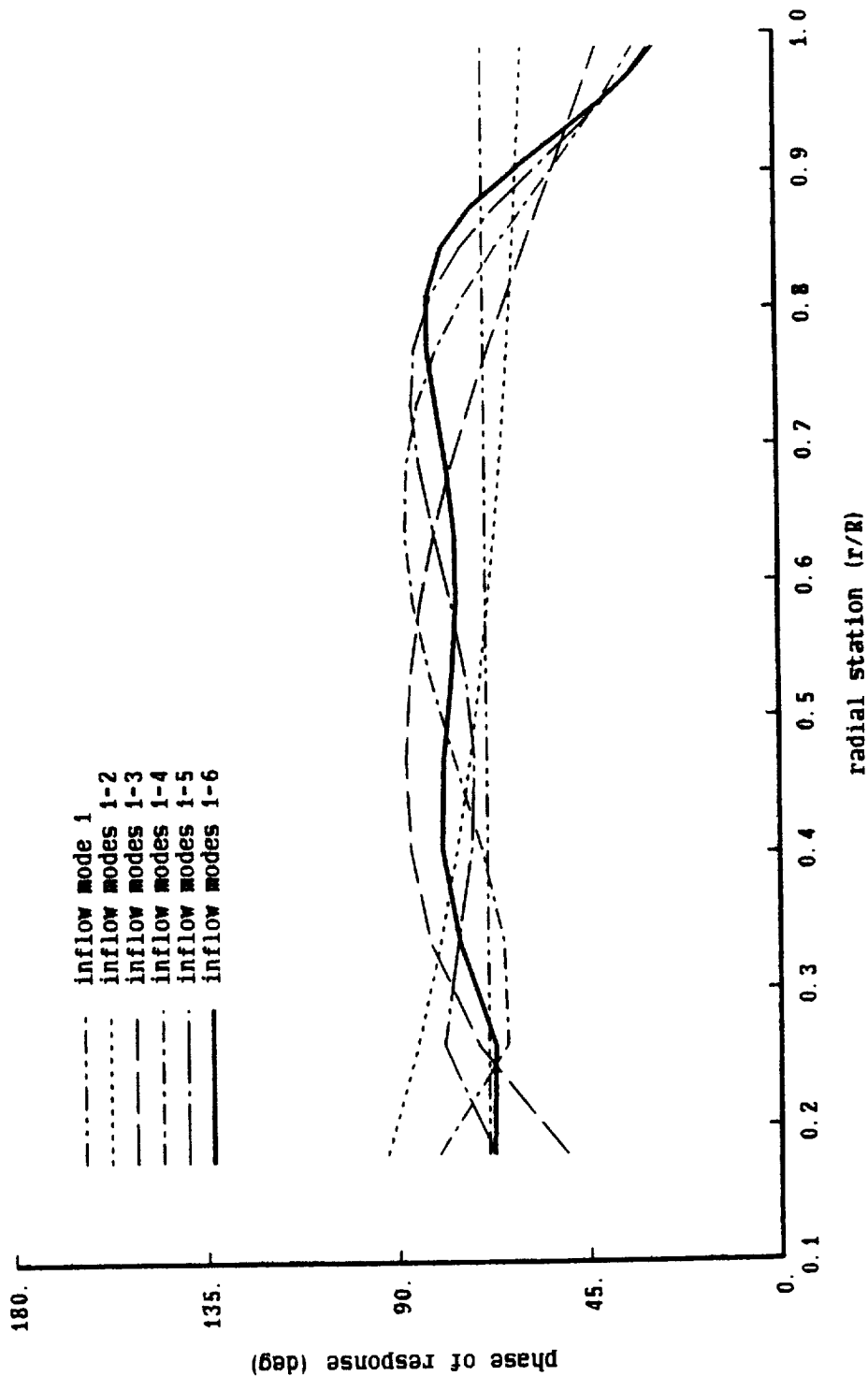


Figure 29a. Inflow response during flap motion; hovering rotor with undistorted wake

hovering rotor, undistorted wake; frequency = 0.0/rev
 3 blades, $CT/\sigma = 0.08$; inflow response to vertical hub velocity

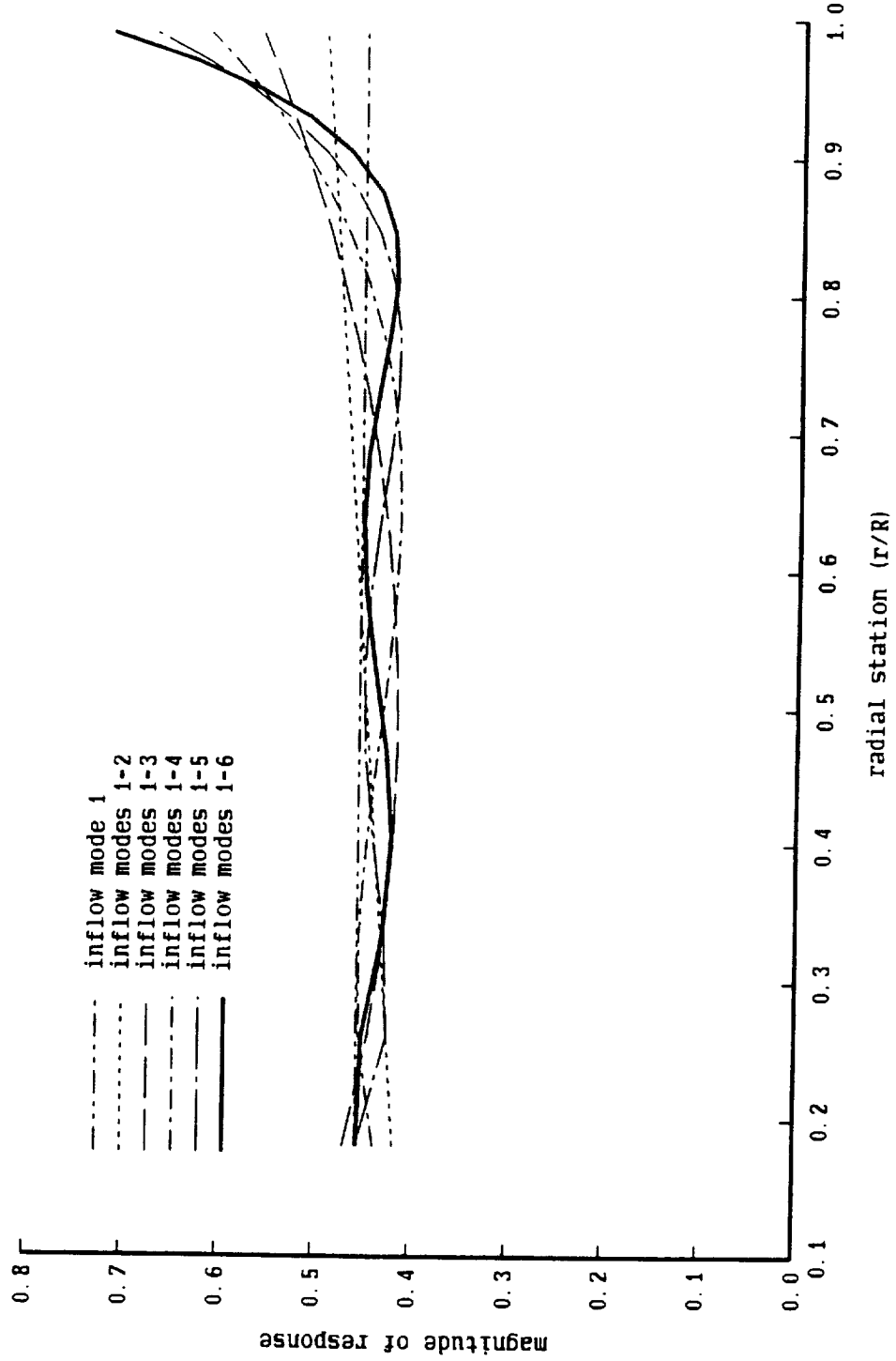


Figure 29b. Inflow response during flap motion; hovering rotor with undistorted wake

hovering rotor, undistorted wake; frequency = 0.40/rev
 3 blades, $CT/\sigma = 0.08$; inflow response to vertical hub velocity

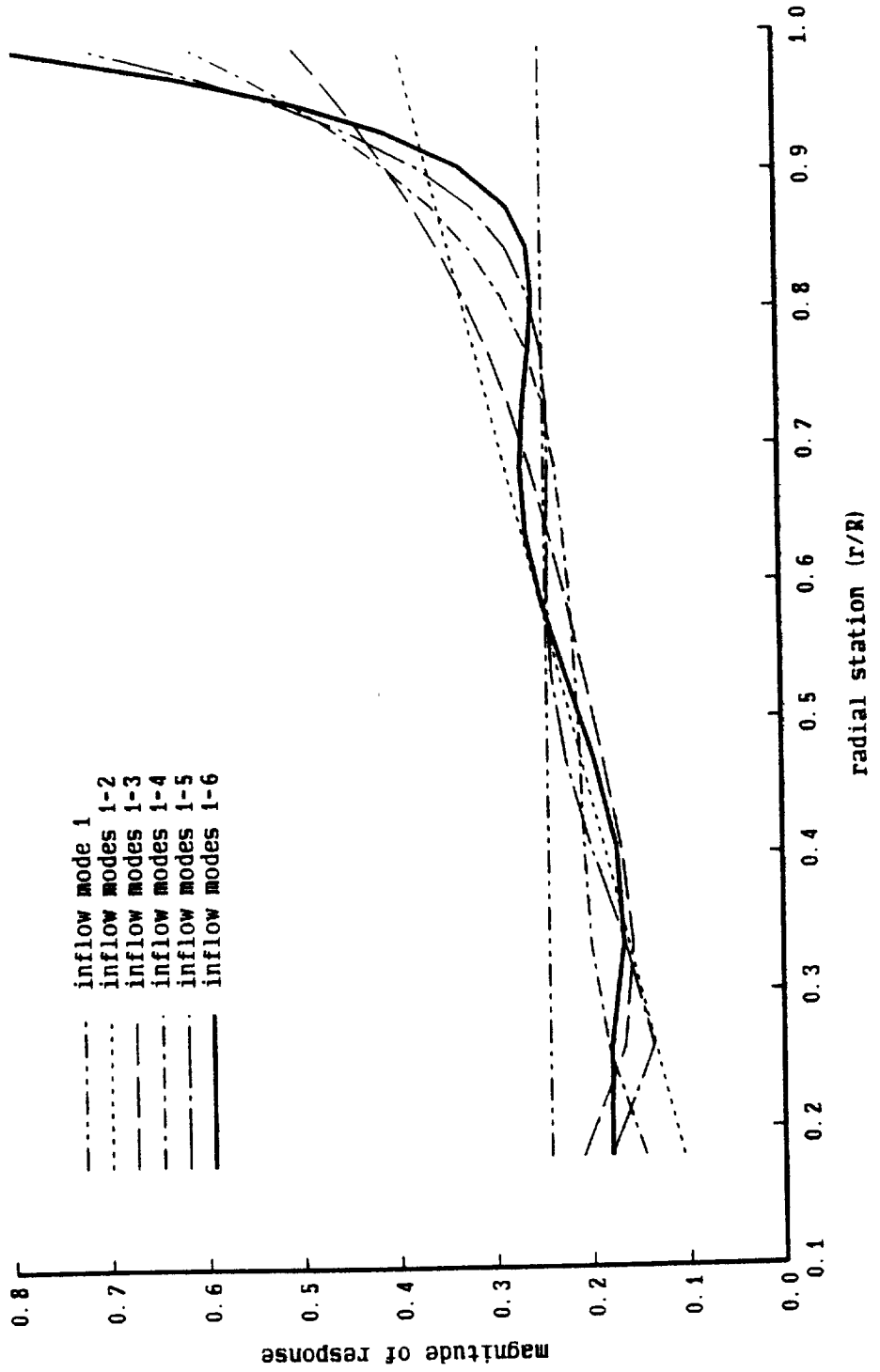


Figure 29c. Inflow response during flap motion; hovering rotor with undistorted wake

hovering rotor, undistorted wake; frequency = 2.25/rev

3 blades, $CT/\sigma = 0.08$; inflow response to vertical hub velocity

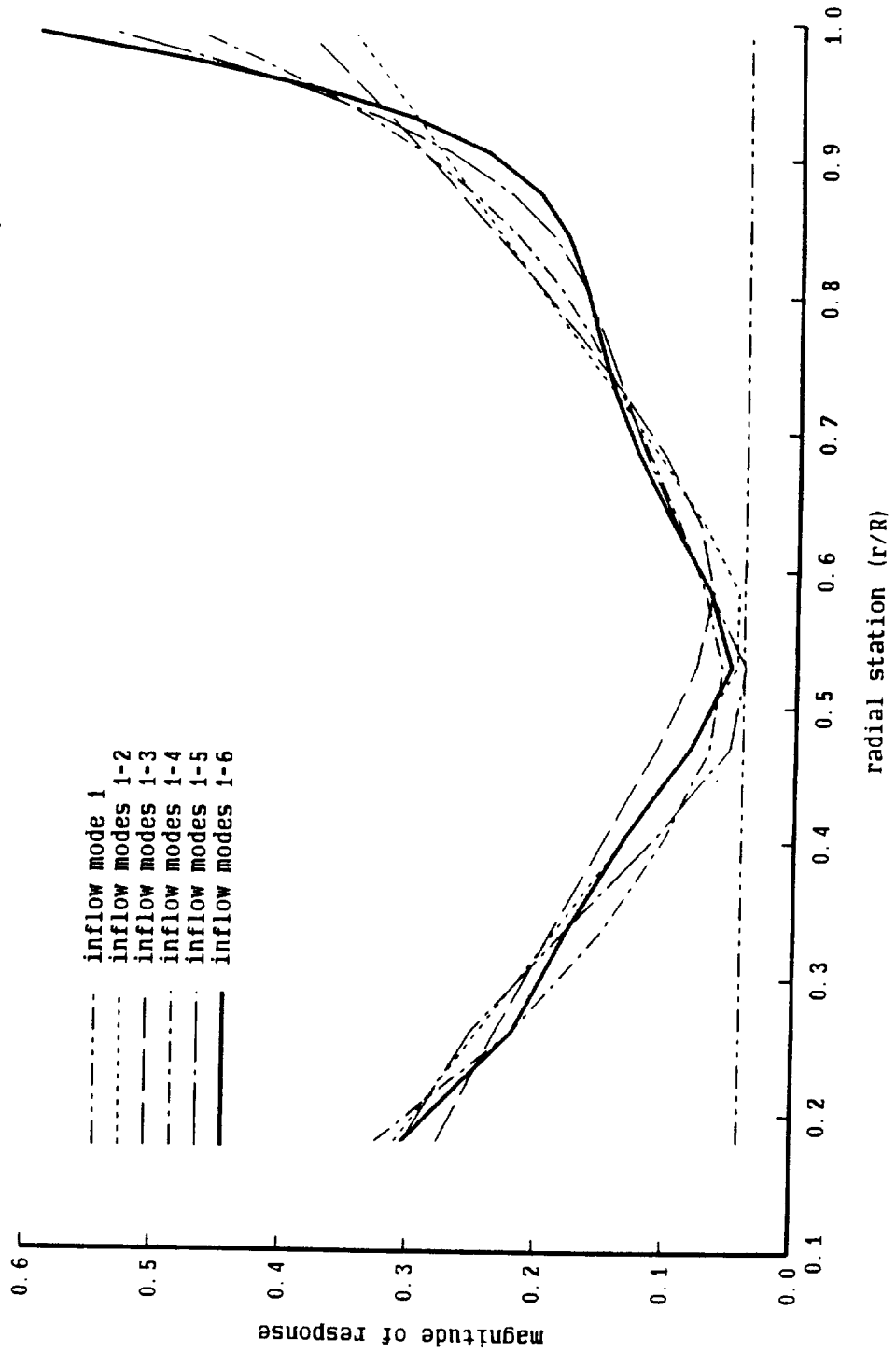


Figure 29d. Inflow response during flap motion; hovering rotor with undistorted wake

hovering rotor, undistorted wake; frequency = 0.40/rev

3 blades, $CT/\sigma = 0.08$; inflow response to vertical hub velocity

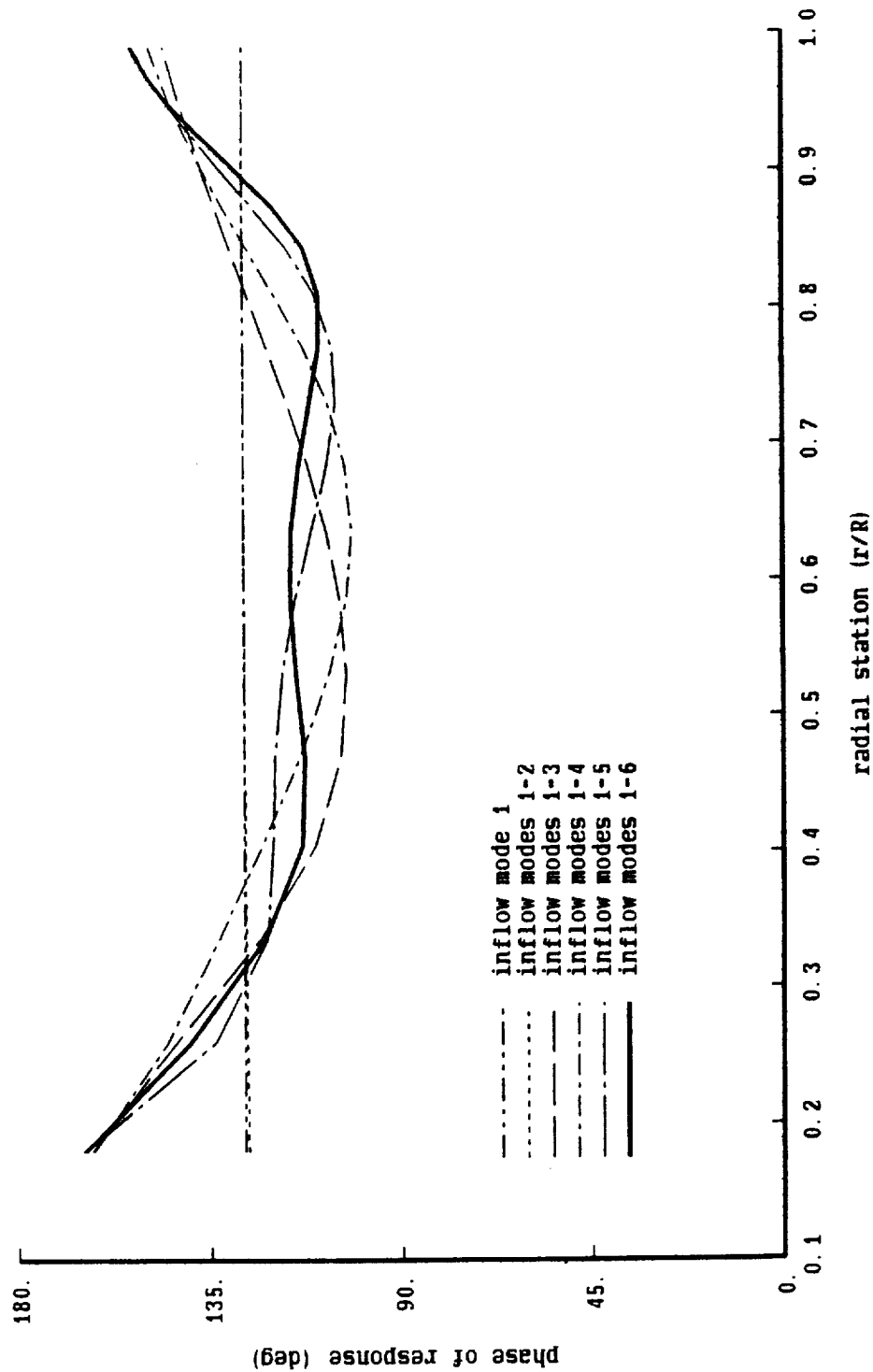


Figure 29e. Inflow response during flap motion; hovering rotor with undistorted wake

hovering rotor, undistorted wake; frequency = 2.25/rev

3 blades, $CT/\sigma = 0.08$; inflow response to vertical hub velocity

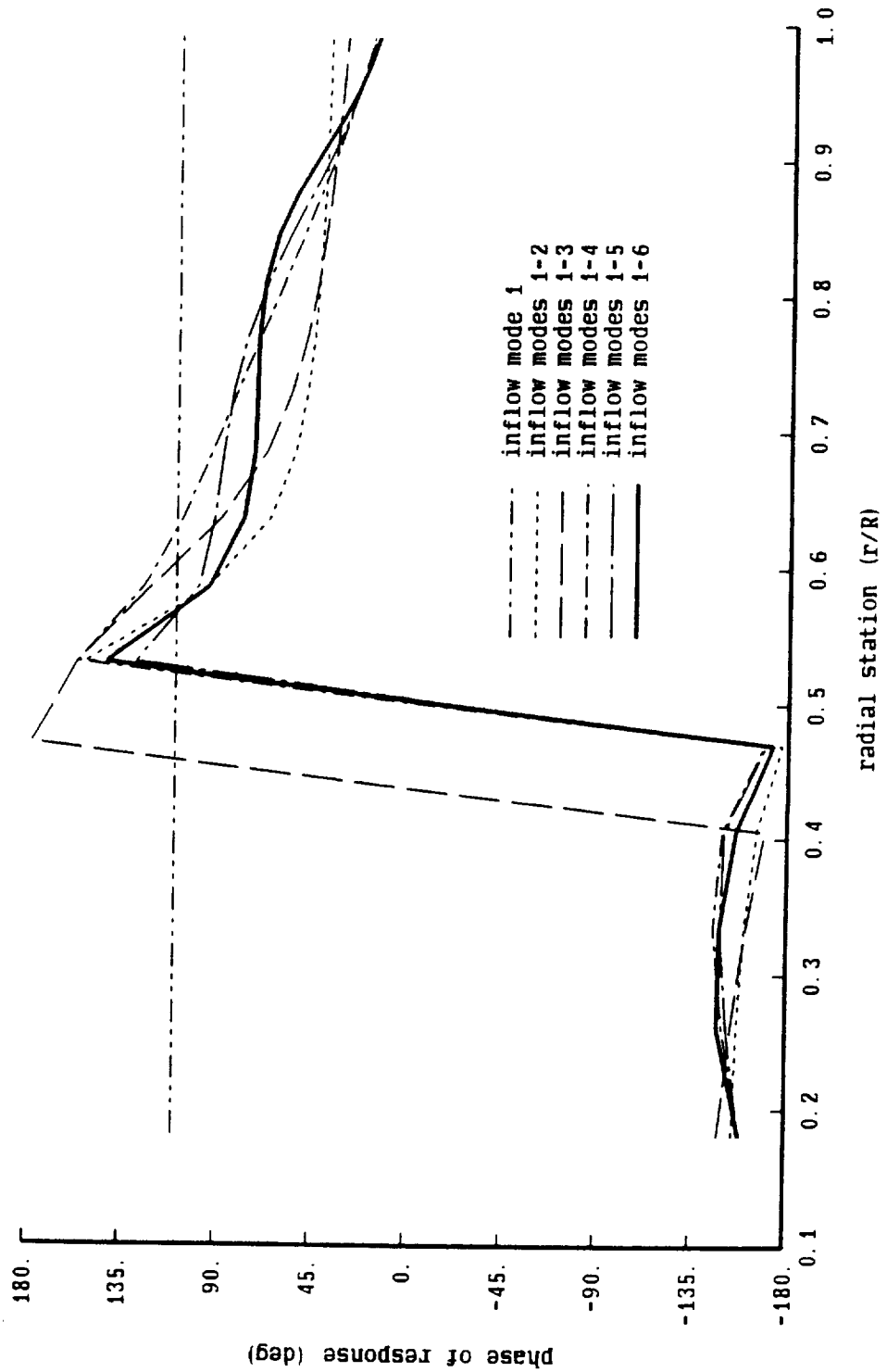


Figure 30. Impulse response of hovering rotor with rolled up wake

nonrotating frame, 3 blades; uniform inflow and circulation at 0.93R

----- shed wake, $\lambda=0$ from $\gamma=0$; $h(0)=1.79$
——— trailed wake, $\lambda=0$ from $\gamma=0$; $h(0)=7.14$

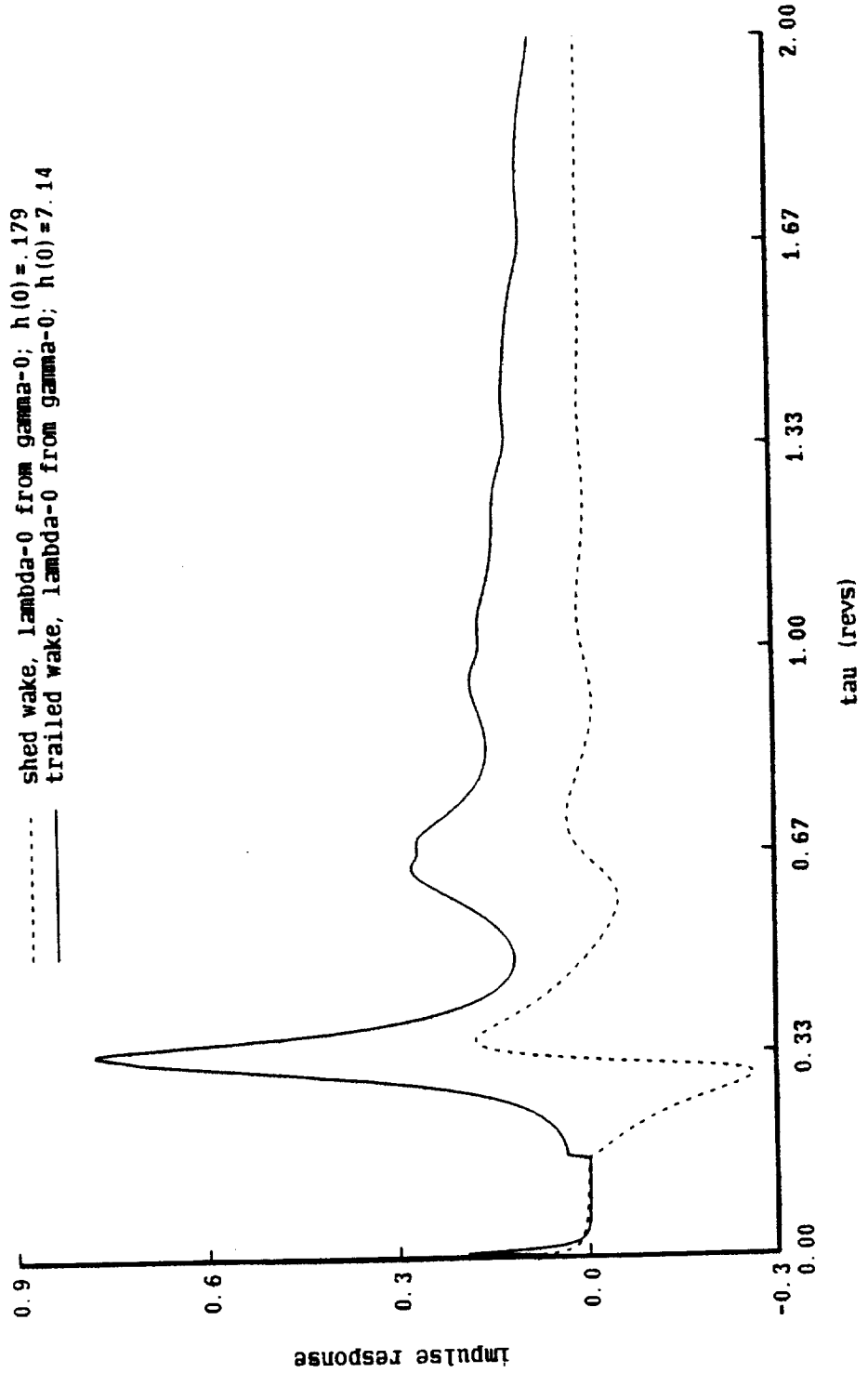


Figure 31a. System function of hovering rotor with rolled up wake

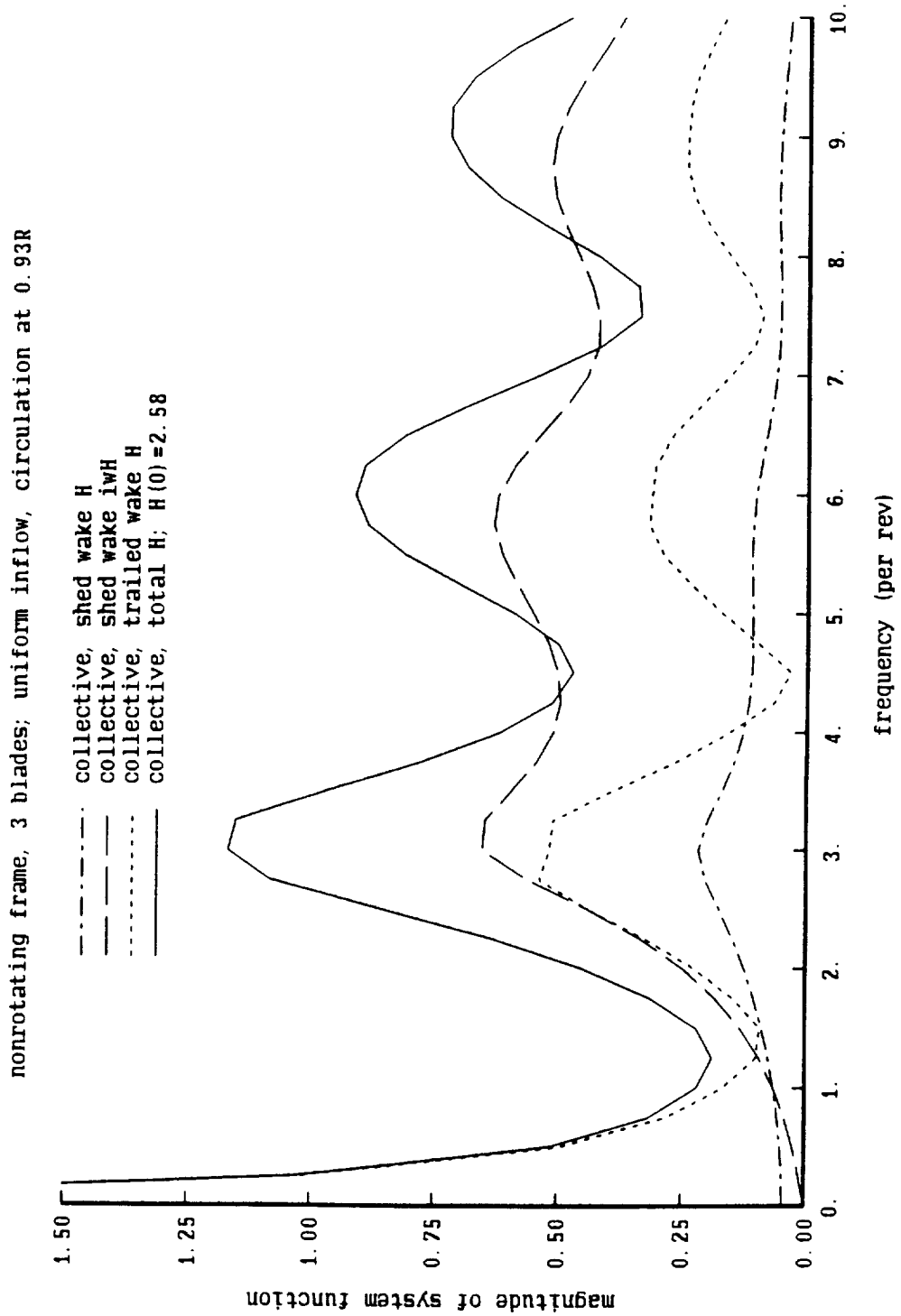


Figure 31b. System function of hovering rotor with rolled up wake

nonrotating frame, 3 blades; uniform inflow, circulation at 0.93R

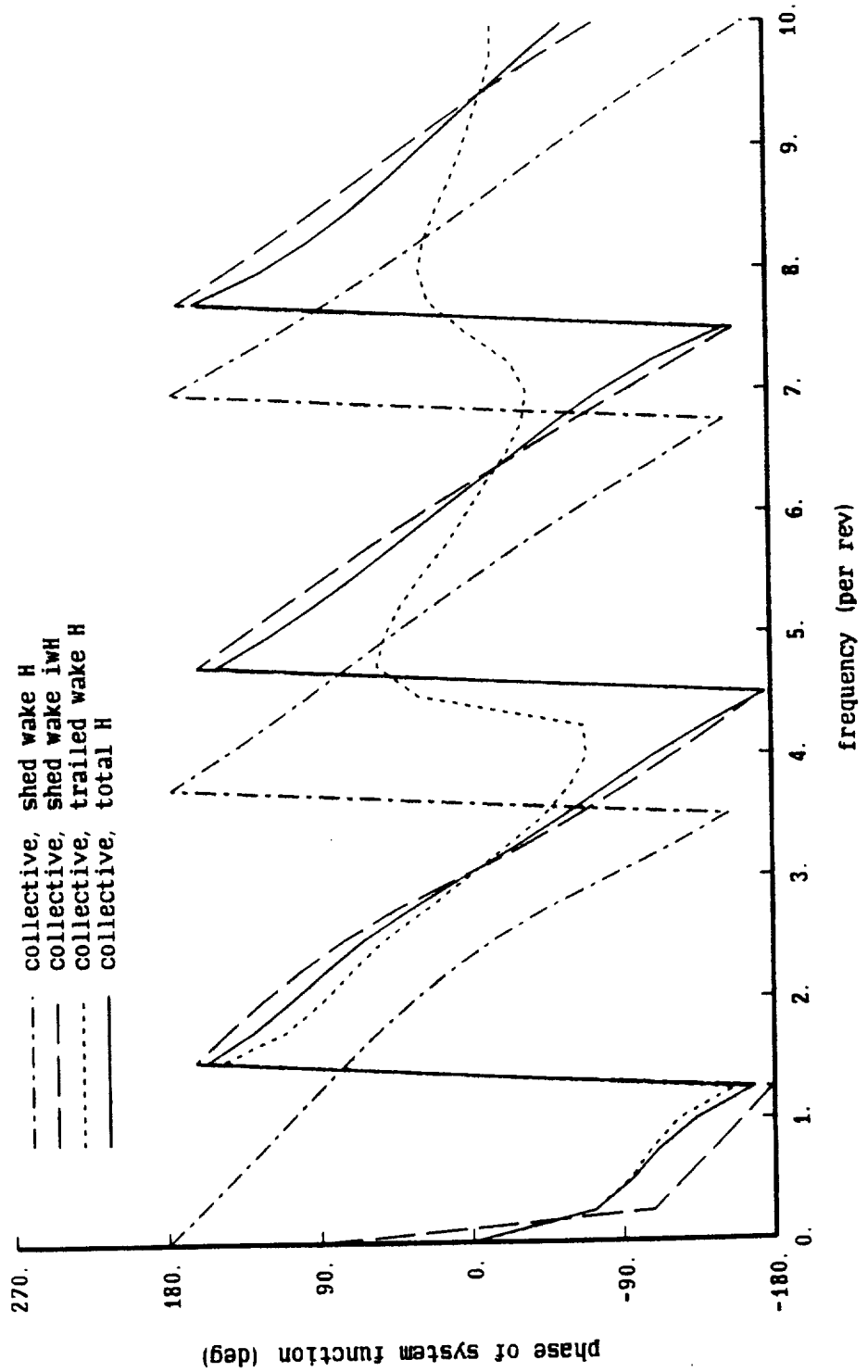


Figure 32a. System function of hovering rotor with rolled up wake

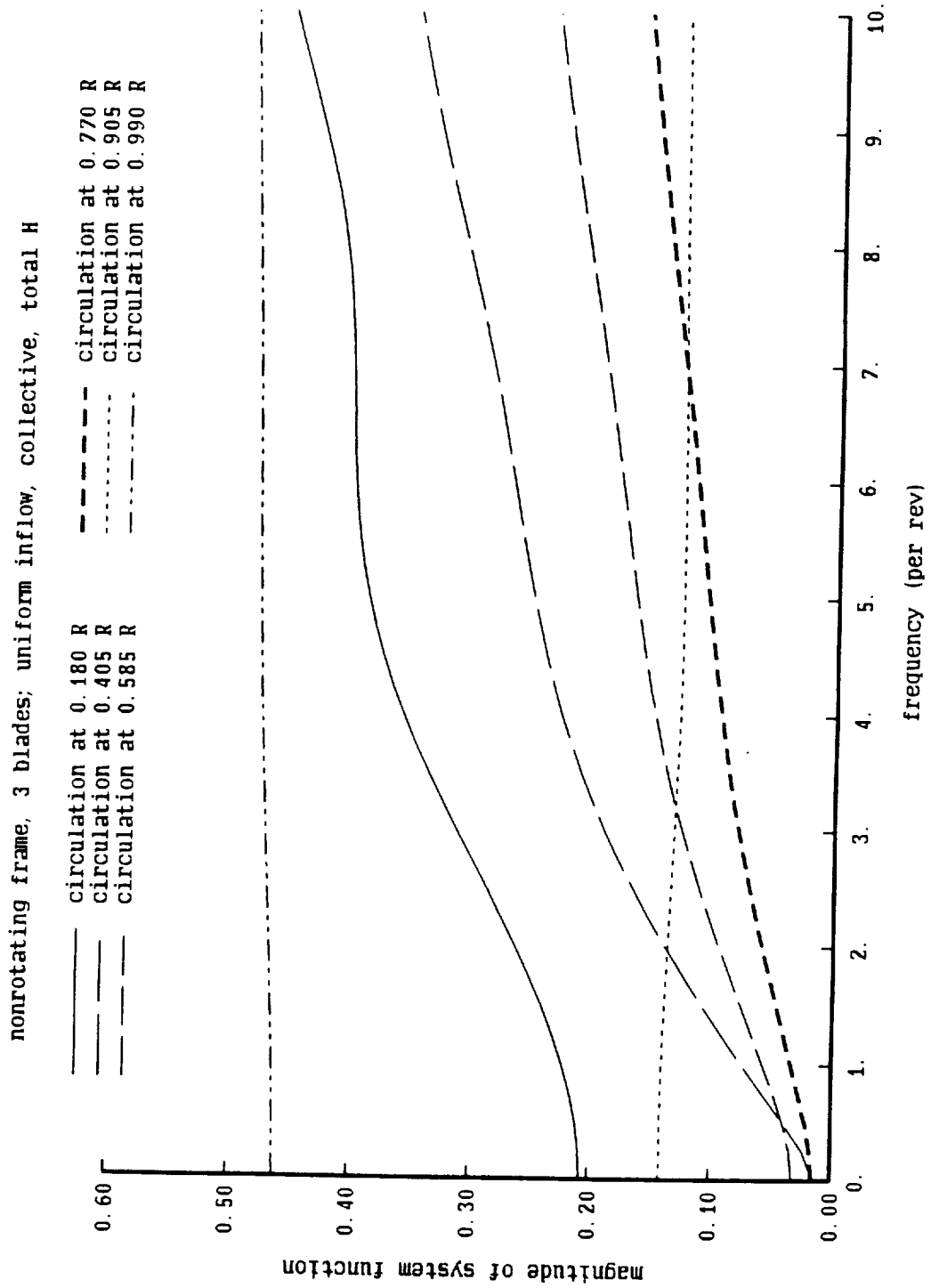


Figure 32b. System function of hovering rotor with rolled up wake

nonrotating frame, 3 blades; uniform inflow, collective, total H

- circulation at 0.180 R
- circulation at 0.405 R
- circulation at 0.585 R
- - - circulation at 0.770 R
- · · circulation at 0.905 R
- · - · - circulation at 0.990 R

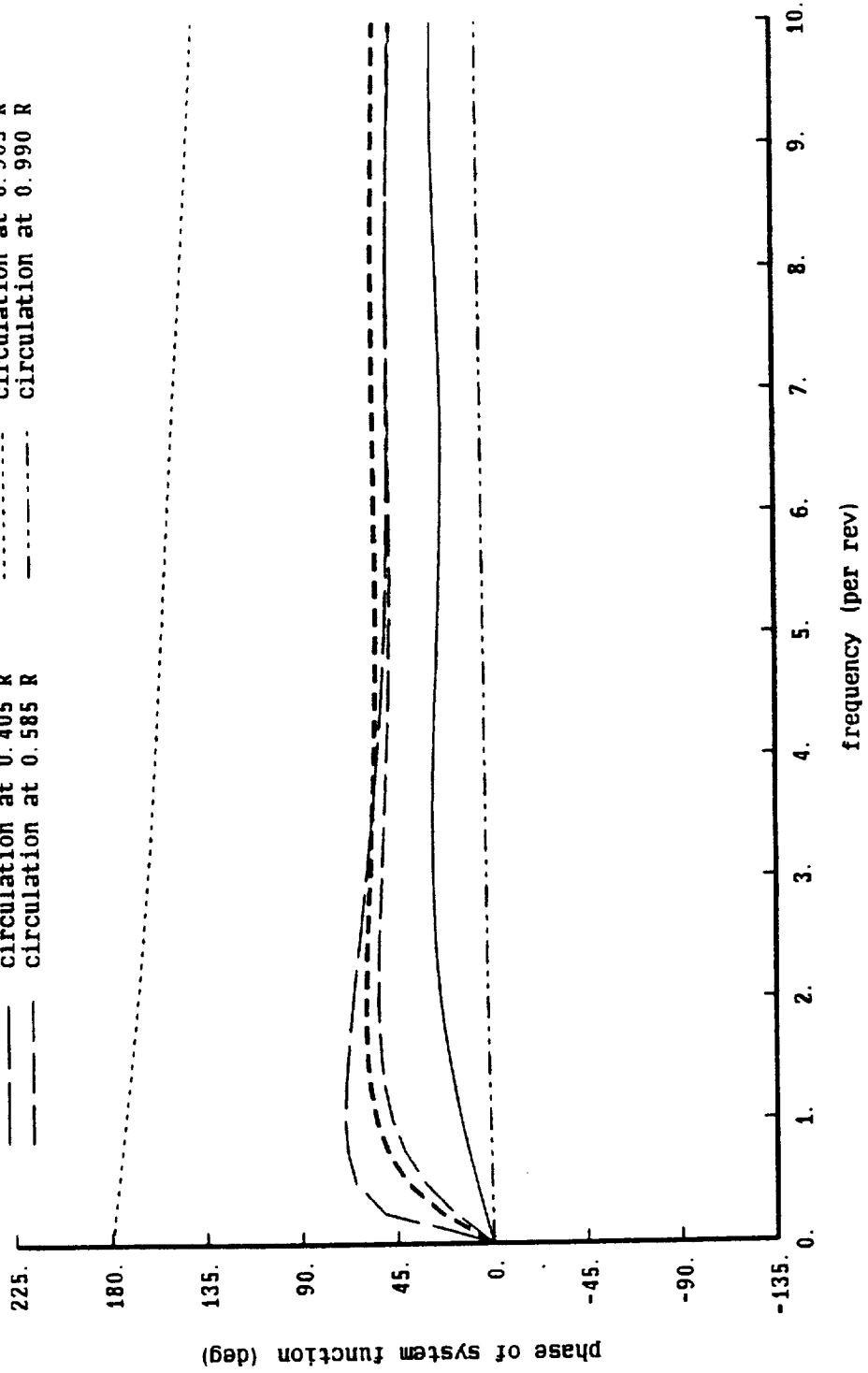


Figure 33a. System function of hovering rotor with rolled up wake

nonrotating frame, 3 blades, $CT/\sigma = 0.08$; rolled up, circ at 0.93R

six inflow modes, order = 6; frequency range = 0-1.5 (wt=16), 1.5-4.5 (wt=1)

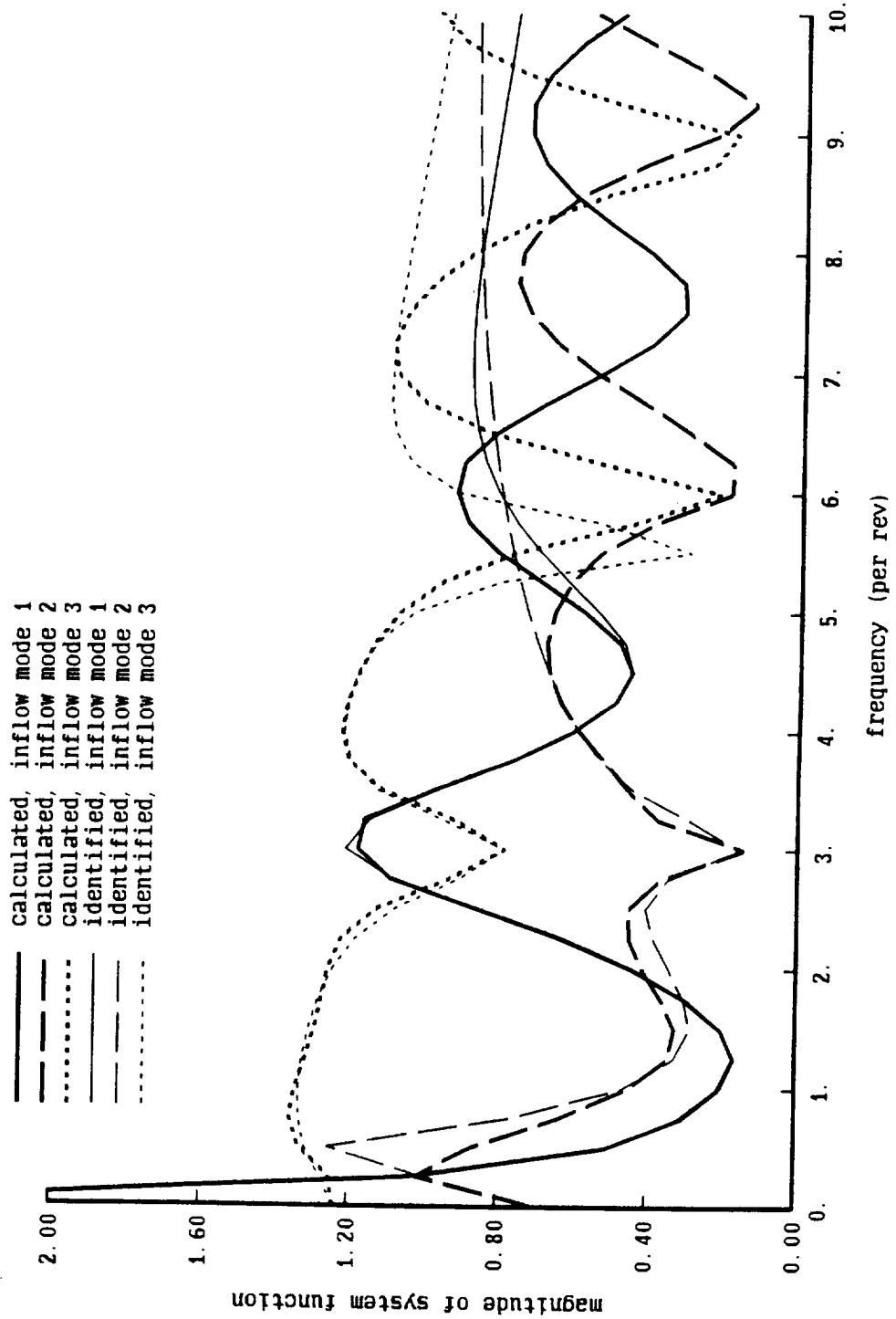


Figure 33b. System function of hovering rotor with rolled up wake

nonrotating frame, 3 blades, $CT/\sigma = 0.08$; rolled up, circ at 0.93R
 six inflow modes, order = 6; frequency range = 0-1.5 (wt=16), 1.5-4.5 (wt=1)

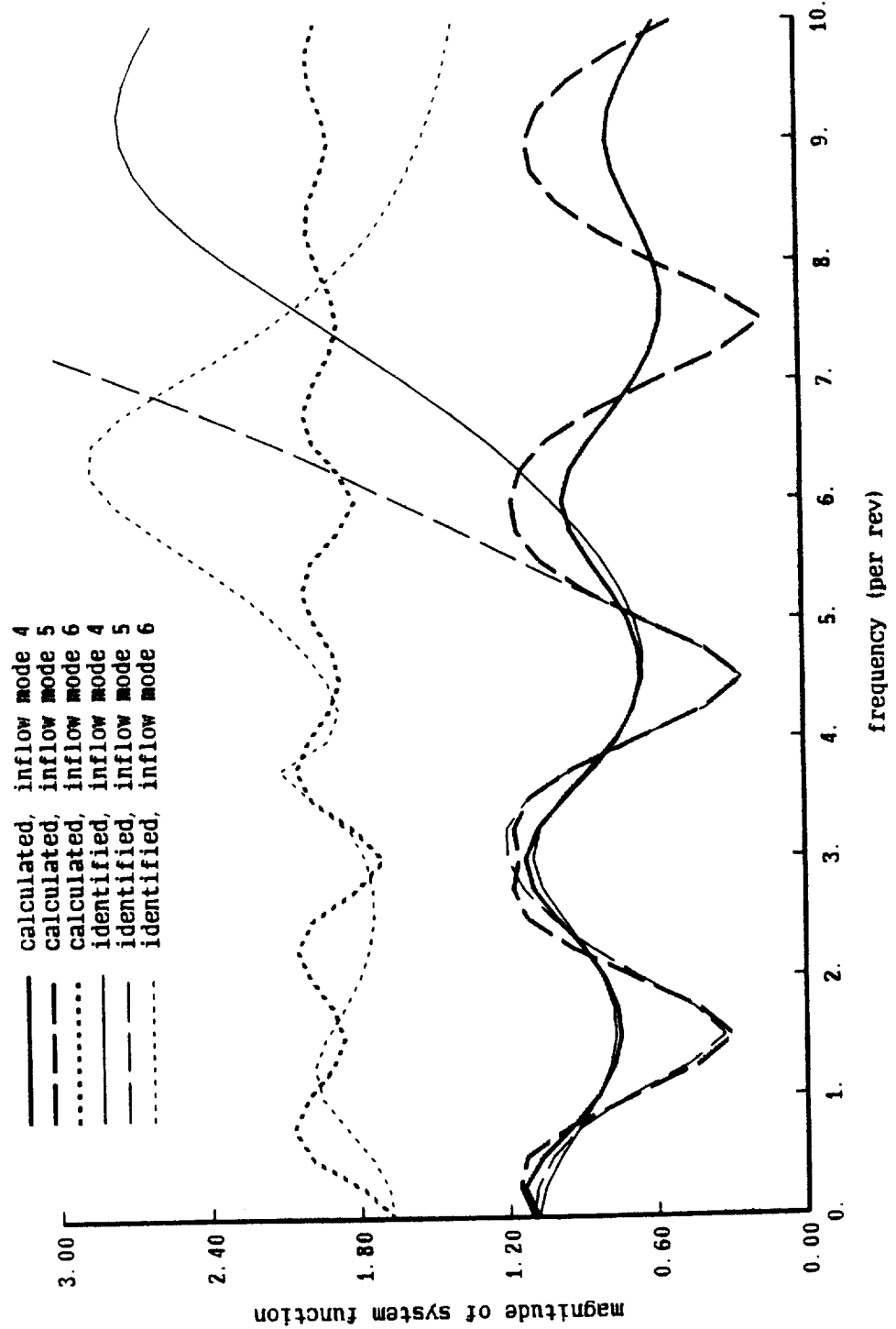


Figure 33c. System function of hovering rotor with rolled up wake

nonrotating frame, 3 blades, $CT/\sigma = 0.08$; rolled up, circ at 0.93R
 six inflow modes, order = 6; frequency range = 0-1.5 (wt=16), 1.5-4.5 (wt=1)

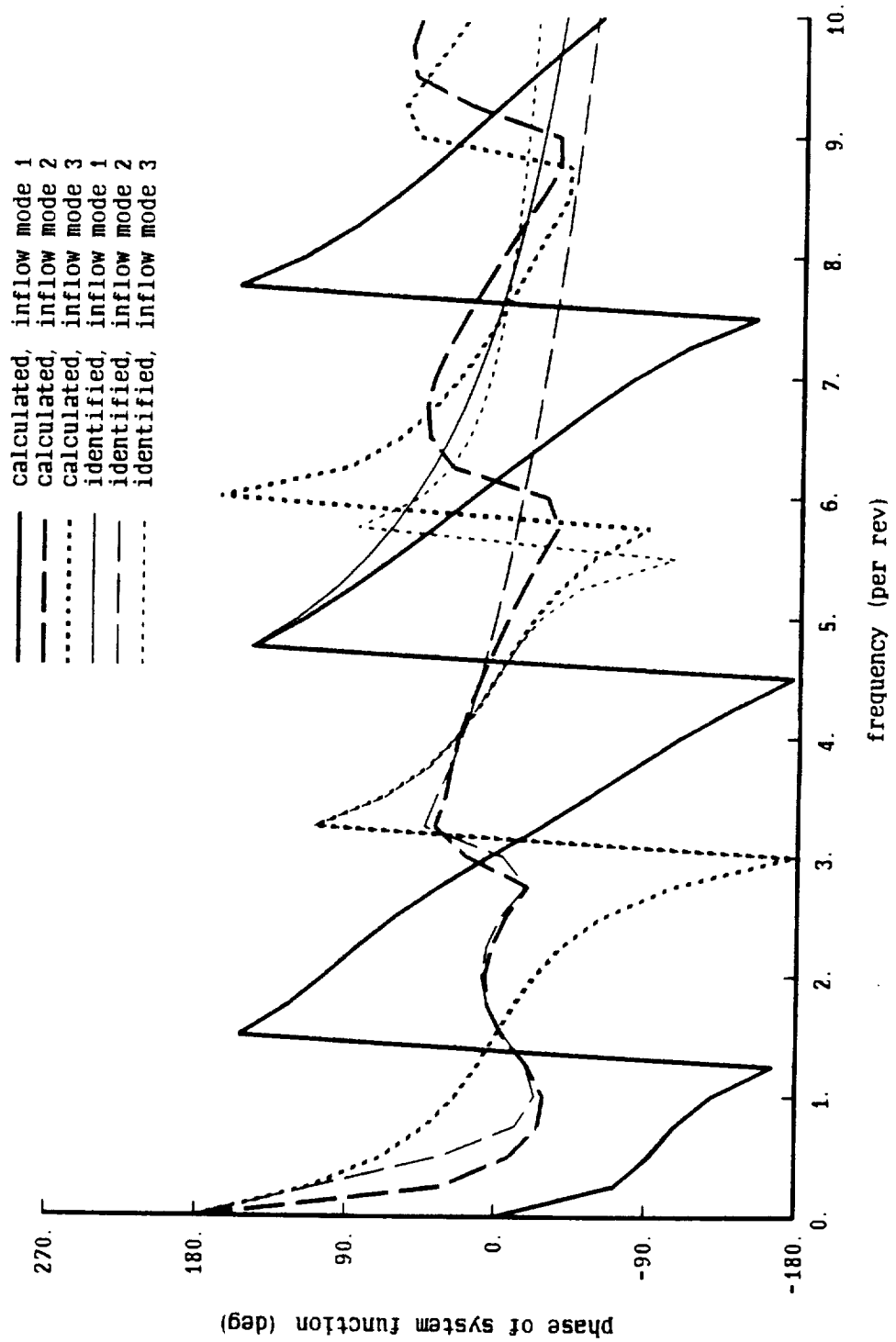


Figure 33d. System function of hovering rotor with rolled up wake

nonrotating frame, 3 blades, $CT/\sigma = 0.08$; rolled up, circ at 0.93R

six inflow modes, order = 6; frequency range = 0-1.5 (wt=16), 1.5-4.5 (wt=1)

- calculated, inflow mode 4
- - - calculated, inflow mode 5
- calculated, inflow mode 6
- identified, inflow mode 4
- - - identified, inflow mode 5
- identified, inflow mode 6

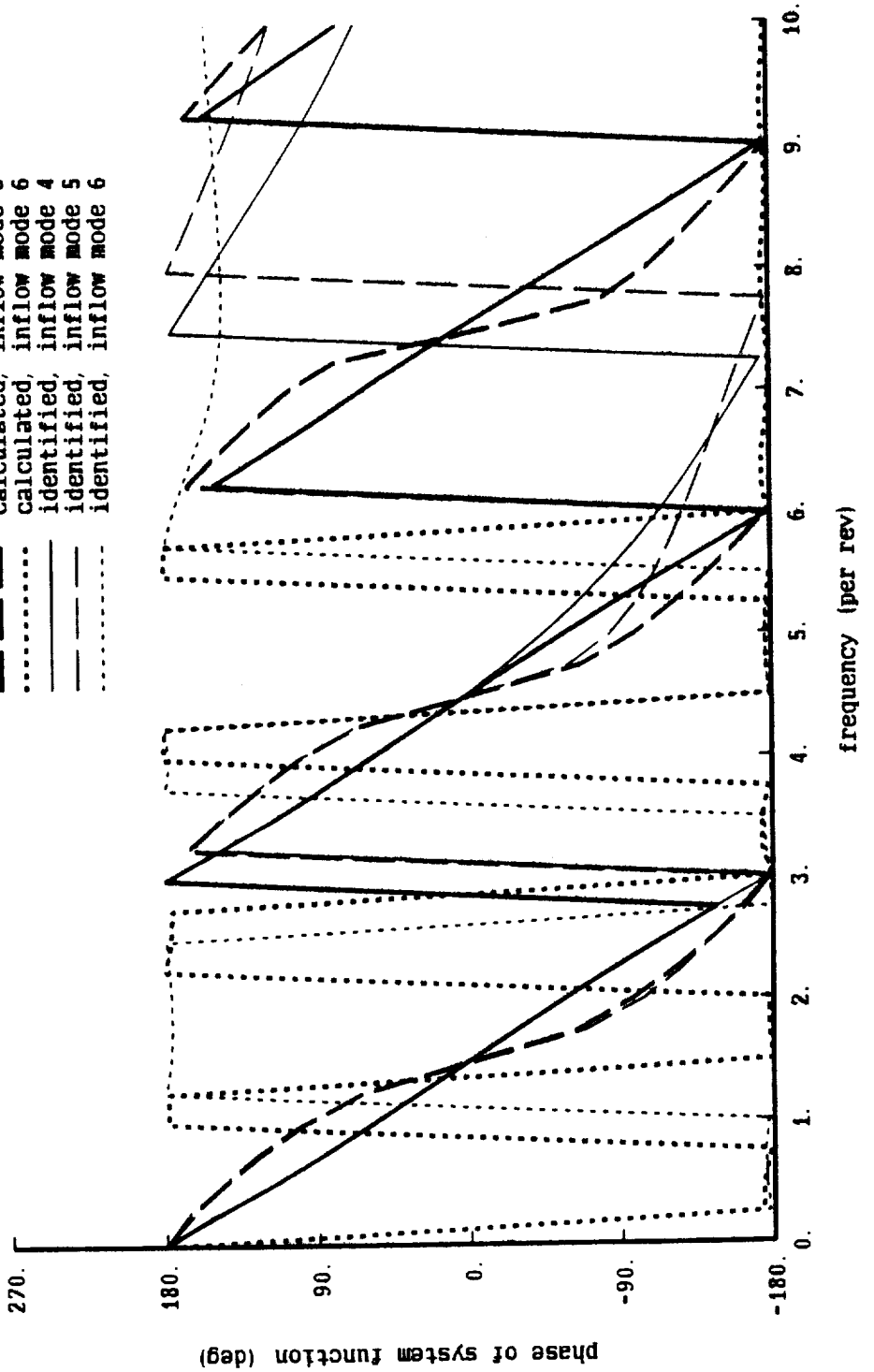


Figure 34a. Flap motion of hovering rotor with rolled up wake

3 blades, $CT/\sigma = 0.08$; coning response to collective pitch

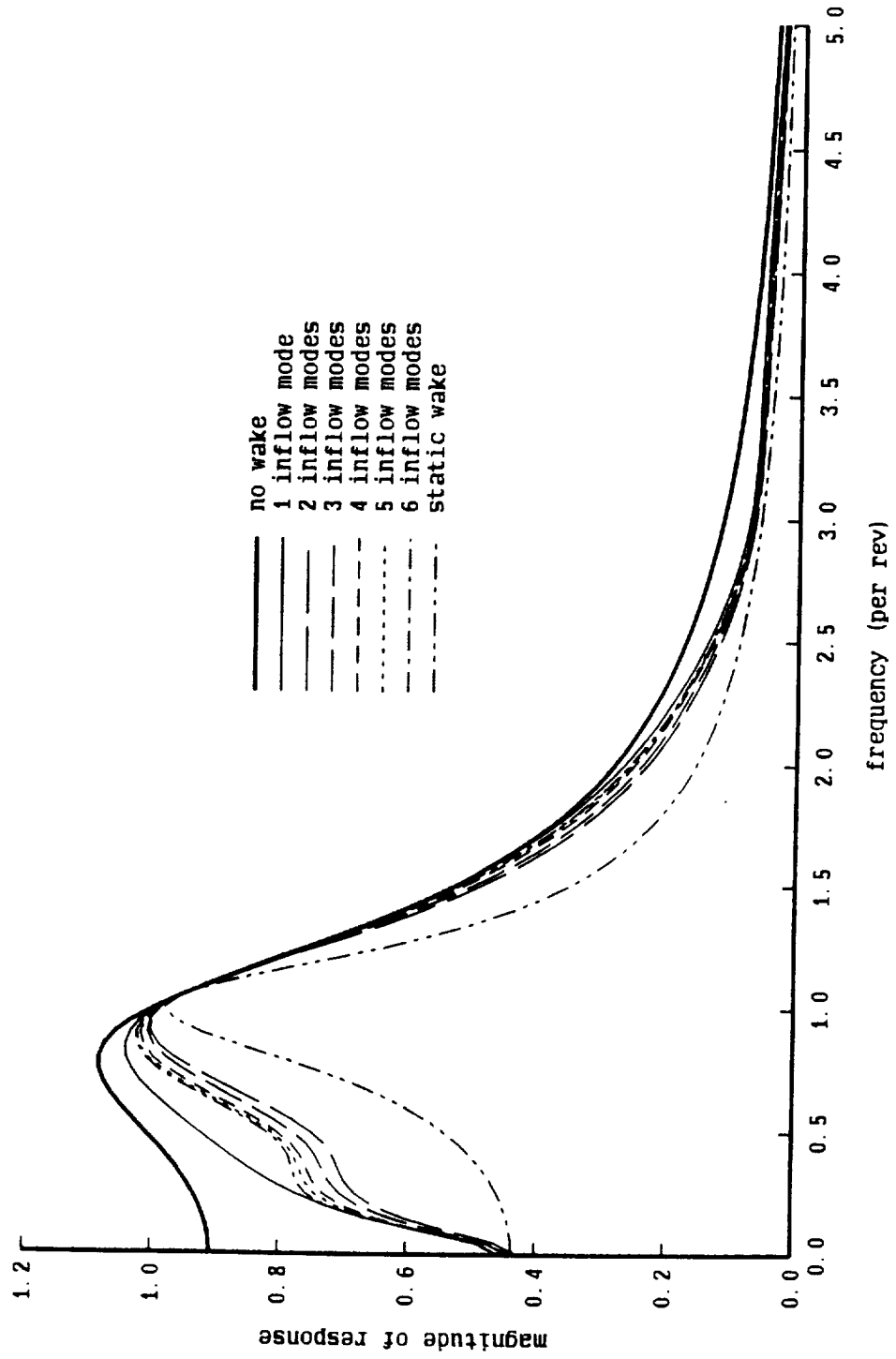


Figure 34b. Flap motion of hovering rotor with rolled up wake

3 blades, $CT/\sigma = 0.08$; coning response to collective pitch

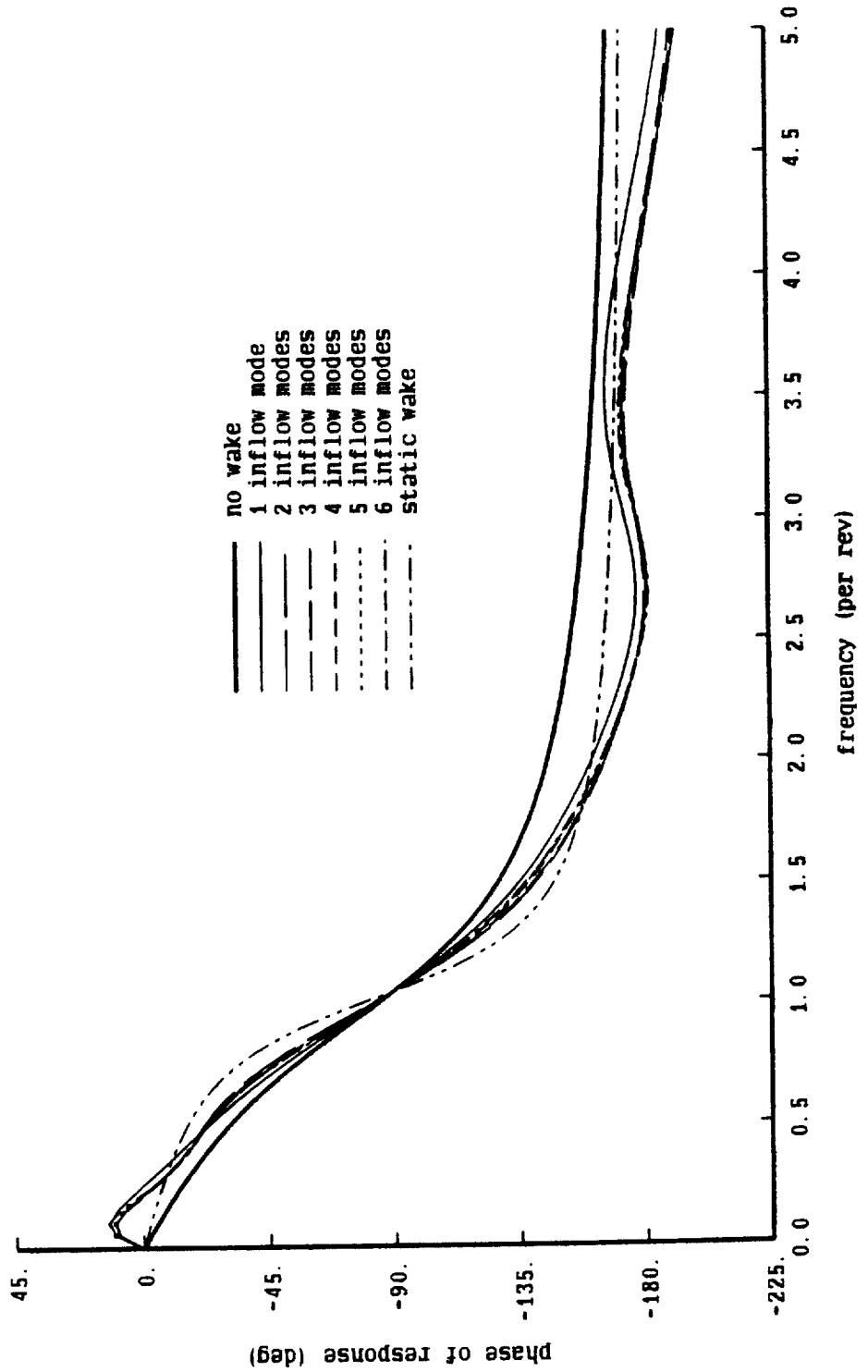


Figure 35a. Flap motion of hovering rotor with rolled up wake

hovering rotor; 6 inflow modes

3 blades, $CT/\sigma = 0.08$; coning response to collective pitch

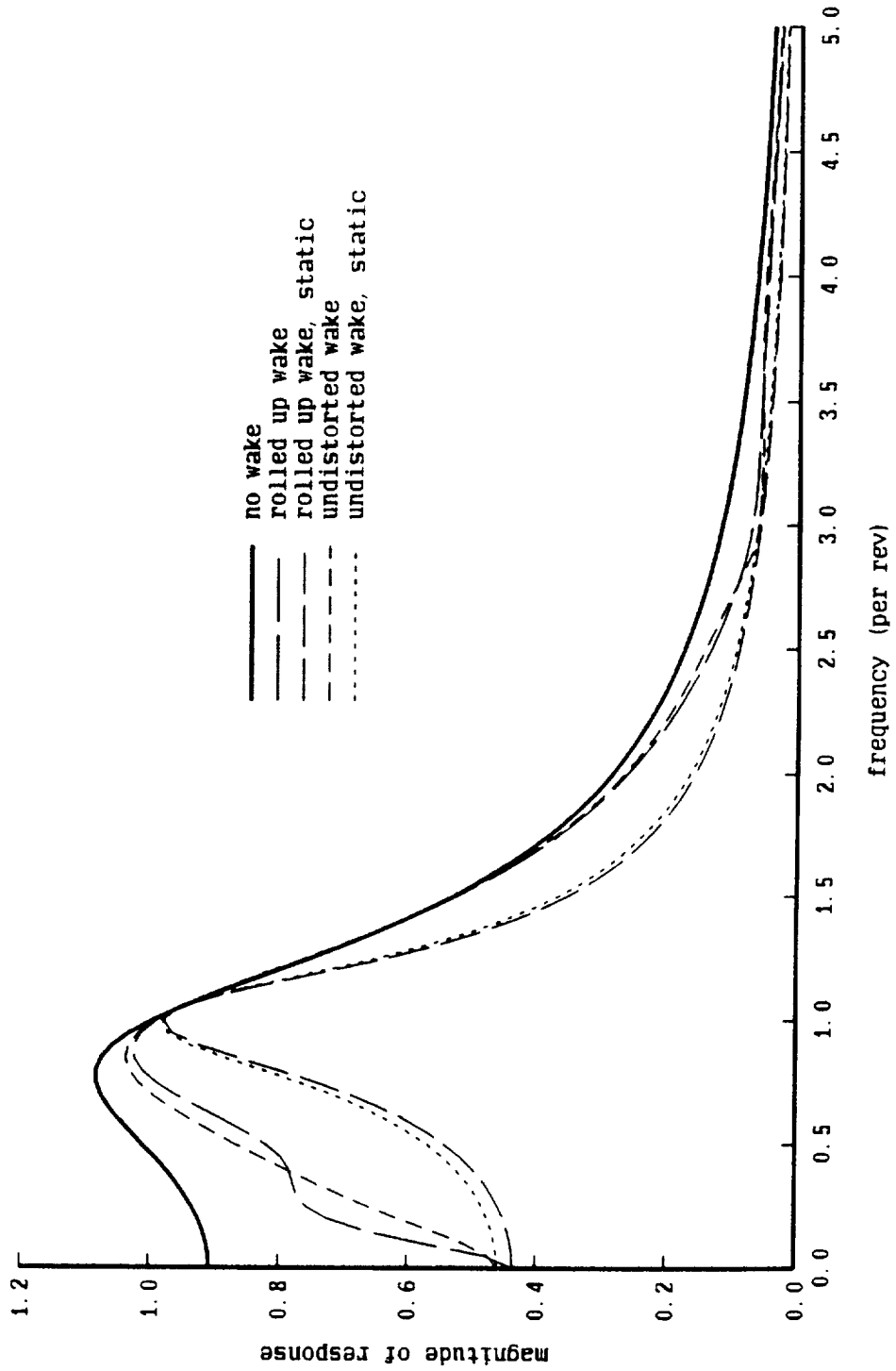


Figure 35b. Flap motion of hovering rotor with rolled up wake

hovering rotor; 6 inflow modes

3 blades, $CT/\sigma = 0.08$; coning response to collective pitch

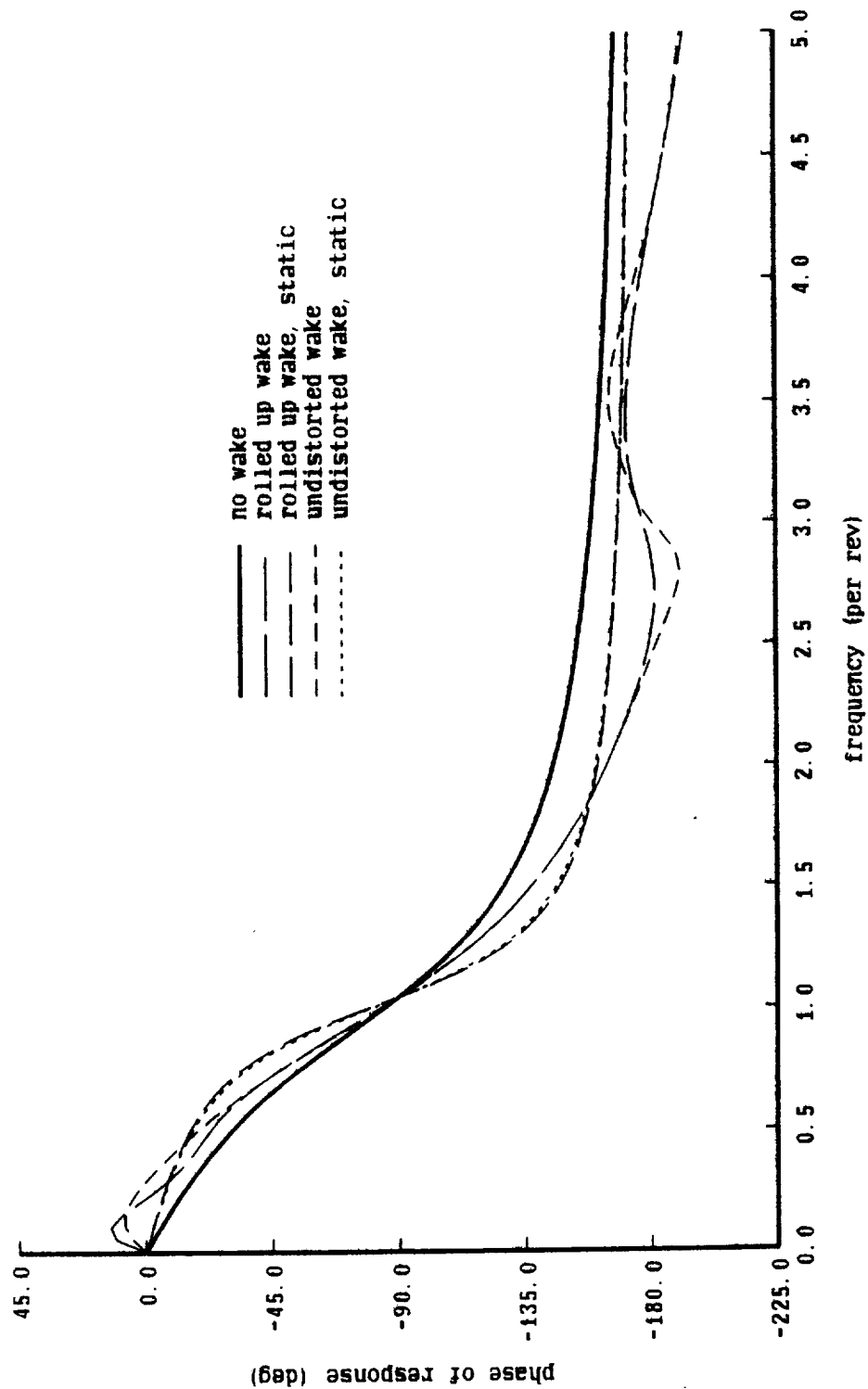


Figure 36a. Inflow response during flap motion; hovering rotor with rolled up wake

hovering rotor, rolled up wake; frequency = 0.0/rev
 3 blades, $CT/\sigma = 0.08$; inflow response to collective pitch

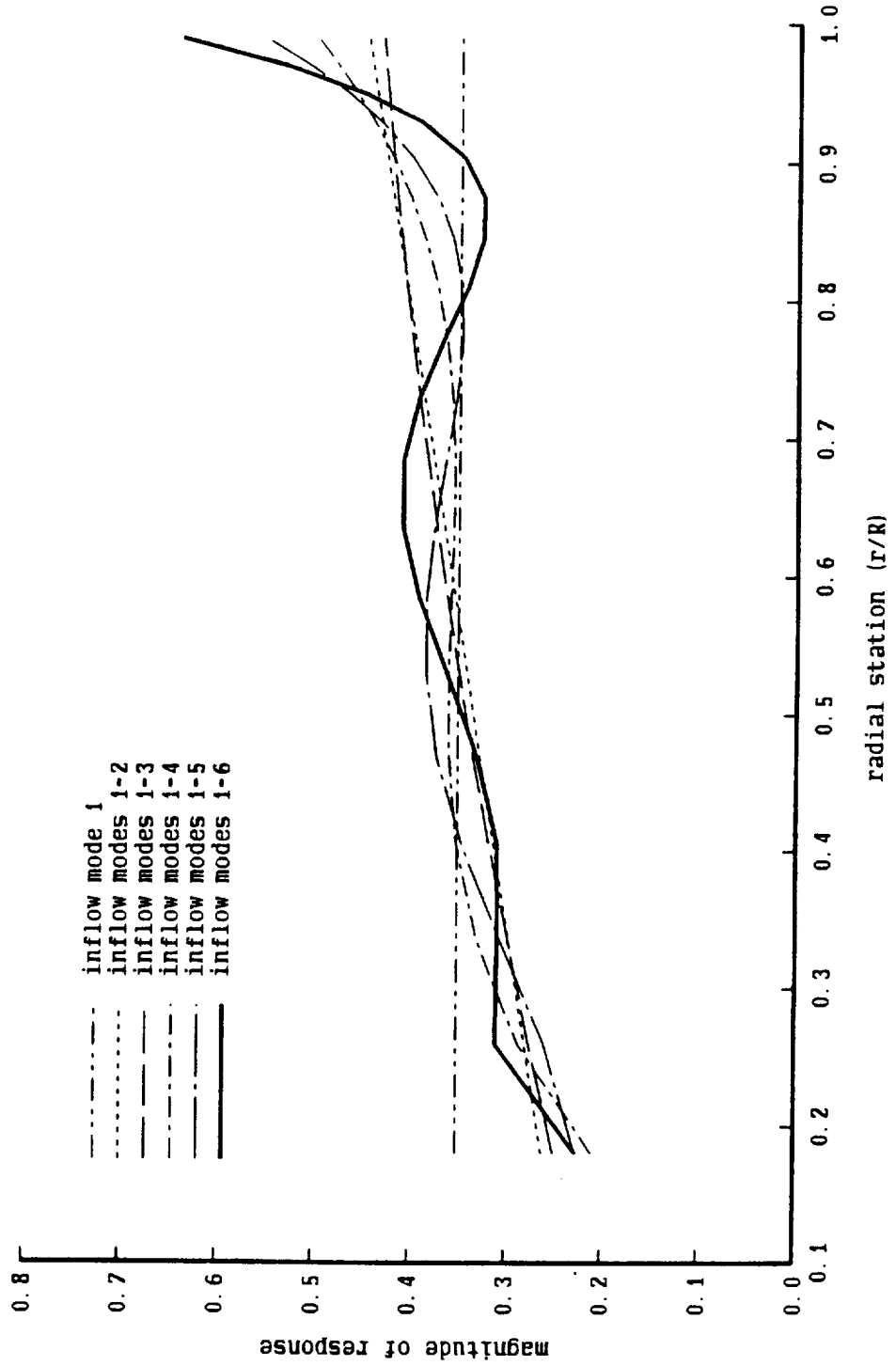


Figure 36b. Inflow response during flap motion; hovering rotor with rolled up wake

hovering rotor, rolled up wake; frequency = 0.40/rev
 3 blades, $CT/\sigma = 0.08$; inflow response to collective pitch

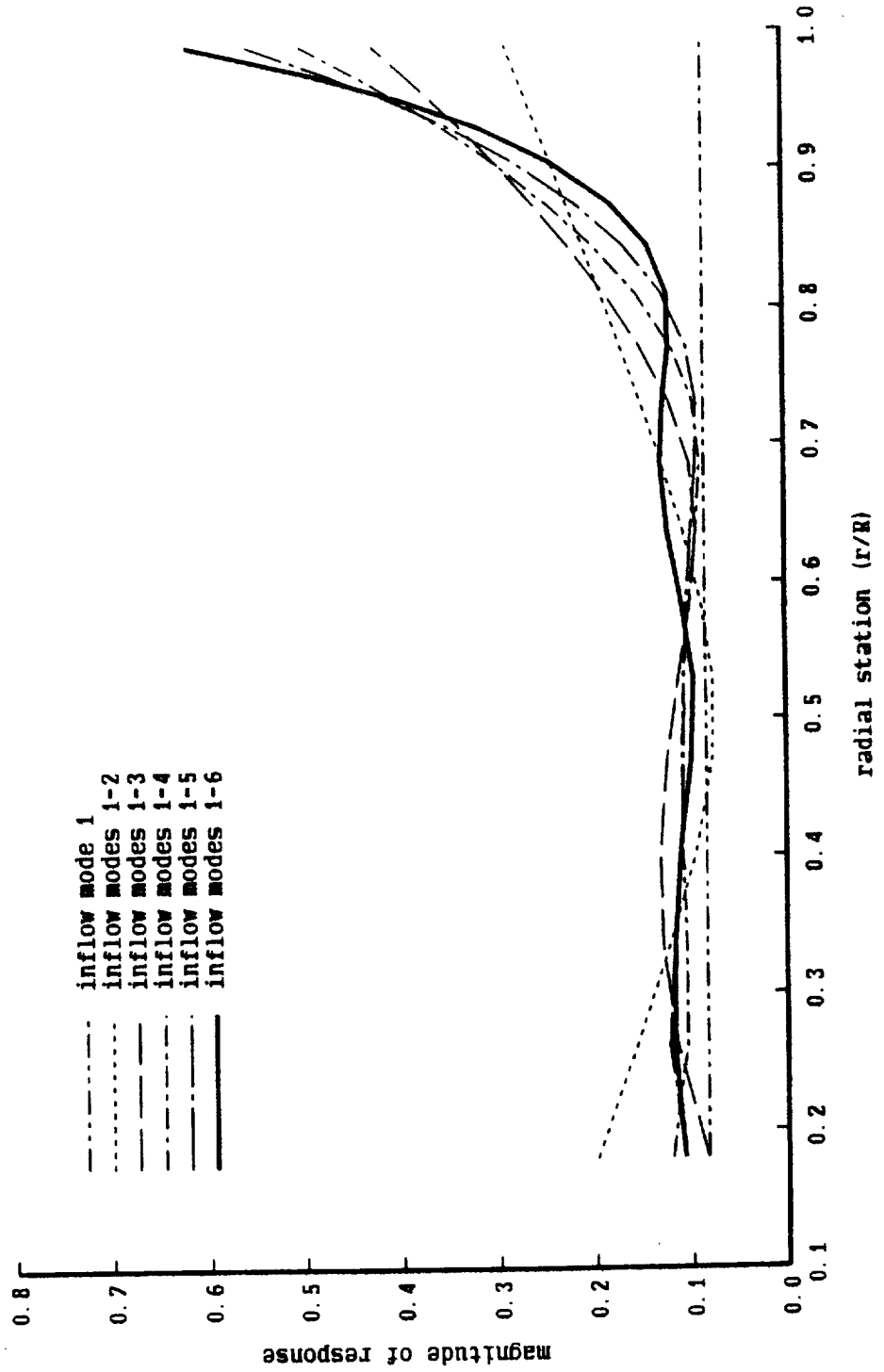


Figure 36c. Inflow response during flap motion; hovering rotor with rolled up wake

hovering rotor, rolled up wake; frequency = 2.25/rev
 3 blades, $CT/\sigma = 0.08$; inflow response to collective pitch

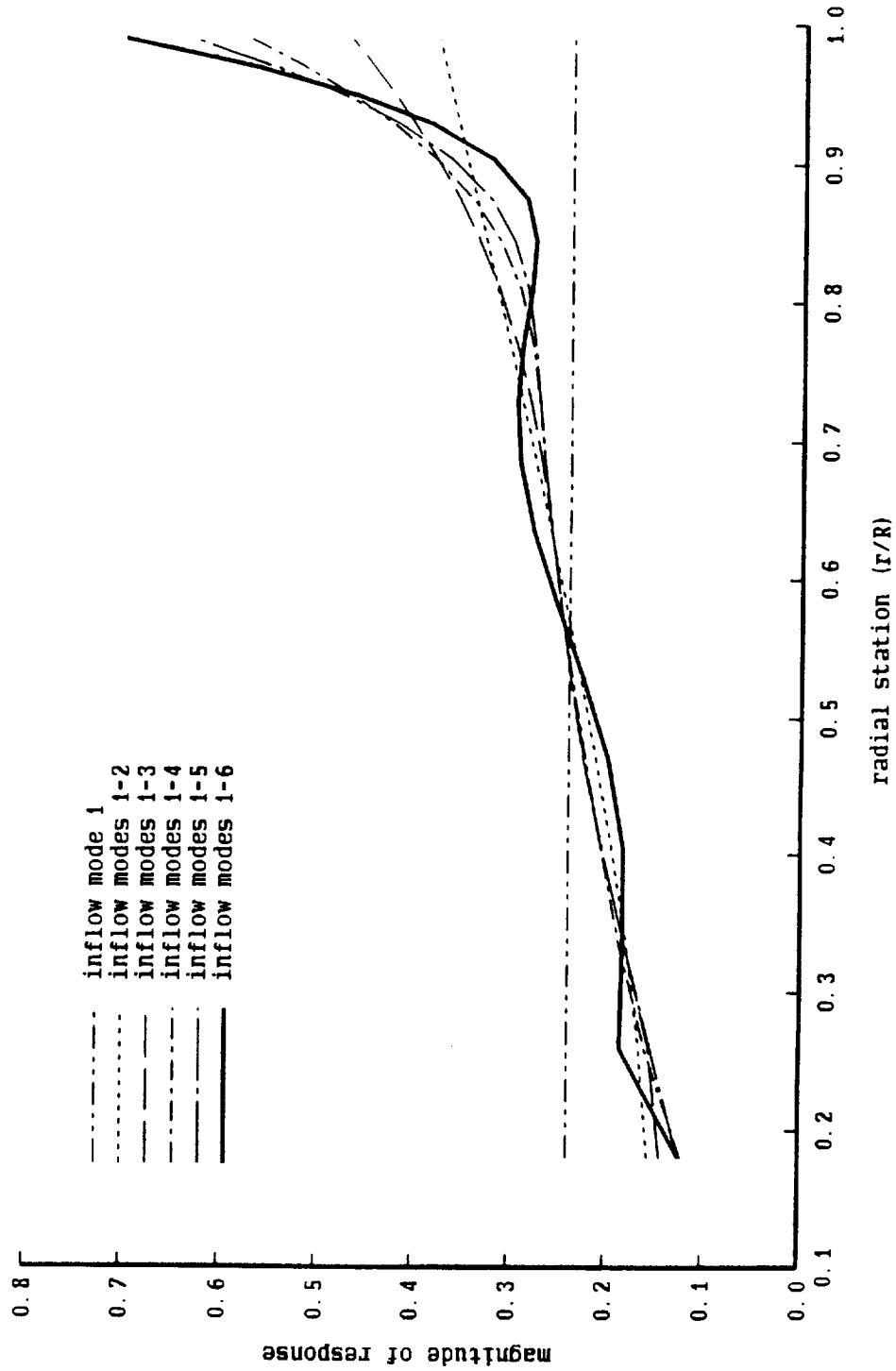


Figure 36d. Inflow response during flap motion; hovering rotor with rolled up wake

hovering rotor, rolled up wake; frequency = 0.40/rev

3 blades, $CT/\sigma = 0.08$; inflow response to collective pitch

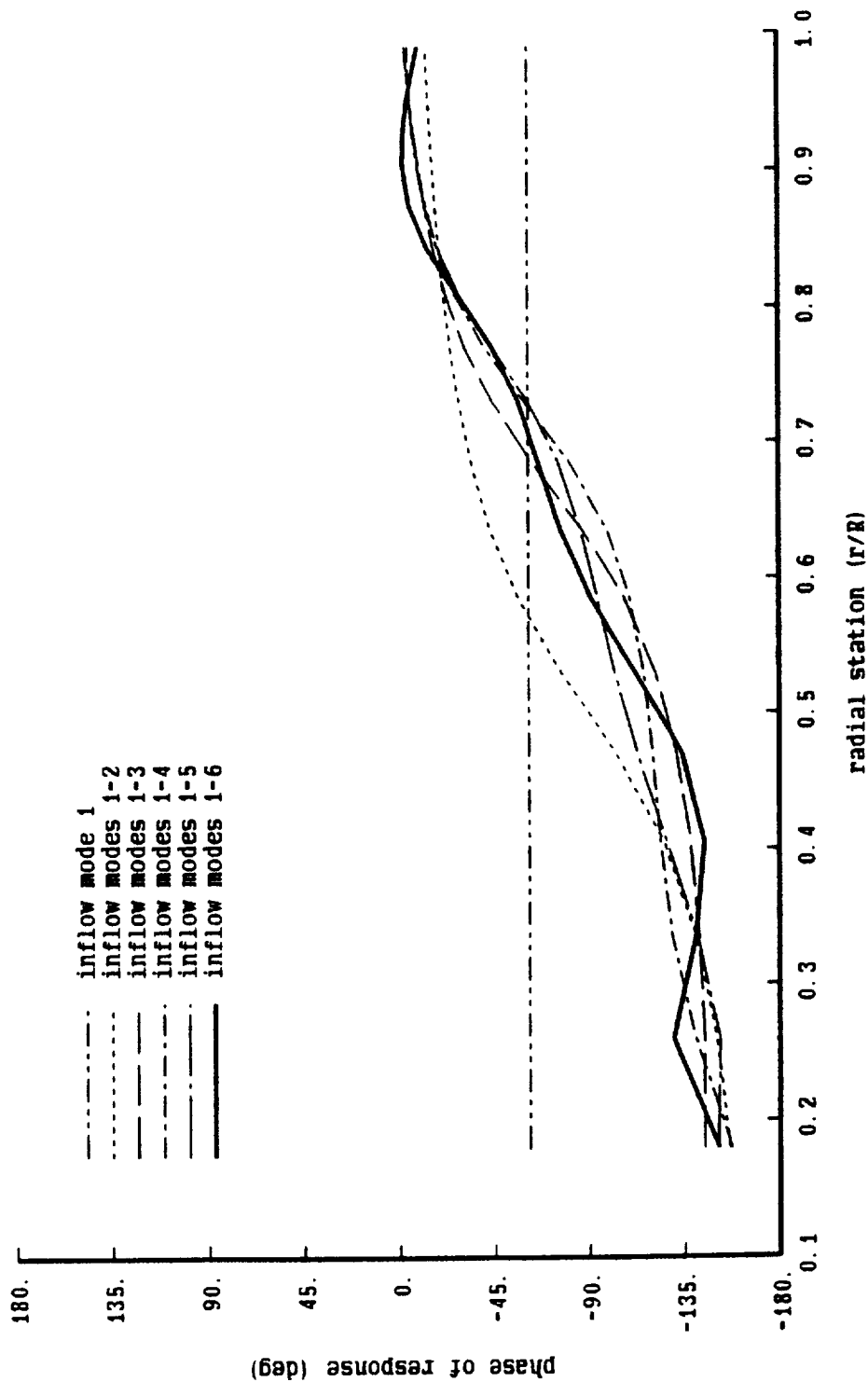


Figure 36e. Inflow response during flap motion; hovering rotor with rolled up wake

hovering rotor, rolled up wake; frequency = 2.25/rev
 3 blades, $CT/\sigma = 0.08$; inflow response to collective pitch

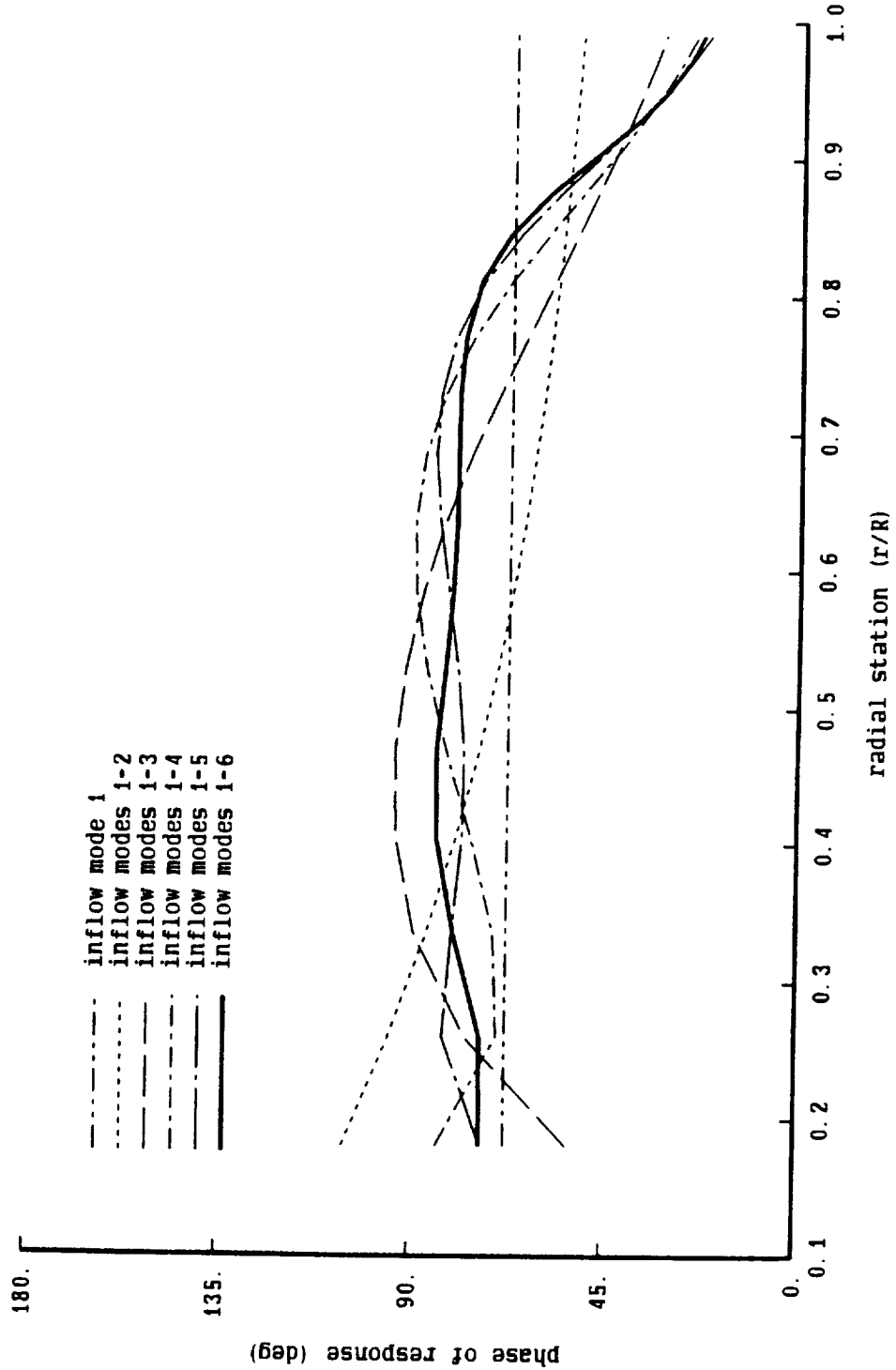


Figure 37a. Inflow response during flap motion; hovering rotor with rolled up wake

hovering rotor, rolled up wake; frequency = 0.0/rev
 3 blades, $CT/\sigma = 0.08$; inflow response to vertical hub velocity

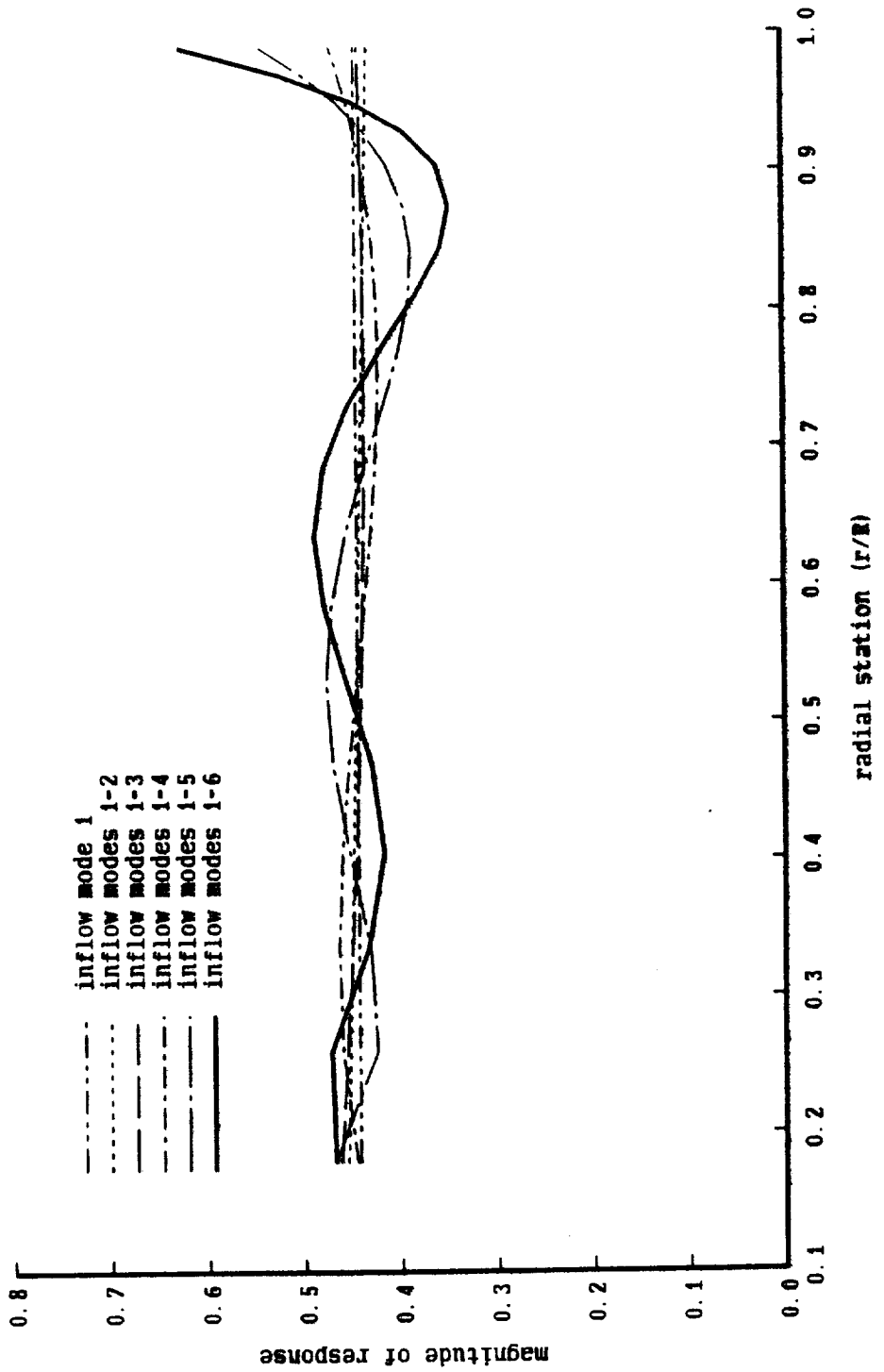


Figure 37b. Inflow response during flap motion; hovering rotor with rolled up wake

hovering rotor, rolled up wake; frequency = 0.40/rev
 3 blades, $CT/\sigma = 0.08$; inflow response to vertical hub velocity

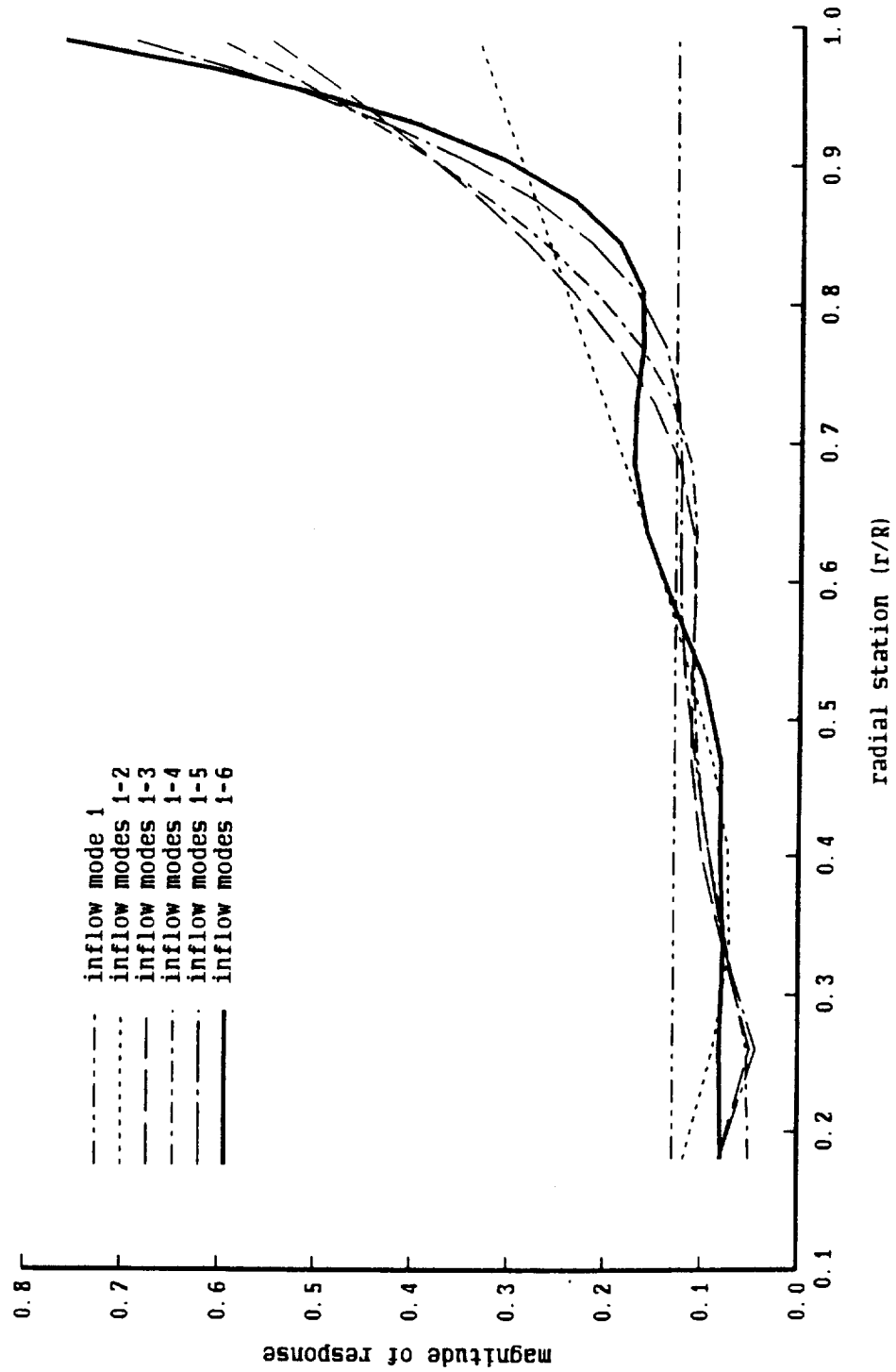


Figure 37c. Inflow response during flap motion; hovering rotor with rolled up wake

hovering rotor, rolled up wake; frequency = 2.25/rev
3 blades, $CT/\sigma = 0.08$; inflow response to vertical hub velocity

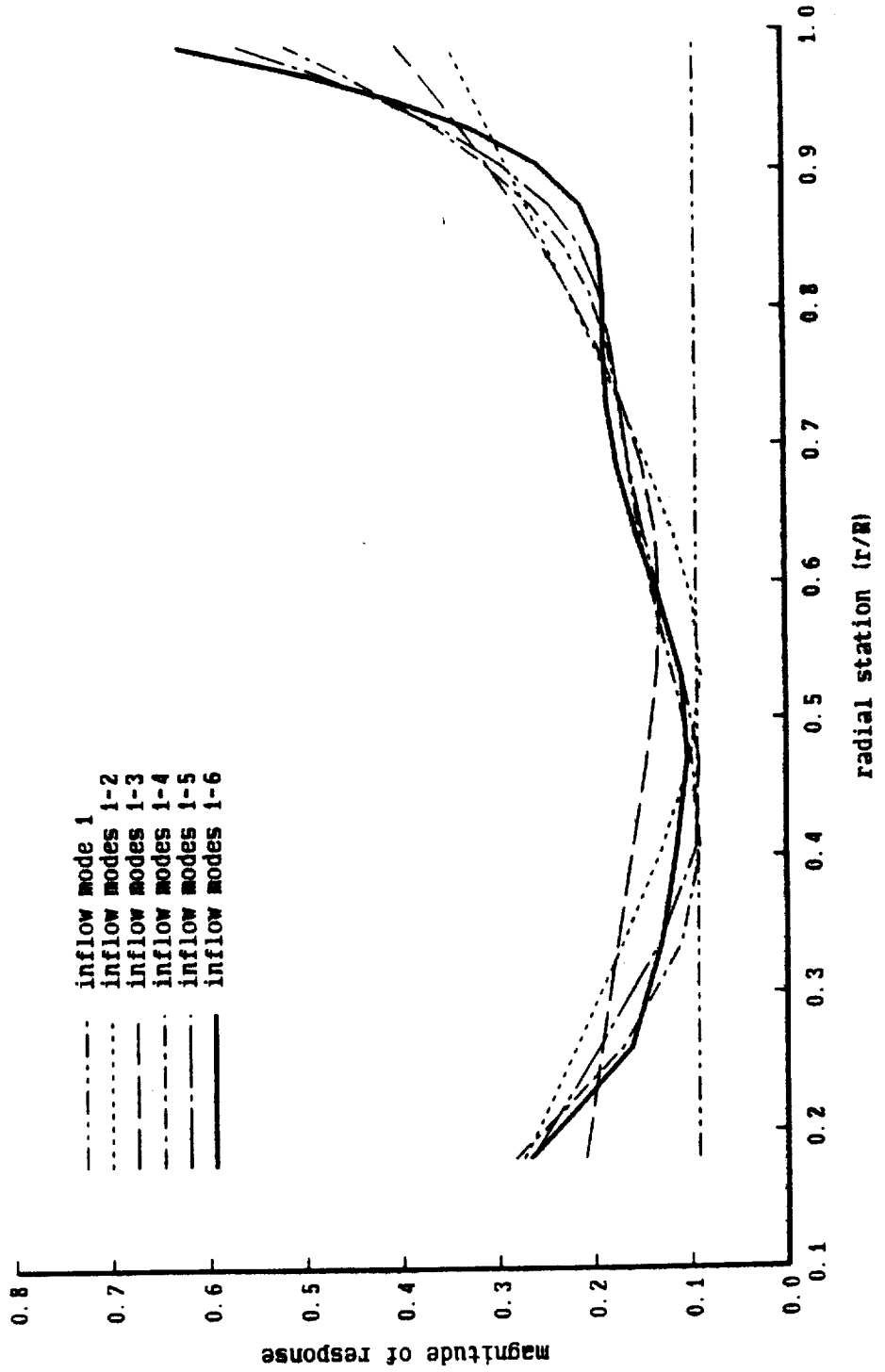


Figure 37d. Inflow response during flap motion; hovering rotor with rolled up wake

hovering rotor, rolled up wake; frequency = 0.40/rev
 3 blades, $CT/\sigma = 0.08$; inflow response to vertical hub velocity

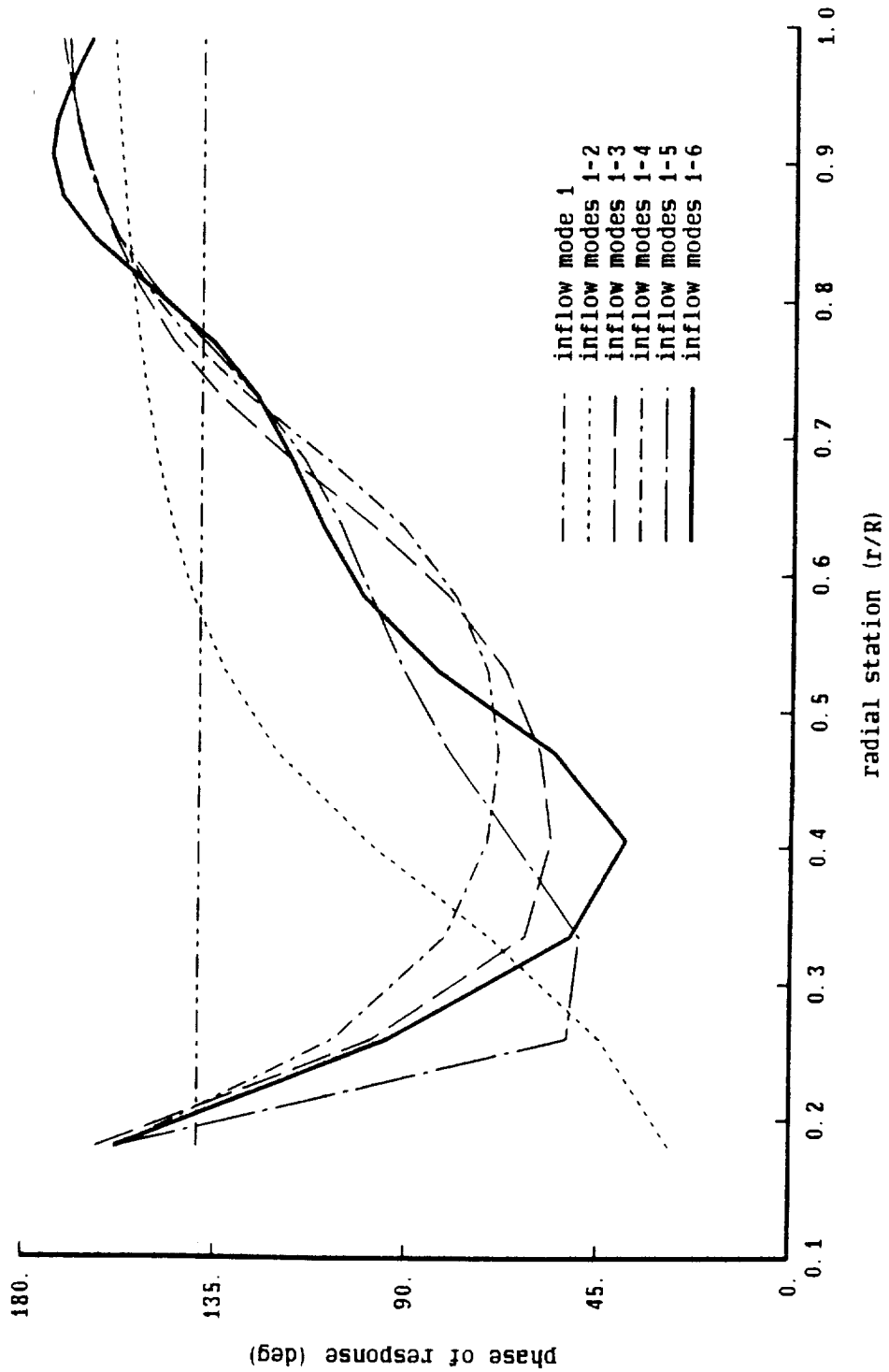


Figure 37e. Inflow response during flap motion; hovering rotor with rolled up wake

hovering rotor, rolled up wake; frequency = 2.25/rev

3 blades, $CT/\sigma = 0.08$; inflow response to vertical hub velocity

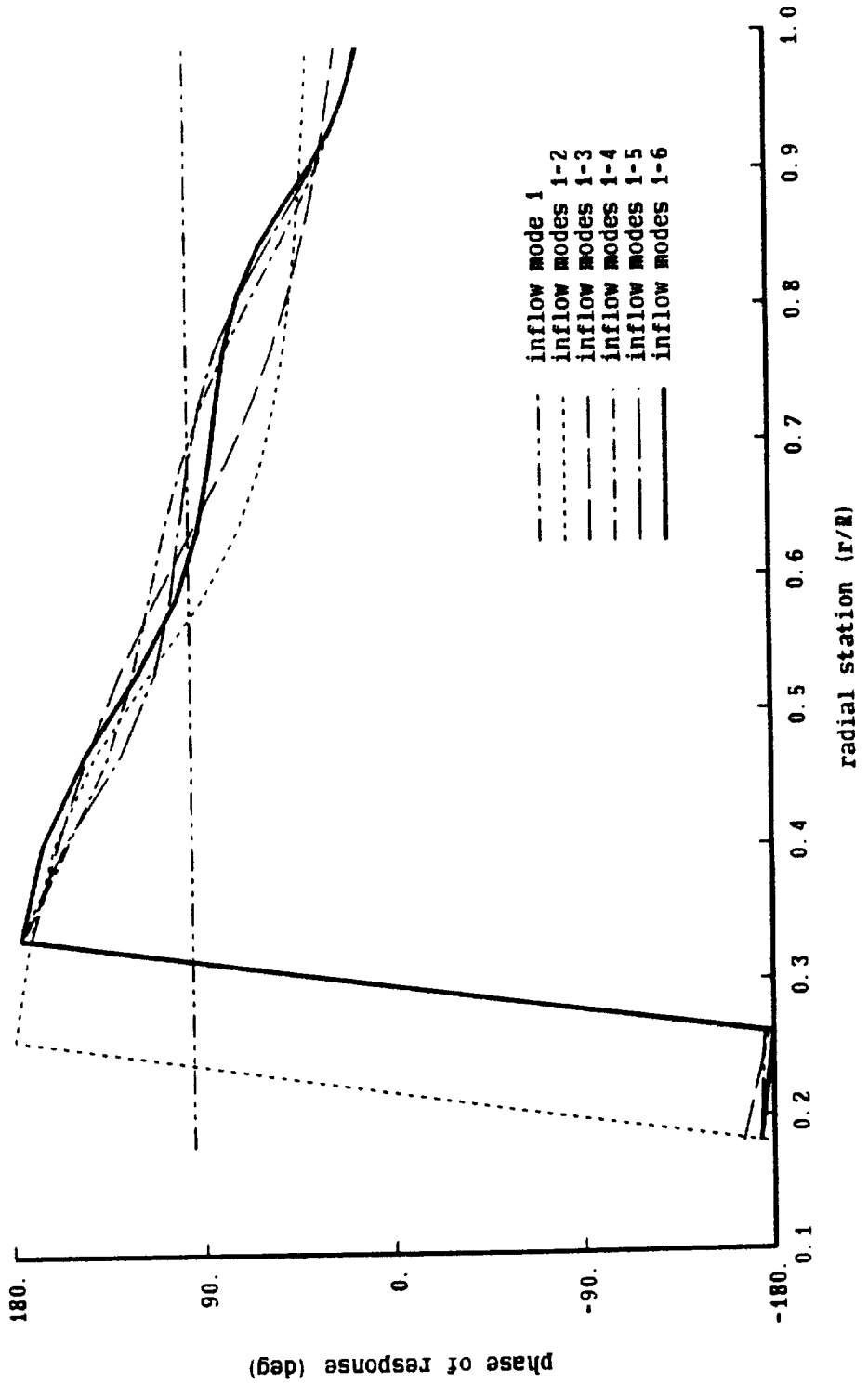


Figure 38a. Inflow response during flap motion; hovering rotor with rolled up wake

hovering rotor; 6 inflow modes

3 blades, $CT/\sigma = 0.08$; inflow response to collective pitch

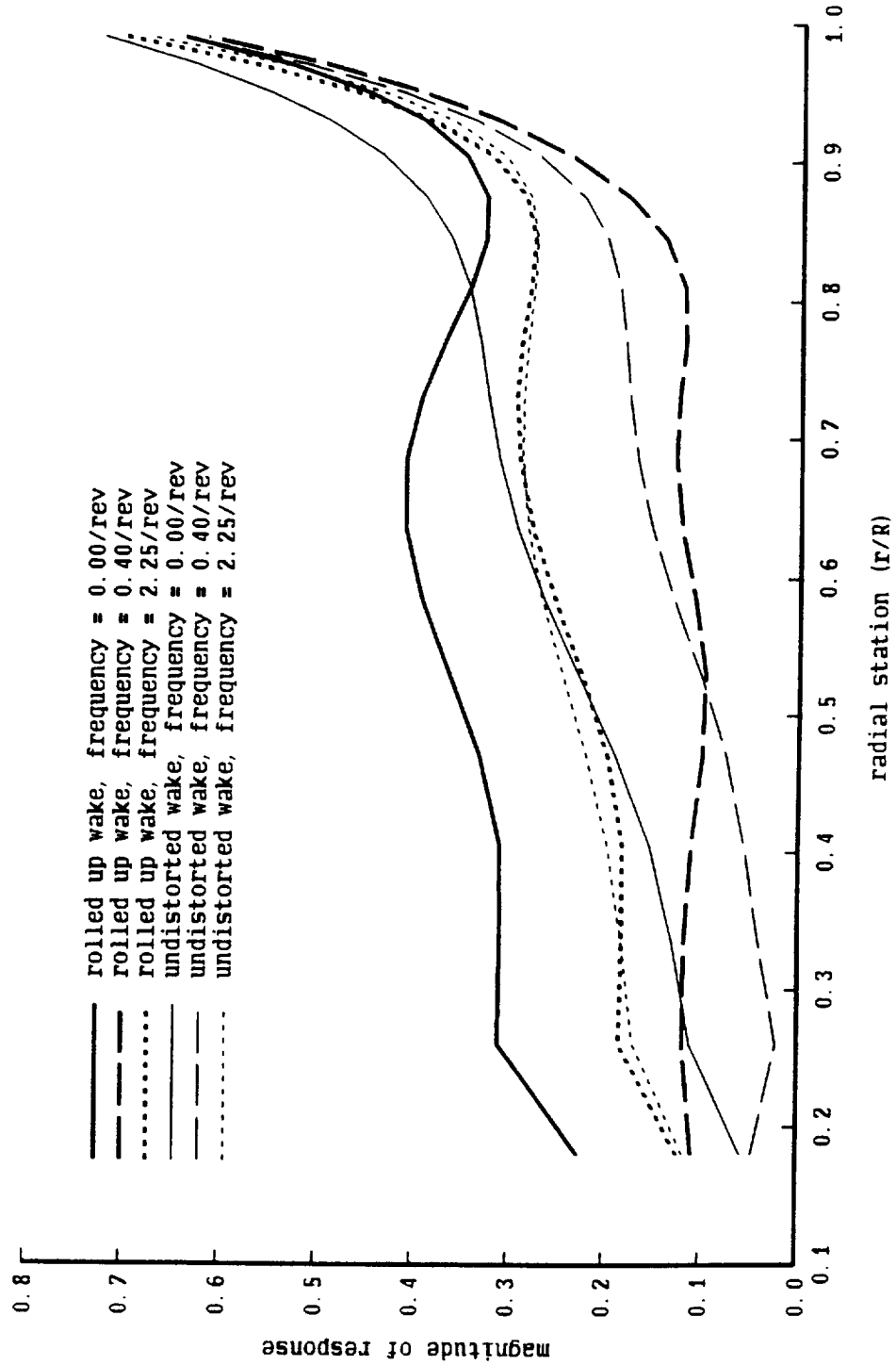


Figure 38b. Inflow response during flap motion; hovering rotor with rolled up wake

hovering rotor; 6 inflow modes

3 blades, $CT/\sigma = 0.08$; inflow response to vertical hub velocity

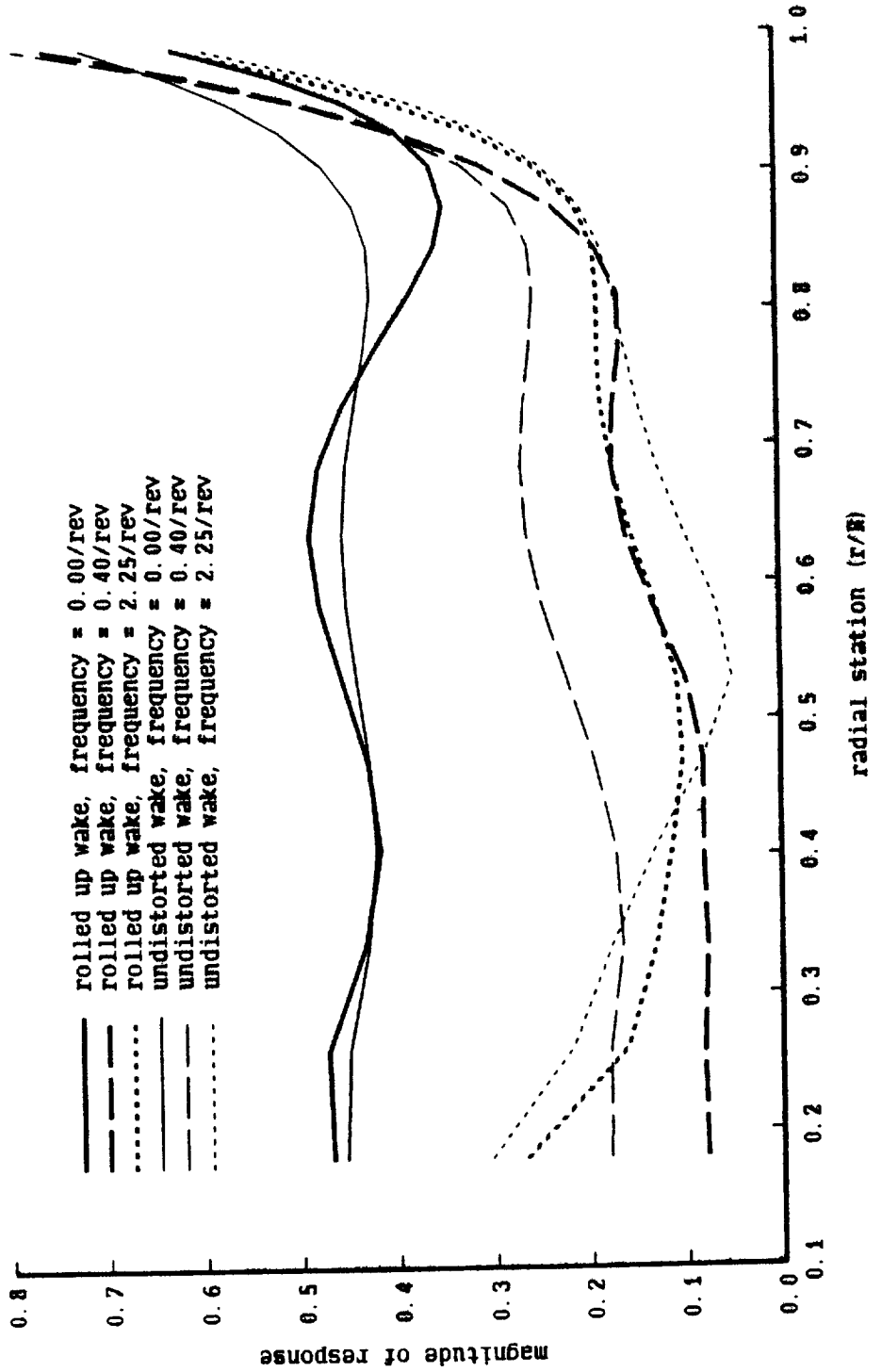


Figure 38c. Inflow response during flap motion; hovering rotor with rolled up wake

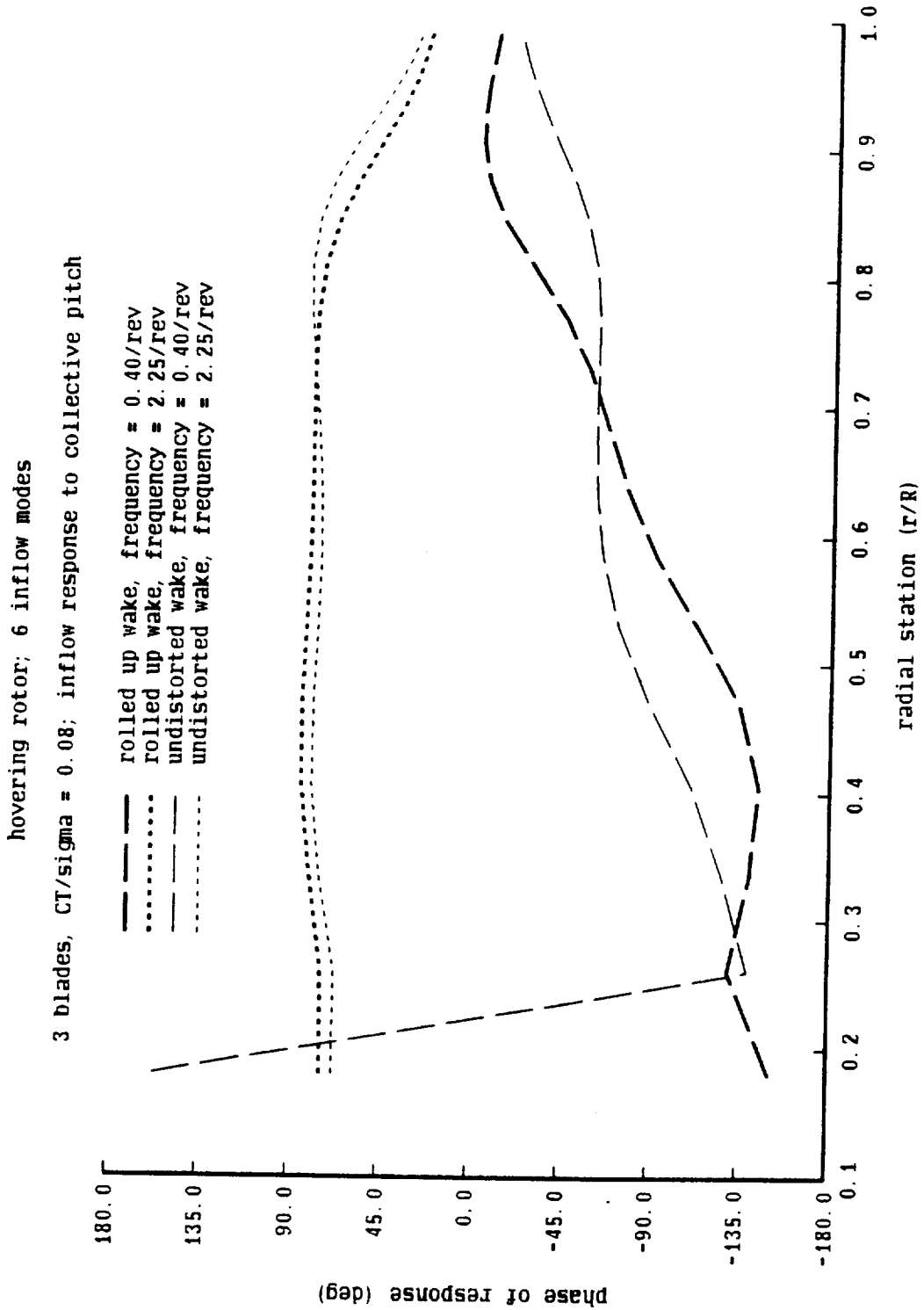


Figure 38d. Inflow response during flap motion; hovering rotor with rolled up wake

hovering rotor; 6 inflow modes

3 blades, $CT/\sigma = 0.08$; inflow response to vertical hub velocity

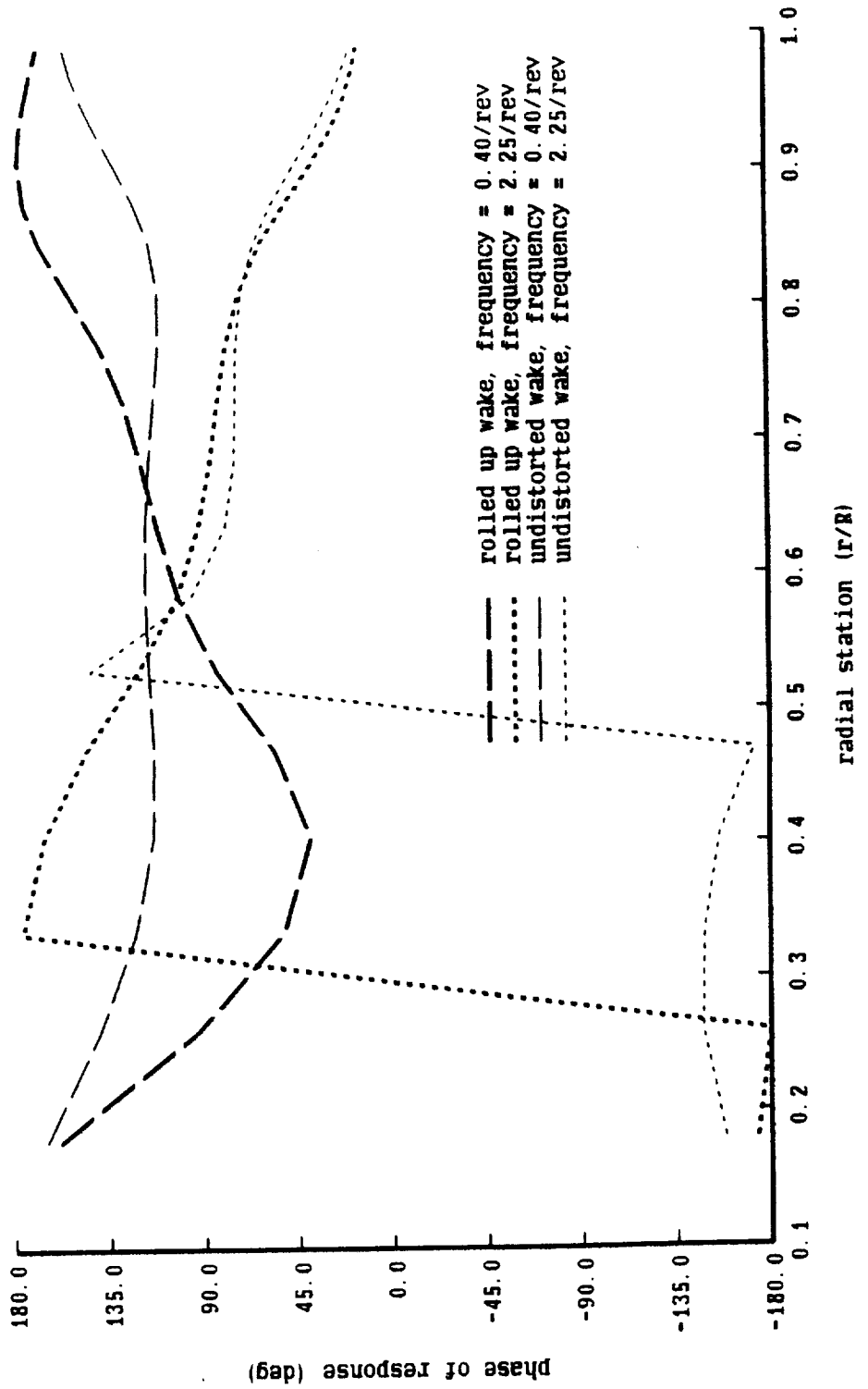
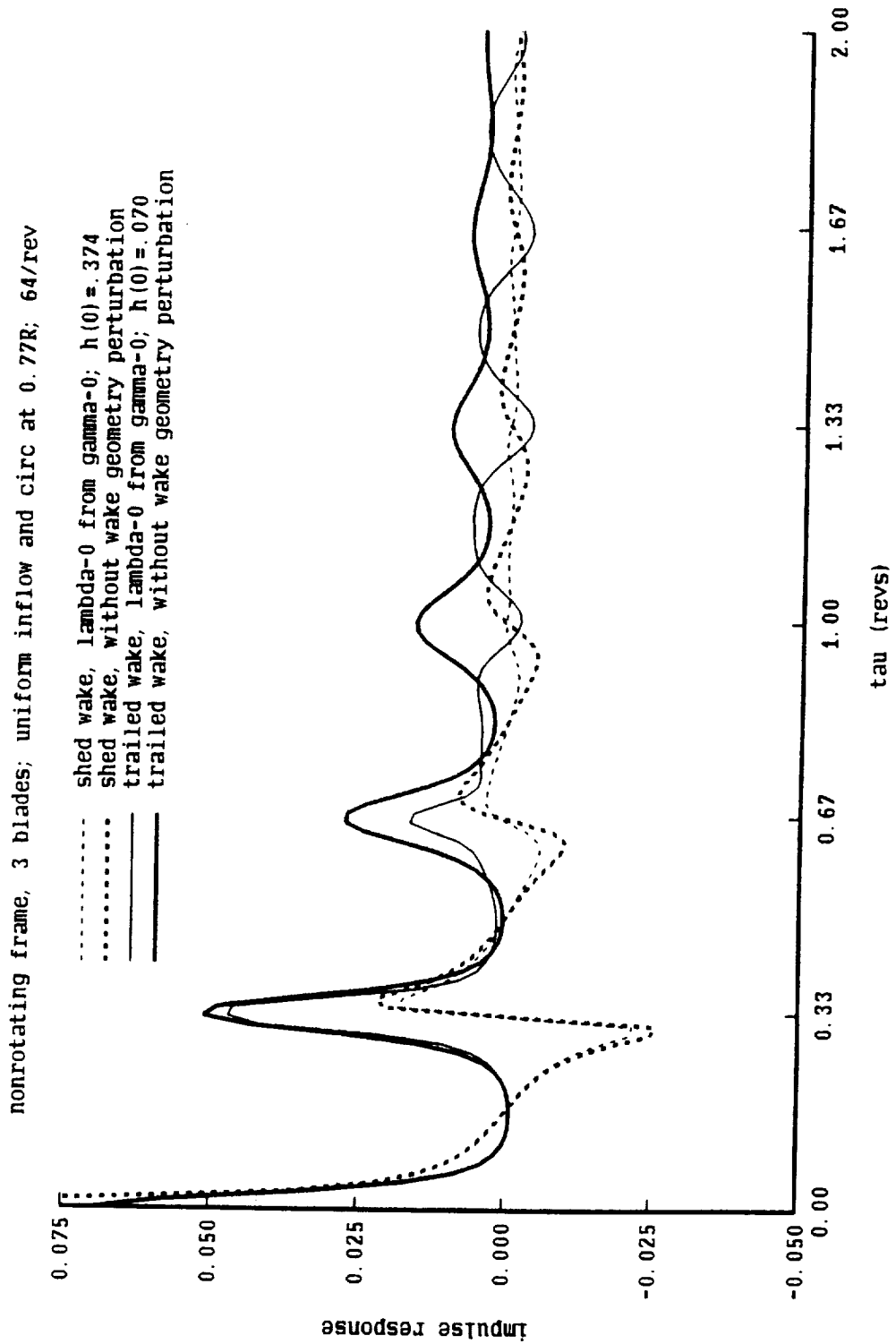


Figure 39. Influence of wake geometry perturbation on impulse response; hovering rotor with undistorted wake





Report Documentation Page

1. Report No. NASA CR-177570		2. Government Accession No.		3. Recipient's Catalog No.	
4. Title and Subtitle Feasibility Investigation of General Time-Domain Unsteady Aerodynamics of Rotors				5. Report Date October 1990	
				6. Performing Organization Code	
7. Author(s) Wayne Johnson				8. Performing Organization Report No. A-90304	
				10. Work Unit No. 505-61-51	
9. Performing Organization Name and Address Johnson Aeronautics P.O. Box 1253 Palo Alto, CA 94302				11. Contract or Grant No. NAS2-13125	
				13. Type of Report and Period Covered Contractor Report	
12. Sponsoring Agency Name and Address National Aeronautics and Space Administration Washington, DC 20546-0001				14. Sponsoring Agency Code	
15. Supplementary Notes Point of Contact: Benton Lau, Ames Research Center, M/S T-042, Moffett Field, CA 94035-1000 (415) 604-6714 or FTS 464-6714					
16. Abstract <p>The feasibility of a general theory for the time-domain unsteady aerodynamics of helicopter rotors is investigated. The wake theory gives a linearized relation between the downwash and the wing bound circulation, in terms of the impulse response obtained directly in the time domain. This approach makes it possible to treat general wake configurations, including discrete wake vorticity with rolled-up and distorted geometry. The investigation establishes the approach for model order reduction; determines when a constrained identification method is needed; verifies the formulation of the theory for rolled-up, distorted trim wake geometry; and verifies the formulation of the theory for wake geometry perturbations. The basic soundness of the approach is demonstrated by the results presented. A research program to complete the development of the method is outlined. The result of this activity will be an approach for analyzing the aeroelastic stability and response of helicopter rotors, while retaining the important influence of the complicated rotor wake configuration.</p>					
17. Key Words (Suggested by Author(s)) Helicopter rotors Unsteady aerodynamics Aeroelasticity				18. Distribution Statement Unclassified-Unlimited Subject Category-02	
19. Security Classif. (of this report) Unclassified		20. Security Classif. (of this page) Unclassified		21. No. of Pages 220	22. Price A10